FAST NEUTRON SCATTERING

by

ABDUL WAHEED, B.Sc. Hons., M.Sc.

Thesis submitted for the degree of

DOCTOR OF PHILOSOPHY

University of Edinburgh

February 1975

ABSTRACT OF THESIS

An associated particle time-of-flight system for the $D(d,n)He^3$ reaction has been developed for studying fast neutron scattering and polarization. The major problem to be overcome in such a system is that most of the pulses in the associated particle detector are from elastically scattered deuterons. In order to eliminate these an Electrostatic Analyser has been designed, developed and tested at different deuteron energies on the 0.5 MeV Van de Graaff accelerator. A review has been made of the previous work on the associated particle technique with the $D(d,n)He^3$ reaction. Graphs are presented showing the relationships between parameters of the neutrons and their associated He^3 particles for 50 keV to 500 keV deuteron energies.

A polarimeter has been designed and developed for studying the angular distribution of polarization and the differential cross-section of neutrons elastically scattered from different nuclei. In order to speed up the data accumulation three pairs of neutron detectors have been fixed to the polarimeter at different scattering angles. The electronic circuits constructed by the author, pulse shape discrimination units, scaler, Or gate units, interface logic units, variable delay units, fast amplifier, fast preamplifier and single channel analyser, are described in the Appendix. Details of the polarimeter are described.

An accurately collimated monoenergetic neutron beam of energy 2.9 MeV was produced at reaction laboratory angle of 49° with respect to the deuteron beam. Differential elastic scattering cross-sections and the angular dependence of the polarization produced from Fe, Cu, I, Hg and Pb has been studied in the range 20° - 160° (Lab) at the neutron energy of

2.9 MeV. A review has been made of previous angular dependence of polarization studies with reference to their optical model fits. The measurements both on the differential elastic scattering cross-section and the angular dependence of the polarization are compared with the optical model calculations.

Differential elastic scattering cross-section and the angular dependence of the polarization for Cu and Pb have also been measured at 16.1 MeV neutron energy using the $T(d,n)He^4$ reaction. A 3 MeV pulsed beam Van de Graaff accelerator at A.E.R.E., Harwell has been used for this study. The measurements on the differential elastic scattering cross-section and the angular dependence of polarization at 16 MeV neutron energy are compared with the optical model calculations at nearby 14 MeV neutron energy, as no 16 MeV calculations are available.

C O N T E N T S

CHAPTER III

THE FAST NEUTRON POLARIMETER

CHAPTER VI

RESULTS AND DISCUSSION

APPENDIX A

CHAPTER I

CHAPTER I

Neutron Scattering

1.1 Introduction

When neutrons are incident on a target nucleus many competing reaction and scattering processes may take place. We are concerned here with elastic scattering.

The experimentally observed elastic scattering of neutrons is comprised of two types of scattering, shape elastic scattering and the compound elastic scattering. The formation of the compound nucleus, suggested by Bohr[1] has been very useful in correlation and interpretation of nuclear reactions. The compound nucleus, in which the incident neutron is completely absorbed, breaks up leading to elastic or inelastic scattering of the neutron or the emission of another particle. The mode of break up of the compound nucleus is independent of its formation and depends on its energy and angular momentum. The compound elastic scattering is a process in which a compound nucleus is formed first and then it decays through the entrance channel leading to elastic scattering of neutrons.

The angular distribution of elastically scattered 14 MeV neutrons from lead was first measured by Amaldi et al[2]. Later on the differential scattering cross-sections for a large number of elements for 1 MeV neutrons were measured by Walt and Barschall[3] and their theoretical interpretation was accomplished by Feshbach et al[4] on the basis of the nuclear optical potential model. The differential elastic scattering cross-section measurements[3,5-10] on lead and bismuth at different neutron energies, reveal that differential cross-section curves are relatively flat at lower neutron energies and with increase in

incident neutron energy the forward peaks become more pronounced and secondary maxima and minima which appear at larger angles move to smaller angles. The changes in shape of differential cross-section curves with increase in atomic weight are similar to the changes which occur with increasing energy, i.e. the forward peak becomes more pronounced and the secondary maxima and minima move to smaller angles.

1.2 Optical Model

The differential elastic scattering cross-sections for nuclei can be described with good accuracy by the optical model[11-17]. In the optical model the neutron-nucleus interaction is represented by a complex potential well. When a neutron enters the nucleus the probability for the formation of a compound nucleus will be smaller than unity and so it has a finite probability of leaving the nucleus without any exchange of energy[4]. The neutron-nucleus interaction is represented by a real potential when there is no energy exchange and a complex potential, that is a potential with a absorption term, is used if there is an energy exchange between neutron and nucleus. The nucleus is treated as a partially transparent medium and the neutrons are considered as being, diffracted, refracted and absorbed by the spherical nucleus. A local central complex potential can be represented by

$$- V(r) = Uf(r) + iWg(r) \qquad ..(1.2.1)$$

where U and W are the amplitudes of the real and imaginary parts of the potential respectively; $f(r)$ and $g(r)$ are the form factors describing the radial variation of the potentials. The imaginary part of the potential is related to compound nucleus formation and includes all nuclear reactions.

Using this model the information about the total cross-section, the differential cross-section for shape elastic scattering and the cross-section for the formation of a compound nucleus can be obtained.

The elastic scattering cross-section can be represented by[4,19]

$$\sigma_{el} = \sigma_{se} + \sigma_{ce} \qquad ..(1.2.2)$$

where σ_{se} is the shape elastic scattering cross-section, the scattering process which does not proceed through an intermediate compound state. σ_{ce} is the compound elastic scattering cross-section. The differential compound elastic scattering cross-section can be calculated by a method proposed by Hauser and Feshbach[18]. They used two statistical assumptions, first about the density of levels of the compound nucleus system and the second one that all compound states for which energy, parity and angular momentum are conserved are populated with a probability proportional to the penetrability of the incident neutron.

Neutrons scattered from nuclei are generally observed to be polarized and to include this fact a further refinement of the potential given by equation (1.2.1) due to Bjorklund and Fernbach[11] is the inclusion of a spin-orbit term. This spin-orbit term however makes only a minor contribution to the differential scattering cross-section mainly in the region of the diffraction minima[20].

The optical model has some limitations in its comparison with the experimental cross-sections. At low incident neutron energies the compound nucleus can usually exist with a series of fairly sharp states well separated in energy. Therefore, scattering cross-sections will show characteristic variations when the energy spread of the incident beam is less than the mean

level spacing of the nucleus. The characteristic variations in elastic scattering cross-section cannot be accounted for by an optical model potential. The experimentally observed elastic scattering cross-sections will not correspond to the calculated shape elastic scattering from the optical model due to the presence of the compound elastic scattering.

At higher energies above several MeV however the compound nucleus levels crowd together and there should be no resonance effects due to single levels and the optical model potential gives a good fit to the experimental cross-sections[14]. The compound elastic scattering is expected to be small in this case due to many energetically possible modes of decay of the compound nucleus.

The optical model is more successful in interpreting the scattering from heavy and medium weight nuclei than for light nuclei since heavier and medium weight nuclei have got much closer energy levels. For medium and heavier nuclei therefore the isolated resonances do not affect the interaction as much as they do for lighter nuclei.

1.3 Polarization

Schwinger[21] suggested that fast neutrons elastically scattered by He^4 should be polarized, i.e. their spin vectors should be aligned preferentially in a plane normal to the scattering plane. It was proposed by Wolfenstein[22], based on the spin-orbit force[23] in $D(d,n)He^3$ reaction that the neutrons produced in the reaction should be polarized even if both the incident particles and the target nuclei are initially unpolarized. The principle of measuring neutron polarization has been given in detail by Haeberli[24].

In the case of elastic scattering, due to the presence of spin-orbit coupling, neutrons with spin up and down are preferentially scattered respect-

ively to one side or the other of the incident beam. The direct method of measuring neutron polarization involves a double process. A typical geometry for fast neutron polarization measurements is shown in Fig. (1). Considering the $D(d,n)He^3$ reaction, when a beam of unpolarizedcharged particles of energy E from an accelerator is incident on an unpolarized target A, then at an angle θ_1 neutrons of energy E_n and polarization P_n are produced. The magnitude of neutron polarization is expressed as:

$$P_n(E, \theta_1) = \frac{N^+ - N^-}{N^+ + N^-} \qquad ..(1.3.1)$$

where N^+ and N^- are the proportions of neutrons having spin vectors aligned parallel and antiparallel to $\bar{n}_1$; where $\bar{n}_1$ is normal to the reaction plane.

The neutrons are then scattered elastically by a sample B through an angle θ_2 and azimuthal angle ϕ (not shown in the figure); ϕ is the angle between the plane of the reaction at target A and the plane of the scattering at sample B. The differential scattering cross-section of sample B is given by

$$\sigma(E_n, \theta_2, \phi) = \sigma(E_n, \theta_2) \left[1 + P_n(E, \theta_1) A_2(E_n, \theta_2) \cos\phi \right] \qquad ..(1.3.2)$$

where $\sigma(E_n, \theta_2)$ is the unpolarized differential elastic scattering cross-section and $A_2(E_n, \theta_2)$ is the analysing power of the scatterer B. The analysing power $A_2(E_n, \theta_2)$ is equal to the polarization $P_2(E_n, \theta_2)$ which would be produced in the elastic scattering of unpolarized neutrons of the same energy E_n, through the same scattering angle θ_2. The equation (1.3.2) can be re-written as,

$$\sigma(E_n, \theta_2, \phi) = \sigma(E_n, \theta_2) \left[1 + P_n(E, \theta_1) P_2(E_n, \theta_2) \cos\phi \right] \qquad ..(1.3.3)$$

when $\phi = 0^\circ$ and $\phi = 180^\circ$ the above equation (1.3.3) gives

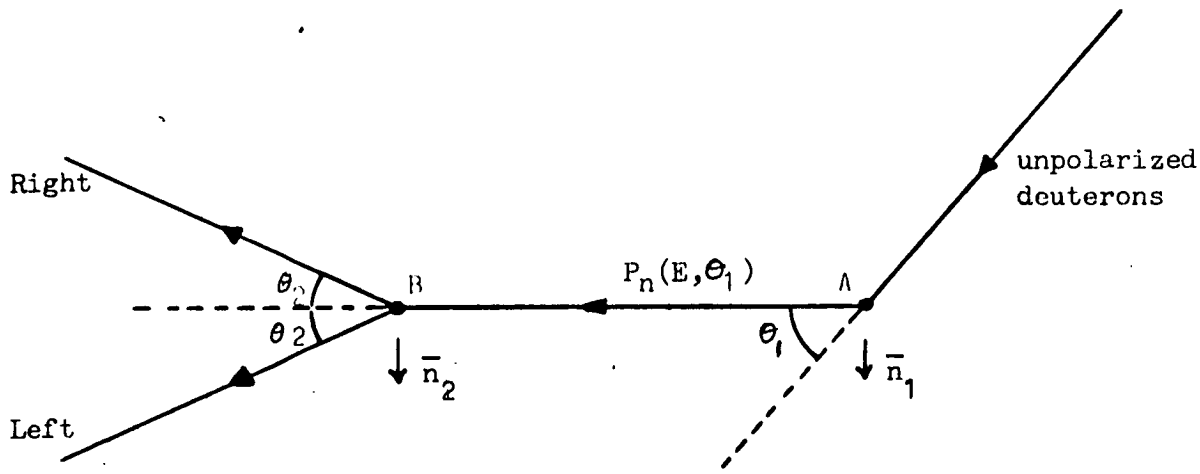

$\bar{n}_1$ and $\bar{n}_2$ are unit vectors normal to the reaction and scattering plane respectively

Fig. (1) Typical geometry for neutron polarization experiment

$$P_n(E, \theta_1)\, P_2(E_n, \theta_2) = \frac{\sigma(E_n, \theta_2, 0) - \sigma(E_n, \theta_2, 180)}{\sigma(E_n, \theta_2, 0) + \sigma(E_n, \theta_2, 180)} \qquad ..(1.3.4)$$

where $\sigma(E_n, \theta_2, 0)$ and $\sigma(E_n, \theta_2, 180)$ are the differential elastic scattering cross-sections when $\phi = 0^\circ$ and $\phi = 180^\circ$ respectively.

If neutron detectors are placed at the fixed scattering angle θ_2 but with $\phi = 0^\circ$ and $\phi = 180^\circ$ and if N_R and N_L be the number of neutrons measured to right ($\phi = 0^\circ$) and to the left ($\phi = 180^\circ$) respectively of the incident neutrons, then the equation (1.3.4) becomes

$$P_n(E, \theta_1)\, P_2(E_n, \theta_2) = \frac{N_R - N_L}{N_R + N_L} \qquad ..(1.3.5)$$

The product $P_n(E, \theta_1)\, P_2(E_n, \theta_2)$ is called the asymmetry ε .

Thus it is clear that using the arrangement of Fig. (1) if the analysing power $P_2(E_n, \theta_2)$ is known for some nucleus, then the value of $P_n(E, \theta_1)$ can be determined for a number of source reactions. Similarly if $P_n(E, \theta_1)$ of a source reaction is known, then $P_2(E_n, \theta_2)$, the polarization resulting from elastic scattering at different angles, can be determined for a number of nuclei.

1.4 Angular Dependence of Polarization

Adair et al[25] first observed the polarization effects in the scattering of neutrons by intermediate and heavy nuclei. A fairly smooth variation of polarization with atomic weight A in the elastic scattering of 0.38 and 0.98 MeV neutrons was shown by Clement et al[26]. For elements near A = 100 the polarization was largest. In comparison with the optical model the fits were generally of a qualitative nature. Cranberg[27] measured polarization of 2.1 MeV neutrons for intermediate and heavy nuclei at angles 50°, 90° and 125°. Olness et al[28] scattered 1.5 MeV neutrons through 51.5° by 18 elements from Y to U.

Ferguson et al[29] measured polarization for 14 elements from Ti to Bi with 0.4, 0.7 and 1.0 MeV neutrons in scattering at 55°. For 4.4, 5.0 and 5.5 MeV neutrons Mahajan[30] measured the polarization produced by elements from Ti to Bi at scattering angles of 40°, 60° and 90° and compared the results with optical model calculations. The model fit was of a qualitative nature.

McCormac et al[31] measured the polarization produced by Be, C, Cu, Zr, Sn and Pb for 3.1 MeV neutrons in the angular range of 30° to 135° and compared the results with optical model calculations. No fit could be obtained by the authors. Bredin[32] used 2 MeV neutrons to measure the angular distributions of polarization for Al, Si, Fe and Co and obtained a qualitative similarity with optical model calculations only for Fe and Co.

Durisch et al[33] measured the angular dependence of polarization produced by Cu and Zr at six angles from 55° to 120° for 3.16 MeV neutrons and the data were compared with optical model calculations; a qualitative similarity could only be obtained for Cu. Elwyn et al[34] measured angular distributions of polarization produced in scattering 0.28 to 0.85 MeV neutrons from Zr, Mo and Cd. A qualitative similarity could be obtained only for Mo and Cd when compared with optical model calculations. The angular distributions of polarization produced by 4 MeV neutrons elastically scattered from Be to Bi were measured by Gorlov et al[35] and the data were compared with optical model calculations; only a qualitative similarity could be obtained with the model fit in most cases and no fit was obtained for I, Pb and Bi.

Wiedemann et al[36] measured the polarization of 3.25 MeV neutrons scattered by Mg, Al, Si and S at angles from 30° to 140°, but could not get any fit to the optical model calculations using parameters of Rosen[15,17]. Ellgehausen et al[37]

measured very accurately the angular distributions of polarization produced by the scattering of 3.25 MeV neutrons by Ti, Cr, Fe, Cu, Zn and Zr between 30° and 140° and compared the data with optical model calculations using the parameters of Rosen[15,17]. A good fit was obtained for all elements except for Zr. The angular dependence of polarization produced by Ti and Cr for 1.5 and 2.0 MeV neutrons was measured by Pasechnik et al[38] in the angular range of 20° to 150°. The polarization data were compared with optical model calculations. A qualitative similarity to the optical model fit could only be obtained for Ti at 1.5 MeV.

Recent measurements and optical model analyses on the angular distribution of polarization of 3.2 MeV neutron scattering from twenty elements from Ti to Bi were done by Zijp and Jonker[39, 40]. A reasonably good agreement was obtained for nearly all the elements except for Mo, Ag, W, Tl and Pb. For eleven elements the measurements were only done for angles from 30° to 75°.

The optical model parameters of Rosen[15, 17], Gorlov et al[35] and Becchetti and Greenless[16] have met with some success in comparison with the experimental polarization measurements. Recently optical model calculations using the parameters of Rosen[15, 17] and of Becchetti and Greenless[16] were done by Zijp and Jonker[39] for comparison with the angular dependence of polarization and differential elastic scattering cross-sections for a number of nuclei from Ti to Bi. The parameters of Rosen[17, 15] gave the best overall agreement for polarization data, but even then only a qualitative similarity could be obtained to the Zn, Sr, Zr and Ba data and no agreement was obtained for W. The calculations done by Kashuba and Kozin[41] using an optical model potential having an imaginary component in the spin-orbit term gave no improvement in fitting the 4 MeV polarization data of Gorlov et al[35].

A summary of measurements on angular dependence of polarization of elastically scattered neutrons of energies 1, 1.5, 2, 3.25, 4 and 24 MeV has been given recently by Galloway[42]. Fig. (2) which is self-explanatory shows the angular dependence of polarization for Cu at about 3.24 MeV neutron energy reported by different authors. Four of the six points by Durisch et al[33] are consistent with more accurate measurements of Ellgehausen et al[37]. The four points of Zijp and Jonker[39] are however in agreement with Ellgehausen et al[37]. For Zn the angular dependence of polarization obtained by Ellgehausen et al[37] is in agreement with the four points reported by Zijp and Jonker[39], but differs in polarity around 120° from the value reported by Hereford[43]. For elements Ti, Cr, Fe, Cu, Zn and Zr at 3.2 MeV neutron energy the angular dependence of polarization measured by Zijp and Jonker[39] agrees as to polarity with the measurements done by Ellgehausen et al[37]. For Fe, Cu and Zn the measurements done by Zijp and Jonker[39] were only at four angles; 30°, 45°, 60° and 75°.

1.5 Proposed Measurements

Additional and more accurate values of the angular dependence of polarization and differential elastic scattering cross-section at 3 MeV neutron energy for a number of nuclei are still required. Similar measurements are also needed at higher energy, say around 16 MeV where no polarization data are yet available.

Keeping in view all these requirements a polarimeter has been designed and developed which can be used to measure simultaneously the angular dependence of polarization and the differential elastic scattering cross-section.

The present measurements are done on the angular dependence of polarization and differential elastic scattering cross-section for Fe, Cu, I, Hg and Pb at

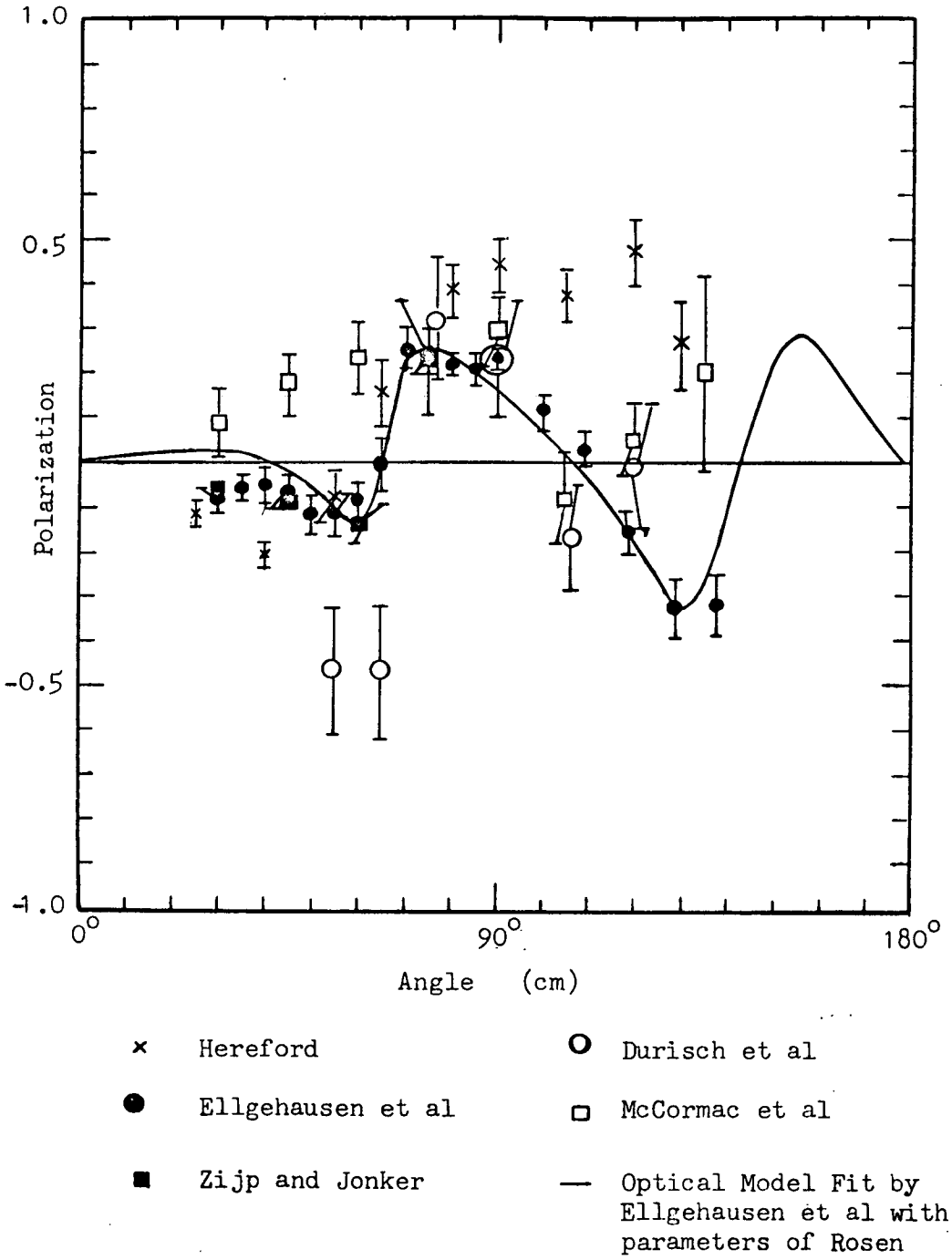

Fig. (2) The angular dependence of the polarization of 3.25 MeV neutrons elastically scattered by Cu

2.9 MeV neutrons in the angular range of 20° to 160° (Lab).

Measurements are also done on the angular distribution of polarization and differential elastic scattering cross-section for Cu and Pb for 16.1 MeV neutrons in the angular range of 20° to 90° (Lab).

1.6 Choice of Experimental Technique

The $D(d, n)He^3$ reaction is often used as a source of neutrons with an energy of a few MeV for polarization and neutron scattering cross-section measurements. The most difficult problem in fast neutron scattering experiments is the high background counting rate in the neutron detectors. This background arises due to scattering of neutrons from the walls and from all other materials in the experimental rooms.

In angular distribution measurements the background problem becomes especially severe at angles corresponding to the minima of the differential cross-section curve. Mahajan[30] found that background contributed between 40% and 85% of the counting rate, depending upon the scattering sample. In the experiment of Gorlov et al[35] the background ranged from 20% of the total number of counts at small scattering angles to 50% at the minima of the differential cross-sections while in the region of large scattering angles, as the detectors were close to the exit aperture of the collimator, the neutron background rose to 80% for several samples. The ratio of the number of scattered neutrons to the number of background counts varied between 0.75 and 10.0 in the experiment of Zijp[40] who used very extensive shielding.

Previous polarization studies have used mechanically collimated neutrons. The associated particle time-of-flight technique offers an alternate approach to producing a collimated, monoenergetic neutron beam for polarization studies.

1.7 Time-of-Flight Technique

Many of the background problems have been overcome by using the time-of-flight technique. In this method the moment of arrival of a neutron in the detector is measured relative to the moment of its production. The moment of production of a neutron at the target is fixed by a start signal. The mono-energetic neutrons from the target on scattering from a scatterer will arrive in the detector at a definite time after their production in the target. This time is determined by the velocity and flight path. Background neutrons are in general randomly distributed in time. In neutron time-of-flight measurement there are two general techniques for establishing a start time for neutrons. One is called an associated particle technique and the other one is the pulsed source method.

1.8 Associated Particle Technique (A.P.T.)

The basic knowledge behind the associated particle time-of-flight technique is that detection of an He^3 particle from the $D(d, n)He^3$ reaction in a given solid angle, means that an associated neutron was produced with known energy and angle of emission with respect to deuteron beam. Scattering experiments are done by placing a scattering sample in the path of the associated neutrons. The pulses from the He^3 particle detector, usually semi-conductor, identifies the time of emission of the associated neutrons and can thus be used as a 'start' signal for a time-of-flight system. The 'stop' signal is derived from the detection of the associated scattered neutrons. The background reduction is achieved from the coincidence requirement of associated scattered neutrons and the He^3 particles.

In this method the neutron and the He^3 detector angles are not independent,

with the result that the direction and the flux of neutrons are accurately known if the position and efficiency of the associated recoil He^3 particle detector are known. The technique provides, at least in principle, an extremely accurate method of producing well collimated, stable neutron beams with accurately known parameters for $D(d, n)He^3$ reaction[44-59]. For a particular reacting deuteron energy and direction of the recoil He^3 particles, the direction and energy of the associated neutrons are uniquely determined by the reaction kinematics.

1.9 Problem in A.P.T.

The main problem in the technique is the low energy He^3 particles. The Q value of the $D(d, n)He^3$ reaction is low and equal to 3.27 MeV. The cross-sections for the $D(d, n)He^3$ and $D(d, p)T$ reactions are approximately equal for low bombarding deuteron energies. H^3, p and deuterons will also reach the He^3 detector. The main trouble is caused by elastically scattered deuterons which arrive at the He^3 detector in overwhelming numbers. Therefore it is very important to separate He^3 particles from the scattered deuterons.

In previous methods the scattered deuterons have been prevented from reaching the detector by using additional magnetic field or electric field or an absorbing foil in front of the detector.

Foils, usually Al or Ni, thick enough to stop the deuterons but not He^3 may be used in front of the detector[46-49, 51]. The use of a thin foil is not however possible for incident deuteron energies much above 100 keV since the thickness of the foil required to stop the scattered deuterons will also stop the He^3 particles[55]. The thickness of the foil will also have to be critical. Some energy loss by the He^3 particles will also occur in the target.

For low bombarding deuteron energies a magnetic or an electrostatic analyser has been used to separate He^3 particles from deuterons[44,45,50,54,59]. The method requires longer flight paths for the He^3 particles. This causes a large variation in the flight times of the He^3 particles of different energies and therefore the coincidence time resolution between neutrons and He^3 becomes poorer[55,56].

Different forms of deuterium target have been used by different authors. Monier et al[52] used heavy ice targets for 50 keV deuteron energy. The target was D_2O frozen on to a 0.795 mm copper-backing maintained at liquid nitrogen temperature and was thick to 50 keV deuterons. At high deuteron energies (2 MeV) Tripard et al[55] used a thin film self-supporting deuterated polyethylene target. A rotating target was used to prolong the targets' useful life. The scattering from and energy loss in the target were minimised considerably so that the He^3 particle detector was used without protecting foil or magnetic or electrostatic analyser. A thin deuterated polyethylene target was also used at 2 MeV bombarding deuteron energy by McFadden et al[57]. Schuster[56] used a deuterated polyethylene target at 10 MeV bombarding deuteron energy. However, the deuterated polyethylene target is effectively restricted to deuteron energies in the MeV range because of the difficulty of producing satisfactory targets for use with low incident deuteron energies[59].

At incident deuteron energies below 400 keV a magnetic analyser to shield the He^3 detector from scattered deuterons was used by Johnson et al[59]. They used a thick drive in deuterium target produced by deuteron bombardment on a liquid nitrogen cooled copper plate.

1.10 Pulsed Source Method (P.S.M.)

This technique uses short neutron bursts spaced at regular time intervals produced at the target by bombarding the target with a pulsed beam of deuterons. The energy resolution may be improved considerably by increasing the flight path provided that a corresponding increase in the pulsed beam current is made to maintain counting rate and signal to background ratio.

1.11 Principle in P.S.M.

A detailed description of the pulsed source time-of-flight technique is given by Neiler and Good[60]. In this technique the time taken by a neutron originating at the source target to reach the detector is measured. The time of origin of a neutron is localised by producing the neutrons in burst of time duration, say dt. A specific neutron will then originate at a certain time with an uncertainty dt. The flight time t in nano-seconds is given by the relation

$$t = \frac{72.3\ d}{E^{\frac{1}{2}}} \qquad ..(1.11.1)$$

where d is the flight path in meters and E is the neutron energy in MeV. On differentiating the above equation (1.11.1) the following relation is obtained,

$$\frac{dE}{E} = \frac{E^{\frac{1}{2}}\ dt}{36.2\ d} \qquad ..(1.11.2)$$

From the above equation (1.11.2) it follows that for a given neutron energy E, the energy resolution can be improved either by increasing d, the flight path or by decreasing dt. Since the counting rate in the neutron detector is governed by an inverse square law of the flight path, therefore, it would be advantageous to decrease dt rather than to increase d. The other important factor to be considered in energy resolution is that dE is proportional

to $E^{3/2}$. The timing spread of a monoenergetic neutron group is caused by the following three factors:

(1) The time width of the beam pulse.

(2) The finite thickness of the scintillator.

(3) The timing accuracy of the detection and associated electronics called the instrumental resolving time.

The pulsed beam is usually obtained by: (1) a simple electrostatic deflection of the external beam called the post acceleration system, (2) pre-acceleration system[61], i.e. pulsing the beam before it is accelerated, (3) Klystron bunching of the external beam[62,63], or (4) Mobley magnet compression method[64].

In the Mobley magnet compression method an rf ion source and a beam chopper is located in the high voltage terminal and the Mobley magnet is a double focussing magnet. The accelerated beam is swept across the Mobley magnet in such a way that Mobley magnet system compresses the pulses to a small width of about 1 ns on to the target. The peak current in such a system is several milliamperes. The time of emission of a neutron may be indicated by a voltage pulse induced in a pick-up tube before the target or by a current pulse direct from the target. The pulses from the tube or the target are used as the start pulses. The stop signal is derived from the detection of a neutron in the detector.

1.12 Choice of Time-of-Flight Method

The associated particle method being economical has been adopted successfully for the scattering and polarization studies with 2.9 MeV neutrons to

be reported here.

For the 16.1 MeV neutron measurements a 3 MeV Van de Graaff pulsed beam accelerator with pulse duration of 1 ns and having an average current of about 10μA at A.E.R.E., Harwell has been used. T(d, n)He^4 is the reaction used for producing 16.1 MeV neutrons at 75°(Lab).

CHAPTER II

CHAPTER II

The Associated Particle System for the $D(d, n)He^3$ Reaction

2.1 An Outline of the Associated Particle Method

The measurement of the flight time of a neutron emitted in the $D(d, n)He^3$ reaction requires the determination of:

(a) The precise instant at which the neutron is emitted from the target, i.e. the instant at which the reaction occurs.

(b) The instant at which the neutron arrives at the end of its flight path.

The instant of emission of a neutron is determined by detecting the recoil He^3 particles in a semi-conductor detector placed inside a reaction chamber and the arrival of the neutron at the end of its flight path is determined by detecting the associated neutron in a liquid scintillator. Timing pulses from the two detectors are fed to the inputs of a time to amplitude converter (TAC), which produces an output pulse, whose amplitude is proportional to the time interval between the arrival of the input pulses. The output pulses from TAC are then displayed by a multichannel pulse height analyser to give a time-of-flight spectrum of the neutrons. The performance of the simple time-of-flight spectrometer outlined above can be improved by using a slow coincidence technique in addition. In this case a coincidence is required between the He^3 particle energy pulse and the linear pulse from the neutron detector. The time-of-flight spectrum on the multichannel pulse height analyser is then obtained gated by the neutron-He^3 coincidence pulse, so eliminating the time spread due to small pulses triggering the time to amplitude converter.

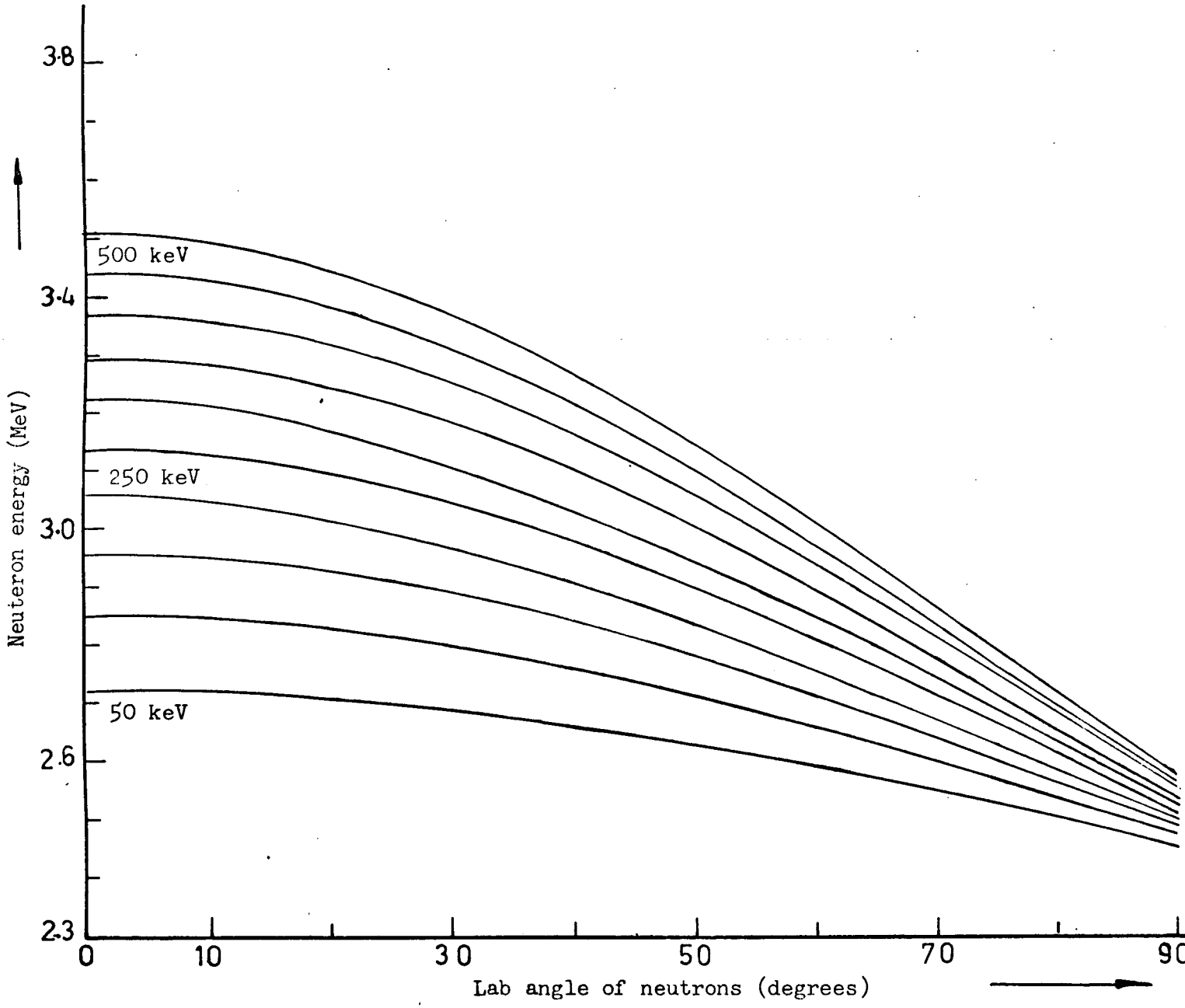

Fig. (3) Neutron energy versus angle of emission for deuteron energy 50 - 500 keV in $D(d,n)He^3$ reaction

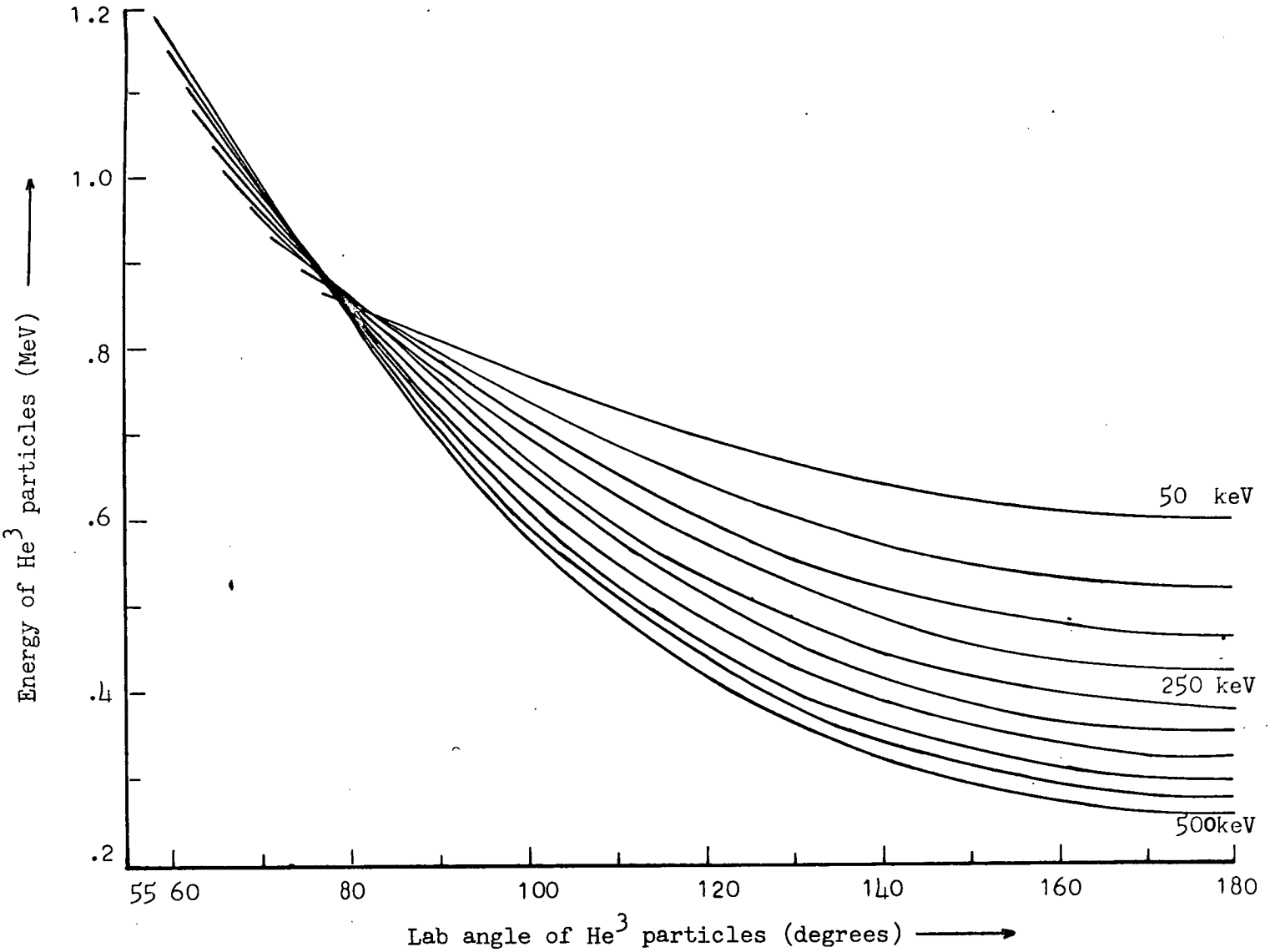

Fig. (4) He^3 particle energy versus angle of emission for deuteron energy 50 keV - 500 keV in 50 keV steps

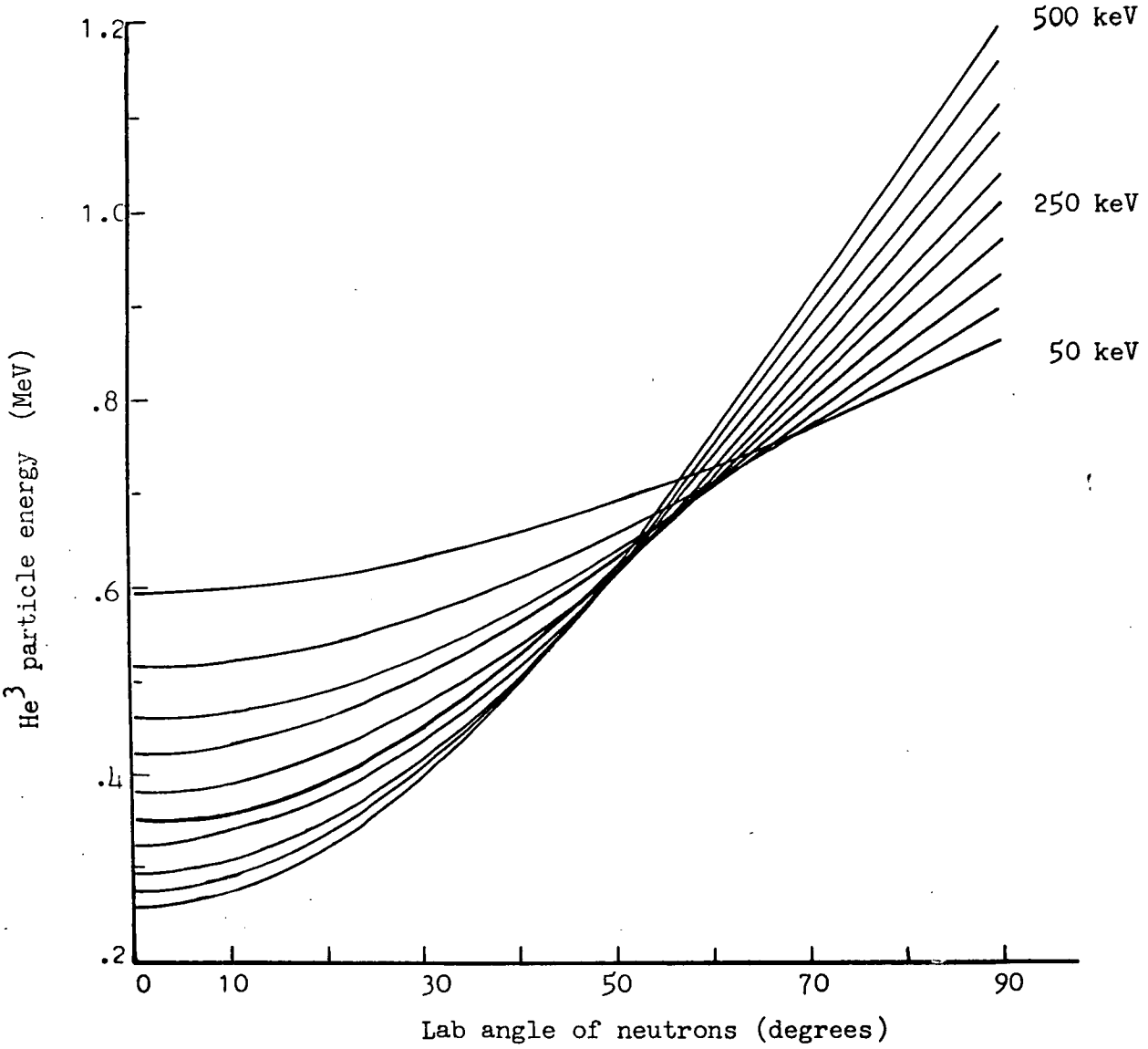

Fig. (5) He^3 particle energy versus angle of neutron emission for deuteron energy 50 keV - 500 keV in 50 keV steps

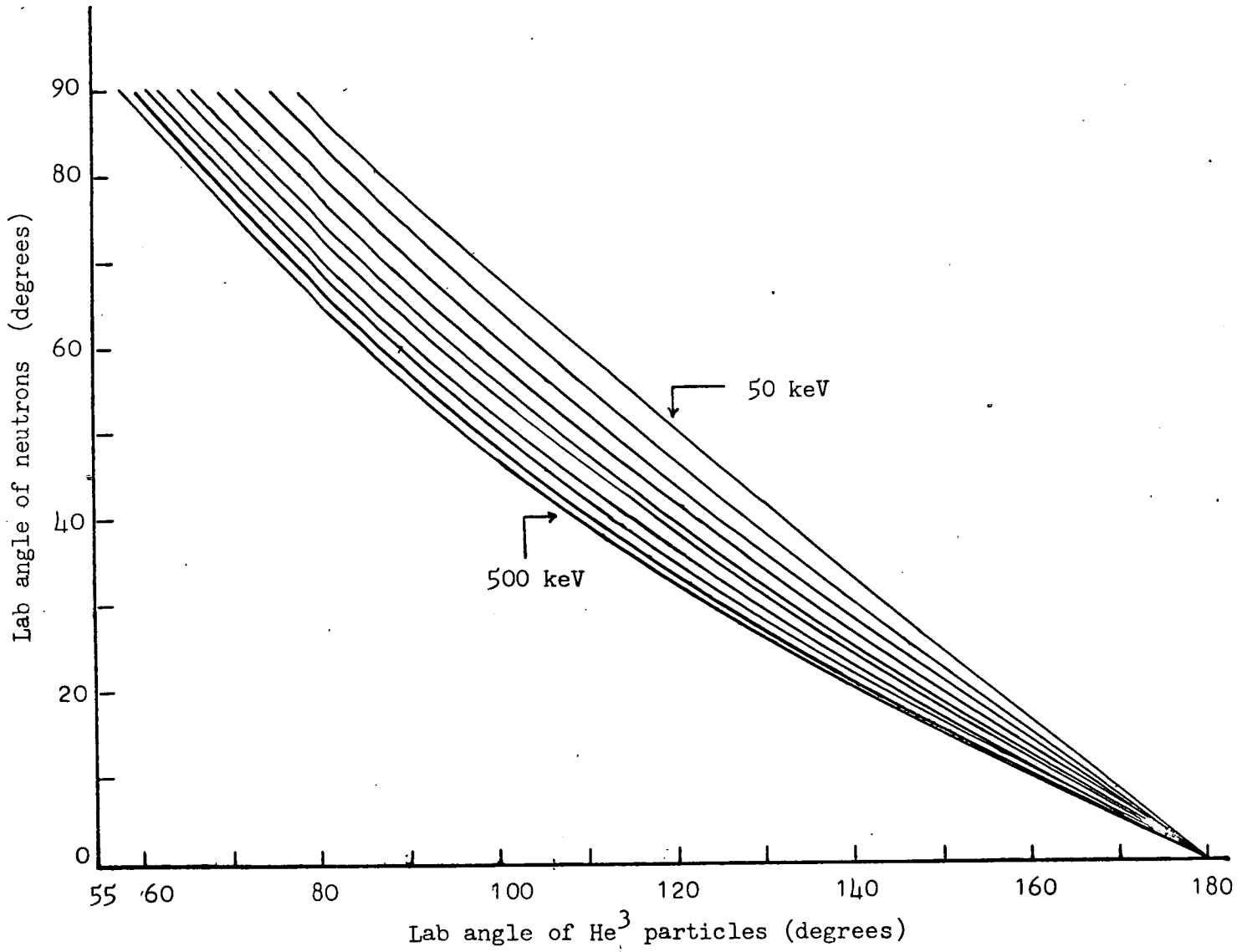

Fig. (6) Angle of neutron emission versus the associated He^3 particle angle for deuteron energies of 50 keV - 500 keV in 50 keV steps

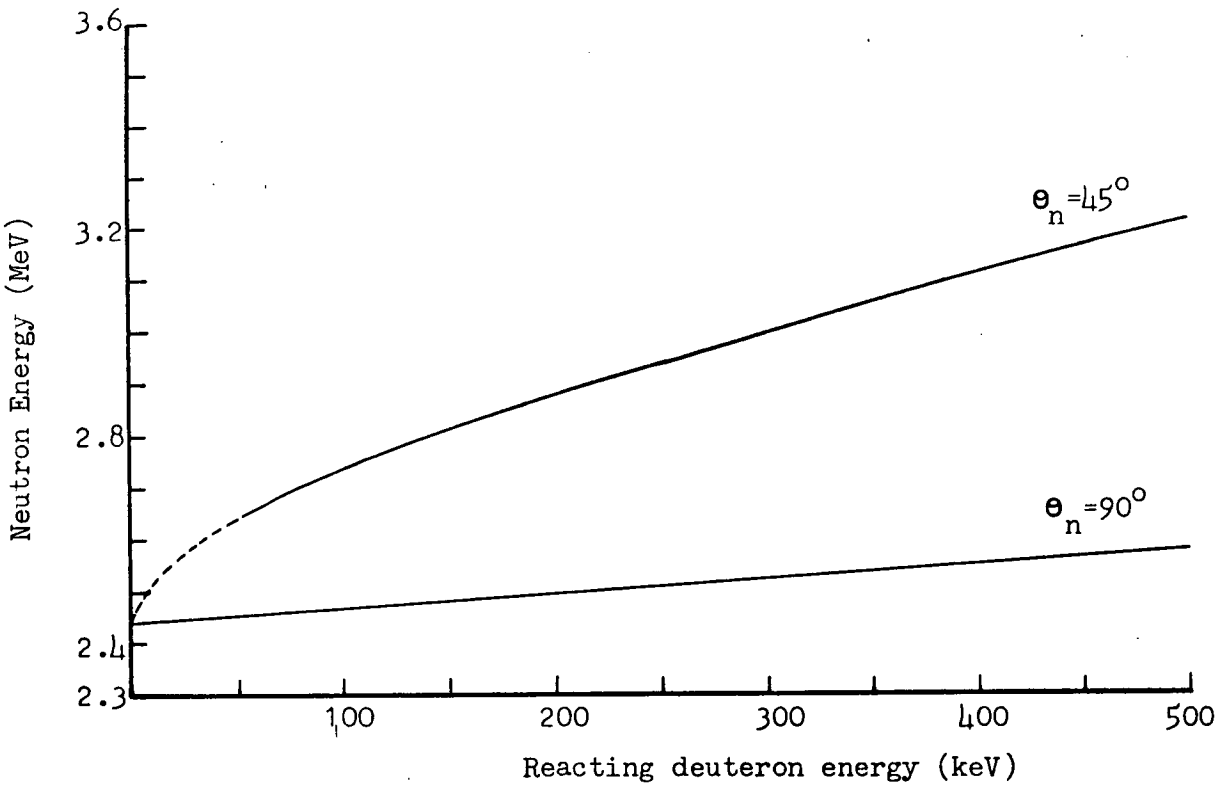

Fig. (7) Neutron energy emitted at 45° and 90° versus reacting deuteron energy.

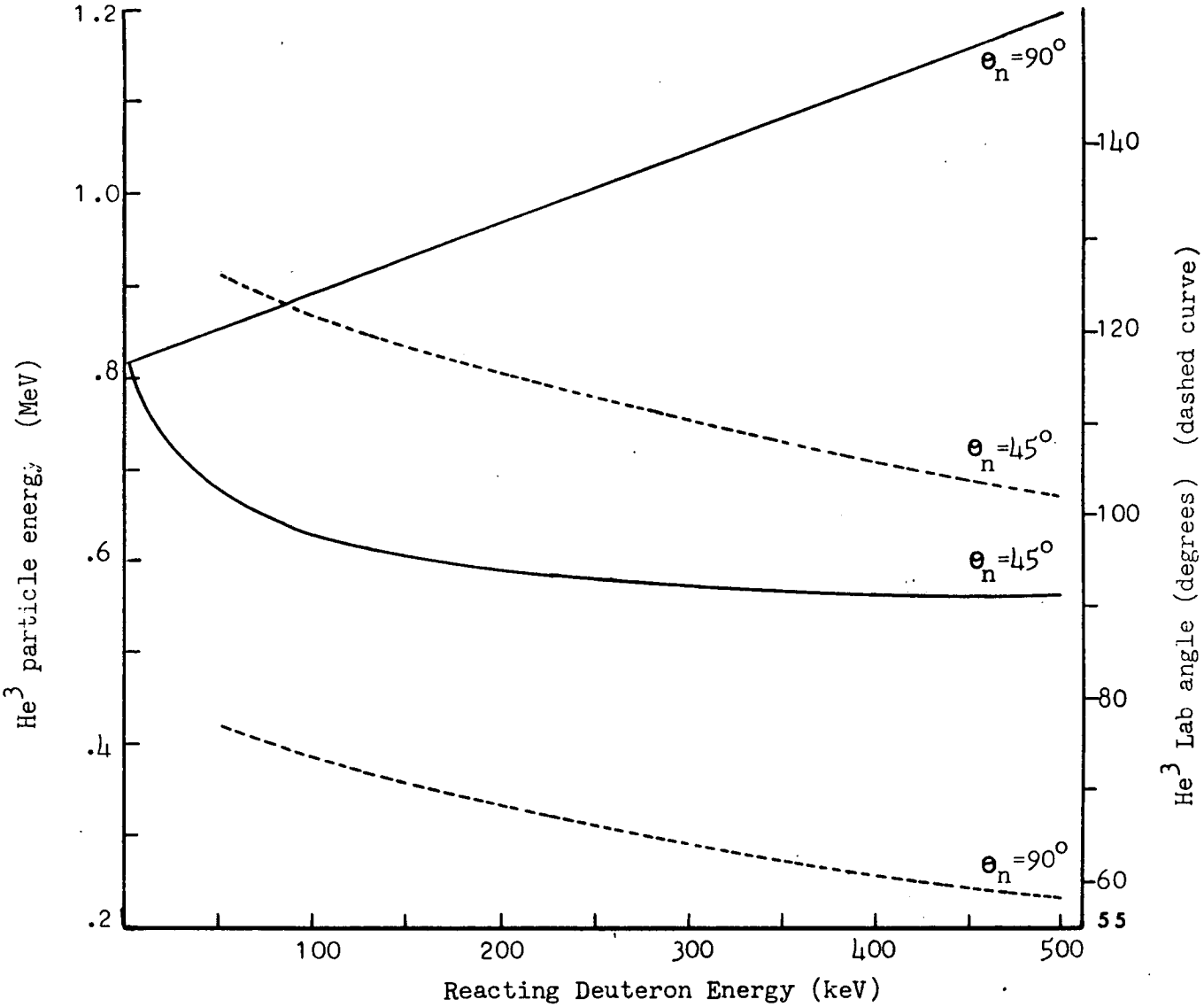

Fig. (8) He^3 particle energies versus reacting deuteron energies with emitted neutrons at $\theta_n = 45^\circ$ and 90° (full curve) and He^3 (Lab) angle versus reacting deuteron energy with $\theta_n = 45^\circ, 90^\circ$ (dashed curve)

As pointed out in section 1.8 of the first chapter in the D(d, n)He^3 reaction for a particular deuteron energy and direction of the recoil He^3 particles, the direction and energy of the associated neutrons are uniquely determined by the reaction kinematics. Figures (3-8) show the behaviour of several quantities relevant to the D(d, n)He^3 reaction as a function of neutron angle and incident deuteron energy. The curves were calculated from the formulae given by Marion and Young[65]. The curves show various relations between neutron and recoil He^3 particle in terms of angles and energies for a neutron emission angle from 0^o to 90^o and bombarding deuteron energy from 50 keV to 500 keV in 50 keV steps of energy increment.

2.2 Simple Reaction Chamber

A simple reaction chamber has been used to detect the low energy He^3 particles and to test the electronic system built for the purpose. The steel reaction chamber had a diameter of 30.5 cm, depth of 8.0 cm and wall thickness of 0.63 cm. The hole in the chamber for the deuteron beam to enter was of diameter 1.2 cm. The deuteron beam from 500 keV Van de Graaff accelerator can be focussed to 2 mm diameter on the water cooled thin TiD target. The surface barrier semi-conductor detector to detect the He^3 recoil particles was placed at an angle of 110^o with respect to deuteron beam. Fig. (9) shows the simple reaction chamber and the surface barrier detector arrangement. An aluminium disc with a hole of 2 mm in diameter was placed in front of the surface barrier detector to collimate the He^3 particles. He^3 energy pulses were fed via a Hewlett-Packard pre-amplifier, type 5554A, and amplifier (Ortec Model 452) to a 400 channels pulse height analyser.

Fig. (10) shows a spectrum obtained at 100 keV incident deuteron energy and 3 μA beam current. This spectrum shows clearly He^3, triton and proton peaks. The proton and triton peaks are due to competing D(d, p)t reaction.

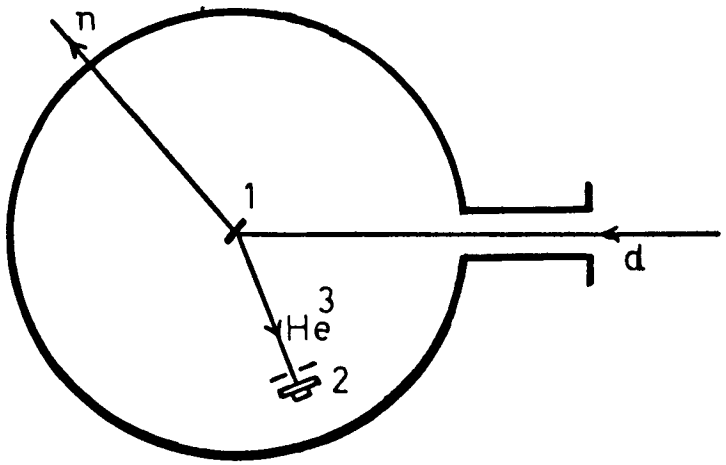

(1) TiD Target

(2) Surface Barrier Detector

Fig. (9) Simple Reaction Chamber

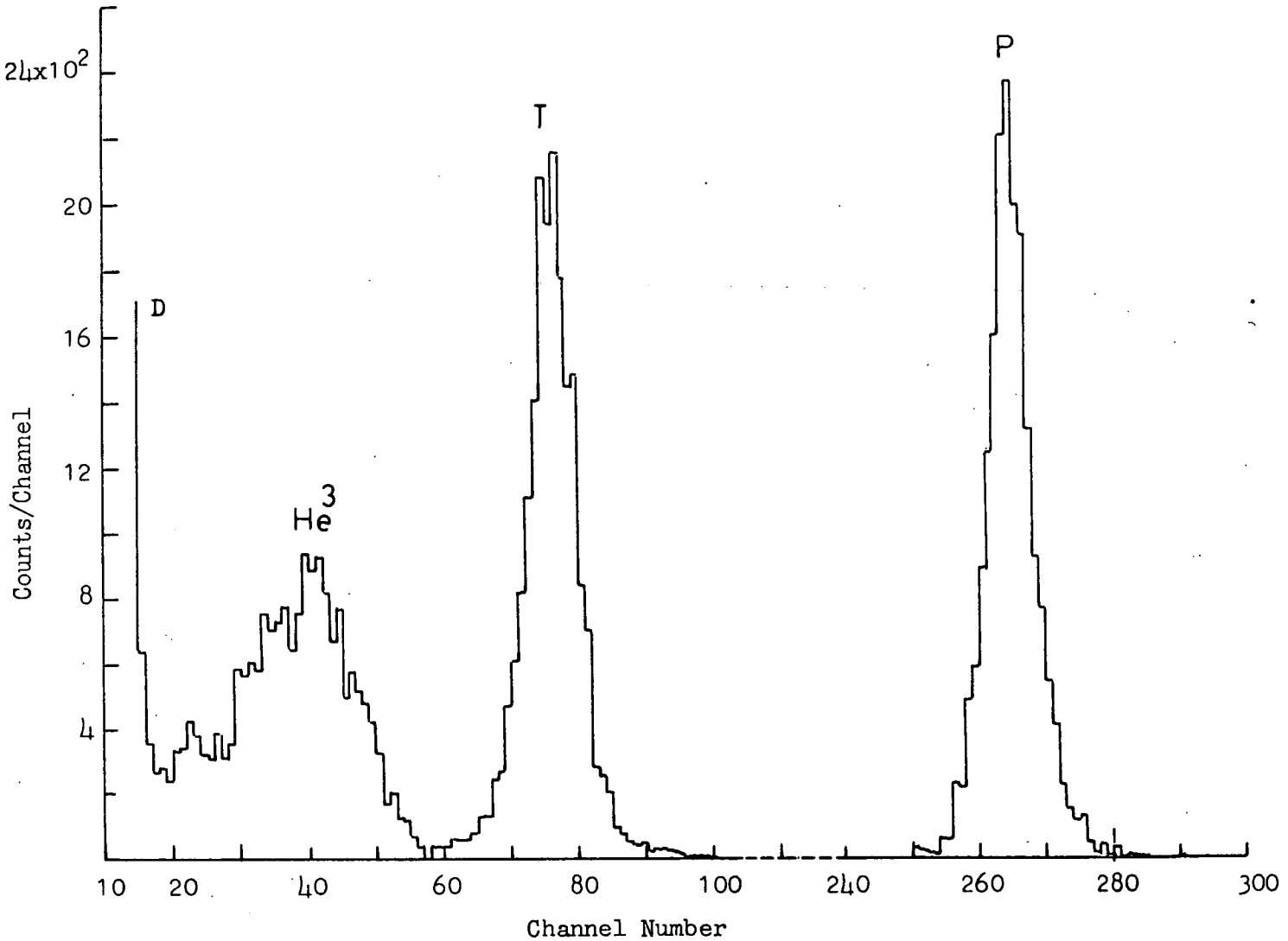

Fig. (10) Pulse height spectrum of charged particles from $D(d,n)He^3$ reaction at 100 keV incident deuterons

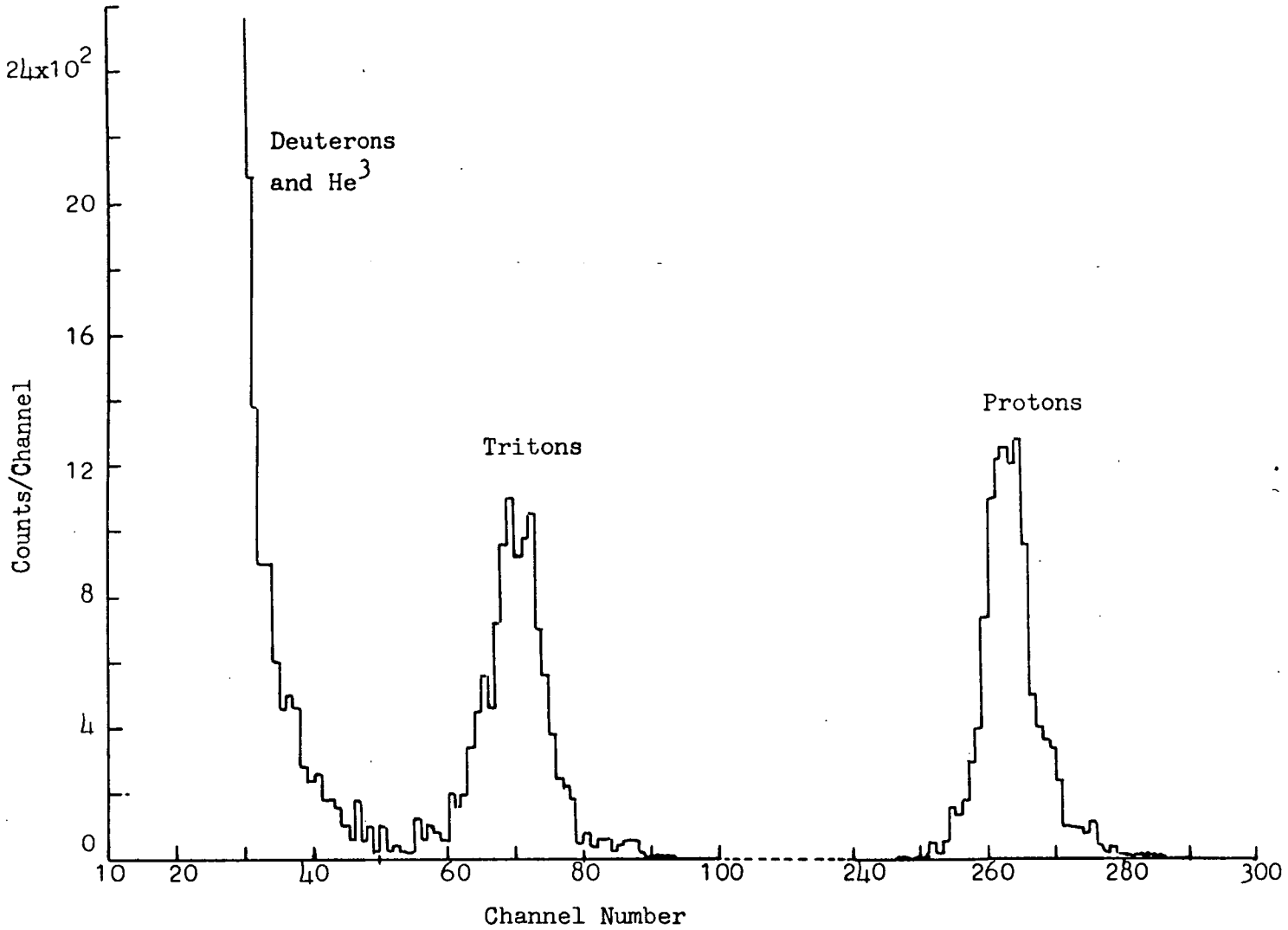

Fig. (11) Pulse height spectrum of charged particles from $D(d,n)He^3$ reaction at 200 keV incident deuterons

At higher incident deuteron current at this energy however the He^3 peak disappeared completely mainly due to overwhelming numbers of elastically scattered deuterons reaching the detector. When the incident deuteron energy was increased to 200 keV or even to 160 keV the He^3 peak merged completely in the elastically scattered deuteron peak. Fig. (11) shows a typical spectrum at 200 keV incident deuteron beam of 2 μA current. The He^3 peak is not clear in this spectrum. To perform the polarization and elastic scattering experiments with sufficient statistical accuracy requires a higher neutron flux on the scattering sample than is available with a few μA of beam current. Therefore to detect the He^3 particles at higher incident deuteron flux and at higher energies, this simple system requires the addition of some kind of arrangement to separate low energy He^3 particles from elastically scattered deuterons.

2.3 Electrostatic Analyser

The discrimination between He^3 and the overwhelming elastically scattered deuterons cannot be achieved by an absorbing foil in front of the He^3 particle detector as for example an Al foil thick enough to stop 300 keV deuterons, would also stop 1 MeV He^3 particles[50]. An electrostatic or a magnetic field can successfully be employed for the discrimination of He^3 particles and deuterons[50, 59]. For particles having mass m, energy E and with charge q times the electron charge e, the radius of curvature r in a magnetic field of strength H is given by

$$r = \frac{(2\ m\ E)^{\frac{1}{2}}}{q\ e\ H} \qquad ..(2.3.1)$$

For deuterons of energy E_d and He^3 particles of energy E_{He3} in a given magnetic field H, the condition for deflection with the same radius of

curvature is given by

$$E_{He3} = \frac{8}{3} E_d \qquad ..(2.3.2)$$

Therefore the condition for complete discrimination between He^3 particles and the elastically scattered deuterons (less in energy than E_d the incident deuterons form the accelerator) is given by[50],

$$E_{He3} > \frac{8}{3} E_d \qquad ..(2.3.3)$$

Similarly the radius of curvature for the particle in an electrostatic field of strength F is given by,

$$r = \frac{2E}{qeF} \qquad ..(2.3.4)$$

For an electrostatic field the condition for complete discrimination is given by[50]

$$E_{He3} > 2 E_d \qquad ..(2.3.5)$$

From the above two conditions for discrimination it can be concluded that the electrostatic deflection would give better discrimination. Other advantages of an electrostatic deflection system are ease of construction and the much smaller mass of material in the target vicinity to contribute to background scattering compared with a magnetic deflection system.

2.4 General Consideration in Design of the Electrostatic Analyser

The electrostatic analyser was designed keeping in view the performing of polarization experiments with the 0.5 MeV Van de Graaff accelerator. The maximum neutron polarization below 500 keV deuteron energy was found to be for neutrons emitted around 49°(Lab). The work done in the field of polarization has been reviewed recently by Galloway[68].

Thus the neutron cone desired for polarization studies is around 49°(Lab) with respect to incident deuteron beam. To achieve this requirement the deflecting plates and the He^3 particle detector are arranged in such a way that these can be rotated around the deuterium target to bring in coincidence with the neutron cone at 49° at any desired deuteron energy from 50 - 500 keV.

In a cylindrical electrostatic analyser a deviation in the direction of a beam of charged particles is caused when it passes through the electric field between two curved conductors. These curved conductors are sections of coaxial cylinders by planes perpendicular to the cylinder axis. A detailed description of an electrostatic analyser can be found in references (69-73).

Let f_1 be the distance of a slit from the plane containing the entrance to the deflecting plates, then the charged particles leaving the slit and passing through the deflecting plates, are focussed at a distance f_2 from the exit plane of the analyser and is given by the expression[70],

$$(f_1 - g)(f_2 - g) = \left(\frac{r}{2^{\frac{1}{2}} \sin (2^{\frac{1}{2}}\phi)}\right)^2 \qquad ..(2.4.1)$$

where r is a mean of radii r_1 and r_2 of the inner and outer plates respectively, ϕ is the angular length of the path between the plates, and

$$g = \frac{r}{2^{\frac{1}{2}}} \cot (2^{\frac{1}{2}}\phi) \qquad ..(2.4.2)$$

The electric field required to traverse a charged particle in a certain radius of curvature can be expressed as[70],

$$E = Z(V_2 - V_1)/(2(\log r_2 - \log r_1)) \qquad ..(2.4.3)$$

where E is the energy of the charged particle in keV, $V_2 - V_1$ is the difference in potential between the deflecting electrodes expressed in kilovolts and Z is

the number of electronic charges carried by the charged particle. The above equation (2.4.3) is however equivalent to the equation (2.3.4).

It was indicated by Allison et al[71] that a small radius of curvature and large $(r_2 - r_1)$ contribute to high collecting power, but there exists a limit that changing r and $(r_2 - r_1)$ for higher collecting power rapidly decreases the energy of the incident charged particle which can be deflected by a given potential difference between the plates and therefore requires a compromise between the two objectives.

A mean radius of 45.0 cm with 44.0 cm and 46.0 cm as radii of curvatures of the inner and outer plates was considered to be suitable inside a chamber from the point of view of rotation around the target (source of He^3 particles) to bring in coincidence with the 49° associated neutron cone at 100 keV to 500 keV incident deuteron energy. From equation (2.4.1) with f_1 = 1.5 cm the value of f_2 was calculated to be 19.08 cm. The angular length ϕ of the path between the plates was 20°. The slit distance from the target was 3.0 cm.

2.5 Description of the Electrostatic Analyser

The plan and sectional views of the analyser are shown schematically in Figs. (12) and (13) respectively. The deflecting plates are of aluminium, 5.0 cm in height, 2.0 cm in width and have an angular length of 20°. The mean radius of the plates is 45.0 cm and the separation between them is 2.0 cm. For best results the radii of the plate surfaces should be constant. The inner surfaces of the plates were polished manually using Dialap Diamond Compound, have no signs of uneven surface or scratches and have a mirror finish.

The deflecting plates are supported on a curved piece of PTFE of 2.0 cm in thickness having two grooves cut 4.0 mm deep with 44.0 cm and 46.0 cm radii of curvature. The width of these grooves are such that the deflecting plates

(1) Deflecting Plates (2) Cold Copper Tube (3) S-B detector housing

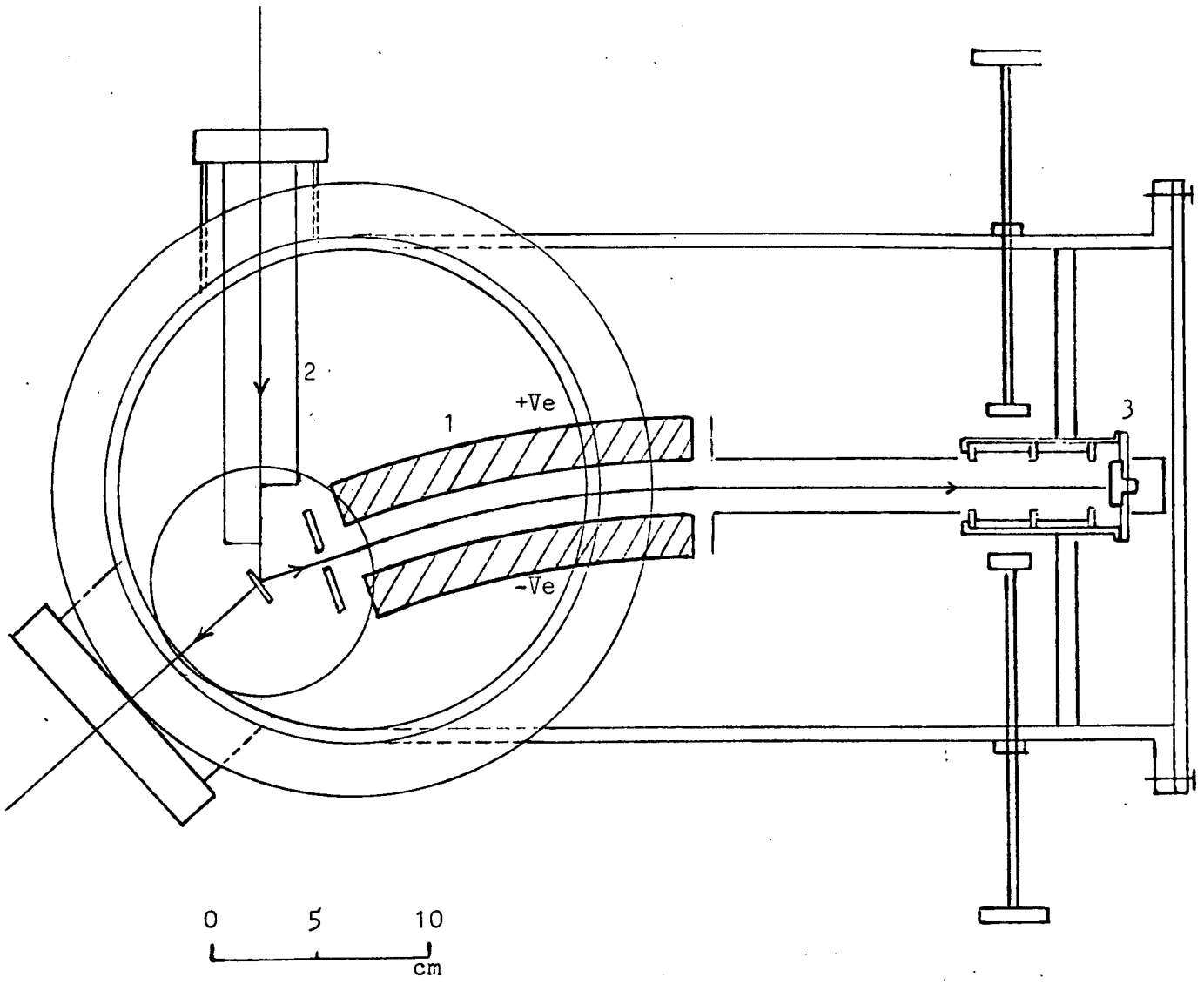

Fig. (12) Plan view of the Electrostatic Analyser

(1) PTFE Insulation (2) Target holder (3) Aluminium arm (4) Deflecting Plates

(5) Graduated perspex window

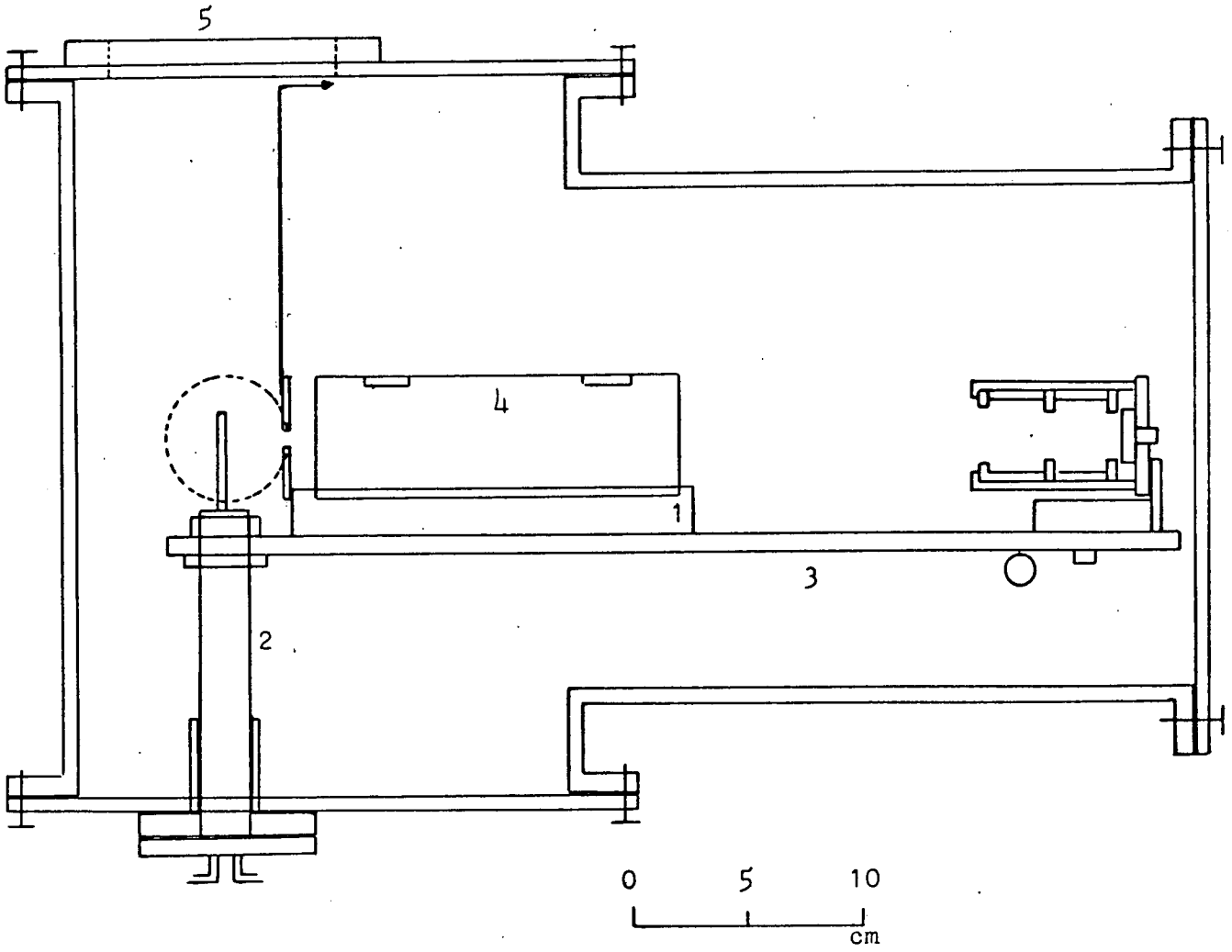

Fig. (13) Sectional view of the Electrostatic Analyser

are pushed tight in and are held up rigidly by screws thereby achieving a 2.0 cm separation between the plates. The PTFE piece holding the deflecting plates is fixed rigidly on to a curved aluminium arm. Two small PTFE pieces having again two grooves of similar width and depth are pushed tight on the top of the deflecting plates at each end and are held rigidly by screws. This ensures that the plates are again held at constant distance apart at the top. One end of the aluminium arm is pivoted on a ball bearing arrangement about the water cooled target holder (with adjustable clamping screwed rings for alignment) and the other end of the arm rests on a metal strip welded to the side walls of the vacuum chamber. A PTFE strip provides insulation between the aluminium arm and the metal supporting strip so that the target current can be measured. The target holder itself is insulated from the rest of the chamber by means of a PTFE ring. The rear end of the aluminium arm can be adjusted vertically by means of two threaded rods in the metal strip. The high voltages to the deflecting plates are applied through two PTFE insulated wires connected to the top of the deflecting plates. Glass tubes are used to cover any sharp edges at the junction of the wires.

The surface barrier detector is placed in a housing which can be moved on the aluminium arm so that the detector can be fixed at any desired distance from the exit of the deflecting plates. Any deuterons scattered from the walls of the chamber are prevented from entering the detector by several diaphragms in the housing. The aluminium arm can be rotated around the target by means of two Wilson seal drive shafts fixed on either side of the chamber.

The stainless steel water cooled deuterium target holder is 0.5 cm in width and 4.0 cm in height with a thickness of only 0.3 cm to minimise scattering material around the neutron source. A TiD target can be soldered on to this holder with good thermal contact. To reduce oil contamination and carbon

deposition on the target a liquid nitrogen cooled copper tube is mounted near the target. An insulated circular disc of aluminium having a circular hole of 0.6 cm in diameter is mounted in the beam line before the liquid nitrogen cooled tube. The deuteron beam therefore enters the system through this circular aperture giving a 2 mm diameter spot on the target. The main advantage of this disc is that by adjusting the deuteron beam focus and position for minimum current (approx. zero) on this disc the beam spot can always be brought close to the same point on the target.

The angle between the target plane and the incident deuteron beam is 30°. A stainless steel disc with a rectangular shaped hole 4.5 mm wide by 8.0 mm high is placed between the target and the entrance to the deflecting plates so as to select the beam of He^3 particles. A potential of -300 volts is applied to this disc to prevent secondary electrons emitted from the target from entering the deflection system. These secondary electrons otherwise would ionize the residual gas resulting in breakdown of the high voltage on the deflecting plates.

Fig. (14) shows the top view of the analyser. A is the nitrogen cooled copper tube, B is the target holder, C and D are the pivot arrangement for holding the aluminium arm, E is the entrance aperture for the He^3 particles and F the deflecting plates. Also in the figure G indicates the PTFE insulating pieces and H the PTFE insulated wires for the high voltage.

The vacuum chamber consists of stainless steel cylinders of diameter 20.6 cm welded together to make a ' ⊢ ' shape. The chamber has a thin mylar window at an angle of 49° with respect to the deuteron beam. This window makes the target visible for alignment purposes and avoids scattering by stainless steel material in the path of neutron cone. The top of the chamber

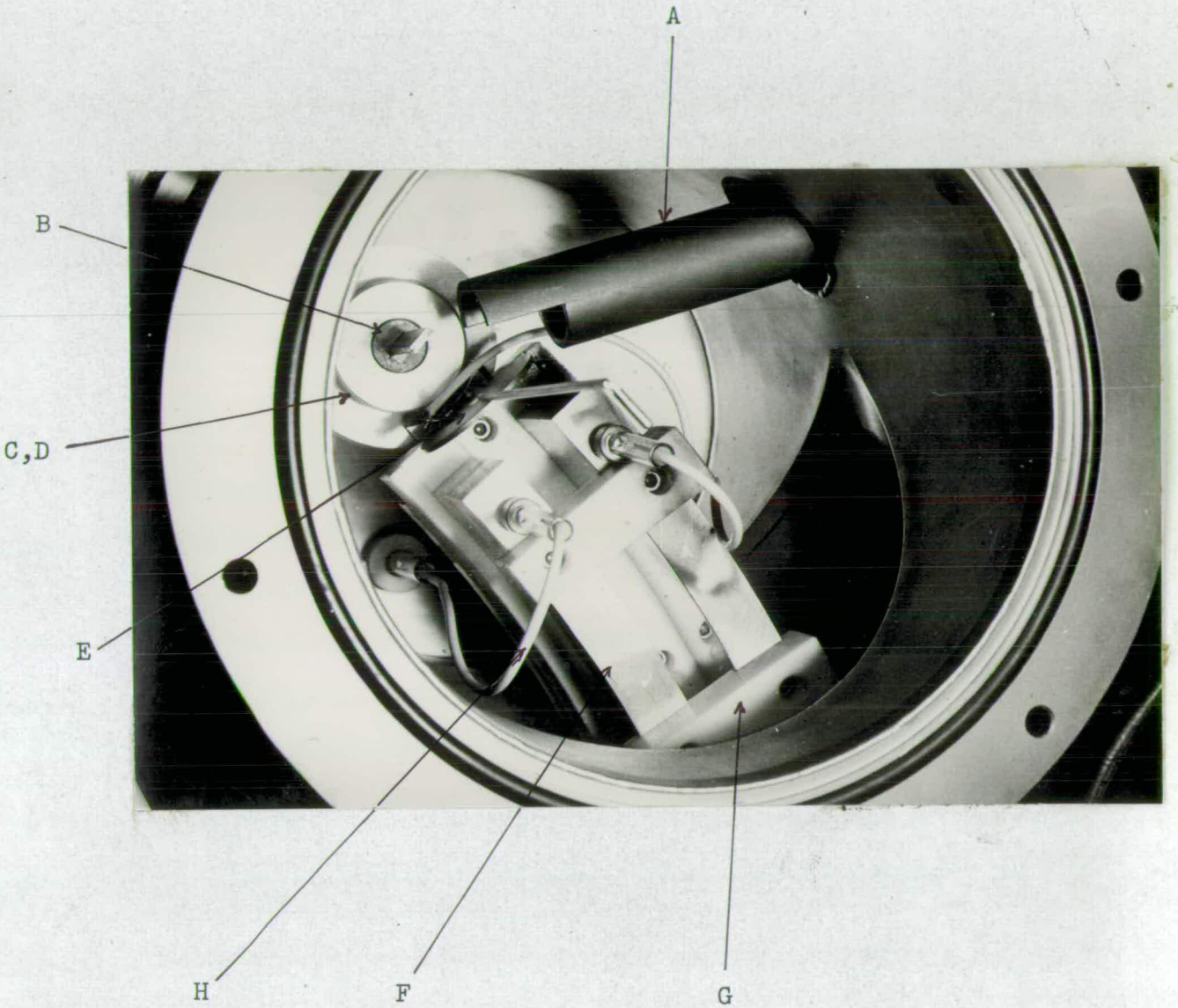

Fig. (14) Photograph showing the top view of the electrostatic analyser

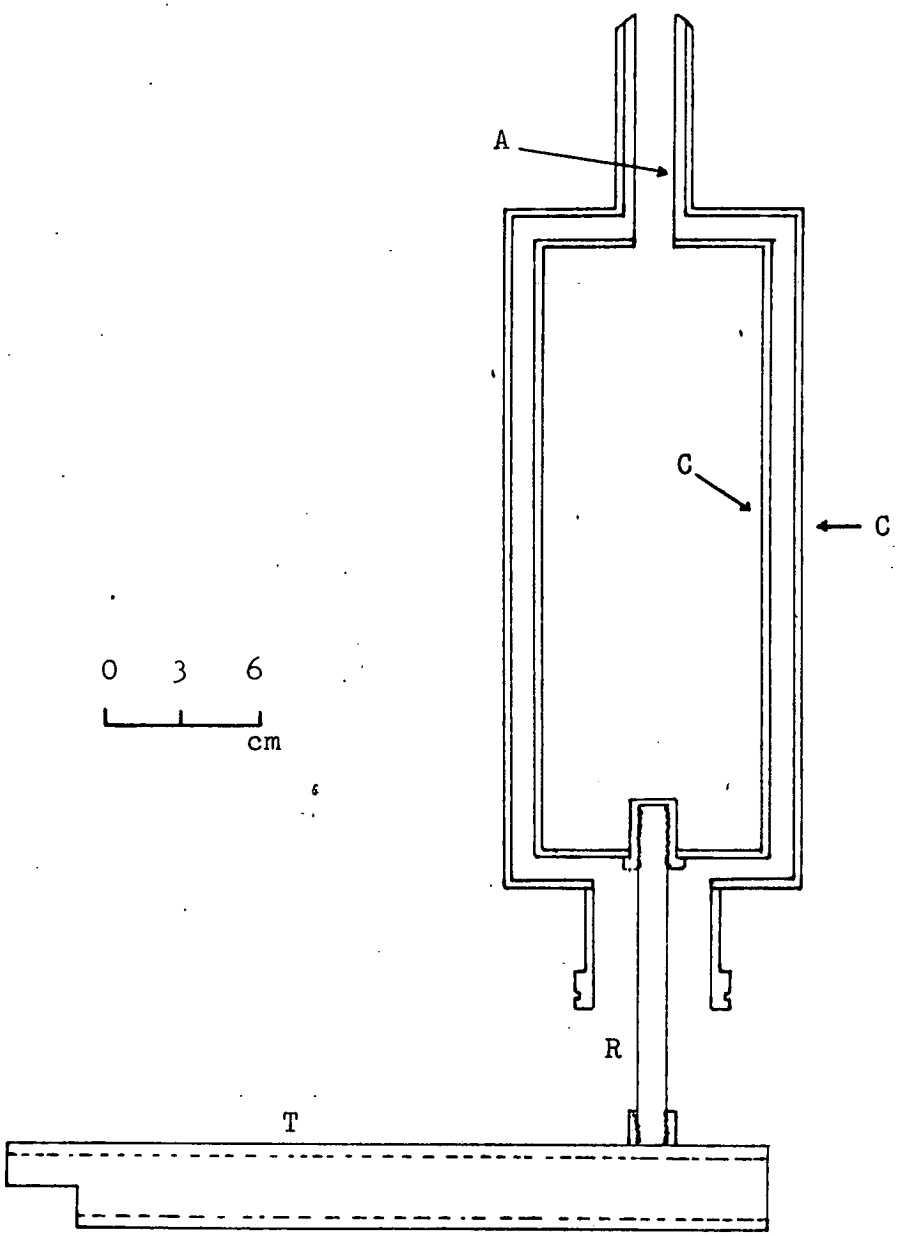

Fig. (15) Liquid nitrogen cold trap

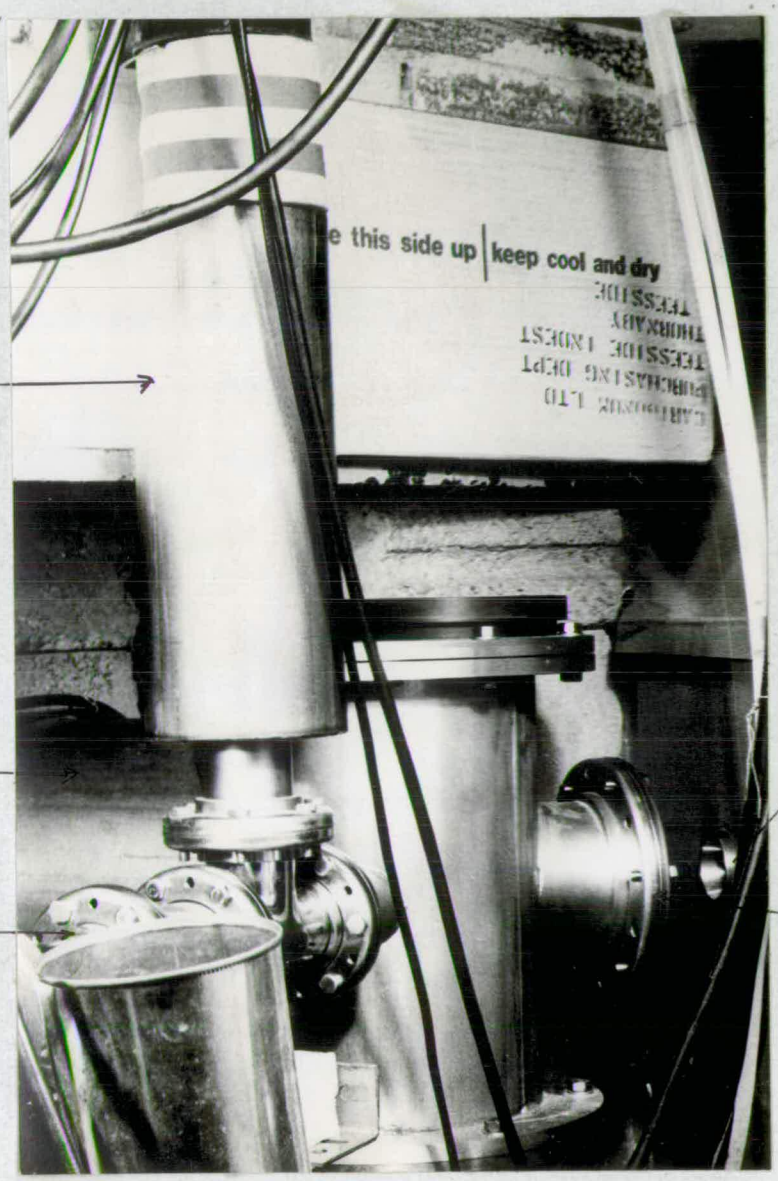

Fig. (16) Photograph showing the vacuum chamber of the electrostatic analyser

is provided with a graduated perspex circular window having its centre passing through the axis of the target holder. The angle of the central entrance of the deflecting plates, i.e. centre of the rectangular hole with respect to the deuteron beam can be read by means of a pointer. The system is free from vacuum grease and the vacuum in the chamber can be brought down easily to 1 x 10^{-6} torr.

The liquid nitrogen cooled copper tube in the vicinity of the target has in fact increased the useful life of the target considerably. Fig. (15) shows the layout of the liquid nitrogen cold trap. Two coaxial stainless steel cylinders C are connected together by means of a thin walled smaller tube A of 0.25 mm in thickness. One end of a copper rod R is screwed to the bottom plate of the inner cylinder C and a copper tube T is attached to its other end. The length of the tube T is sufficient that it reaches close to the target. The inner cylinder is filled with liquid nitrogen which in turn cools down the copper tube T by conduction. Fig. (16) shows the system as a whole indicating the vacuum chamber, the mylar window and the liquid nitrogen cold trap. The vacuum chamber rests on an adjustable stand.

2.6 The Neutron Detector

The neutron detector used in checking the performance of the associated particle system was a bubble free liquid scintillator of type NE213 mounted directly on to a 56 AVP photomultiplier. The scintillator container was a thin walled aluminium cylinder of thickness 2.0 mm, diameter 5.08 cm and of length 15.24 cm and was specially made for the polarization experiment. A thin walled 5 ft. long PTFE tube of 2 mm in diameter was attached at the top of the scintillator container to keep the neutron detector free from bubbles

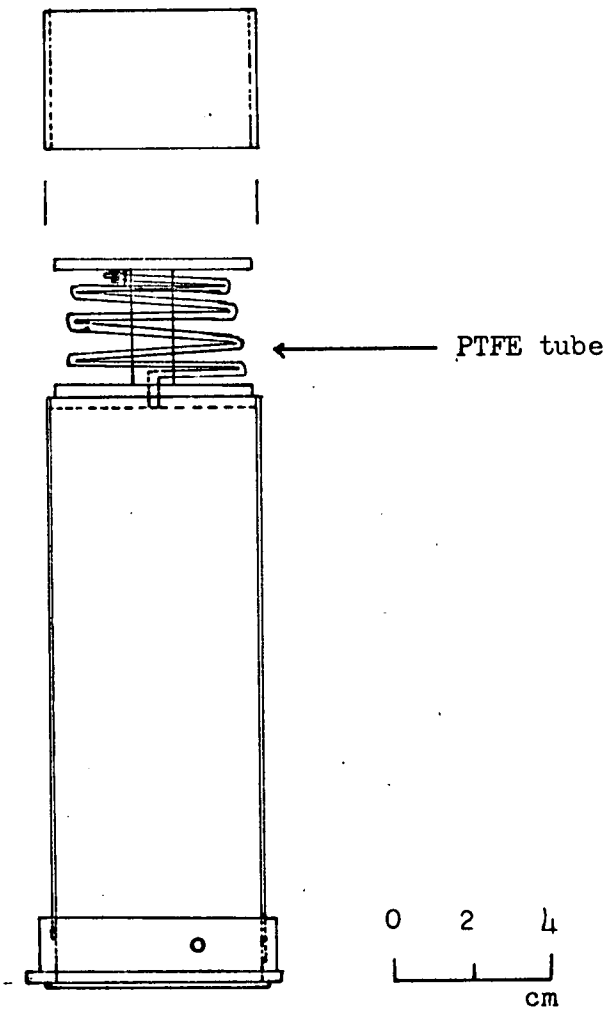

Fig. (17) NE 213 Liquid Scintillator Container

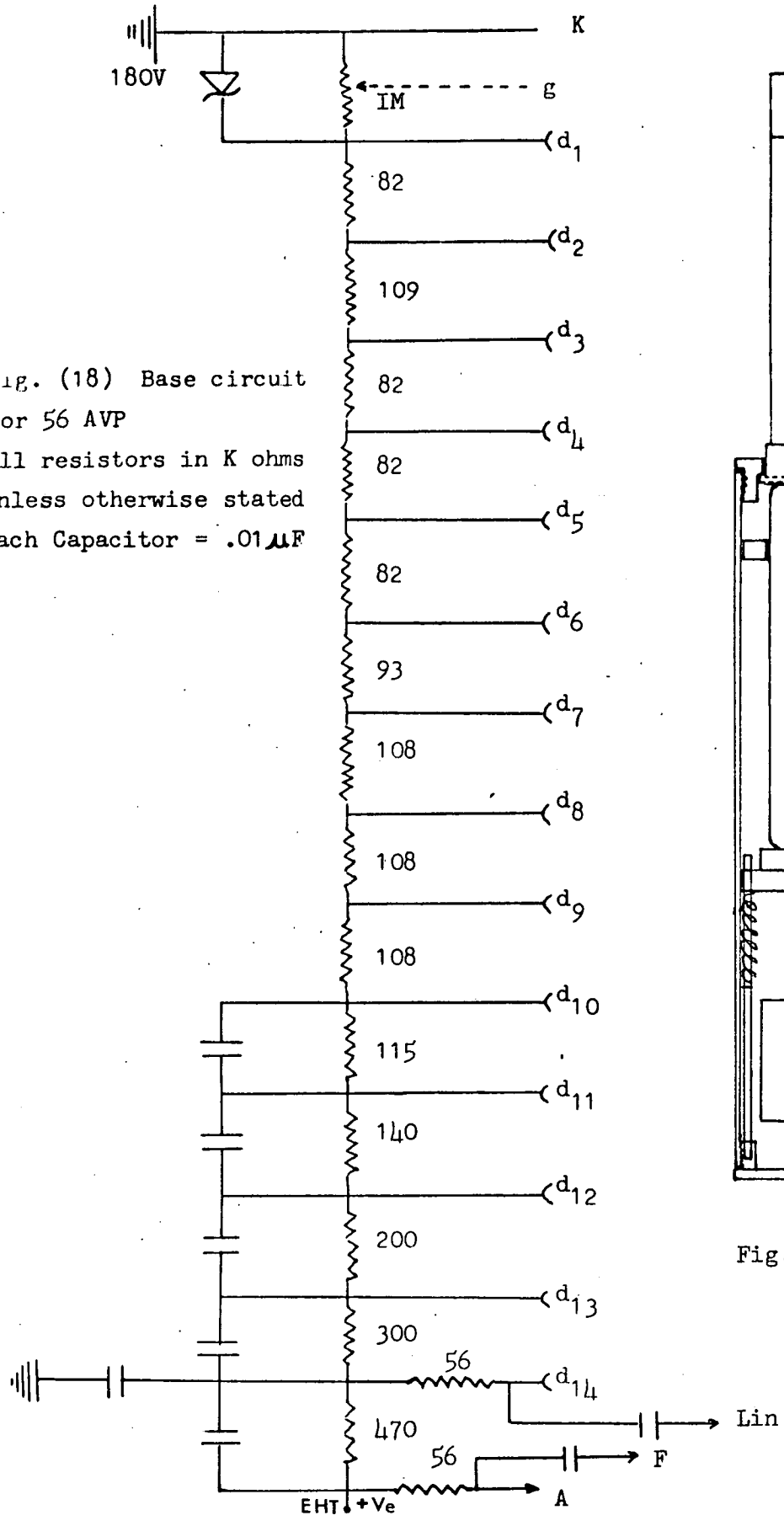

Fig. (18) Base circuit for 56 AVP
All resistors in K ohms unless otherwise stated
Each Capacitor = .01 μF

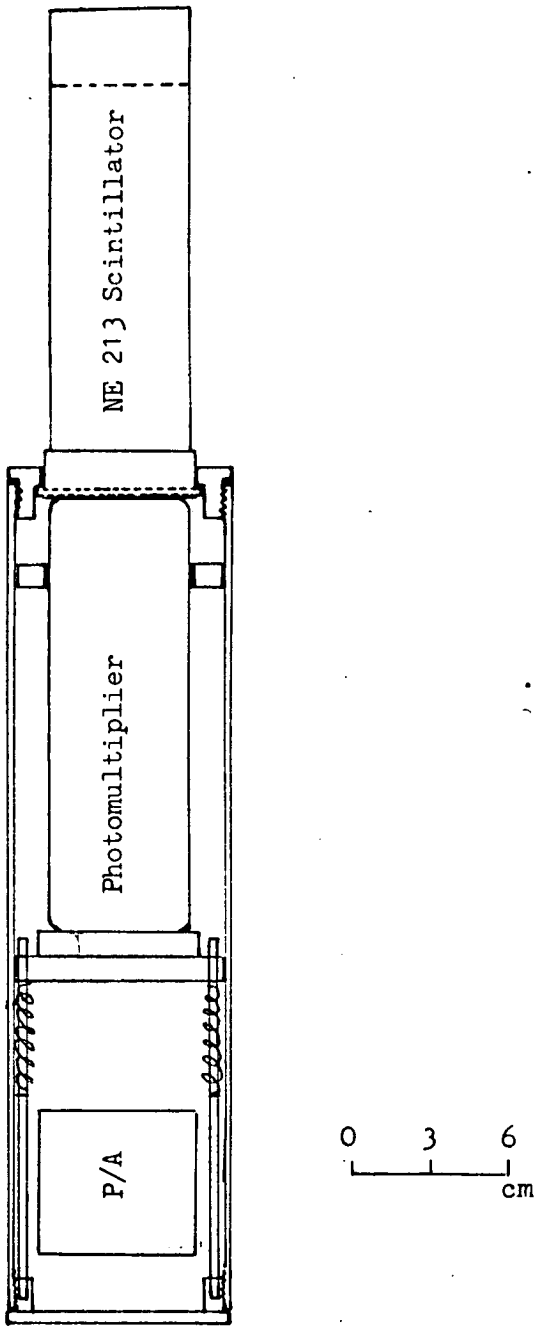

Fig. (19) Neutron Detector

by capillary action. The filling of the scintillator was done in the laboratory. Fig. (17) shows the diagram of the liquid scintillator container. The glass window of the scintillator was coupled to the photocathode of the photomultiplier by using an optical contact grease. The circuit diagram of the carbon resistor dynode chain of the photomultiplier is shown in Fig. (18). The pulses from the 14th dynode of the photomultiplier were found to be the most suitable for pulse shape discrimination purpose. The fast pulses to denote the instants at which neutrons were detected in the liquid scintillator were taken from the anode of the photomultiplier. The photomultiplier light tight container with liquid scintillator mounted is shown in Fig. (19).

2.7 Neutron-Gamma Pulse Shape Discrimination

Organic scintillators are efficient detectors for charged particles, gamma-rays and neutrons. The intensity of light emitted by a particular organic scintillator after it has been excited by the incoming radiation decays with fast and slow components. The relative intensities of these fast and slow components depend upon the nature of the incident exciting radiation. For NE 213 the ratio of the intensity of the slow component to the fast component is larger for fast neutrons than for gamma-rays. The difference in the ratio results in current pulses of different shapes from the photomultiplier for gamma-rays and neutrons. The pulse shape discrimination (PSD) is obtained by distinguishing between these different pulse shapes. Different techniques were used by numerous authors for this purpose[74-81].

In a commonly used method the photomultiplier is operated under the conditions of space-charge saturation between anode and the last dynode. A positive pulse could be obtained from the last dynode for neutrons and a negative pulse for the case of gamma-rays[77-79].

The use of cross-over of an integrated and doubly differentiated pulse from a single dynode of the photomultiplier has been made a means of particle identification[80,81]. In this method a pulse whose amplitude is a measure of the time of cross-over is obtained. The zero cross-over point of a doubly differentiated pulse depends on the rise time of the original signal. The rise time of a pulse from the photomultiplier after a differentiation will be different for gamma-rays and for neutrons, so after double differentiation the cross-over instant of the pulse carries the information necessary for particle identification. Hence PSD can be obtained by measuring the time delay between the origin of the pulse and its zero cross-over point. A time difference of some tens of nanoseconds can be conveniently obtained between the points of cross-over of the pulses produced by recoil electrons and by recoil protons. Different shapes of a pulse from a photomultiplier after integration and differentiation are shown in Fig. (20).

Throughout this work zero cross-over timing technique was employed for pulse shape discrimination against gamma-rays. A block diagram for neutron-gamma PSD is shown in Fig. (21). The linear pulses from the last dynode of the photomultiplier through a pre-amplifier were used for both a linear amplifier and a PSD unit. The circuit[82] of the PSD unit was constructed and is given in the appendix. Discriminators were used at the outputs of the linear amplifier and of the PSD unit for setting linear bias level and gamma-rays rejection respectively. The discriminators contained variable delays up to 3μsec so that the optimum time relation between the two discriminator pulses could be obtained for the following coincidence gate (AND). The resultant coincidence pulses were shaped by an interface logic unit (not shown) to meet the requirements of the coincidence input of the pulse height analyser. A pulse height

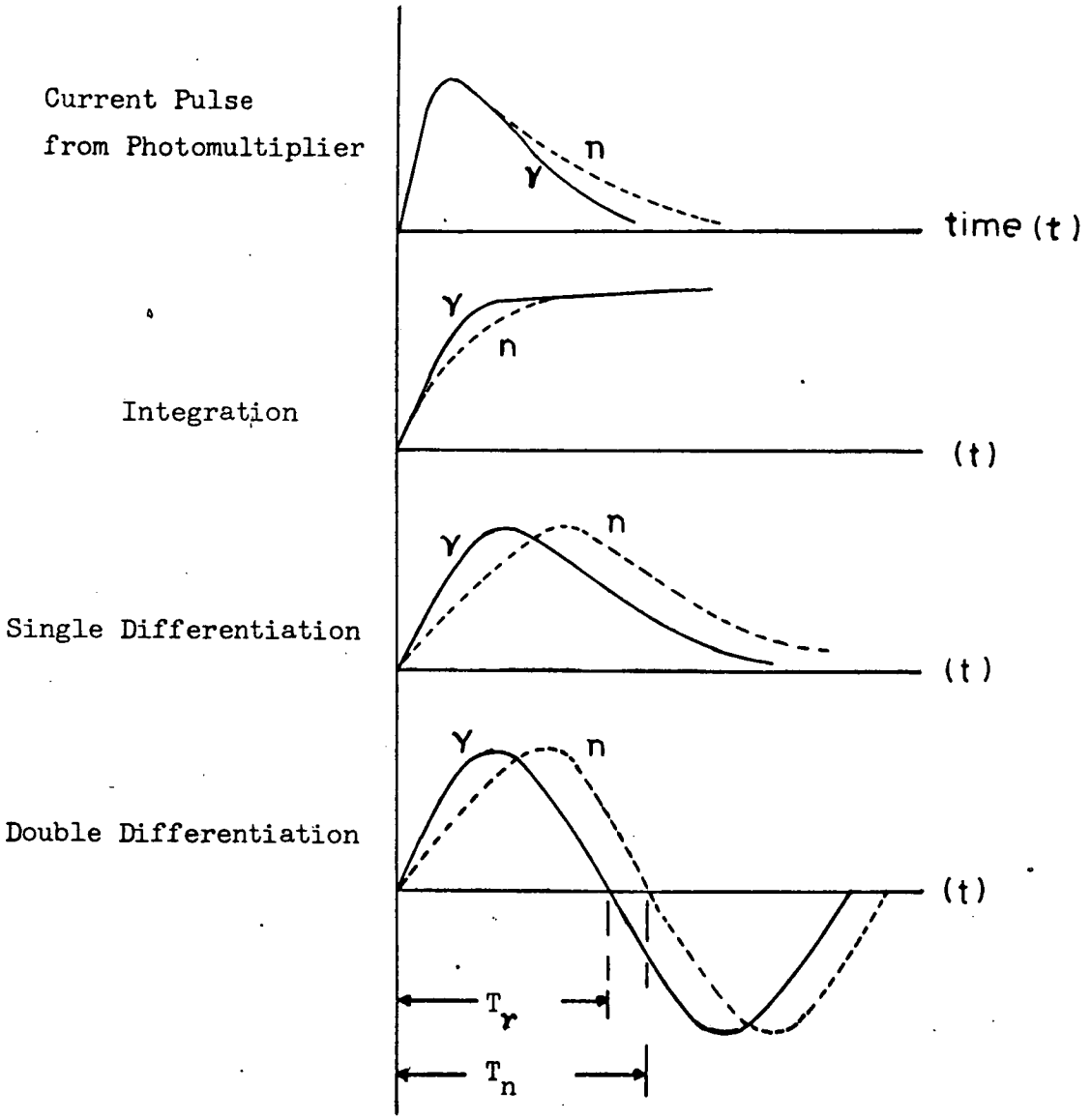

Fig. (20) Photomultiplier linear pulse shapes

P/A - Preamplifier Amp - Amplifier DISC - Pulse Height Discriminator

PSD - Pulse Shape Discriminator PHA - Pulse Height Analyser AND - Coincidence Unit

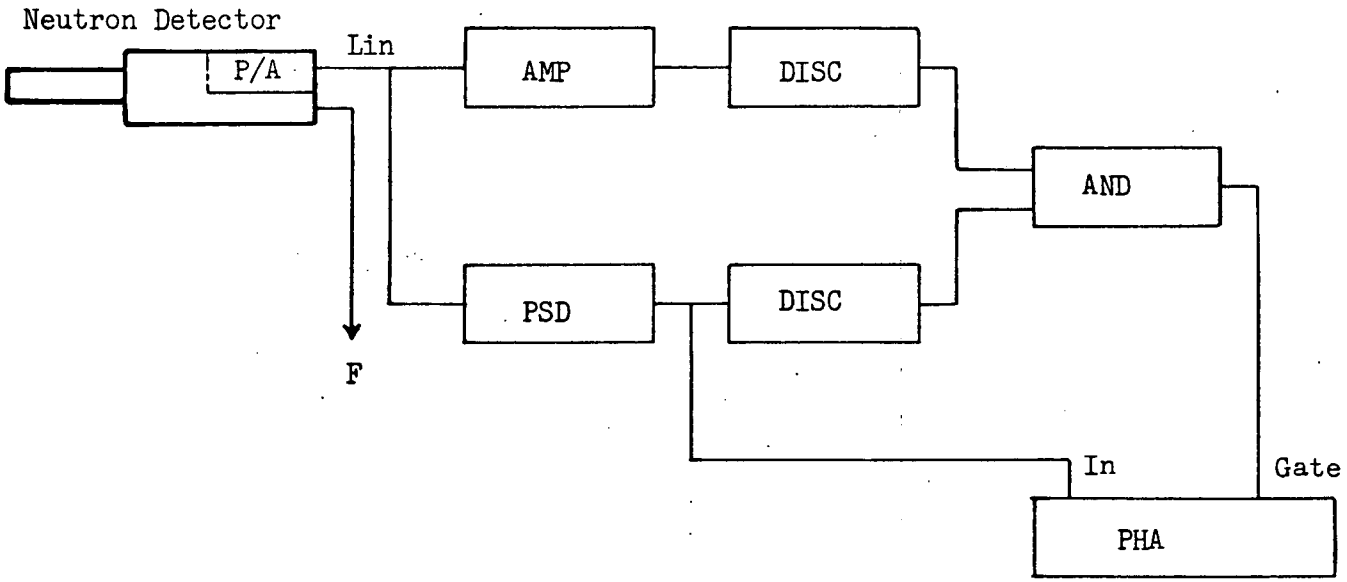

Fig. (21) The electronic block diagram for neutron-gamma pulse shape discrimination

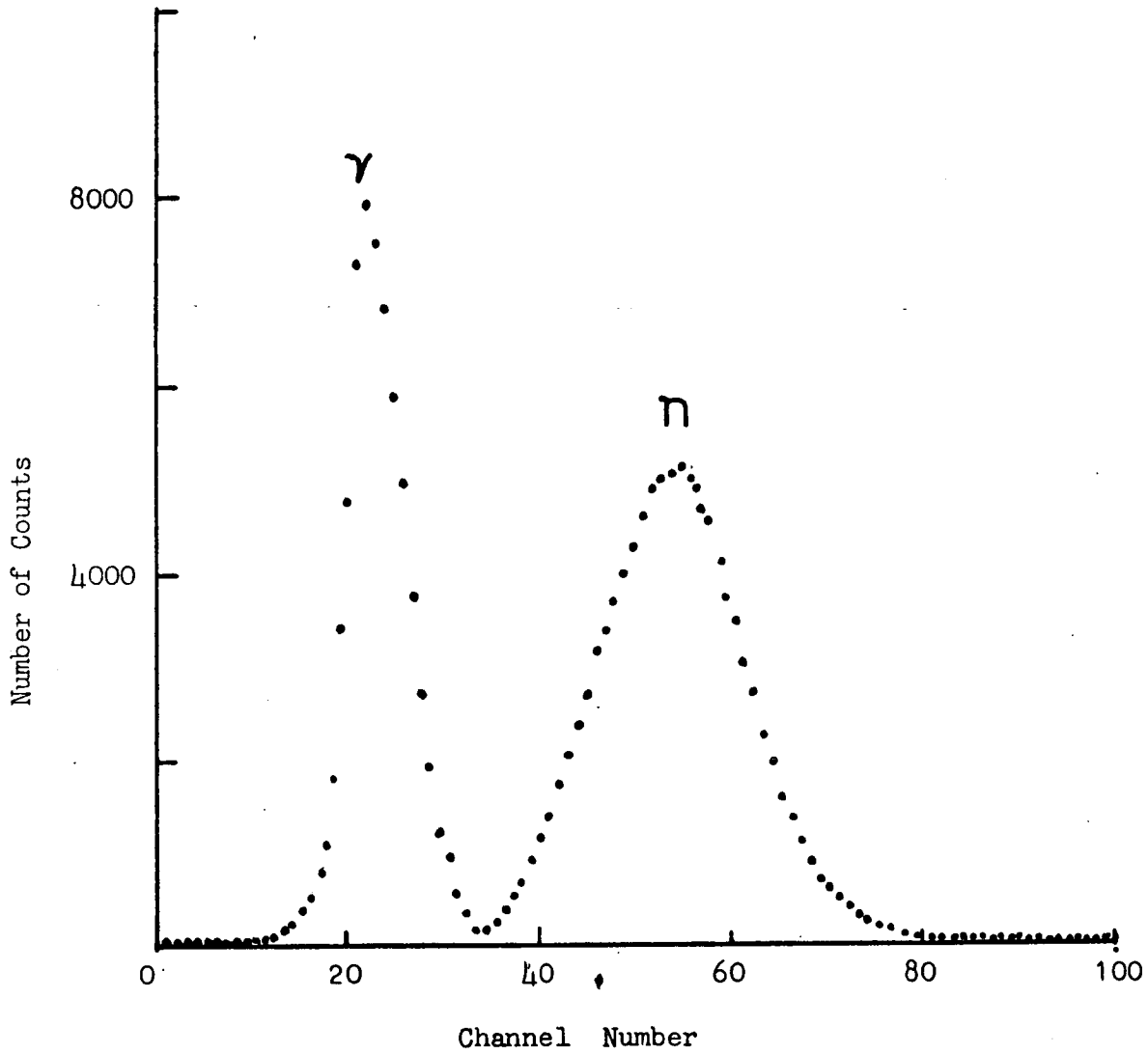

Fig. (22) Pulse shape discrimination spectrum with Am-Be neutron source

spectrum of the output from the PSD unit is shown in Fig. (22) for the case of an Am-Be neutron source. In this pulse height spectrum the multichannel pulse height analyser was gated by the coincidence pulses to accept events in the scintillator with a light output greater than that due to 340 keV recoil electrons. Two peaks were observed, one due to gamma-rays and the other due to neutrons. The discriminator threshold level at the output of the PSD unit was set in the valley between the two peaks to remove pulses due to gamma-rays.

2.8 Electronics of the System

A simplified block diagram of the electronics in the associated particle time-of-flight method is shown in Fig. (23). Detailed schematic drawing of the electronics used for the polarization and cross-section measurements by this technique is shown in Chapter III.

The current pulses from the anode of the photomultiplier and a fast pre-amplifier connected directly to the associated particle detector provided the timing signals for neutrons and He^3 particles respectively. For timing signals from the He^3 particle detector a fast low noise pre-amplifier and an insertion fast amplifier was built following the design of Sherman et al[83]. The circuit diagrams are shown in the appendix. The fast pulses from the fast pre-amplifier were further amplified by the insertion fast amplifier. The fast pulses having rise time less than 4 n sec were again amplified by a fast amplifier, an Ortec model 454 Timing Filter Amplifier (TFA). Following this linear amplification, the fast signals trigger a Constant Fraction Timing Discriminator (CFD), Ortec model 463. The CFD discrimination level was set sufficiently high above the noise. The pulses from CFD were used, being delayed in a fast delay amplifier, Ortec model 427A, as the 'stop' pulse in

P/A - Preamplifier Amp - Amplifier DISC - Discriminator PSD - Pulse shape discriminator
AND - Coincidence Unit F.A. - Fast Amplifier F.D. - Fast Discriminator FPA - Fast P/A
IFA - Insertion F.A. TFA - Timing Filter Amplifier CFD - Constant Fraction Discriminator
FDA - Fast Delay Amplifier CPA - Charge Sensitive P/A SCA - Single Channel Analyser
TAC - Time to Amplitude Converter

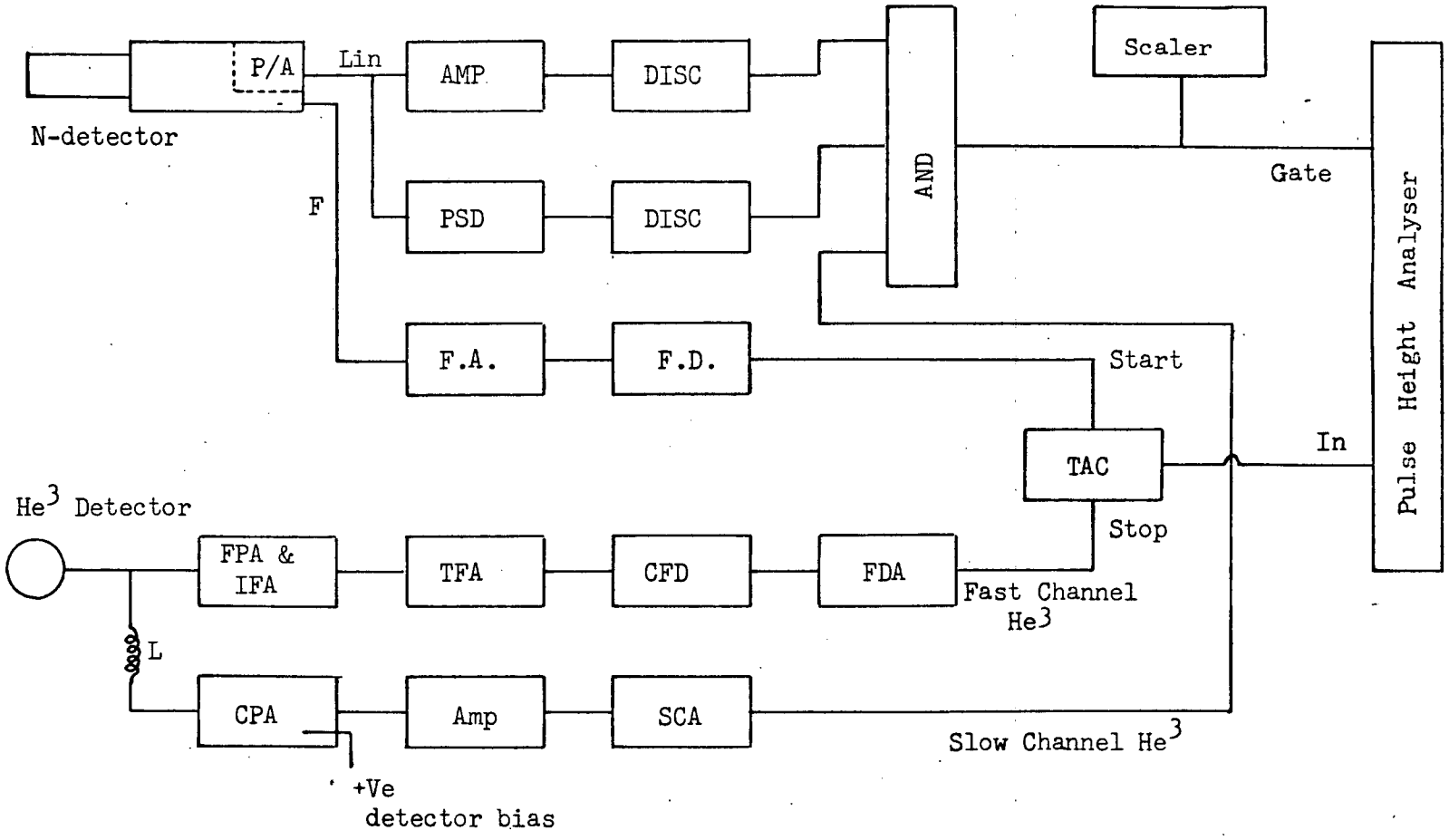

Fig. (23) A block diagram showing the arrangement of the electronics used with the associated particle method.

a time to amplitude converter, TAC, Nuclear Enterprise model 4645. The fast anode pulses of the photomultiplier after being amplified in a fast amplifier (Nuclear Enterprise model 4634) were used to trigger a fast leading edge discriminator (Nuclear Enterprise model 4635). The start signal to the TAC was provided from this fast discriminator.

The energy signals of He^3 particles were obtained from the charge sensitive pre-amplifier CPA (Hewlett-Packard model 5554A) being connected to the He^3 particle detector through an inductor 'L'. This inductor was made large enough to delay the charge transfer to the CPA sufficiently, thereby allowing full voltage amplitude at the input of the fast pre-amplifier. The energy signals were amplified by an amplifier AMP (Ortec model 452) and were fed to a single channel analyser SCA (Ortec model 406A). The lower level threshold of the SCA was set sufficiently high to select only slow pulses due to He^3 particles.

As explained earlier PSD, Amp, two discriminators (Disc) and the coincidence unit AND connected to the linear signal from the photomultiplier acts to detect neutrons and reject gamma-rays. For detecting a coincidence between neutrons and the associated He^3 particles the third input of the coincidence gate AND was used. The resultant coincidence pulses from AND were shaped properly by an interface logic unit (not shown) to meet the requirement of the coincidence input of the multichannel pulse height analyser. The neutron-He^3 time-of-flight spectrum from TAC is obtained on the pulse height analyser being gated by the neutron-He^3 coincidence pulses. In this way only associated neutrons corresponding to the recoil He^3 particles would be detected.

2.9 Performance of the Electrostatic Analyser

The performance of the electrostatic analyser was tested at various

deuteron energies ranging from 200 keV to 400 keV. The neutron detector, NE 213 of dimensions 2" x 6", was placed at a distance of 52.0 cm from the target and in the neutron cone at 49^{o} angle with respect to deuteron beam in such a way that the axis of the scintillator was normal to the incident neutrons in the cone.

Initially the behaviour of the analyser was tested at 200 keV incident deuterons on the TiD target at both low and higher deuteron currents. The voltage to be applied to separate He^3 particles from deuterons could be calculated from equation (2.4.3). The voltages for the deflecting plates were taken from two 50 kV power supplies manufactured by Brandenburg (model 807R). Different voltages on the deflecting plates were tried in order to see the effect of separation between He^3 particles and the deuterons and are shown in Fig. (24). The best separation therefore could be obtained when the deflection voltages were $\pm$ 9 kV on the deflecting plates. Fig. (25a) shows the linear He^3 spectrum when the pulse height analyser was gated by the neutron-He^3 coincidence pulses, the neutron detector being placed in the neutron cone. The time-of-flight spectrum obtained is shown in Fig. (25b) and exhibits a good peak to background ratio. The time resolution of the spectrum was obtained by delaying the start pulse by known times with different lengths of cable. The time resolution was found to be 22 ns at FWHM. There are various factors which effect the time resolution and will be discussed in the next section. Fig. (25c) shows the time-of-flight spectrum at higher deuteron current of 50μA. The spectrum was flat when the neutron detector was removed from the neutron cone as shown in Fig. (25d).

The deuteron energy was then increased to 250 keV. The direct He^3 spectrum is shown in Fig. (26a). Figs. (26b) and (26c) show the He^3 spectra

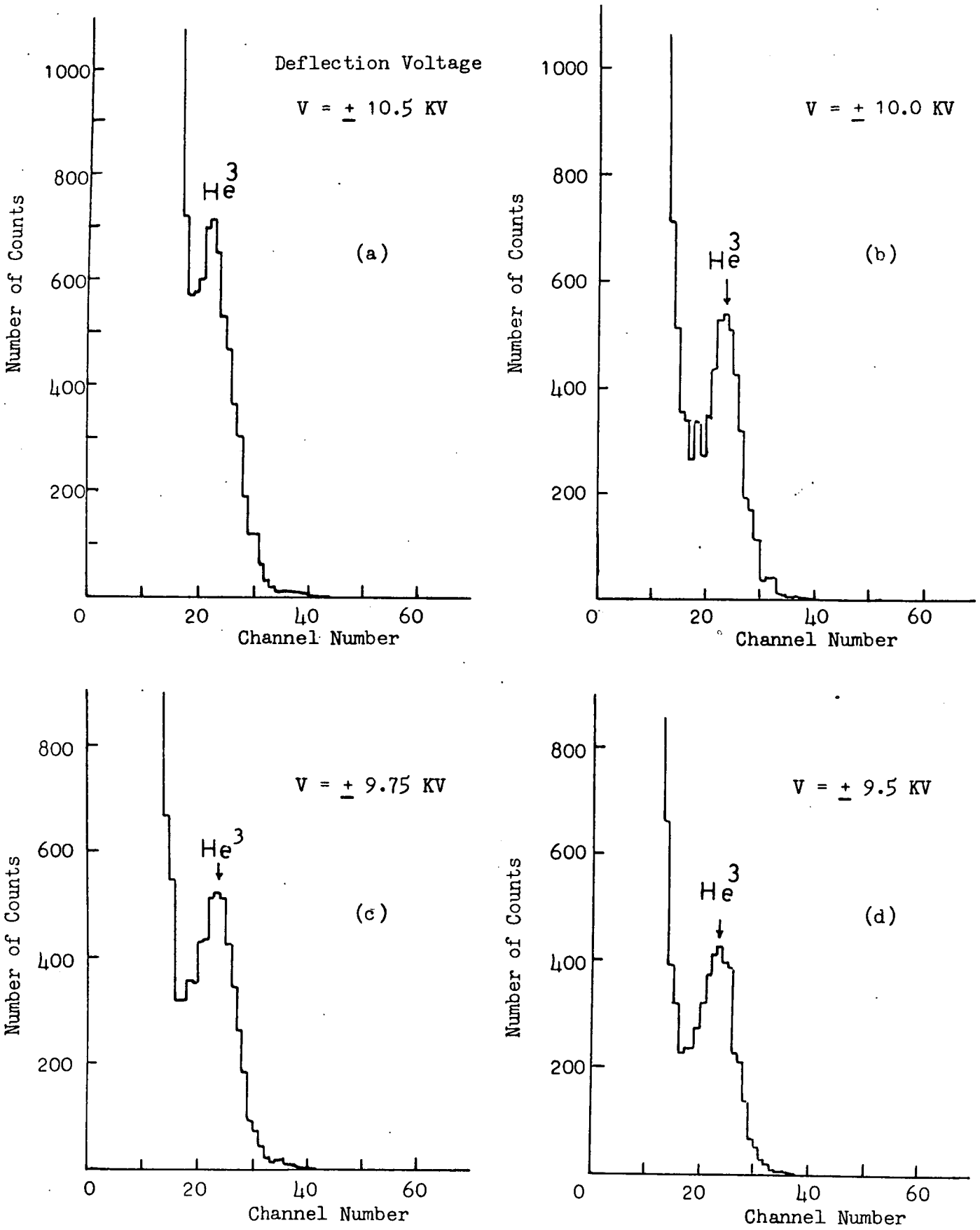

Fig. (24) He^3 particle spectra at different deflection voltages (V) on the deflecting plates of the Electrostatic Analyser

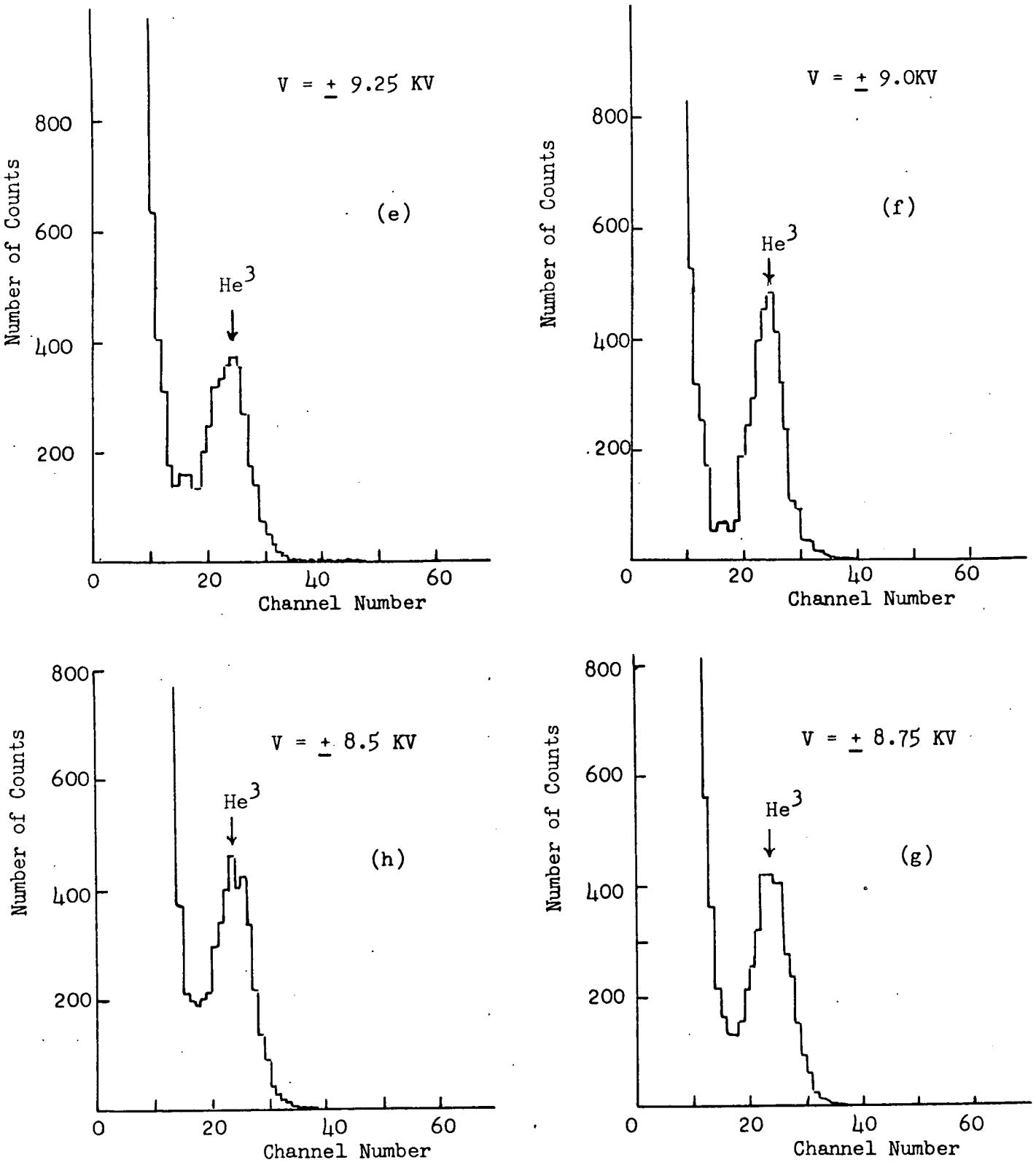

Incident deuteron energy (E_d) = 200 keV; He^3 particle detector angle $\theta_{He^3} = 112^o$ (Lab).

Fig. (24) continued

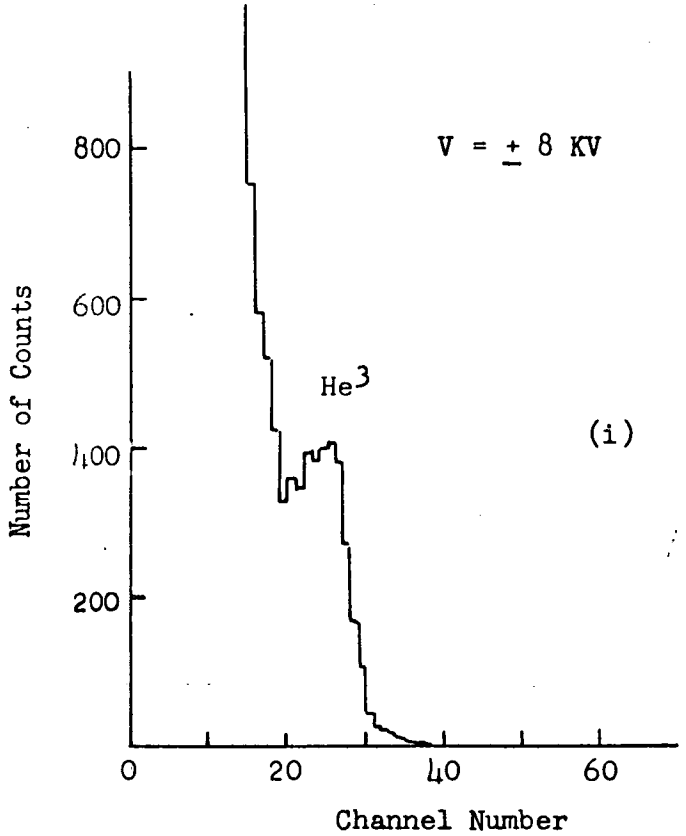

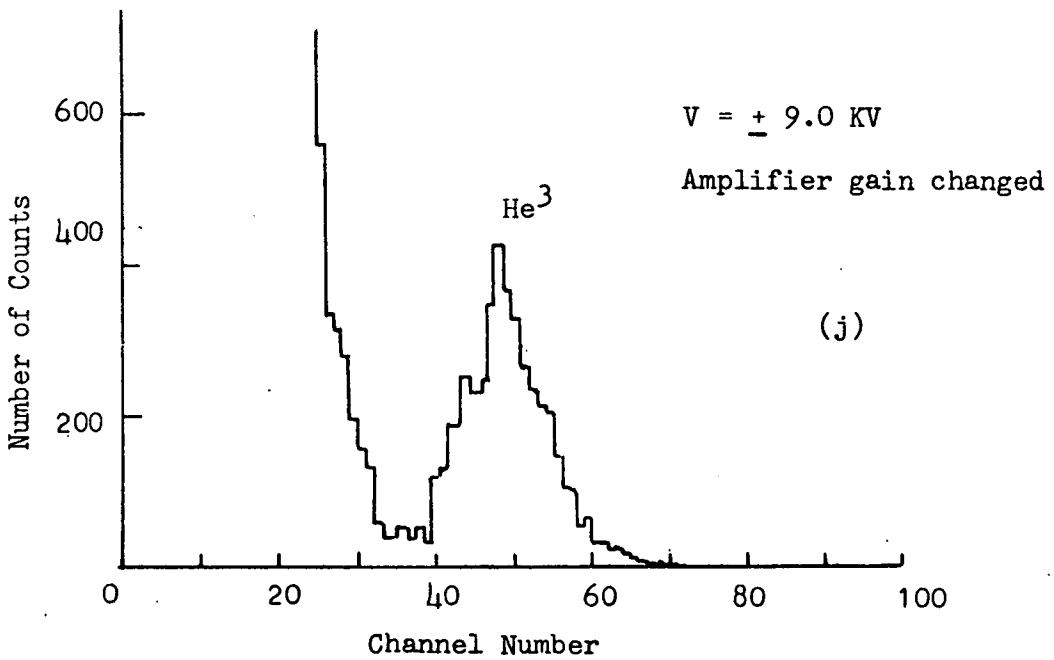

Fig. (24) continued

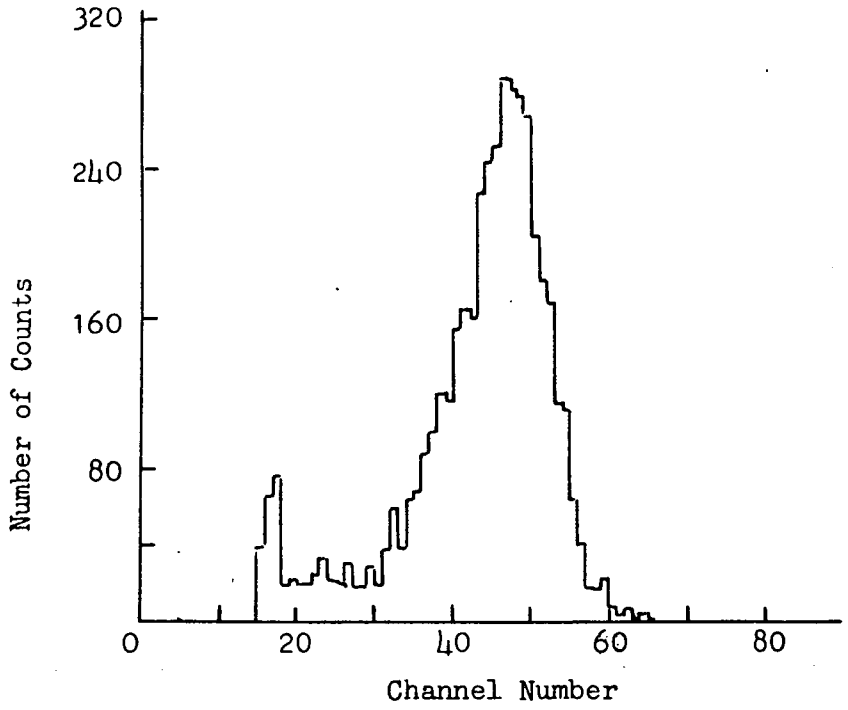

Deflecting Plates Voltage
V = ± 9.0 KV

Fig. (25a) He^3 linear spectrum in coincidence with associated neutrons, E_d = 200 keV

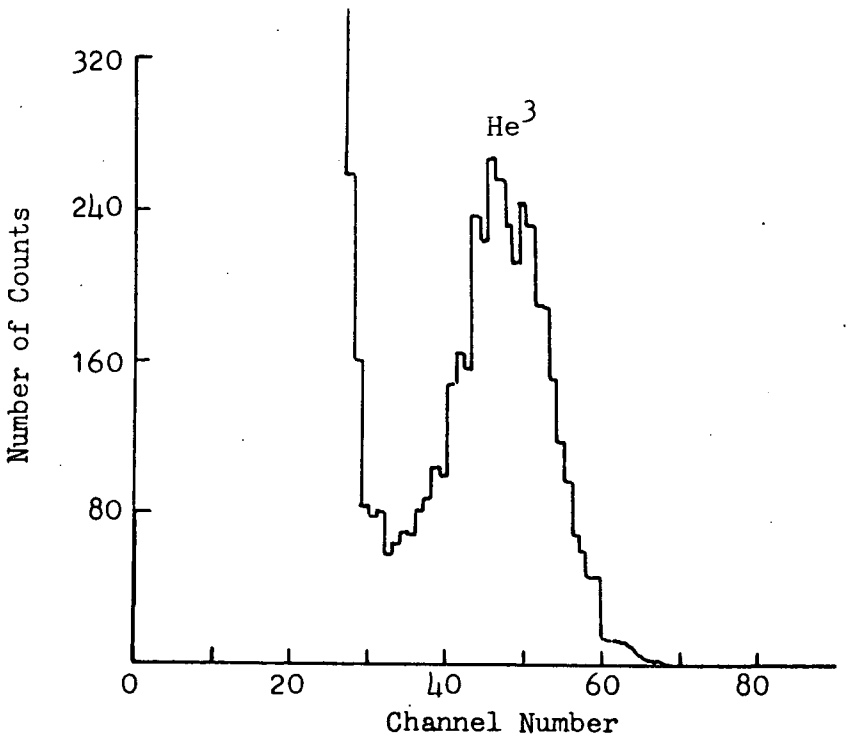

Direct He^3 linear spectrum for comparison with Fig. (25a)

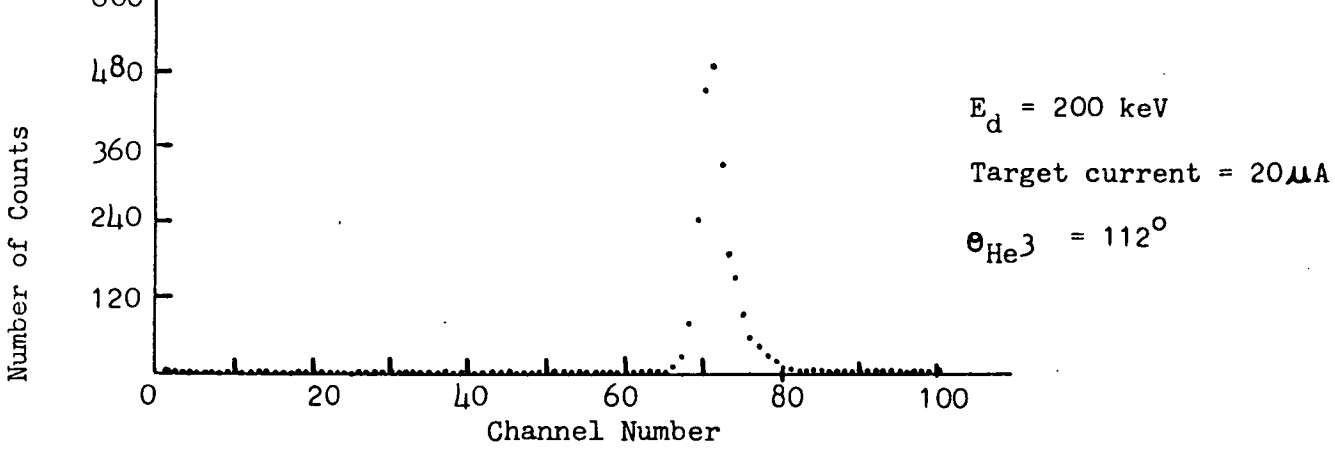

Fig. (25b) Associated Particle Time-of-Flight Spectrum

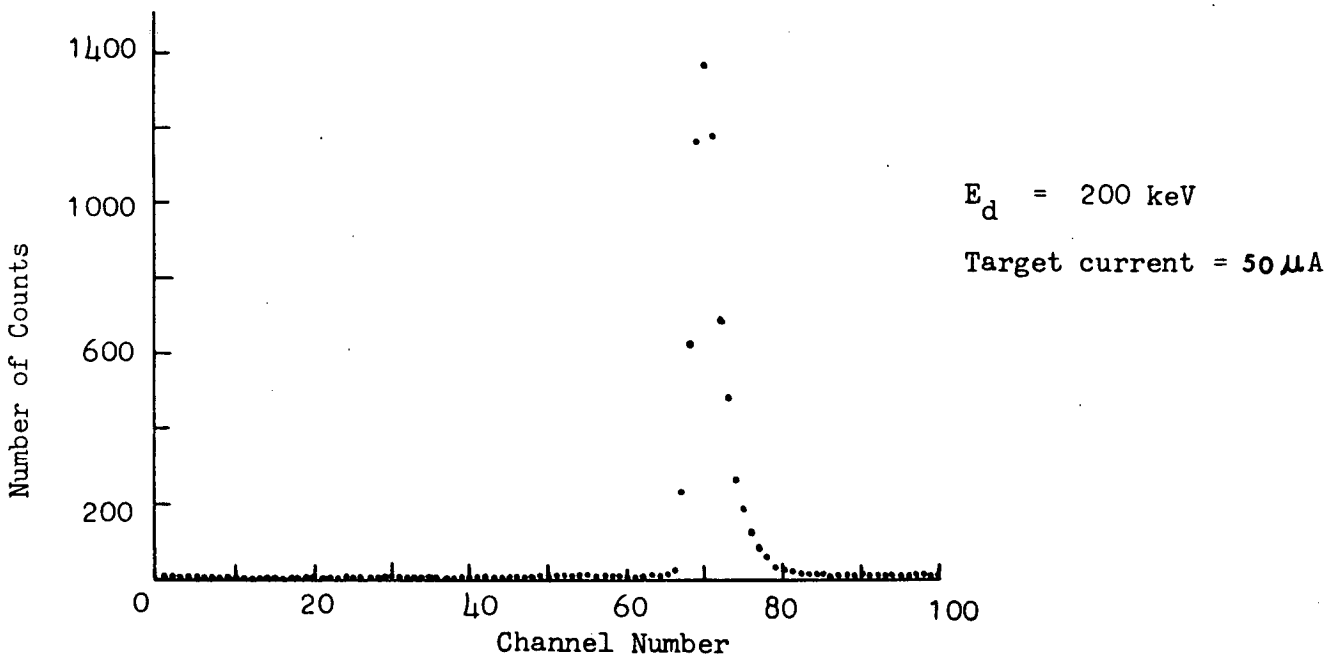

Fig. (25c) Associated Particle T.O.F. Spectrum

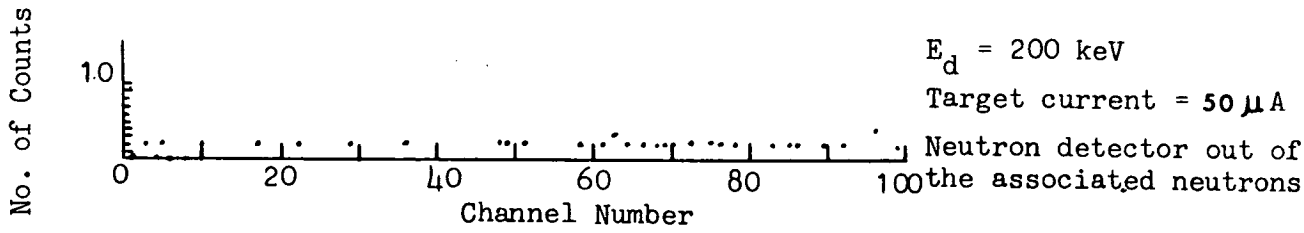

Fig. (25d) Associated Particle T.O.F. Spectrum

in coincidence with neutrons when the neutron detector was placed in the associated neutron cone and out of cone respectively. The only peak shown in Fig. (26c) is due to random coincidences between deuterons and background neutrons. Figs. (26d) and 26e) show the time-of-flight spectra at lower and higher deuteron currents of 12 μA and 50 μA on the target respectively.

At 300 keV deuteron energy the separation between He^3 particles and the deuterons is shown in Fig. (27a). The He^3 spectrum in coincidence with neutrons when the neutron detector was placed in the associated neutron cone and out of cone respectively are shown in Figs. (27b) and (27c). Fig. (27c) shows the peak due to random coincidences between the deuterons and background neutrons. The time-of-flight spectra at 10 μA and 50 μA incident deuteron currents are shown respectively in Figs. (27d) and (27e). The time-of-flight spectrum was flat when the neutron detector was moved out of the neutron cone.

Figs. (28a) and (28b) show the He^3 spectrum without and with neutron-He^3 coincidence at 350 keV deuteron energy respectively. The direct He^3 spectrum in Fig. (28a) indicates that the separation between He^3 particles and the elastically scattered deuterons is very poor mainly due to the higher deuteron energy. The random coincidences between the deuterons and background neutrons are shown in Fig. (28c), the neutron detector being out of the neutron cone. The time-of-flight spectra at 12 μA and 45 μA deuteron currents are shown respectively in Figs. (28d) and (28e). The background level under the time-of-flight peak in Fig. (28e) has increased and the background to peak ratio is about 1:5 mainly due to the poor separation between deuterons and He^3 particles at this energy.

The deuteron energy was still increased further up to 400 keV. The separation at this energy between He^3 particles and the deuterons became

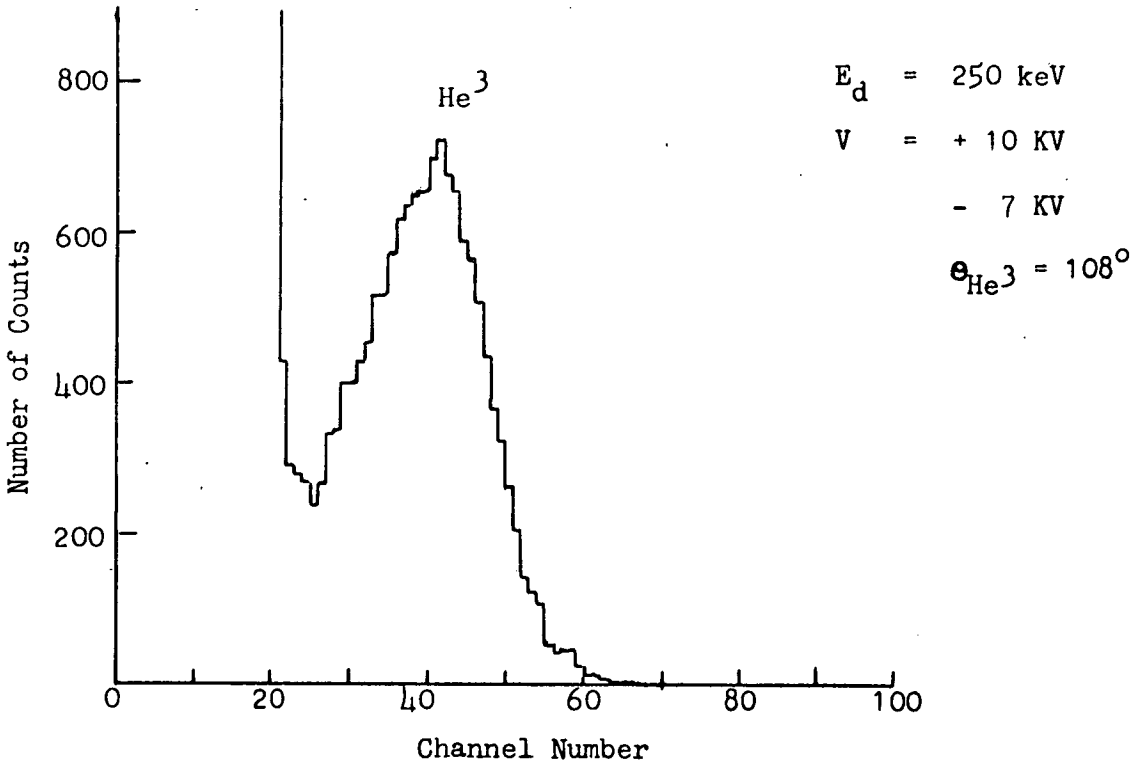

Fig. (26a) Direct He^3 linear spectrum

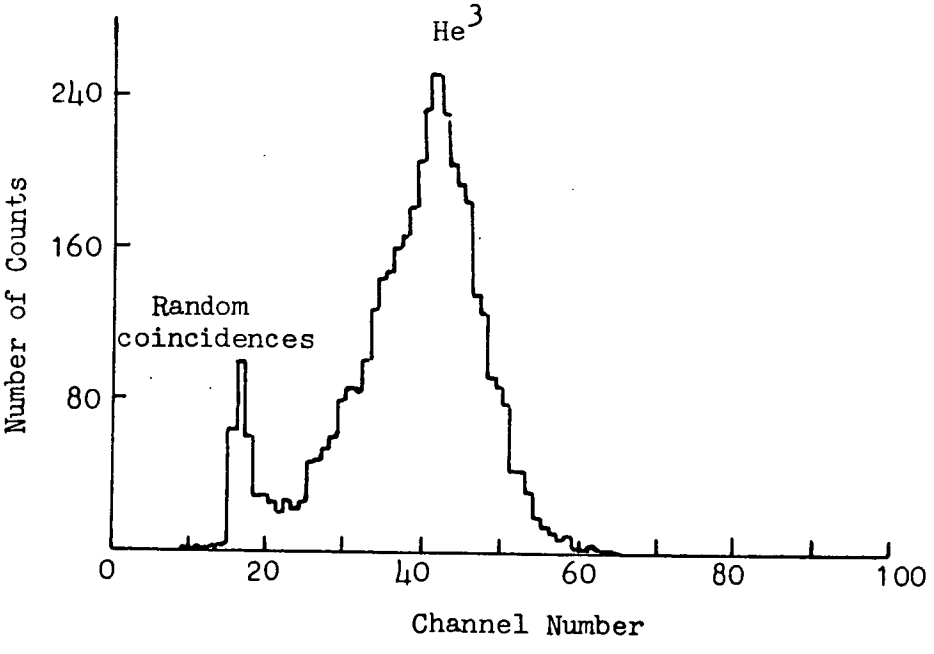

Fig. (26b) He^3 linear spectrum in coincidence with the associated neutrons

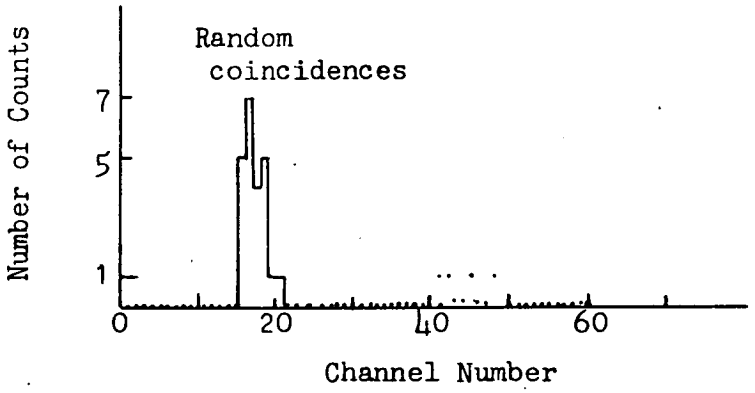

Fig. (26c) He^3 linear spectrum in coincidence with neutrons

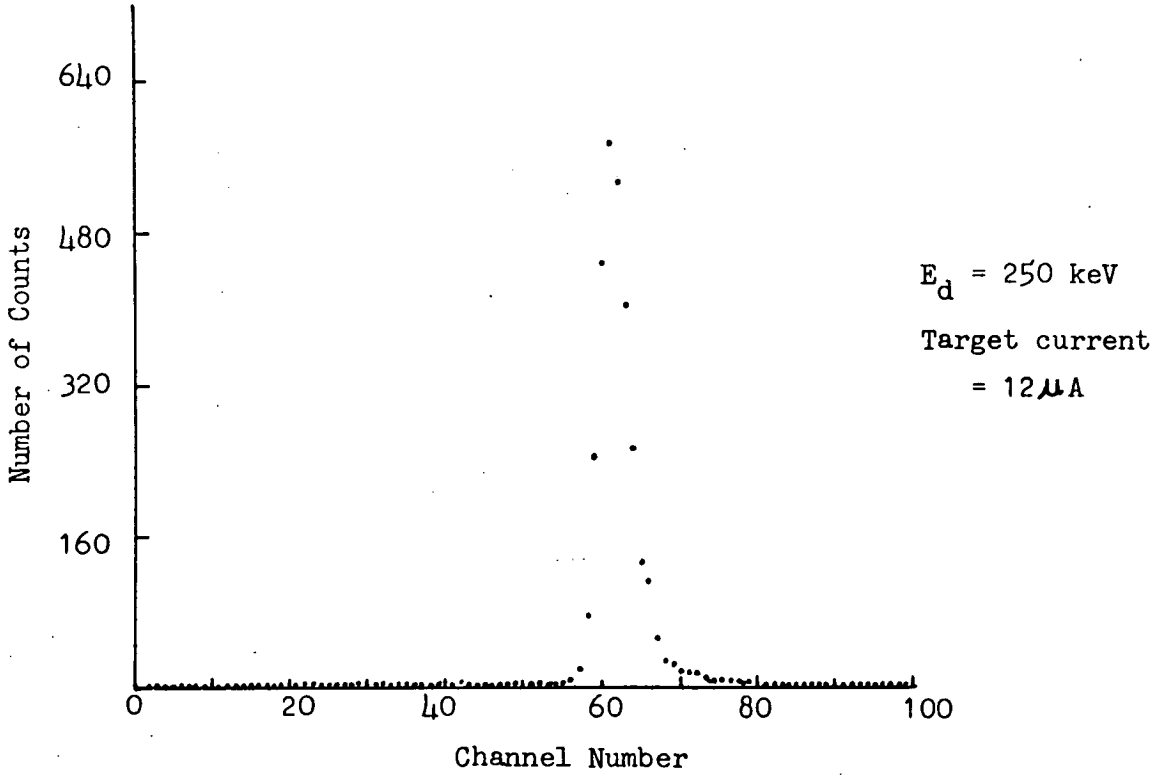

Fig. (26d) Associated Particle T.O.F. spectrum in the neutron cone

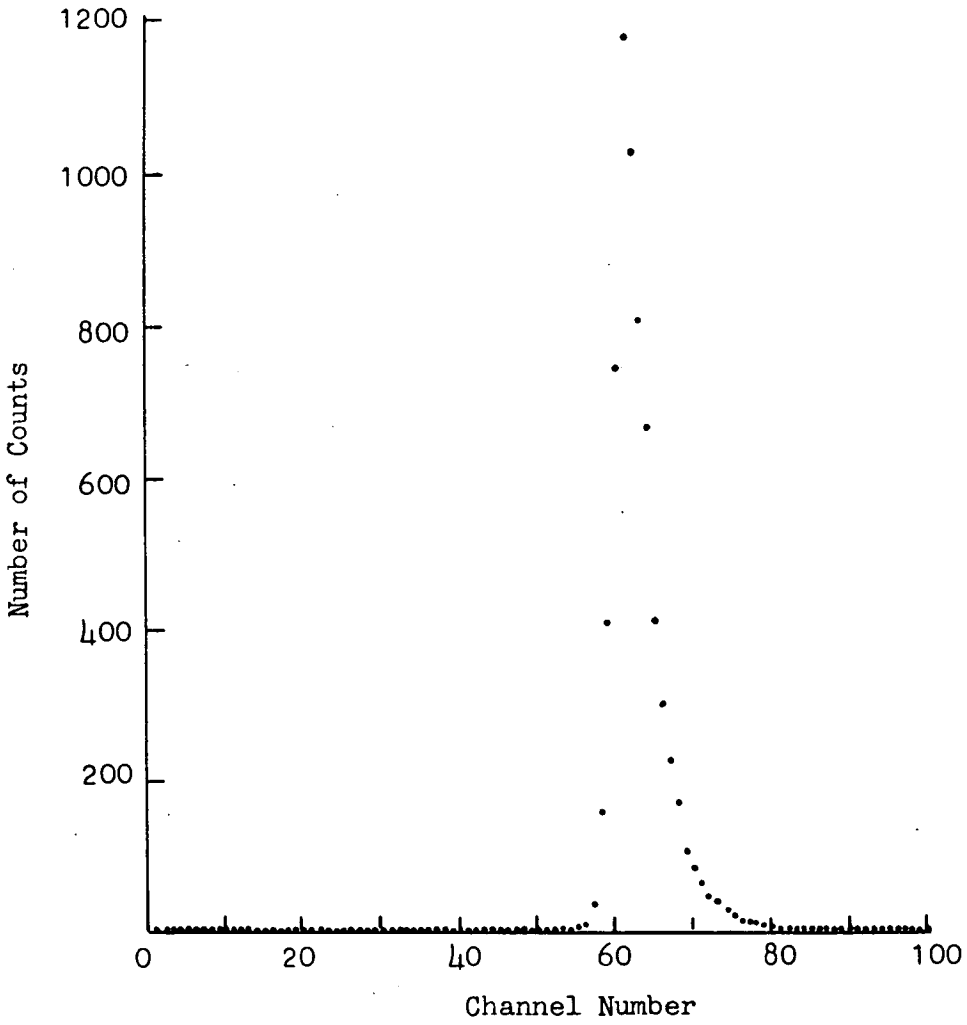

Fig. (26e) Associated Particle T.O.F. spectrum at 250 keV incident deuteron energy and 50μA target current. $\theta_{He^3} = 108^{\circ}$; V = +10 KV, -7 KV, θ_n (neutron detector angle) = 49°.

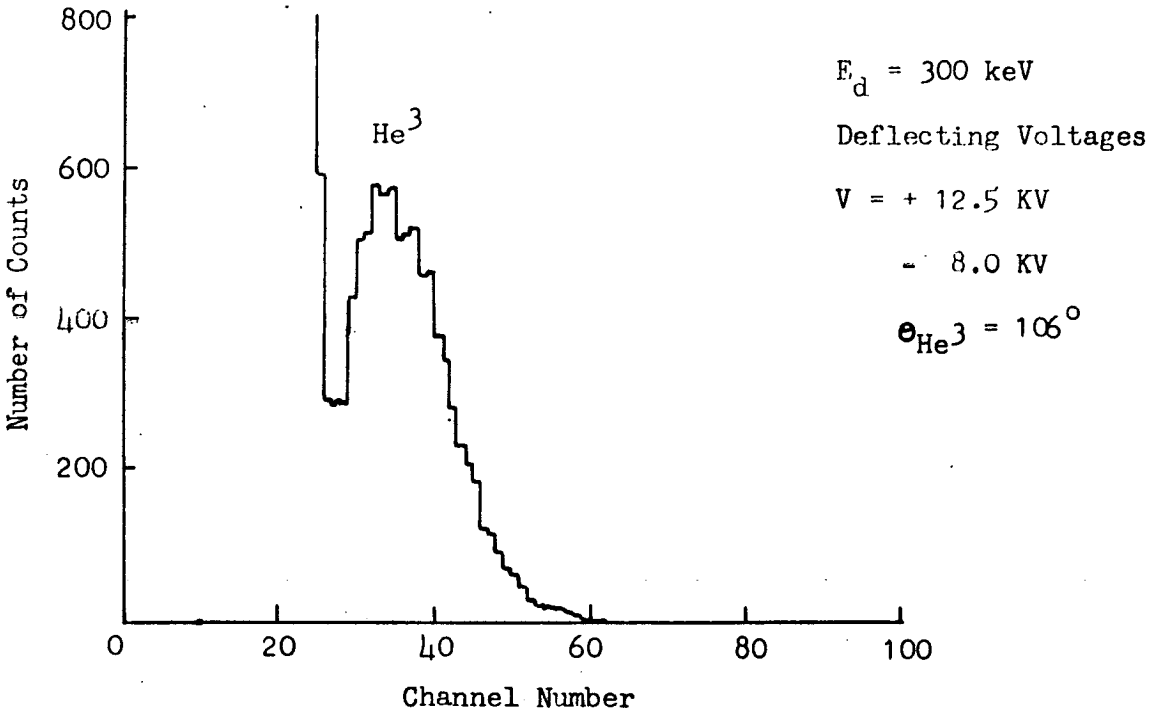

Fig. (27a) Direct He^3 linear spectrum

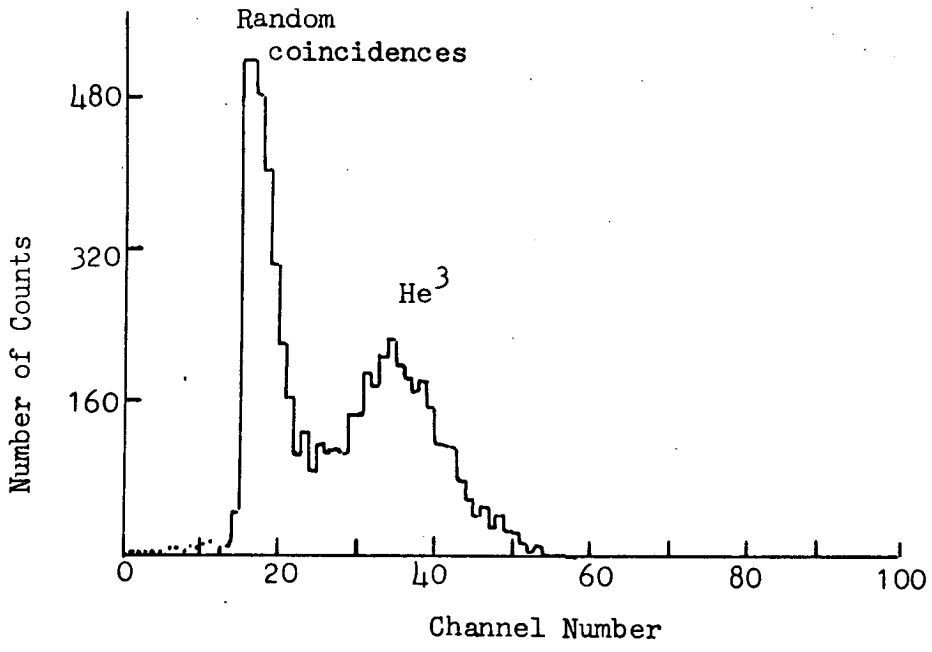

Fig. (27b) He^3 linear spectrum in coincidence with the associated neutrons

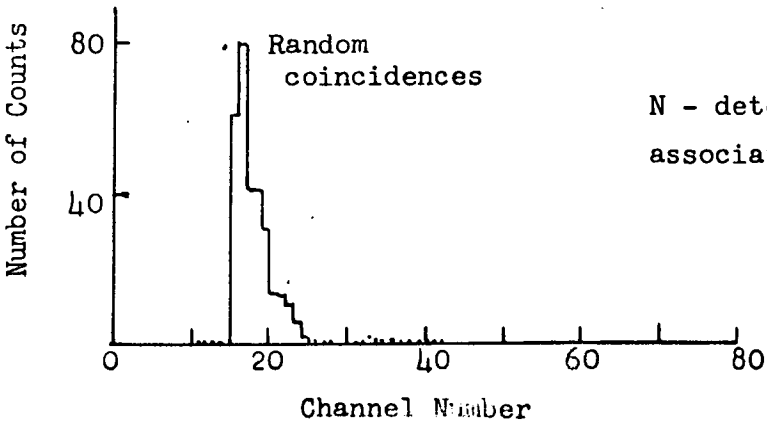

Fig. (27c) He^3 linear spectrum in coincidence with neutrons

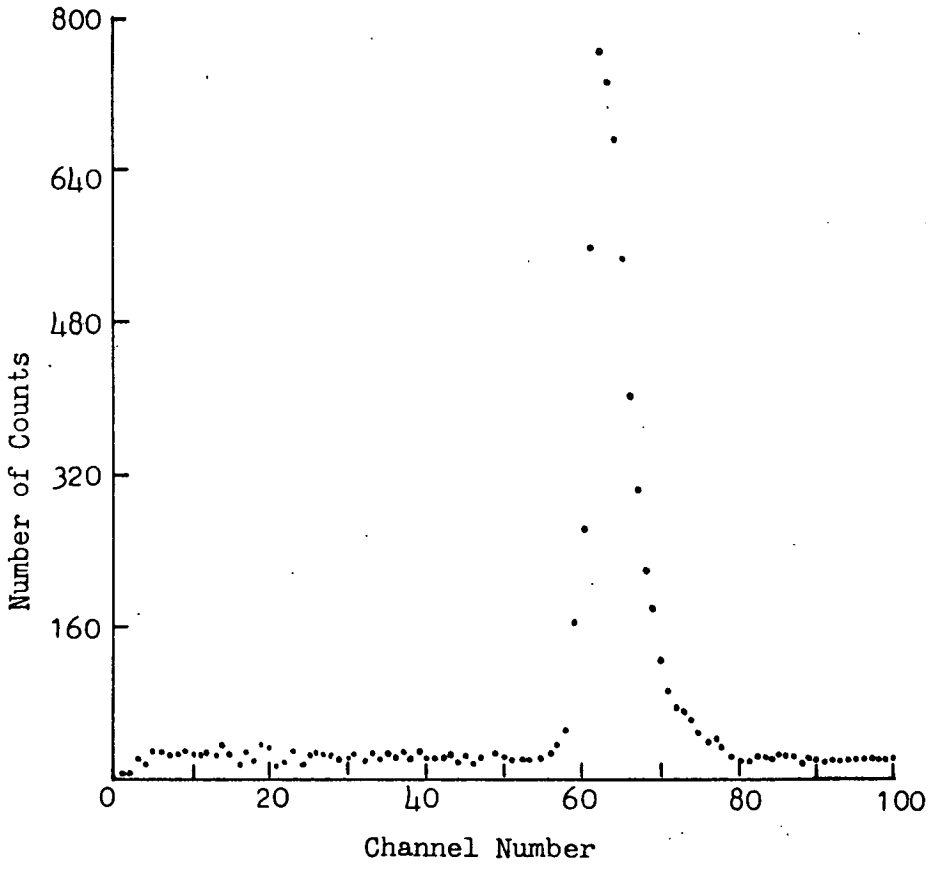

Fig. (27d) Associated Particle T.O.F. spectrum at E_d = 300 keV and target current of 10μA

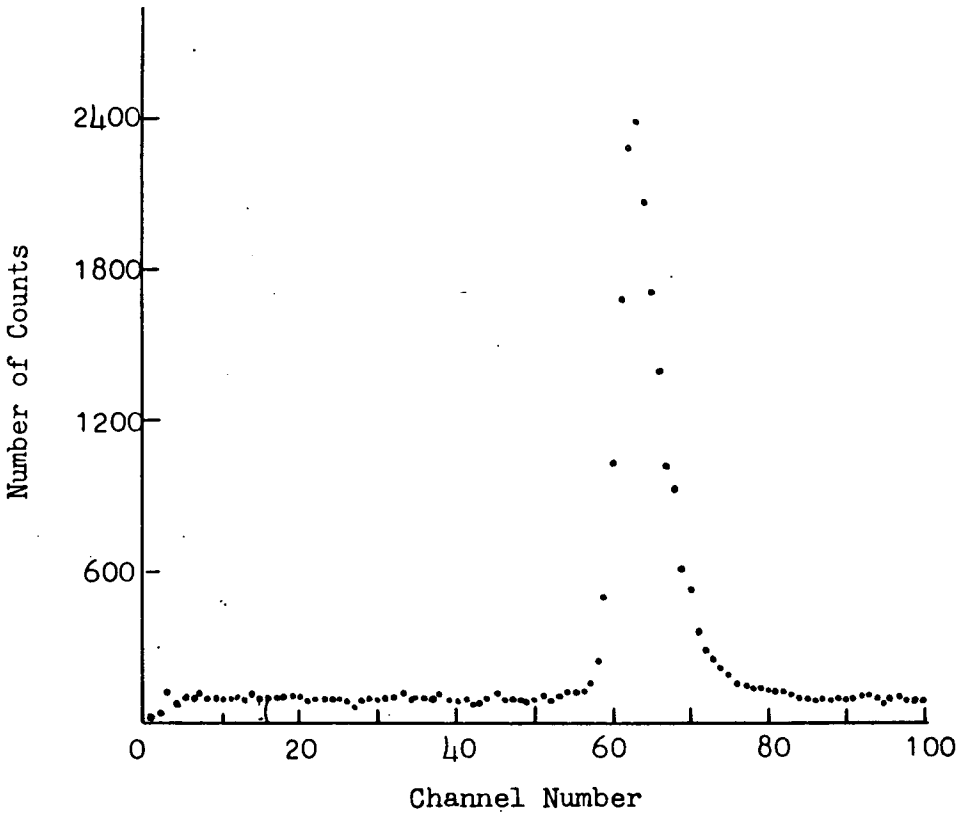

Fig. (27e) Associated Particle T.O.F. spectrum at

E_d = 300 keV and target current = 50μA

θ_{He^3} = 106°

θ_n = 49° and V = +12.5 KV; -8.0 KV

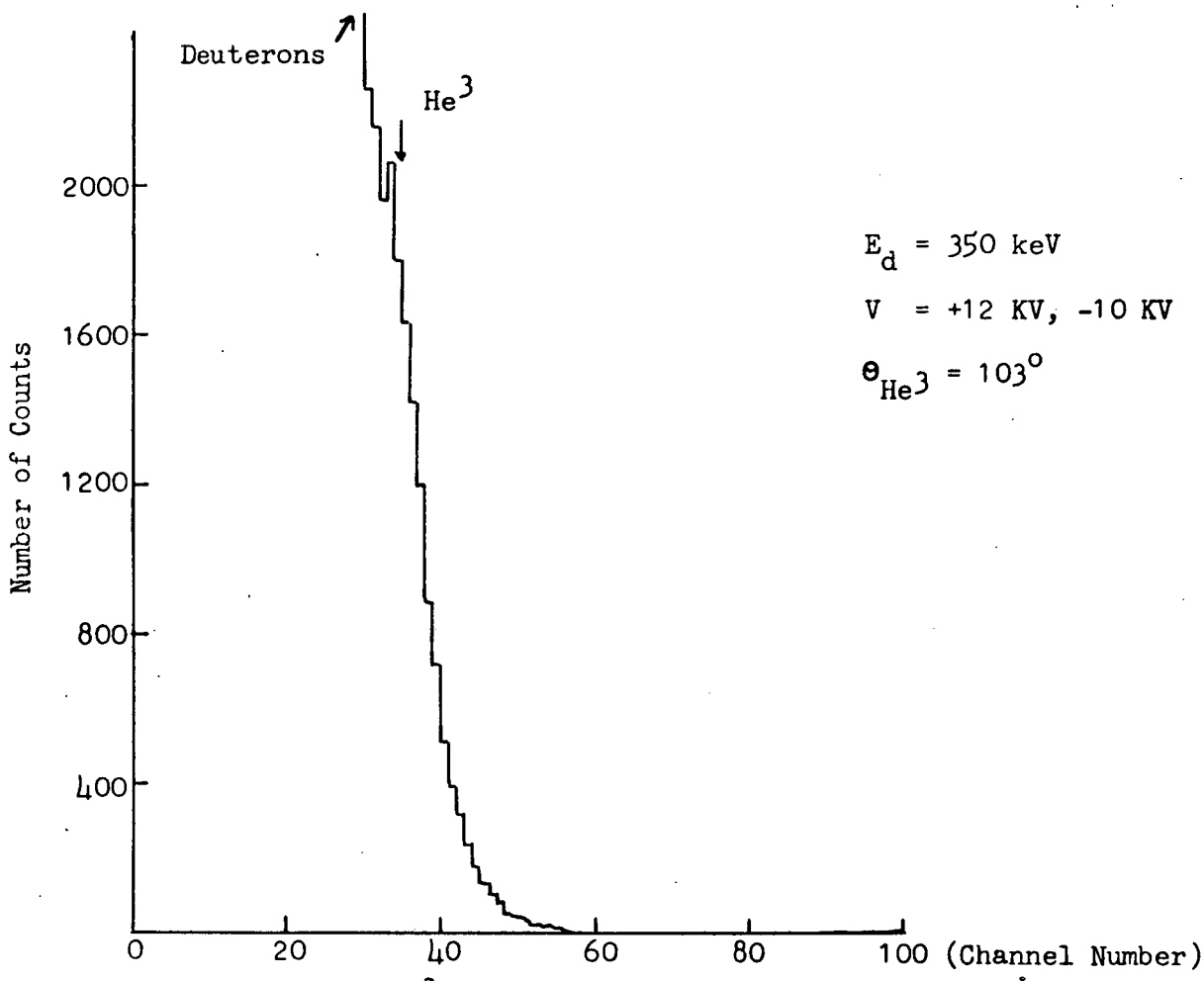

Fig. (28a) Direct He^3 linear spectrum

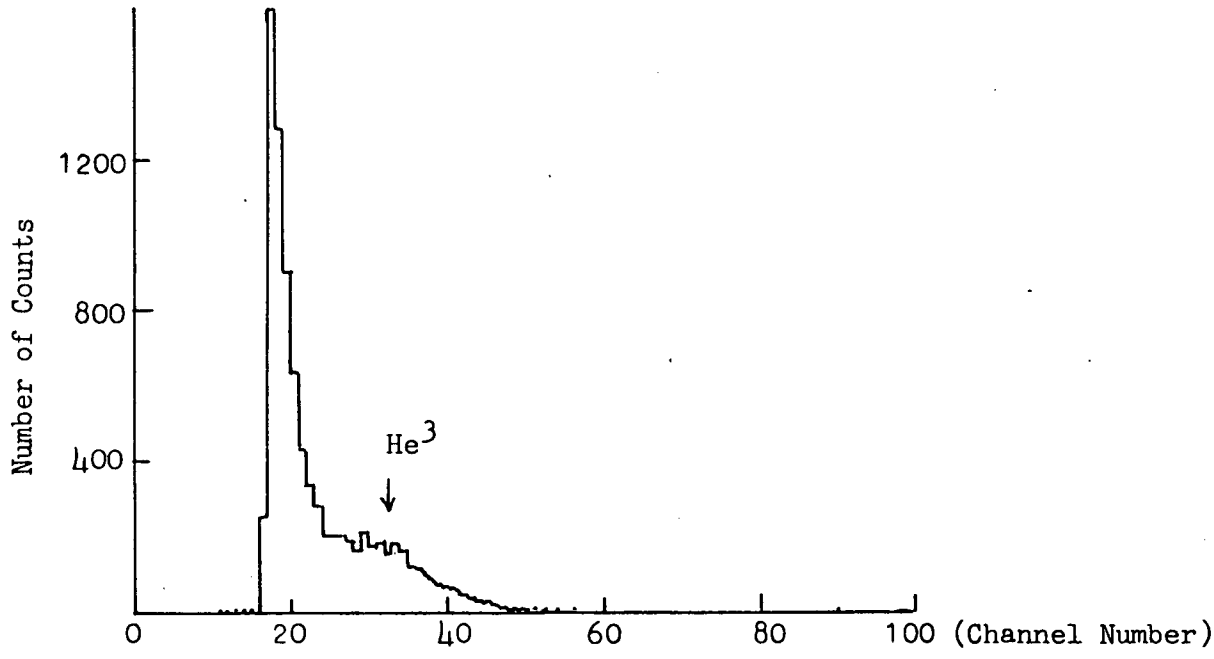

Fig. (28b) He^3 linear spectrum in coincidence with associated neutrons

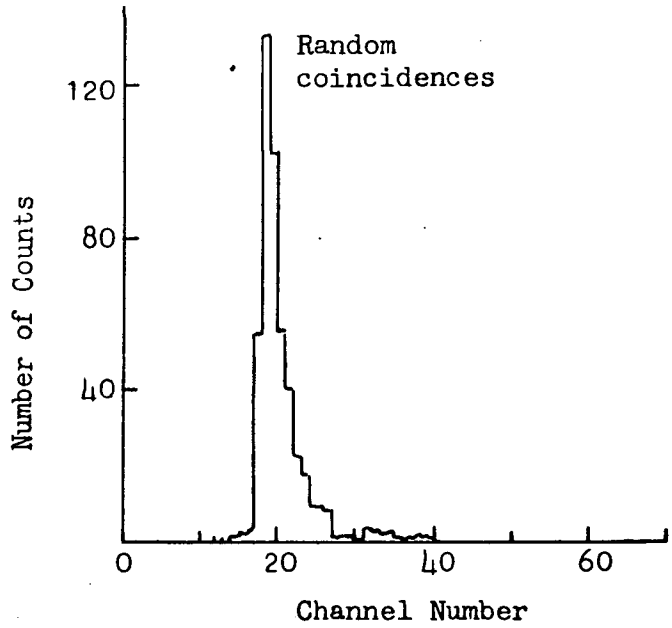

N - detector out of the associated neutron cone

Fig. (28c) He^3 linear spectrum in coincidence with neutrons

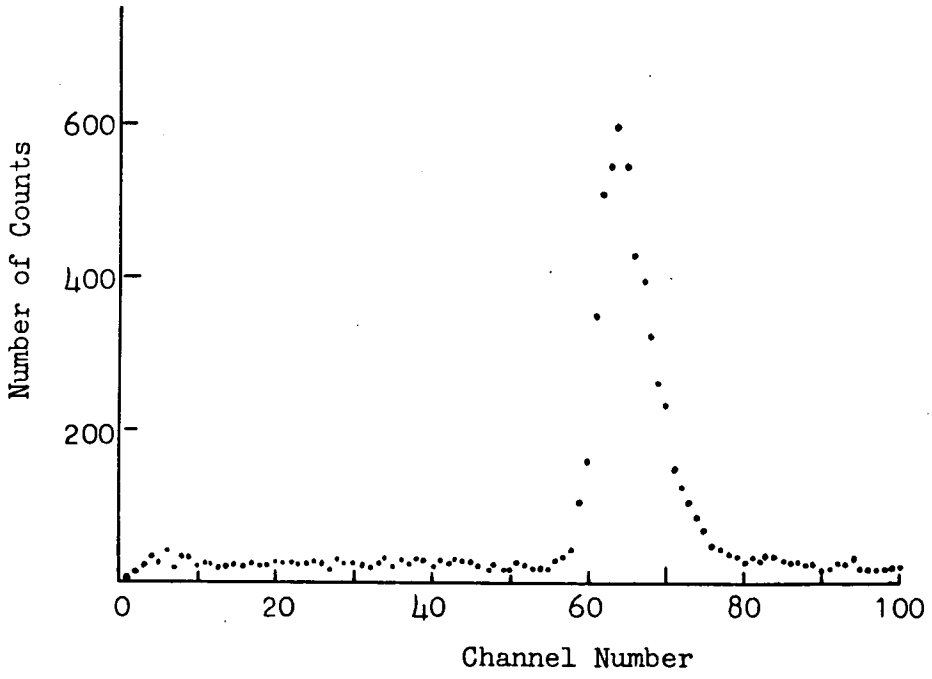

Fig. (28d) Associated Particle T.O.F. spectrum at E_d = 350 keV and target current of 12μA

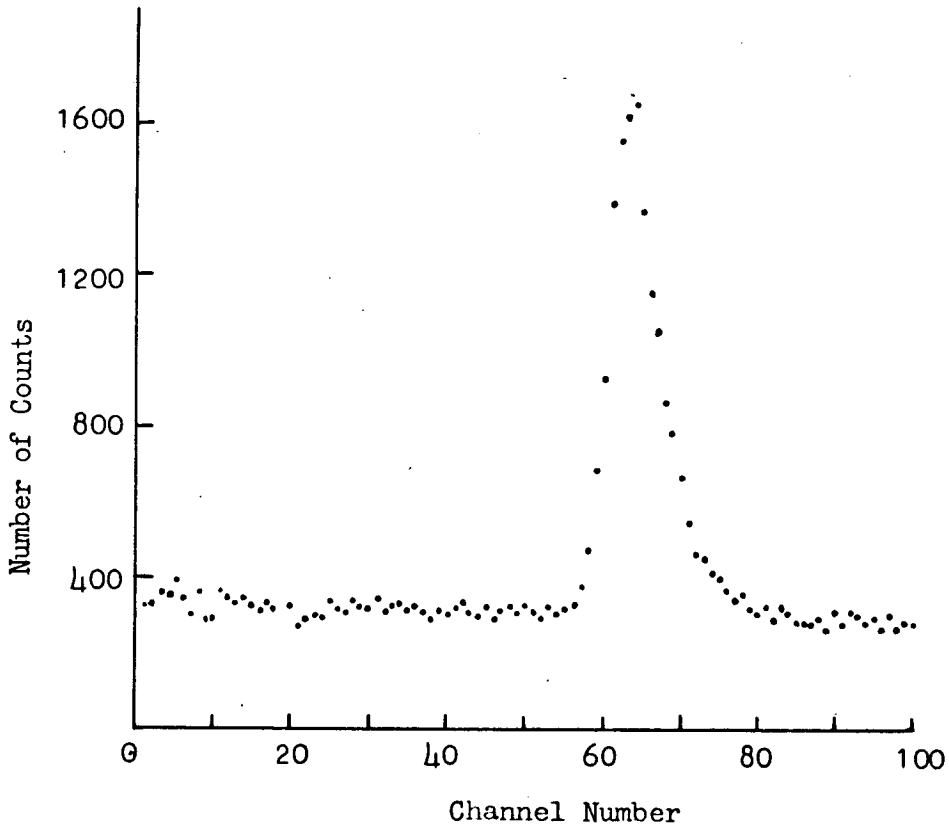

Fig. (28e) Associated Particle T.O.F. spectrum at E_d = 350 keV and target current of 45 μA

θ_{He^3} = 103° V = +12KV, -10KV θ_n = 49°

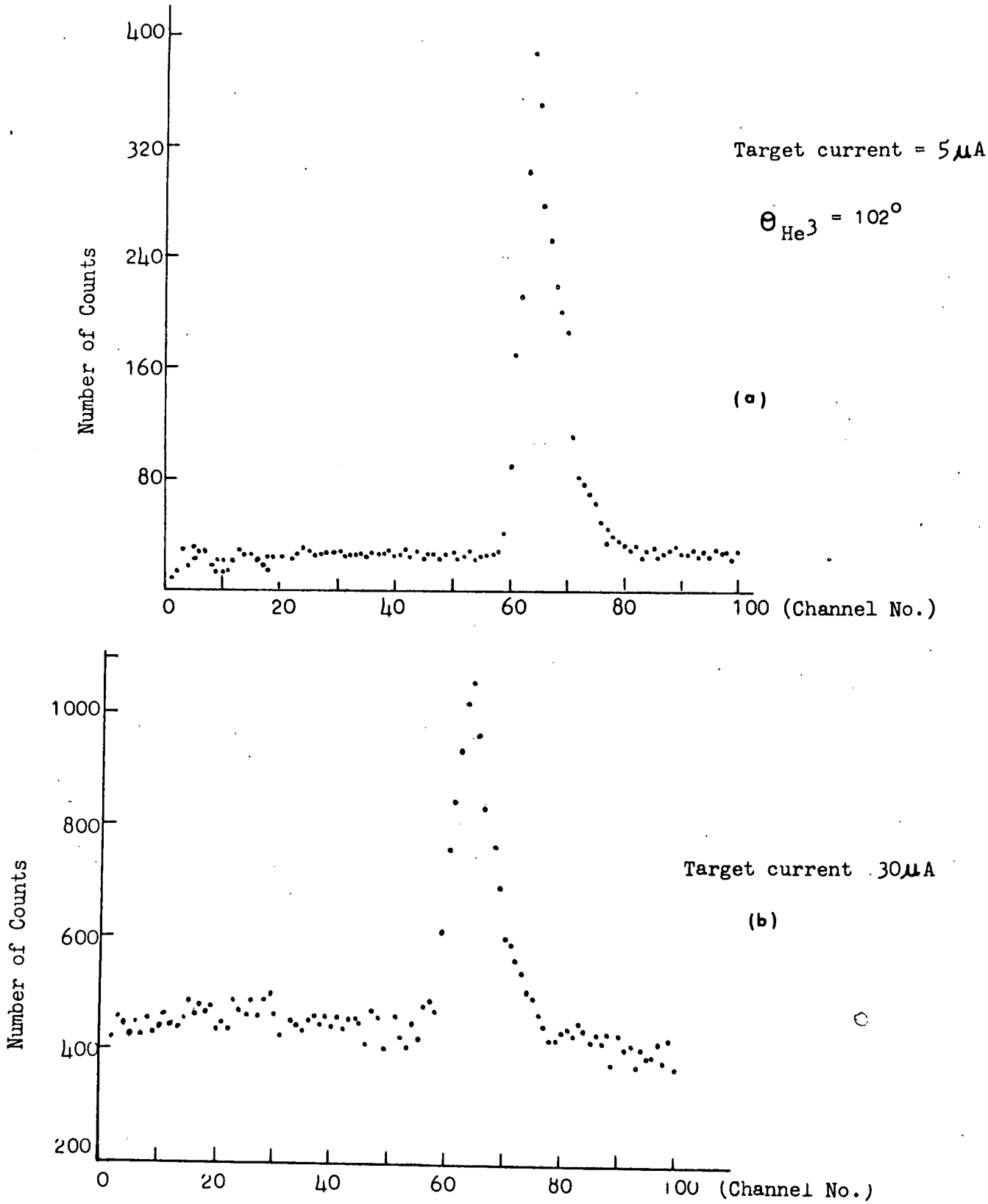

Fig. (29) Associated Particle T.O.F. Spectra at 400 keV incident deuterons

impossible. Figs. (29a) and (29b) however show the time-of-flight spectra at 5μA and 30μA deuteron currents respectively. The background level under the time-of-flight peak in Fig. (29b) has increased further at this energy and the background to peak ratio is 1:3.3 .

In all the above tests the neutron detector was placed in front of the target without any collimator or shield around it. The He^3 particle detector angle was changed as required at the various deuteron energies for the fixed associated neutron cone angle around 49^o.

2.10 Factors Effecting the Time Resolution

The various predominant factors which contribute to the overall time uncertainty in the associated particle time-of-flight system is represented by[59],

$$\Delta T^2 = \Delta T_d^2 + \Delta T_n^2 + \Delta T^2_{He3} + \Delta T^2_{inst} \qquad ..(2.10.1)$$

where ΔT_d is the transit time of a 2.8 MeV neutron across the neutron detecting medium, the scintillator, ΔT_n is the time spread due to finite neutron energy spread and can be written as

$$\Delta T_n = 72.3d \left(\frac{1}{\sqrt{E_{n_1}}} - \frac{1}{\sqrt{E_{n_2}}} \right) \qquad ..(2.10.2)$$

where d = the flight path of neutrons in meters. $E_{n_1} - E_{n_2} = \Delta E_n$, the energy spread of neutrons in MeV, T_n is the time in nano-seconds.

ΔT_{He3} is the variation in flight times of He^3 particles of varying energy, which cause the most severe limitation on the time resolution for the $D(d, n)He^3$ reaction. ΔT_{inst} accounts for the remaining instrumental time dispersion.

The time resolution in an associated particle time-of-flight system using

an electrostatic analyser is usually large, mainly due to longer flight paths of He^3 particles and a considerable energy variation of these particles. For Puts et al[50] experiment the time resolution was 27 nanoseconds FWHM largely as a result of the time uncertainty in the arrival of He^3 particles.

2.11 Selection of the Reacting Deuteron Energy for Scattering Experiment

The factor which was considered in choosing the reacting deuteron energy for the scattering experiments was that the neutron beam intensity should be sufficiently large without introducing any serious difficulties in separating elastically scattered deuterons and He^3 particles. The neutron intensity, i.e. the reaction cross-section increases with the increase of reacting deuteron energy. The previous spectra show that at or above 350 keV the separation of He^3 particles from the deuterons is rather difficult. Therefore an intermediate energy of 300 keV was chosen. The target thickness at this energy was 200 keV.

CHAPTER III

The Fast Neutron Polarimeter

3.1 Introduction

A system was designed and developed for the neutron polarization studies and the differential elastic scattering cross-section measurements, the name Fast Neutron Polarimeter is given to it. Fig. (30) shows the schematic drawing of the polarimeter. Briefly, the collimated neutrons from the target are scattered by a cylindrical shaped scattering sample and are detected by six detectors at a distance of 30 cm symmetrically placed to 'right' and 'left' of the scatterer at three different angles of scattering. The six detectors are held by rotating arms pivoted at the centre of a graduated circular table. The scattering sample is held by a holder mounted at the centre of the table, so that the detectors can be rotated around the scattering sample. The six detectors and the scattering table are mounted on a cradle, a two wheeled arrangement, which may be rotated accurately through angles up to 360° about an axis joining the neutron producing target to the centre of the scattering sample. The present chapter describes the construction of the polarimeter in some detail with the associated electronics.

3.2 The Fast Neutron Polarimeter

The factors considered in the design of the polarimeter were the following:

(1) Detectors and Scatterer arrangement.

(2) Requirement for the rotation of the detectors and scatterer arrangement for azimuthal angle 0° to 360°.

(3) Shielding and collimation arrangement for avoiding the

neutron backgrounds in the detectors.

(4) Introduction of a collimated beam monitor for normalisation and cross-section measurements.

(5) The facility of rotating the detectors around the scattering sample at any desired scattering angle.

Fig. (30) shows the schematic drawing of the polarimeter. The details of the polarimeter are also given in the same figure. Reference can also be made to Fig. (31). The scattering table having the scattering sample and the six detectors is fixed on a wheel having 62 cm and 86 cm as the internal and outer diameter, the thickness being 2 cm. This wheel is fixed by means of three steel rods of 3.0 cm in diameter and 57.5 cm long to another exactly similar wheel. These two wheels rest on four rotating bearings mounted on four stands. Thus the wheels are free to rotate about an axis joining their centres. The four stands having the four rotating bearings are fixed rigidly on a thick square steel plate having four jacking screws with four ball races under them for its up and down adjustment. The sideways adjustment of the plate is achieved by another four screwed rods fixed on a frame structure. Therefore the accurate alignment of the rotating wheels, thus the polarimeter, can be easily achieved. The plate can also be fixed rigidly in its position by these four screwed rods with two additional screwed rods fixed to the frame structure at the rear end. A collimator was placed in front of the target for neutron collimation and shielding purposes. Thus the polarimeter and the collimator rest on the frame structure with four wheels and four jacking screws to manoeuvre it into position.

The polarimeter is rotated by means of a motor fixed at the rear end having a pulley attached to its shaft. Switching the motor on and off is

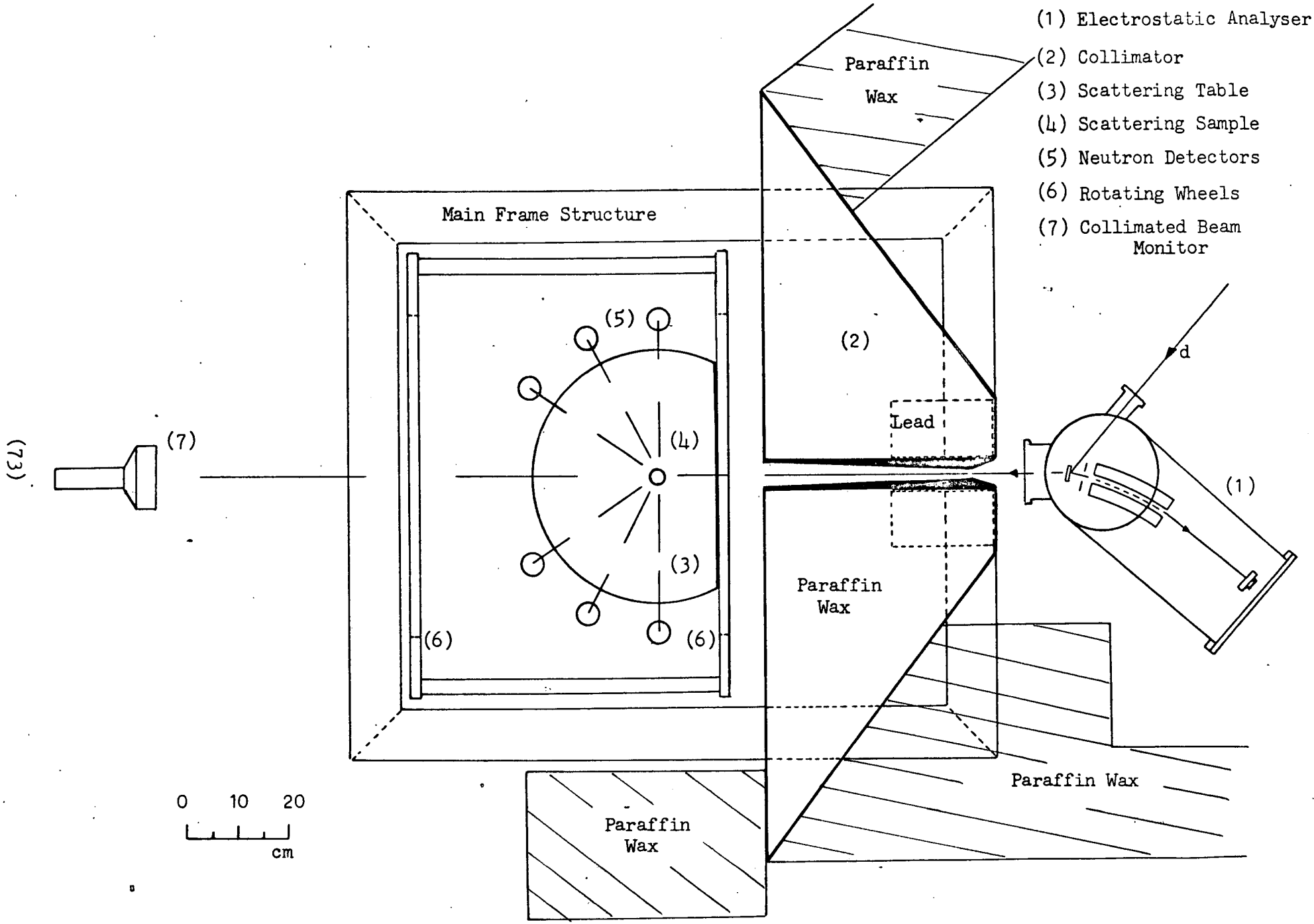

Fig. (30) The Polarimeter with the Associated Particle Time-of-Flight System

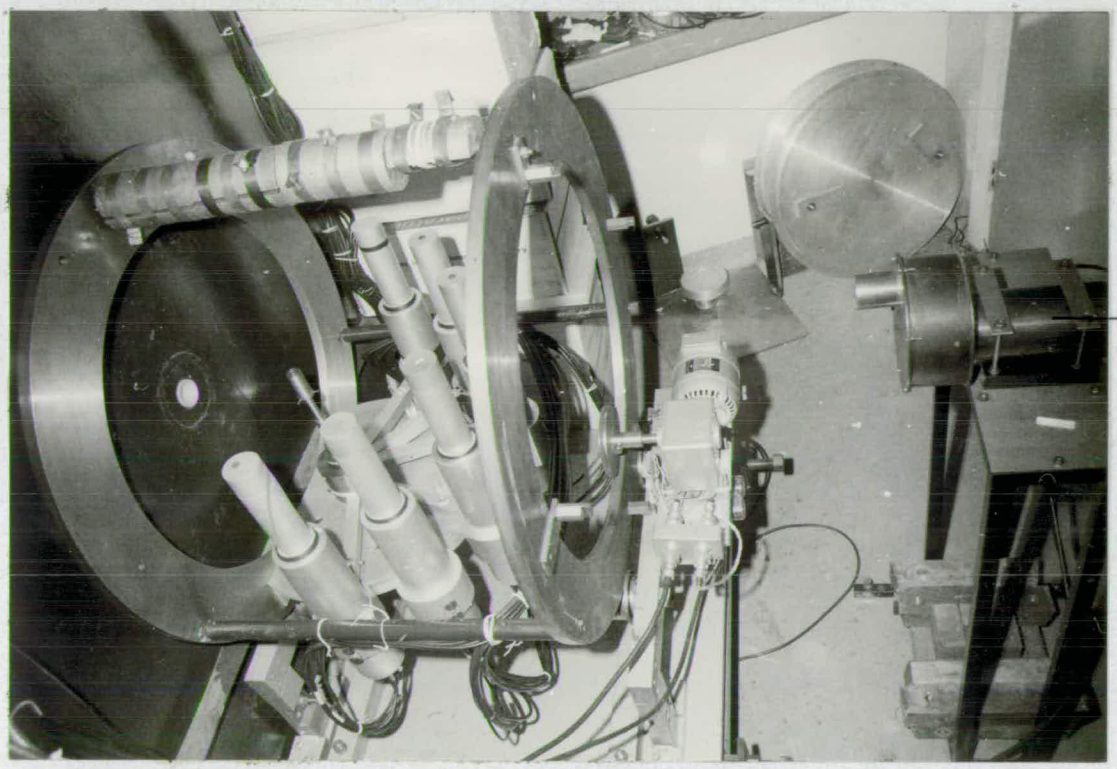

Fig. (31) Photograph of the Fast Neutron Polarimeter

by means of two relays so that the rotation of the polarimeter can be controlled by an automatic arrangement[84]. For polarization studies the polarimeter is required to be stopped at any desired position $\phi = 0, \pi/2, \pi$ and $3\pi/2$, this end being achieved by means of four microswitches arranged in order and operated by four small projecting hexagon rods fixed to the rear wheel. When the polarimeter rotates to $\phi = 3\pi/2$, to avoid twisting of cables connected to the detectors the direction of rotation is automatically reversed. The automatic system is controlled by the data in and stop switches of the pulse height analyser so that at the end of the accumulation of the data the polarimeter starts to rotate to the next desired position.

For normalisation and elastic differential scattering cross-section measurements a neutron detector, hereafter called the collimated beam monitor, was placed truly on the axis of the polarimeter. Checking of the axial alignment of the polarimeter was performed with the collimated beam monitor removed. The target was viewed through a telescope placed at the rear of the polarimeter through a series of cylindrical and disc alignment inserts with 2 mm diameter axial holes. The cylindrical inserts were fitted accurately into each end of the collimator tube and the two disc alignment inserts were fitted accurately into the holes of the two wheels. Alignment accuracy of these holes to within about 0.25 mm was achieved. The scattering sample and the neutron detectors were placed in the polarimeter with their axes normal to the scattering plane. The height of the scattering sample holder was adjusted with the aid of the telescope so that half the height of the scattering sample was on the axis of the polarimeter. The liquid scintillators were also marked by a line at half their height and the neutron detectors were adjusted so that these marked lines lie at the same height as the axis of

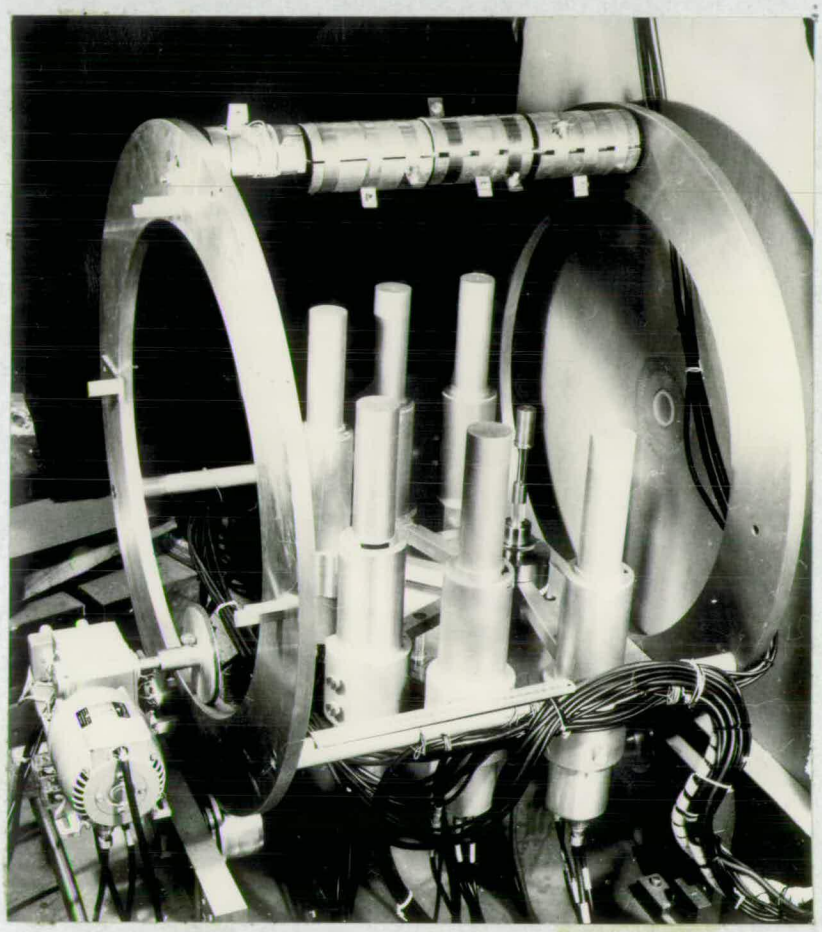

Fig. (32) Photograph (The Fast Neutron Polarimeter)

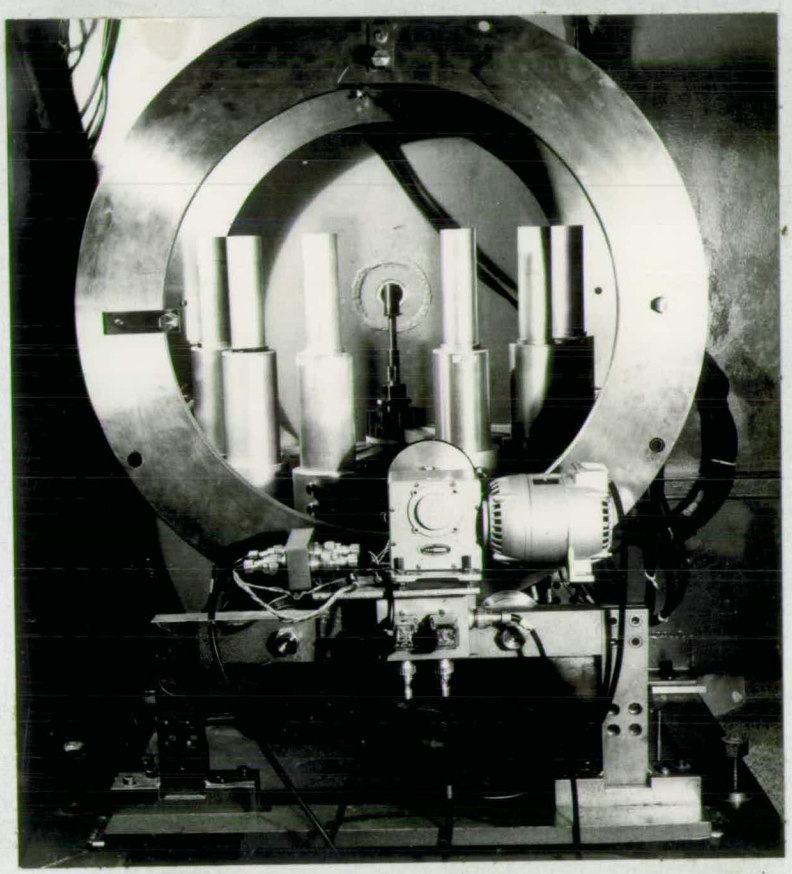

Fig. (33) Photograph of the Fast Neutron Polarimeter

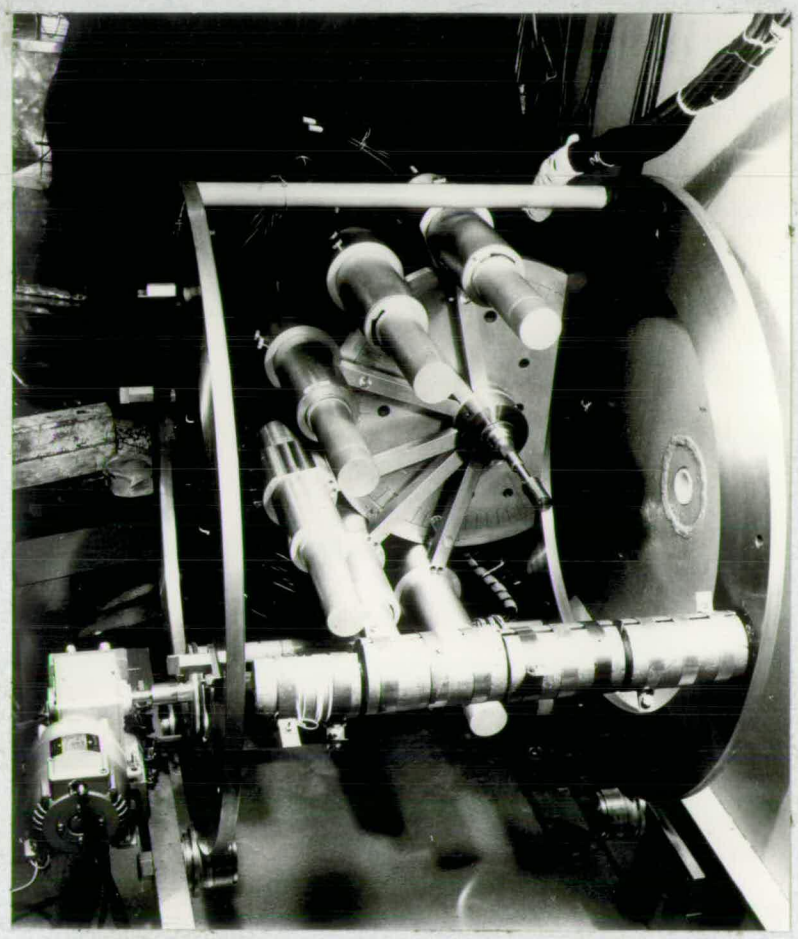

Fig. (34) Photograph (The Polarimeter rotated to Pos. 4)

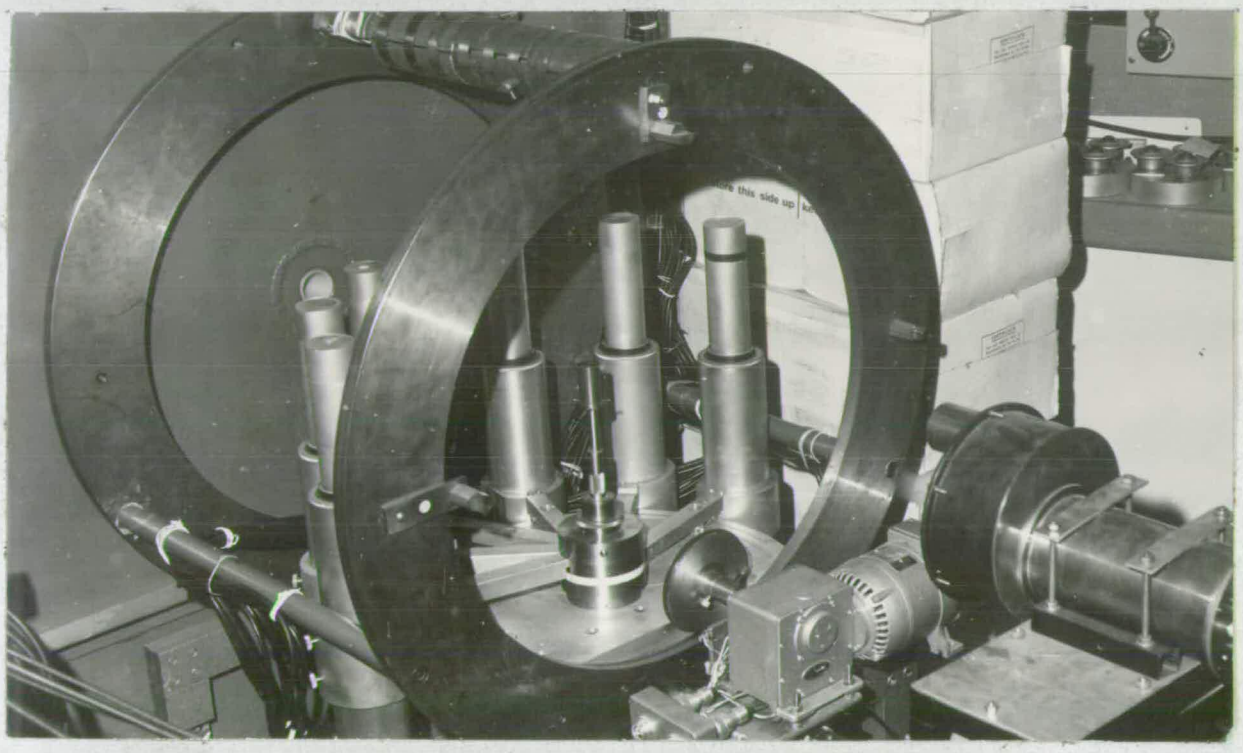

Fig. (35) The Fast Neutron Polarimeter for backward scattering angles

the polarimeter.

Figs. (31), (32), (33) and (34) show different views of the polarimeter. In Fig. (31) the collimated beam monitor is also shown. Fig. (34) shows the polarimeter rotated through $\phi = 3\pi/2$. It is worthwhile to mention some detail about the mounting of the neutron detectors. As is clear from Fig. (34) the six detectors are mounted on the table through six arms fixed to two rotatable stainless steel rings at the centre of the table, the other ends being supported on the table by ball bearings. Perspex viewers with lines marked are provided on the arms for setting the detectors accurately at desired angles. The extreme two detectors at 'left' or 'right' are fixed at 56° apart and a third detector is fixed in the middle making an angle of 28° with either side detector. In this way the three detectors are moved together keeping the angles between the detectors the same. The maximum scattering angle that can be set in the present arrangement is 90°. For scattering angles greater than 90° the polarimeter can be lifted up and rotated through 180° so that the scattering table is moved away from the collimator thereby setting the detectors at backward scattering angles. Fig. (35) shows the polarimeter rotated for scattering angles greater than 90°. The detectors can be clamped to the table by means of screws underneath the table.

3.3 The Neutron Detectors

To reduce the measuring time six neutron detectors were used. The detectors were NE 213 liquid scintillators of cylindrical shape with a length of 15.24 cm and a diameter of 5.08cm. Their axes were placed perpendicular to the scattering plane. Two kinds of photomultipliers were used, 56 AVP and EMI 9814B. The dynode chain for 56 AVP is given in Fig. (18).

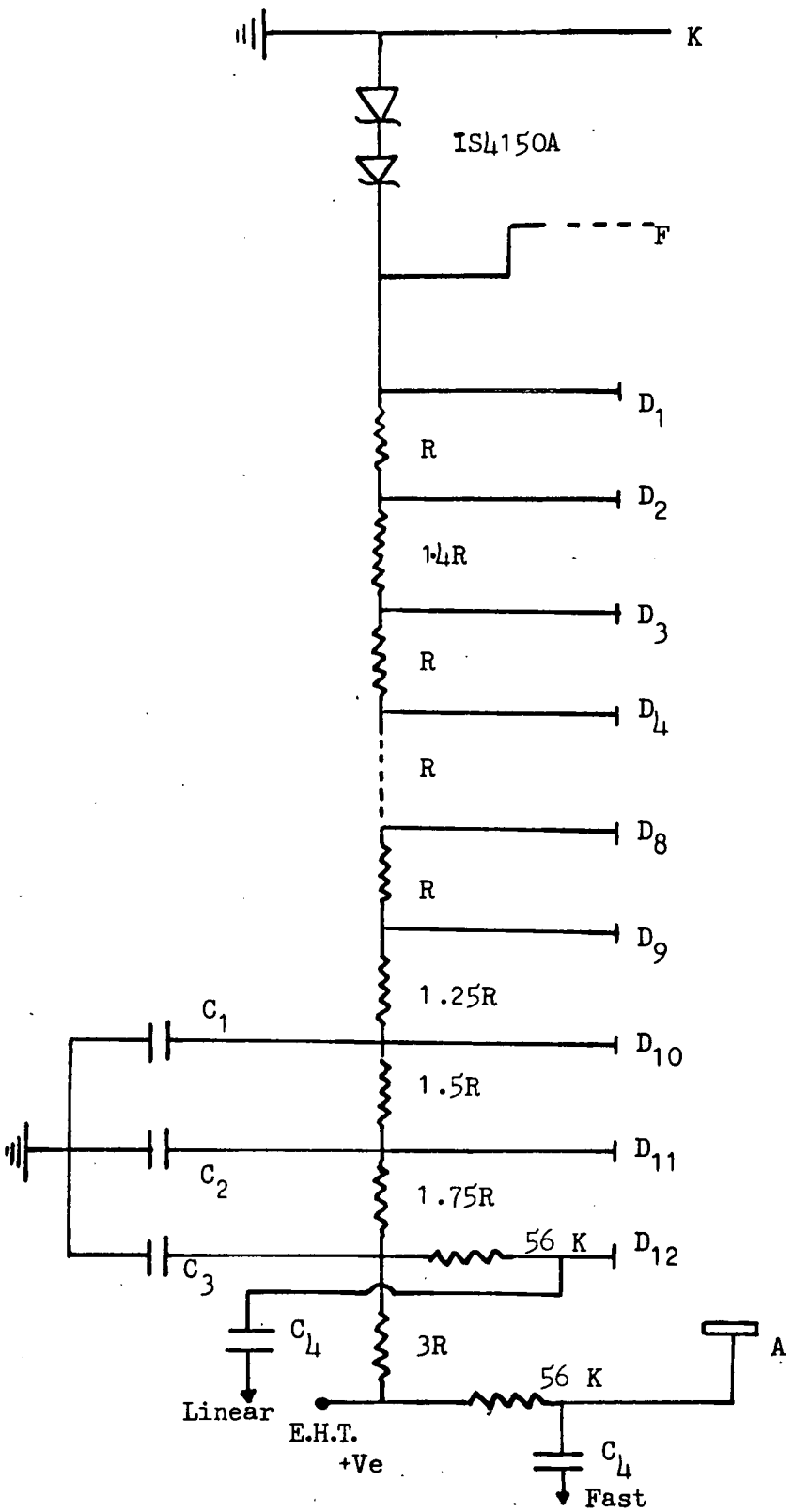

R = 150 K ohms

C_1 = 2200 PF

C_2 = 4700 PF

C_3 = 10000 PF

C_4 = 10000 PF

Fig. (36) Base Circuit for E.M.I. 9814B

The dynode chain for EMI 9814B, given in Fig. (36), is according to EMI directives. The linear signals from the last dynode were taken through a pre-amplifier kept inside the light tight aluminium cylindrical shaped photomultiplier container. The bias of all the detectors was set at about 1.9 MeV neutron energy. The fast signals for timing purposes were taken from the anode of the photomultiplier. The 56 AVP photomultipliers were wrapped in mu-metal cylinders to avoid the influence of stray magnetic field and so avoid gain shift when the polarimeter was rotated. However no mu-metal cylinders were found necessary around the EMI photomultipliers and no gain shift on rotation of the polarimeter showed up.

The relative percentage detection efficiencies for neutrons entering a scintillator at different distances from the photomultiplier were determined by irradiating small slices of the scintillator from the top to the bottom parallel to the window of the photomultiplier using collimated neutrons from an Am-Be neutron source. The relative detection efficiencies in different regions of the scintillator were found to be constant for both the scintillators tested. The pulse shape discrimination against gamma-rays in all the detectors was by the zero-cross over timing technique and pulse shape discimination units were constructed for this purpose. The technique is described in section 2.7 of the previous chapter.

3.4 Target Yield Monitor

For normalisation and to estimate the flux of neutrons produced in the $D(d, n)He^3$ reaction a target yield monitor was constructed. The detector was a scintillator of type Li I(E U), enriched to 96% in Li^6 having a 2 mm active layer. The scintillator was surrounded by 4" of paraffin wax to thermalise

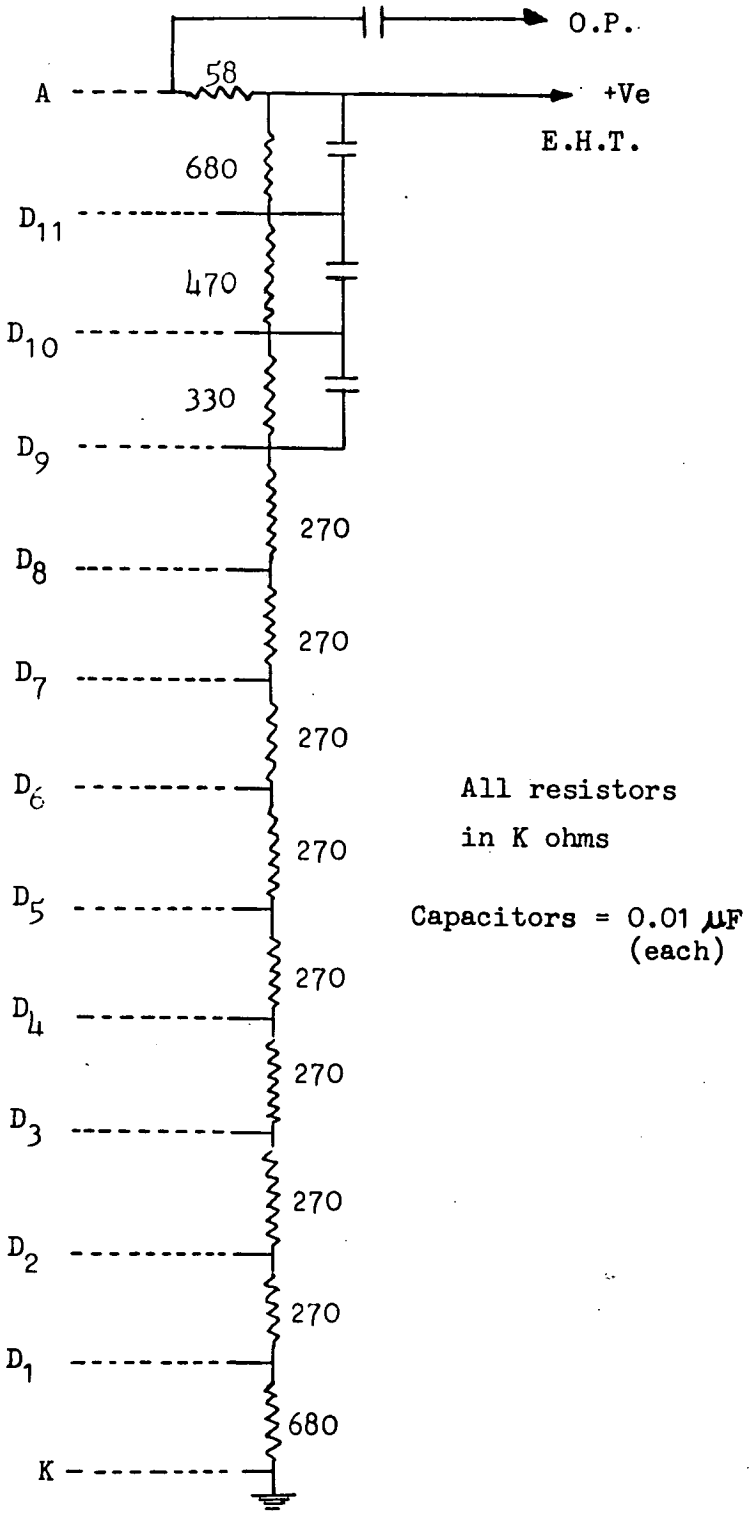

Fig. (37b) Dynode Chain of 6260 (EMI)

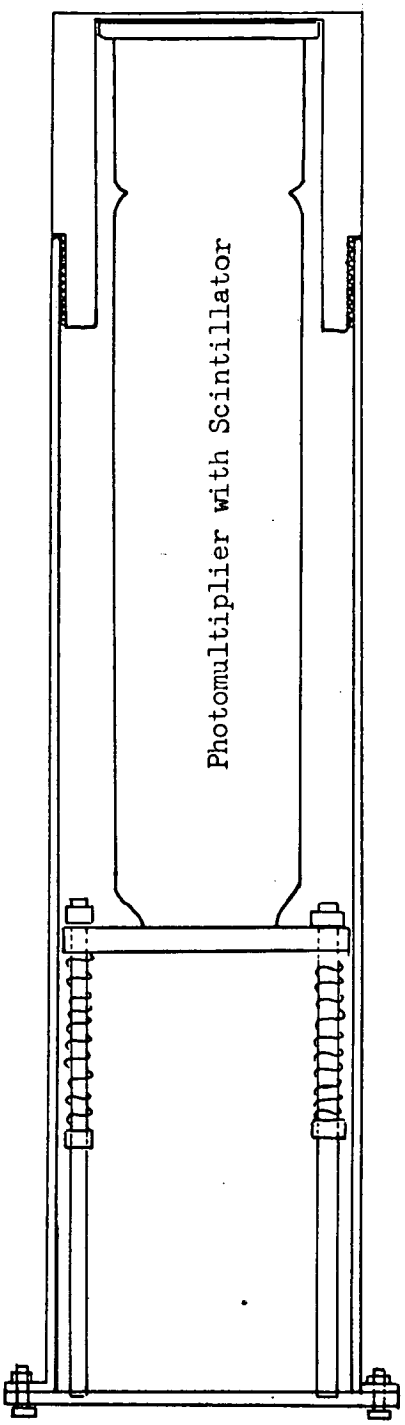

Fig. (37a) Light tight container

the fast neutrons. The photomultiplier used with this scintillator was EMI 6260. The details of the construction of the light tight container for the photomultiplier and the scintillator and the circuit diagram of the carbon resistor dynode chain are given in Figs. (37a) and (37b) respectively. The neutrons are detected by the $Li^6(n,\alpha)H^3$ reaction and the cross-section of this reaction for thermal neutrons is very large. Discrimination against gamma-ray background is obtained by pulse height discrimination. The gamma-ray pulses are usually very small in amplitude as compared to the pulses produced by the thermal neutrons.

3.5 The Collimated Beam Monitor

The collimated beam monitor (CBM) was constructed as a part of the polarimeter. The CBM detector is again NE 213 bubble feee liquid scintillator of 12.7 cm in diameter and 3.8 cm in thickness contained in a glass cell. The nitrogen expansion bubble is kept in a small glass bulb above the sensitive volume. The light guide, (perspex) cut from a section of circular cone, having diameters of 10.2 cm and 4.0 cm at the faces with a height of 2.5 cm was used to couple the scintillator to an EMI 9814B photomultiplier. The dynode chain circuit constructed was the same as shown previously. Pulse shape discrimination against gamma-rays was again by the zero-cross over timing technique.

The collimated beam monitor was placed accurately with its axis on the axis of the polarimeter. The distance of the CBM from the target was chosen so that the neutron full cone irradiated completely all the area of the scintillator, as calculated from the collimated beam geometry.

Fig. (38) shows the electronic system used with the collimated beam monitor. The timing pulses taken from the anode of the photomultiplier after

Key: Same as in Fig. (23)

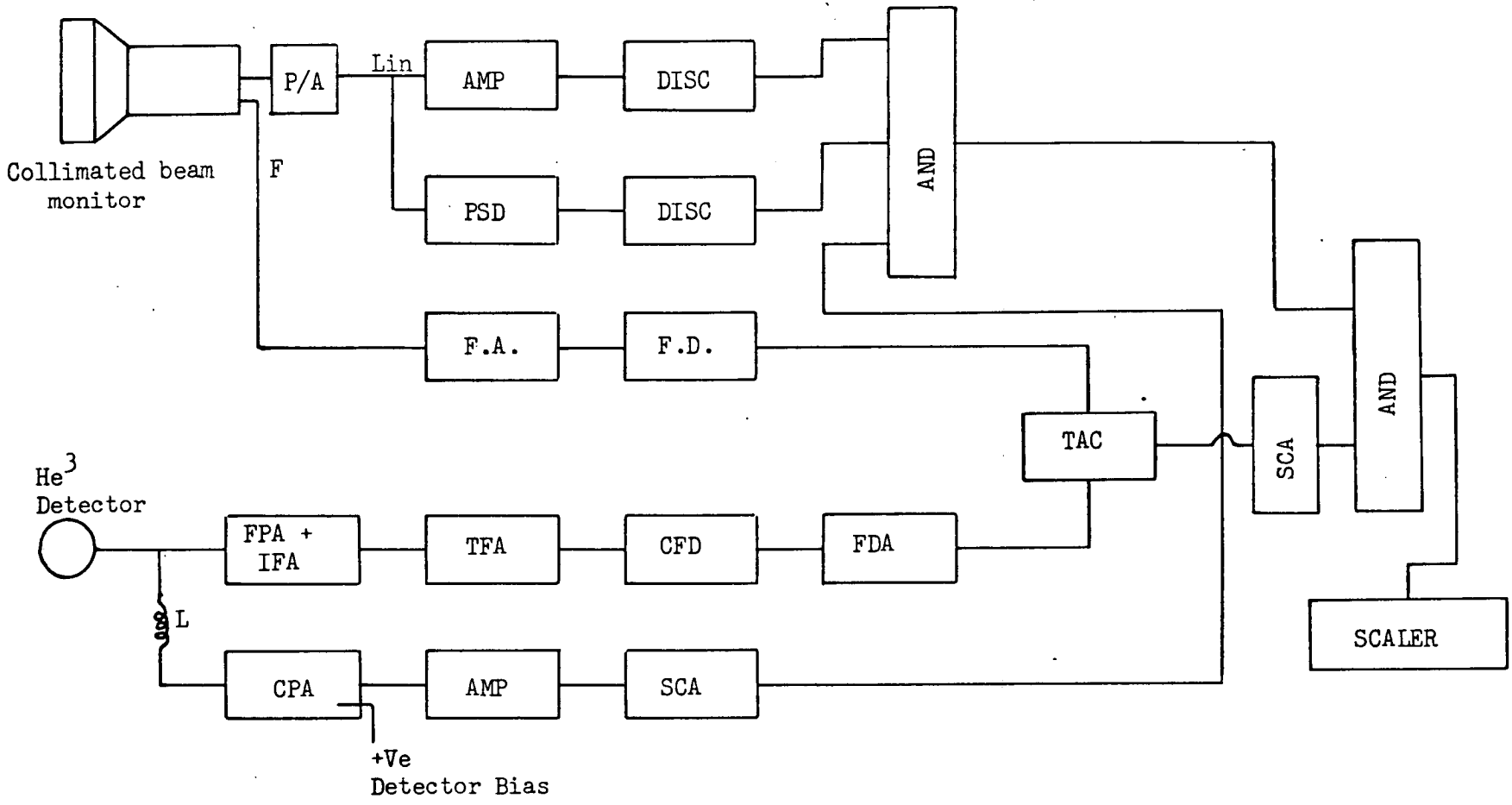

Fig. (38) A block diagram showing the arrangement of the electronics used with the A.P.M. for the collimated beam monitor

amplification in the fast amplifier, NE 4634, triggered a leading edge fast discriminator, NE 4635, which in turn provided start signals for a time to amplitude converter (TAC), Ortec model 447. As explained earlier in Section 2.8, the stop signals are taken from the surface barrier detector being delayed in a fast delay amplifier, Ortec model 427A. To eliminate background and so to determine the number of events under the associated particle time-of-flight peak, the output pulses from TAC were fed to a single channel analyser. A timing single channel analyser was constructed based on the circuit by Gottlieb[85] for this purpose. The circuit is given in the appendix. The lower and upper bias levels of the single channel analyser (SCA) were set so as to select only the time-of-flight peak. As explained earlier in Section 2.8 a coincidence was required between neutrons and He^3 particles in the slow channel. The output pulses from SCA were fed to a triple coincidence unit AND, the second input being connected to the neutron-He^3 coincidence pulses from the slow channel. The various delays are not shown in the figure, but the pulses were delayed properly to meet the coincidence requirements. The resultant coincidence pulses were fed to a scaler. A scaler[86] with six digits having nixie tubes as the display was constructed for this purpose, the circuit is given in the appendix.

3.6 Electronics of the System

The system of electronics used for the polarization and differential elastic scattering cross-section measurements is shown schematically in Fig. (39). The amplifier, a PSD unit, two discriminators and an AND (1μs resolving time) on the linear output of each detector provide the pulse shape discrimination against gamma-rays and linear bias levels. As explained earlier in Section 2.8 the slow signals of He^3 particles were taken from the

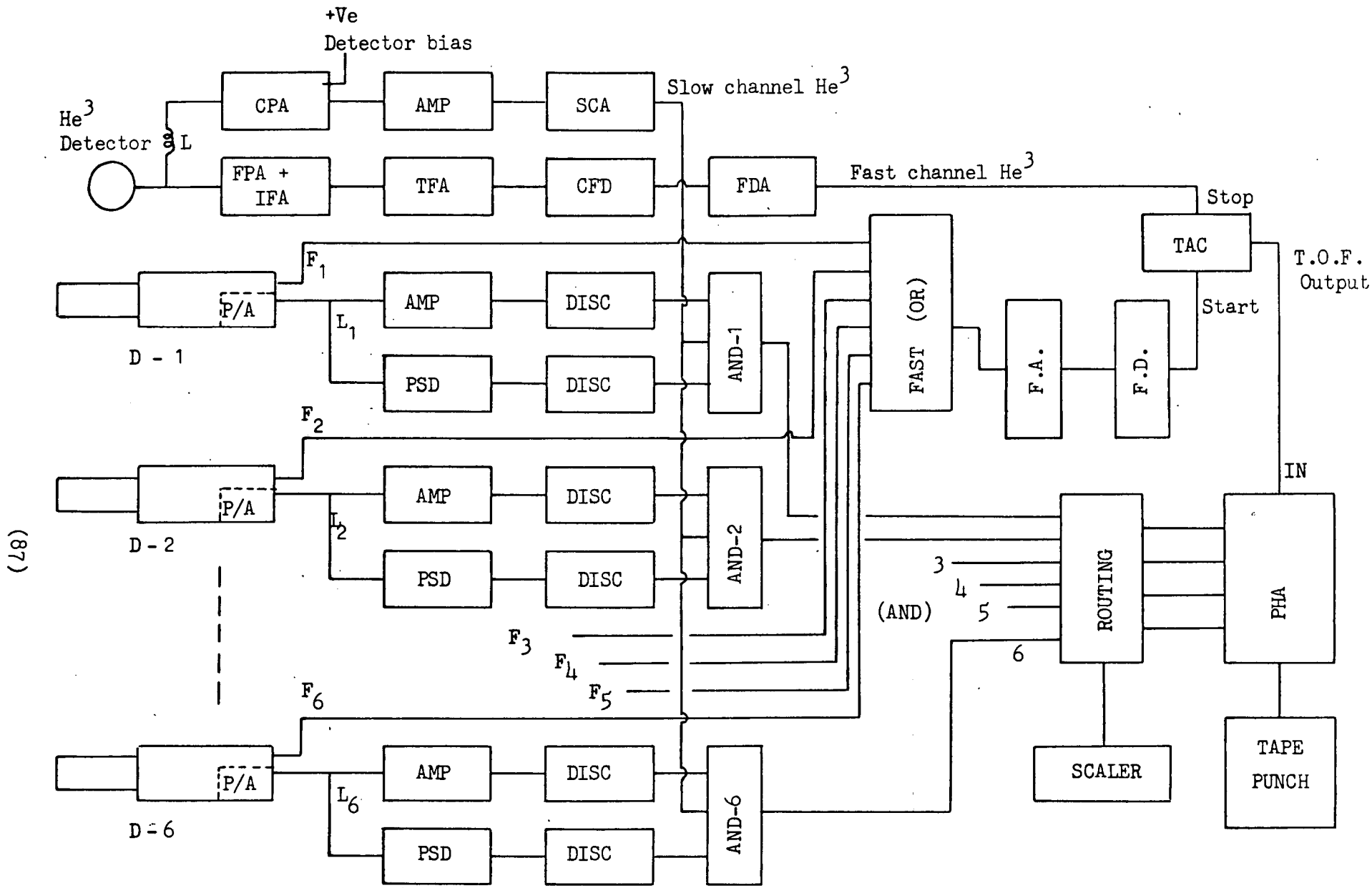

(87)

Key: Same as in Fig. (23)

Fig. (39) A block diagram showing the arrangement of the electronics used with A.P.M. for the Polarimeter

output of SCA, Ortec model 406A, and the output from the fast delay amplifier, Ortec model 427A, provides the fast channel of He^3 particles.

On the fast channel of neutrons, the anode pulses from all the six neutron detectors were fed to a fast OR unit, Linear Fan In LRS model 127. The output pulses were taken to the fast NE 4634 amplifier and after amplification triggered a fast leading edge discriminator, NE 4635. The output pulses from the fast discriminator were used as the start pulses in a time to amplitude converter TAC, NE 4645, the stop pulses being provided from the fast channel of He^3 particles. Therefore the resulting output from the TAC had six time-of-flight spectra corresponding to the six neutron detectors and by a routing arrangement these were accumulated in selected sections of the memory of a multichannel pulse height analyser. A Laben 400 channel pulse height analyser was used with a paper tape punch facility, so that the data could be quickly transferred on to a paper tape.

3.7 Shielding Arrangement

The associated particle method produces a well collimated neutron beam, therefore extensive shielding is not required. However some shielding of the neutron detectors from the primary source was necessary to reduce the background count rate. High background in the neutron detectors will cause high accidental coincidence rates. The side detectors were shielded from the neutrons produced at the target by a collimator shown diagramatically in Fig. (30) and also in Fig. (31). The collimator was of a trapeze shape having end faces 30 cm square and 150 cm square near and away from the target respectively. The length of the collimator was 46 cm. The collimator contained a cylinder of lead as shown in Fig. (30) close to the target to

provide attenuation of neutron flux by inelastic scattering. The rest of the collimator was filled with paraffin wax to further degrade the incident neutron energies. The collimator tube for the neutron beam consists of a brass cylinder of about 5 cm in diameter into which inserts were placed to provide a throat and a taper. Around the throat brass inserts were used and polythene inserts in the remaining parts. The throat and taper geometry was chosen in such a way that the whole of the scattering material was illuminated in the collimated neutron beam and the tapered inserts just failed to be directly illuminated by the target. This was done to reduce contamination of the direct neutron beam with contributions scattered from the collimator walls. To reduce neutron background further the target itself was surrounded by concrete and paraffin wax blocks about 30 cm in thickness.

CHAPTER IV

CHAPTER IV

Scattering of 2.9 MeV Neutrons

4.1 Introduction

A collimated beam of 2.9 MeV neutrons was produced using the associated particle method with the $D(d, n)He^3$ reaction as described in Chapter II. The energy of the incident deuteron was 315 keV and the associated neutron cone was produced at 49° (Lab). The neutrons were scattered from cylindrical samples for measurements of differential elastic scattering cross-sections and angular distributions of polarization. The measurements were made on five scatterers, Fe, Cu, I, Hg and Pb chosen as examples of medium and heavy nuclei. The scatterers were 2.59 cm in diameter and 5.22 cm in height and were placed with their axes normal to the scattering plane. Polarization angular distributions and differential elastic scattering cross-sections were measured from 20°-160° at 14° intervals between 20°-90° and 28° intervals between 90°-160°. These measurements required many periods of 50 to 100 hours of continuous running which was spread over ten months. This chapter describes the experiment and the results along with the necessary corrections for finite geometry, flux attenuation and multiple scattering.

4.2 Scatterer and Detector Arrangement

The experimental arrangement is shown in Fig. (30) indicating the electrostatic analyser, mechanical collimator, scattering sample, six detectors and the collimated beam monitor. The scatterer was placed at 88 cm from the neutron source and 22 cm from the exit of the collimator. The scatterer was mounted in a small stainless steel cup having thin walls. The cup itself was fixed by a thin walled stainless steel tube to the main mounting on the

scattering table, thereby ensuring a minimum of background scattering material in the neutron beam. The scatterer can be easily removed from the cup and the mounting is shown in Fig. (32).

The polarimeter with its collimator was first set at about 49^{o} with respect to deuteron beam. The axial alignment of the polarimeter to the deuterium target was done as described in section 3.2, the He^{3} particle detector and the deflecting plates with the aperture being already aligned properly in height with respect to the target. Thus the He^{3} particle detector, target beam spot and the axis of the polarimeter as well as the collimator were all in the same plane. The electronic system of the polarimeter is described in section 3.6. The racks of the electronics including the pulse height analyser are illustrated in Fig. (40).

4.3 The Experimental Measurements

(a) Beam Profile

After careful alignment the neutron beam profile was measured, the scattering sample being removed from the neutron beam. One of the set of six neutron detectors was used for this purpose (NE 213, 15.24 cm in height and 5.08 cm in diameter) mounted on the scattering table with its longitudinal axis perpendicular to the incident neutrons, the usual arrangement of all the detectors on the polarimeter as shown in Fig. (32). Before measuring the beam profile the neutron detector was positioned at 0^{o} on the scattering table. The He^{3} particle detector was rotated around the target by means of the Wilson seal drive and was positioned to give the maximum number of counts under the time-of-flight peak. This process ensured that the He^{3} particle detector had been positioned at the exact angle of He^{3} particle emission in relation to the

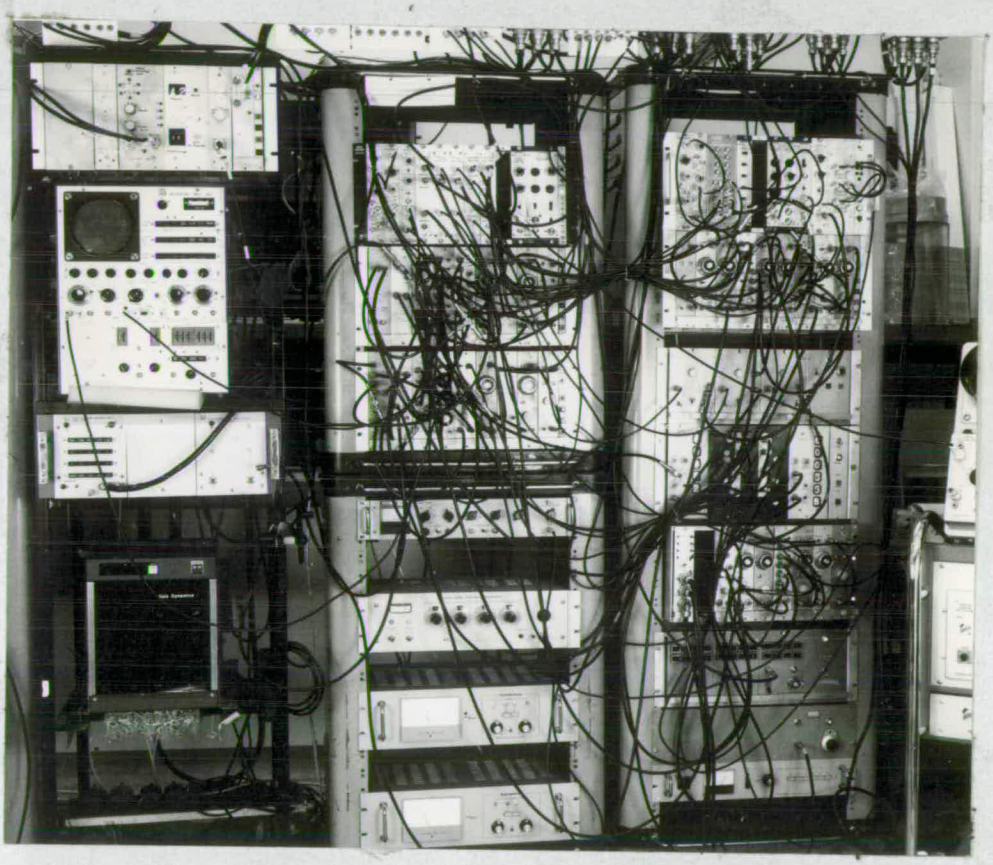

Fig. (40) Photograph showing the racks of electronics

associated neutron cone as detected by the neutron detector.

For beam profile measurements the neutron detector set initially at 0° was rotated to either side of 0° in 5° intervals and the number of counts under the time-of-flight peak was determined at each angle. In this measurement the polarimeter was set with the azimuthal angle $\phi = 0^{\circ}$. This scaning of the neutron beam determined the horizontal beam profile. For the vertical beam profile measurement the polarimeter was rotated through $\phi = \pi/2$ and again the neutron detector was moved to either side of 0° in 5° intervals. The beam profile so measured is shown in Fig. (41) and has FWHM 14.6° in good agreement with the value calculated from the geometry of the system. The calculated value is 14.8°.

(b) Flux Monitors and Detector Efficiencies

For determination of the differential elastic scattering cross-section the neutron flux incident on the scattering sample has to be known. However with the additional neutron detector (collimated beam monitor) in the collimated beam it is possible to determine the effective neutron flux provided the ratio of the detection efficiency of the collimated beam monitor to the detection efficiency of each scattered neutron detector is known, as will be discussed in section 4.4.

The experimental arrangement of the collimated beam monitor with its electronics was described in section 3.5. The collimated beam monitor was placed at a distance of 181 cm from the target so that the 12.7 cm diameter NE 213 liquid scintillator would adequately cover the collimated neutron cone and was sufficiently far away from the scatterer and other detectors to avoid contributing to the background.

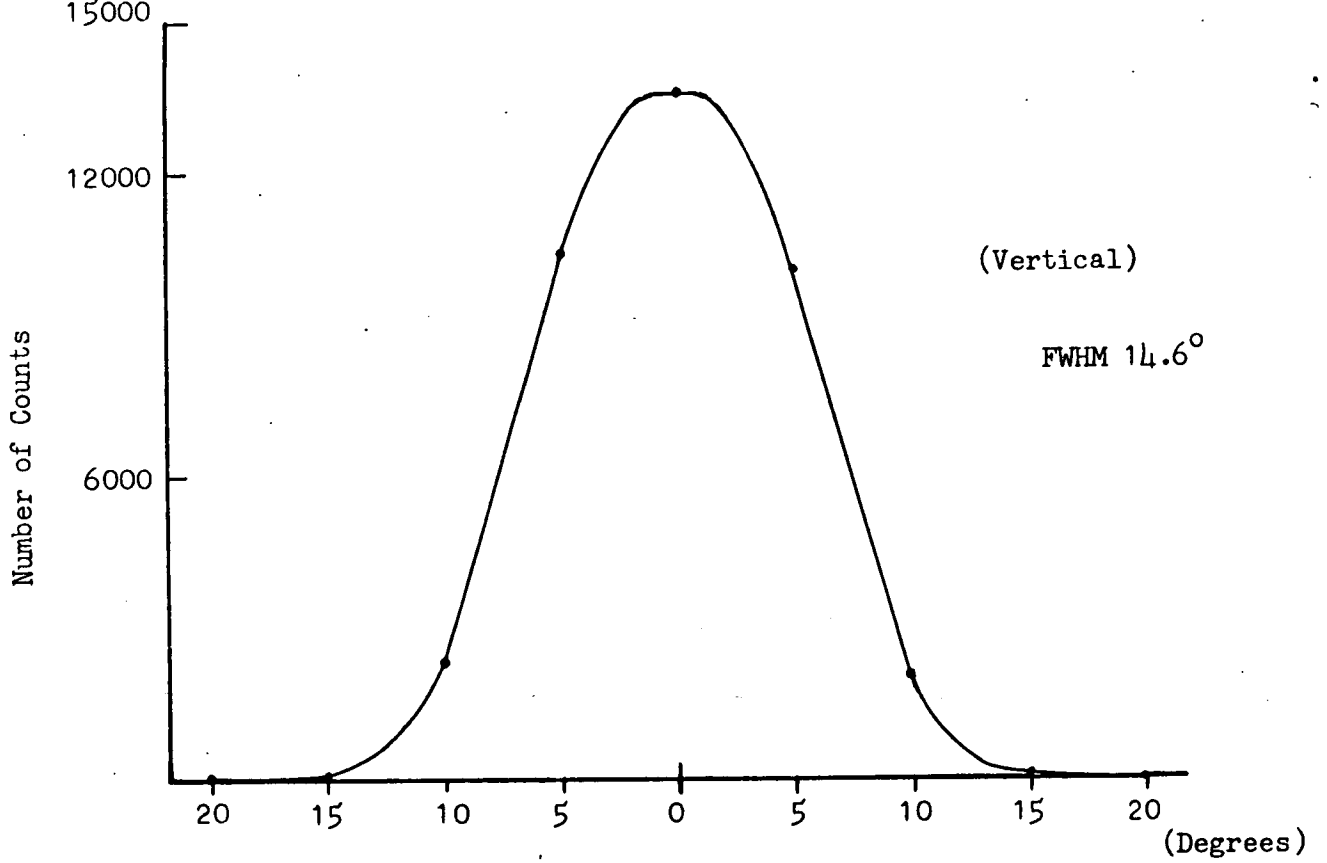

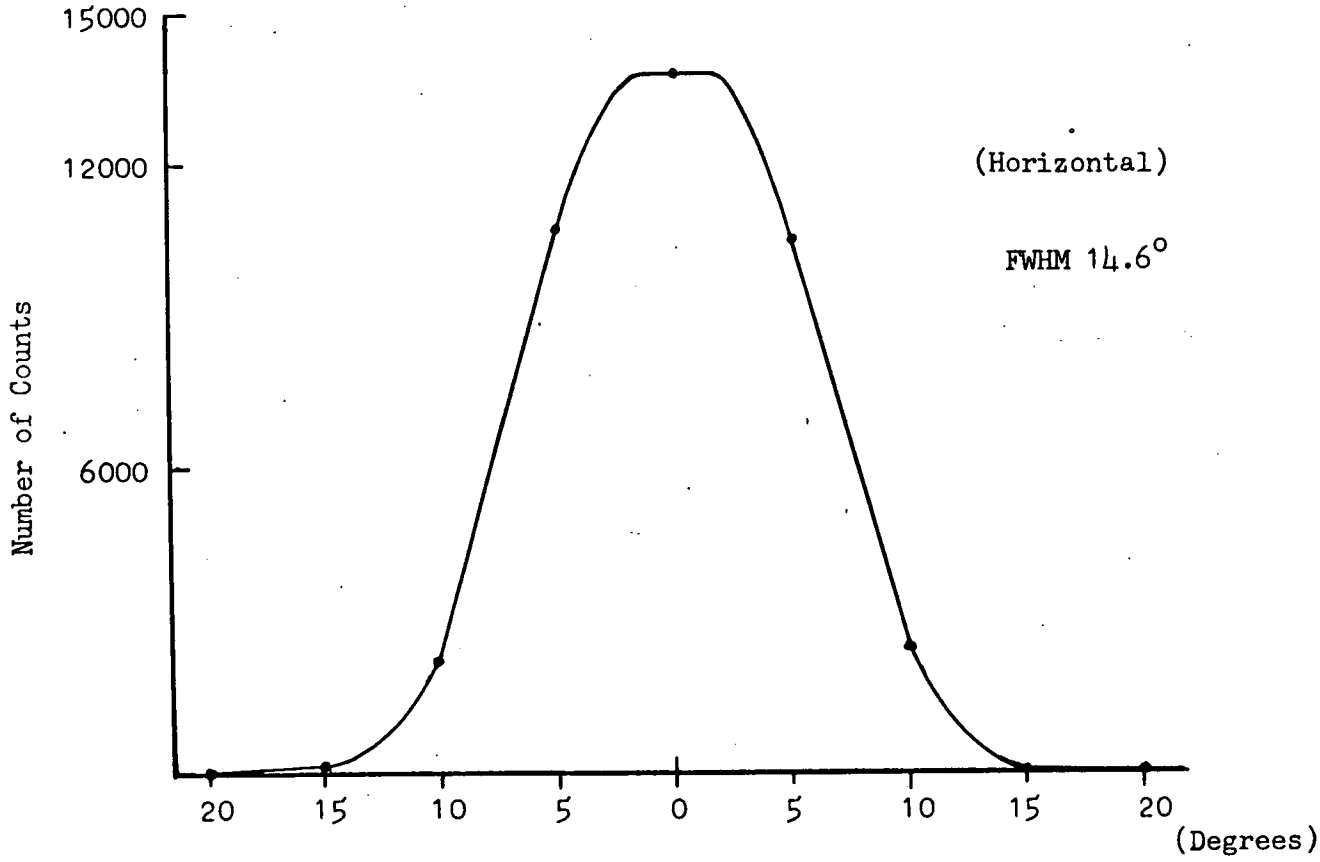

Fig. (41) Beam Profile (angles indicated by the scattering table)

4.4 Cross-section Calculation

The differential elastic scattering cross-section per unit solid angle is given by the formula[87],

$$\sigma(\theta) = \frac{Sr^2}{IN} \qquad ..(4.4.1)$$

where S is the scattered neutron flux at the detector at an angle of scattering θ from a scatterer having a number of nuclei N, I is the incident flux at the scatterer and r is the average distance between the scatterer and the neutron detector. The value of I can be determined using the collimated beam monitor as described below and separate runs for measuring S and I are not required.

If ϵ_d is the efficiency of the scattered neutron detector, ϵ_m that of the collimated beam monitor and N_o is the total number of neutrons/sec incident on the scatterer, n_d the number of scattered neutrons detected/sec and Ω_d the solid angle subtended by the scattered neutron detector at scattering angle θ, then

$$\sigma(\theta) = \frac{n_d A_s}{N_o \epsilon_d \Omega_d N} \qquad ..(4.4.2)$$

where A_s is the area of scatterer presented to neutron beam from target, i.e. $I = \frac{N_o}{A_s}$.

The neutron flux determined by the collimated beam monitor can be written as

$$F = \frac{n_m}{\epsilon_m A_m} \qquad ..(4.4.3)$$

where n_m is the number of neutrons detected/sec by the collimated beam monitor having surface area A_m.

If r_T is the distance of the scatterer from the target and r_o the distance of the collimated beam monitor from the target, then

$$N_o = \frac{F\, r_o^2\, A_s}{r_T^2} \qquad ..(4.4.4)$$

$$= \frac{n_m}{\epsilon_m A_m} \frac{r_o^2}{r_T^2} A_s \qquad ..(4.4.5)$$

By substitution in equation (4.4.2) it follows,

$$\sigma(\theta) = \frac{n_d}{n_m} \frac{\epsilon_m}{\epsilon_d} \frac{r_T^2}{r_o^2} \frac{A_m}{\Omega_d} \frac{1}{N} \qquad ..(4.4.6)$$

Here n_m is the counting rate in the collimated beam monitor without the scatterer in the neutron beam and if n_m^1 is the counting rate in the collimated beam monitor with the scatterer in the neutron beam for the same incident flux, then the transmission factor T is given by

$$T = \frac{n_m^1}{n_m} \qquad ..(4.4.7)$$

Knowing T the value of n_m can be obtained from equation (4.4.7). The transmission factor T is obtained by comparing the normalised yields in the collimated beam monitor for the scatterer in and then out of the neutron beam, the target yield monitor, TYM, providing the normalisation factor. The above relation (4.4.6) can also be found in reference 95.

During the actual measurement of cross-section and polarization the transmission factor T was determined for every scattering sample many times and an average value obtained. To avoid any change in running conditions of the accelerator during the transmission factor measurements, the two runs

with scatterer in and out of the neutron beam were made for short times and repeated to get good statistical accuracy. The ratio of the efficiencies for each scattered neutron detector $\frac{\epsilon_m}{\epsilon_d}$ was determined in separate runs when each detector was placed in turn at 0^o. In these measurements the scatterer was removed and the normalised counting rate obtained in the collimated beam monitor directly irradiated by the neutron beam was compared with the normalised counting rate in each of the six scattered neutron detectors alternately placed at zero degrees. Then,

$$\frac{\epsilon_m}{\epsilon_d} = \frac{n_m}{n_d} \frac{M_d}{M_n} \qquad ..(4.4.8)$$

where n_m, n_d are the neutron counting rates detected in the collimated beam monitor and the scattered neutron detector respectively and M_d, M_n are the corresponding counting rates in the TYM.

The values of $\frac{\epsilon_m}{\epsilon_d}$ were determined thoroughly for all the six detectors. Care was taken that during each of the above mentioned measurements the amplifier gains and the discriminator bias levels did not change and the running conditions of the accelerator remained the same.

4.5 The Experimental Data

Before starting each experimental set of runs the linear and pulse shape discrimination bias levels of each neutron detector and the collimated beam monitor were checked by using Na^{22}, Cs^{137} gamma-ray sources and Am-Be neutron source respectively. After these checks the 0.5 MeV Van de Graaff accelerator at the Physics Department was run on the target for neutron polarization and differential elastic scattering cross-section measurements with 2.9 MeV neutrons.

With reference to Fig. (38), the lower and upper levels of the single

channel analyser associated with the collimated beam monitor was set on the time-of-flight peak to eliminate the background part of the time-of-flight spectrum and a coincidence between the single channel analyser pulses and the neutron-He^3 coincidence pulses further reduced the background level under the time-of-flight peak. These settings of the single channel analyser were checked frequently during the actual overall measurements and the system was so stable that no changes in the settings were required.

The focussing of the beam was adjusted for minimum current on the deuteron beam entrance aperture. Also the beam was steered on the target for maximum number of counts under the time-of-flight peak in the collimated beam monitor by maximising the counting rate in the collimated beam monitor scaler. The focussing condition of the beam was very important in the experiment in order to avoid random coincidences. To check on the background level a third scaler was used to record the total number of coincidence pulses between neutron and He^3 particles from all the six detectors. All these checks ensured good focussing of the deuteron beam on the target. The He^3 linear pulses were also checked on an oscilloscope.

The experimental data was collected when the cradle was at an angle $\phi = 0$ (Pos. 1) and $\phi = \pi$ (Pos. 3) for the polarization studies and also initially $\phi = \pi/2$ (Pos. 2) and $\phi = 3\pi/2$ (Pos. 4) to check for any instrumental asymmetry. The time-of-flight spectra associated with each run were recorded onto a paper tape by a high speed tape punch coupled to the pulse height analyser after every 2000 secs and after each run the cradle was rotated to the next position. The measurements lasted for more than 1700 hours in periods of 50 to 100 hours of continuous running to cover all the scattering angles 20°-160° for all the scatterers.

It is very important to avoid carbon deposition on the target since the consequent loss of energy by the He^3 particles could prevent their detection and so the number of counts in time-of-flight spectrum would decrease. Although the cooled copper tube shown in Fig. (14) increased the useful life of the target, it was necessary to change it after about 250 to 300 hours of running. Considerable care was taken when changing the target to ensure that the accurate alignment of the system was maintained, both by making accurate measurement of the target position in the vacuum chamber with a depth gauge and by viewing the target by telescope aligned along the axis of the neutron collimator.

4.6 The Experimental Data Analysis

The basic step in processing of the data was to sum up all the corresponding spectra recorded on punched paper tapes for the cradle at a particular position. A Digital Equipment Corporation PDP-11 computer available in the Physics Department was used for this purpose. The resulting summed spectra were printed out and also were punched out on paper tape by a high speed punch coupled to the computer. This process was repeated four times for each of the four cradle positions so producing four master paper tapes and four print-outs.

The number of counts under a time-of-flight peak was determined for each detector and the background level under the peak subtracted. This gave the numbers of scattered neutrons detected by each of the six detectors for positions 1-4 of the cradle. Expression (4.4.6) was used to calculate the differential elastic scattering cross-sections for each case. The cross-sections for azimuthal angles 0, $\pi/2$, π, and $3\pi/2$ and the same scattering angle θ were averaged. Typical time-of-flight spectra for scattering angles

30° and 90° for Cu are shown in Figs (42a) and (43a) respectively. Separate runs were done to check on the background level without the scatterer in the beam and the time-of-flight spectra were flat in those cases. Typical spectra for background at 30° and 90° are shown in Figs. (42b) and (43b). To be convinced about the determination of background level under the peak the intensity of the background level with scatterer in and out were compared for many sets of runs and were found when appropriately normalised to be the same.

A small time-of-flight peak was observed with scatterer out at the backward angle 160°. The true number of counts of the scattered neutrons at 160° was obtained using the collimated beam monitor for normalisation and subtracting the background number of counts under the time-of-flight peak. This background contribution was about 18% in the best case and 45% in the worst case.

The iodine and mercury scatterers were each contained in a very thin walled stainless steel cylinder having a screwed stopper. The background measurements for I and Hg were done using an identical empty stainless steel container. The background due to the container was very small, less than 1%.

4.7 Finite Geometry Effects and Multiple Scattering Corrections

It is necessary to employ within limits a large scattering sample so as to distinguish scattered neutrons from background and also to obtain data at a reasonable speed. Flux attenuation, multiple scattering and angular resolution of the target-scatterer and scatterer-detector geometries are the effects introduced by the finite dimensions of the scatterer. In the flux attenuation effect, the primary neutron beam is attenuated by the scatterer so that the scattering nuclei farthest from the source are not exposed to the full intensity.

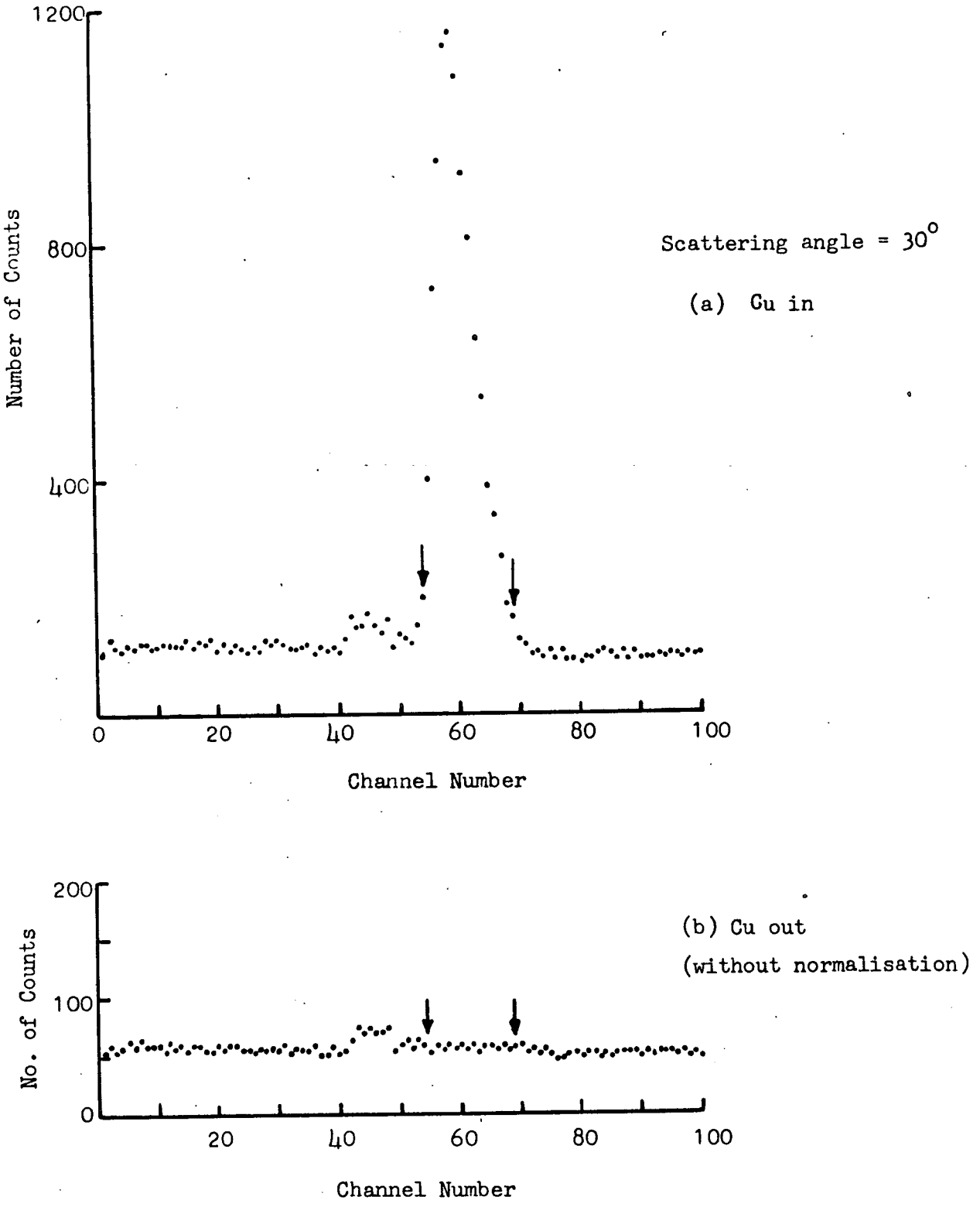

Fig. (42) Associated Particle T.O.F. Spectra for neutrons elastically scattered by Cu at 30°

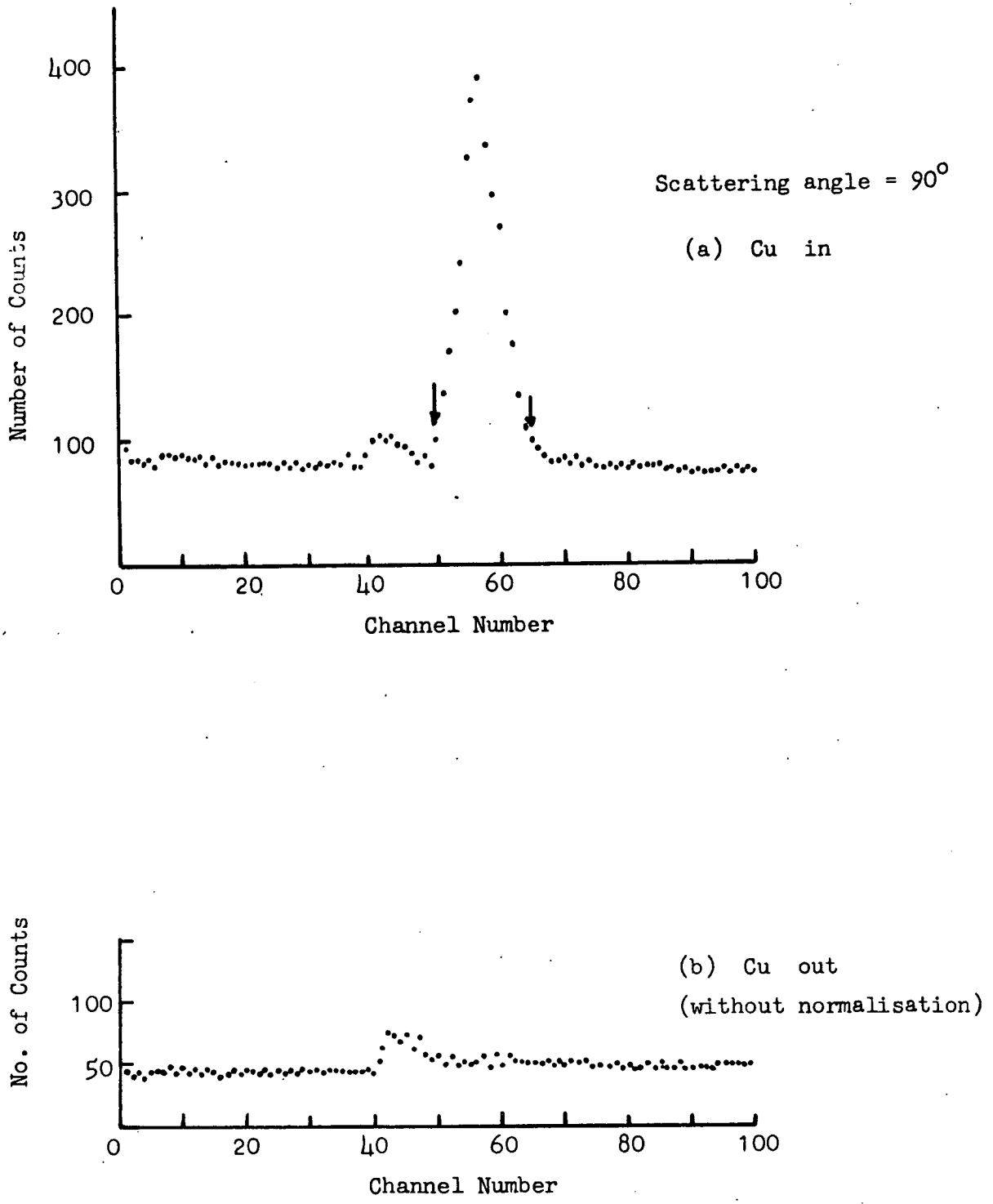

Fig. (43) Associated Particle T.O.F. Spectra of neutrons elastically scattered by Cu at 90°

The effect is termed multiple scattering when the neutrons are scattered two or more times before emerging from the scatterer towards the detector.

These effects were calculated by different authors using analytical methods[88,89] or Monte Carlo random walk techniques[89-94]. Some authors calculated these effects using a combination of both, analytical and Monte Carlo methods[89,93]. By tracing neutron histories by the Monte Carlo methods, the effects of flux attenuation, finite geometry and multiple scattering may be taken into account.

The experimentally observed elastic differential cross-sections for Fe, Cu, I, Hg and Pb were corrected for neutron flux attenuation, multiple scattering in the scatterers and for the finite angular resolution of the target-scatterer and scatterer-detector geometries using the Monte Carlo code due to Holmqvist et al[92]. The code was supplied by Drigo[102].

The program in the first step calculates the neutron flux attenuation correction $\frac{F}{\bar{F}}$; where F is the neutron flux at the point of the scatterer centre without any scatterer in position and $\bar{F}$ is the neutron flux at the same point with a scatterer in position and is given by:

$$\frac{F}{\bar{F}} = \frac{N \sigma_T n V}{R A} \qquad ..(4.7.1)$$

where σ_T is the total scattering cross-section, n is the number of nuclei per volume element in the scatterer, V is its volume, R is the number of neutrons interacting elastically or non-elastically at least once in the sample and N is the number of neutrons penetrating the area A of the scatterer with no scatterer in position.

In the second step the computer calculates the correction for the loss of neutrons in the scatterer by non-elastic collision processes. The observed

elastic neutron angular distribution is transformed to the centre-of-mass co-ordinate system and the experimental angular distribution is fitted by a Legendre polynomial expansion. The differential elastic scattering cross-sections are then calculated at 41 equispaced points (corresponding to the detectors of the detector band). The program then calculates the corrected angular distribution for flux attenuation and the loss of neutrons due to non-elastic collisions. Finally the program calculates the multiple scattering corrections in the sample and gives the angular distribution corrected for finite-geometry effect, flux attenuation and multiple scattering.

The program was written in IBM 7090 machine language and therefore had to be adapted for the available IBM 370/158 computer. The values of total scattering cross-sections and non-elastic cross-sections required as input data of the program were taken from reference 106.

4.8 The Experimental Results

The experimental differential elastic scattering cross-section of Cu is shown in Fig. (44). The graph shows the uncorrected experimental angular distribution and the distribution corrected for flux attenutation and the loss of neutrons due to non-elastic collisions in the scattering sample. The solid curve joining the circles is the Monte Carlo calculated angular distribution corrected for all the effects of flux attenuation, finite geometry and multiple scattering. The multiple scattering correction for Cu sample is between 10% to 18% at different scattering angles. 10% being at 20°. The experimental differential elastic scattering cross-sections of Fe, Cu, I, Hg and Pb corrected for finite geometry effects, flux attenuation and multiple scattering are given in Tables 4.8.1 - 4.8.3 and shown in Figs. 44-48.

Table 4.8.1

Differential Elastic Scattering Cross-sections

of Fe and Iodine

Angle (cm)	Iron $\sigma(\theta)$ mb/sr	Iodine $\sigma(\theta)$ mb/sr
20°	961 ± 7	1597 ± 16
34°	570 ± 6	1102 ± 10
48°	235 ± 3	489 ± 7
62°	62 ± 1	149 ± 2
76°	25 ± 1	126 ± 3
90°	44 ± 1	58 ± 1
104°	66 ± 2	46 ± 2
132°	74 ± 2	99 ± 3
160°	87 ± 2	105 ± 3

Table 4.8.2

Differential Elastic Scattering Cross-sections of Copper

Angle (cm)	Copper $\sigma(\theta)$ mb/sr
20°	1009 ± 13
30°	705 ± 9
40°	403 ± 6
50°	170 ± 4
60°	61 ± 2
70°	32 ± 1
80°	52 ± 2
90°	80 ± 2
104°	97 ± 4
132°	54 ± 2
160°	37 ± 2

Table 4.8.3

Differential Elastic Scattering Cross-Sections of Hg and Pb

Angle (cm)	Mercury $\sigma(\theta)$ mb/sr	Lead $\sigma(\theta)$ mb/sr
20°	3410 ± 27	3831 ± 30
34°	1602 ± 17	1942 ± 21
48°	360 ± 5	470 ± 6
62°	42 ± 1	193 ± 4
76°	135 ± 3	280 ± 6
90°	197 ± 4	301 ± 5
104°	134 ± 3	254 ± 6
118°		172 ± 6
132°	64 ± 2	111 ± 3
146°		170 ± 6
160°	115 ± 3	350 ± 7

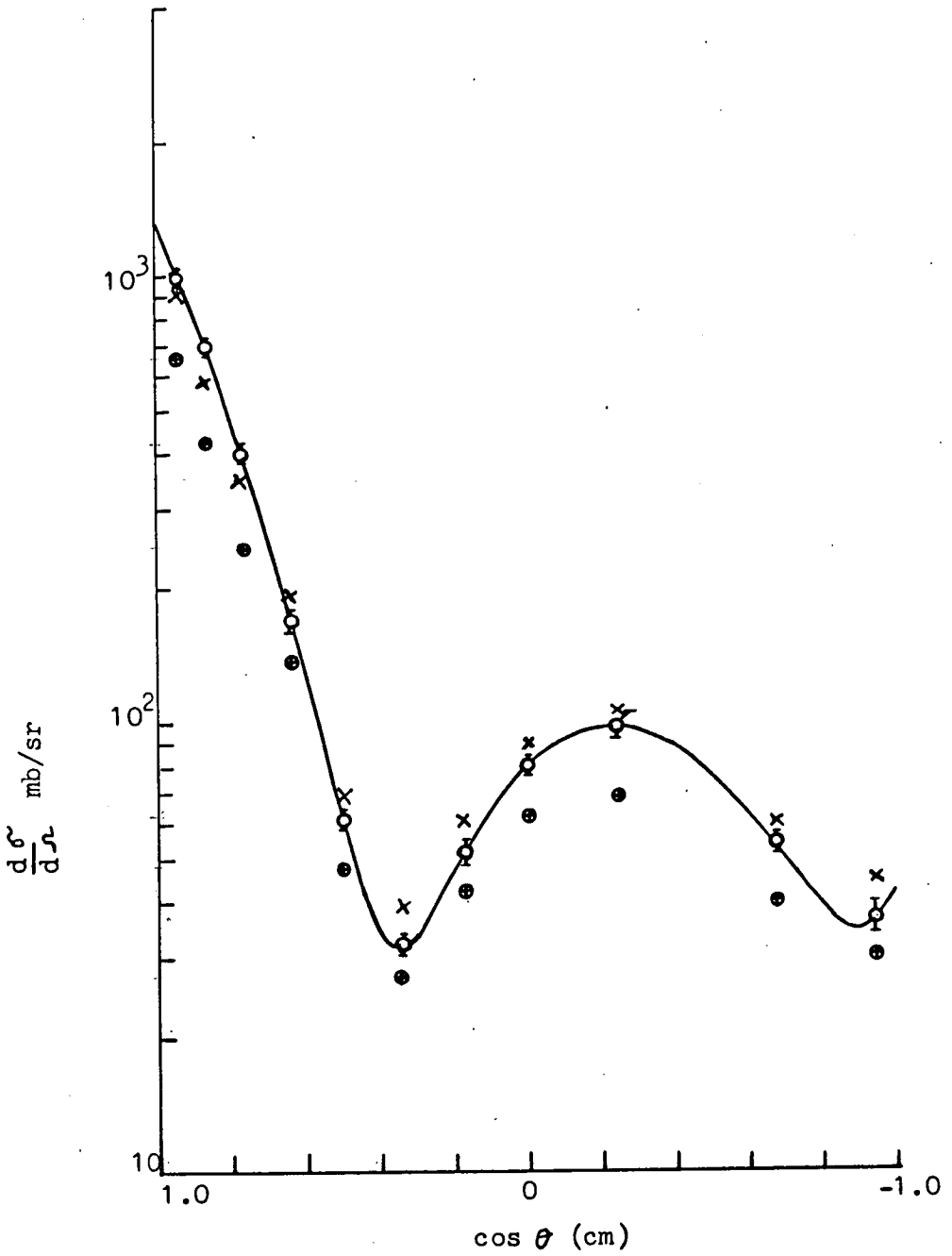

Fig. (44) Differential elastic scattering cross-section of copper

because of insufficient energy resolution. The bias of the detectors was set at about 1.9 MeV neutron energy to minimise the contribution from inelastic scattering. For 2.9 MeV incident neutron energy only excited states of much less than 1 MeV excitation can contribute significantly. The scattering samples used were natural in abundance. The following are the compositions of the scattering samples given in percentage; (those less than 10% are neglected)

(a) Fe - Fe^{56} 91.68

(b) Cu - Cu^{63} 69.1; Cu^{65} 30.9

(c) I - I^{127} 100

(d) Hg - Hg^{198} 10.02; Hg^{199} 16.84; Hg^{200} 23.13; Hg^{201} 13.22; Hg^{202} 29.8;

(e) Pb - Pb^{206} 25.1; Pb^{207} 21.7; Pb^{208} 52.3 .

Considering the above isotopes the possible cases where the contribution from inelastic scattering might occur will now be discussed. To estimate this, the levels of the isotopes whose excitation might contribute are considered with the published data on inelastic scattering cross-section or differential inelastic scattering cross-sections. The excitation levels of Fe, Cu, I, Hg and Pb are given in Table (4.10.1).

For Fe^{56} Gilboy and Towle[105] determined the differential inelastic scattering cross-section of the 0.847 MeV level for 3 MeV neutrons. The differential inelastic scattering cross-section is isotropic and is about 55 mb/sr. Due to excitation of the 0.847 MeV level of Fe^{56} the 2.9 MeV neutrons

after inelastic scattering would emerge with an energy of about 2 MeV and would not be detected efficiently, being close to the detector bias. The inelastic scattering contribution is estimated to be zero.

For Cu Cranberg and Levin[113] measured the inelastic cross-section at 90° for the 0.98 ± 0.04 MeV excited level as 38 mb/sr for 2.45 MeV neutrons. For Cu^{63} and Cu^{65} the inelastic scattering cross-sections have been determined by Holmqvist and Wiedling[118] for the excited levels of 668 keV; 961 keV; 764 keV and 1114 keV from 0.7 - 1.4 MeV neutron energy. At 2.9 MeV neutron energy the angular distributions of gamma-rays in the $Cu^{63,65}$ (n, n'γ) reaction was studied by Felsteiner and Serfaty[119]. From the above data the inelastic scattering contribution for the case of Cu is estimated to be about 2 mb/sr, a very small contribution.

For I excited levels have been determined by Barnard et al[115] for neutron energies of 0.4 - 1.9 MeV. This element has very low excitation levels. Some information on inelastic scattering cross-sections could be obtained only for low incident neutron energies[120,121,122]. The inelastic scattering cross-section may not be extrapolated to higher energies because the shape of the inelastic curve is not very clear. Guernsey and Wattenberg[120] show a dip in the inelastic scattering cross-section at a neutron energy of about 1 MeV for the lowest excitation level of I. However from the available data (for 0.8 MeV neutrons) the inelastic cross-section is estimated to be about 55 mb/sr. This looks like an over-estimation of the inelastic cross-section since it is larger than the measured elastic scattering cross-section at the minimum of the curve. A complete knowledge of differential inelastic scattering cross-sections around 3 MeV neutron energy for different excitation levels of I would be required to completely account for any inelastic contrib-

ution from I.

The excited levels of Hg were determined by De Villiers et al[116] for a neutron energy of 0.3 - 1.5 MeV and the total inelastic scattering cross-sections for these different levels was determined. Taking into account the natural abundance of Hg isotopes and assuming isotropic angular distribution for inelastic scattering the contribution is estimated to be about 19 mb/sr. This correction if applied will lower the minima of the differential cross-section curve but the overall shape of the curve will not change considerably. However the above estimation is based on data at the lower neutron energy of 1.5 MeV and may be an over-estimate.

Cranberg et al[114] measured the differential inelastic scattering cross-section of Pb^{206} and Pb^{207} for incident neutrons of 2.5 MeV. The excited levels of interest here are 0.803, 0.572 MeV. Taking into consideration the natural abundance of the Pb isotopes the inelastic scattering contribution is estimated to be about 5 mb/sr; a small contribution as compared to the elastic cross-section.

From the above discussion it follows that the inelastic scattering contribution for Fe, Cu and Pb may be considered to be zero. For Hg the estimated inelastic cross-section is not important at angles other than the minima of elastic scattering cross-section curve.

Table (4.10.1)

Excitation Levels of the Nuclei

	Element	(Ref)	Isotope	Excitation Level (MeV)
(1)	Fe	(117)	Fe^{56}	0.847; 2.09; ....
(2)	Cu	(117)	Cu^{63}	0.668; 0.962; 1.33; 1.414; 1.55; 1.86; 2.5; ....
			Cu^{65}	0.769; 1.114; 1.48; 1.62; 1.74; 2.09; ....
(3)	I	(115)	I^{127}	0.057; 0.203; 0.375; 0.418; 0.618; 0.629; 0.652; 0.717; 0.745; 0.991; ....
(4)	Hg	(116)	Hg^{198}...Hg^{202}	0.160; 0.208; 0.380; 0.440; 0.50; 0.610; 0.980; ....
(5)	Pb	(117)	Pb^{206}	0.803; 1.165; 1.341; 1.46; 1.684; 1.784; 1.998; ....
			Pb^{207}	0.572; 0.899; 1.632; 2.338; 2.625; ....
			Pb^{208}	2.62; 3.20; 3.48; 3.71; ....

4.11 Neutron Polarization Calculation

The asymmetries produced by the scatterers were evaluated in the following manner.

Let the number of neutrons scattered from a scatterer in a given time to the 'right' be N_R and to the 'left' be N_L, then the right-left ratio is defined as,

$$r = \frac{N_R}{N_L} \qquad ..(4.11.1)$$

From equation (1.3.5) it follows that

$$P_n P_2 = \frac{\frac{N_R}{N_L} - 1}{\frac{N_R}{N_L} + 1} \qquad ..(4.11.2)$$

The measured asymmetry is therefore given by

$$\epsilon = P_n P_2 = \frac{r - 1}{r + 1} \qquad ..(4.11.3)$$

The use of two detectors symmetrically placed to the 'right' and 'left' of the scatterer allows faster data collection but the detectors still require to be interchanged to compensate entirely for differences in detection efficiency. In this case the expression for r may be written as[24]

$$r = \left[\frac{N_{R_1}}{N_{L_1}} \quad \frac{N_{R_2}}{N_{L_2}}\right]^{\frac{1}{2}} \qquad ..(4.11.4)$$

where N_{R_1}, N_{L_1} are the 'right' and 'left' numbers of neutrons respectively detected by detector 1, and N_{R_2}, N_{L_2} are the numbers of 'right' and 'left' scattered neutrons respectively detected by detector 2.

For polarization determination the measurements were made in the reaction

plane $\phi = 0$ and $\phi = \pi$, the summing of the tapes for Pos. 1 and Pos. 3 of the cradle being done as described in section 4.6 to obtain two master tapes and two print outs. The number of scattered neutrons was determined from the time-of-flight peak associated with each detector as described in section 4.6 and equation (4.11.4) was used to calculate the 'right' - 'left' ratio r for each scattering angle.

The checks for any instrumental asymmetry were also performed. Firstly the absence of any gain shifts in any of the neutron detectors was checked by fixing a Na^{22} source on each detector in turn and the number of counts above the linear discriminator level was recorded for a fixed time at each of the four positions of the cradle. This process was repeated several times for each detector. No gain shifts were recorded in any of the six detectors.

A further check for any instrumental asymmetry consisted of detecting the scattered neutrons from the Cu scatterer when the cradle was at $\phi = \pi/2$ (Pos. 2); and $\phi = 3\pi/2$ (Pos. 4). The asymmetry should be zero in this plane and the satisfactory value 0.002 ± 0.007 at 20° scattering angle was found.

4.12 Polarization of the $D(d, n)He^3$ Neutrons

The polarization of neutrons produced in $D(d, n)He^3$ reaction below the deuteron energy of 1 MeV has been studied by many authors. The measurements of Behof et al[96]; Boersma et al[97]; Mulder[98]; Roding and Scholermann[99]; Davie and Galloway[100]; and Maayouf and Galloway[101] are plotted in Fig. (53). A review of the measurements of polarization in the $D(d, n)He^3$ reaction is given by Galloway[68]. The value of neutron polarization is estimated to be -15% with an uncertainty of 1% at 315 keV incident deuteron energy and this

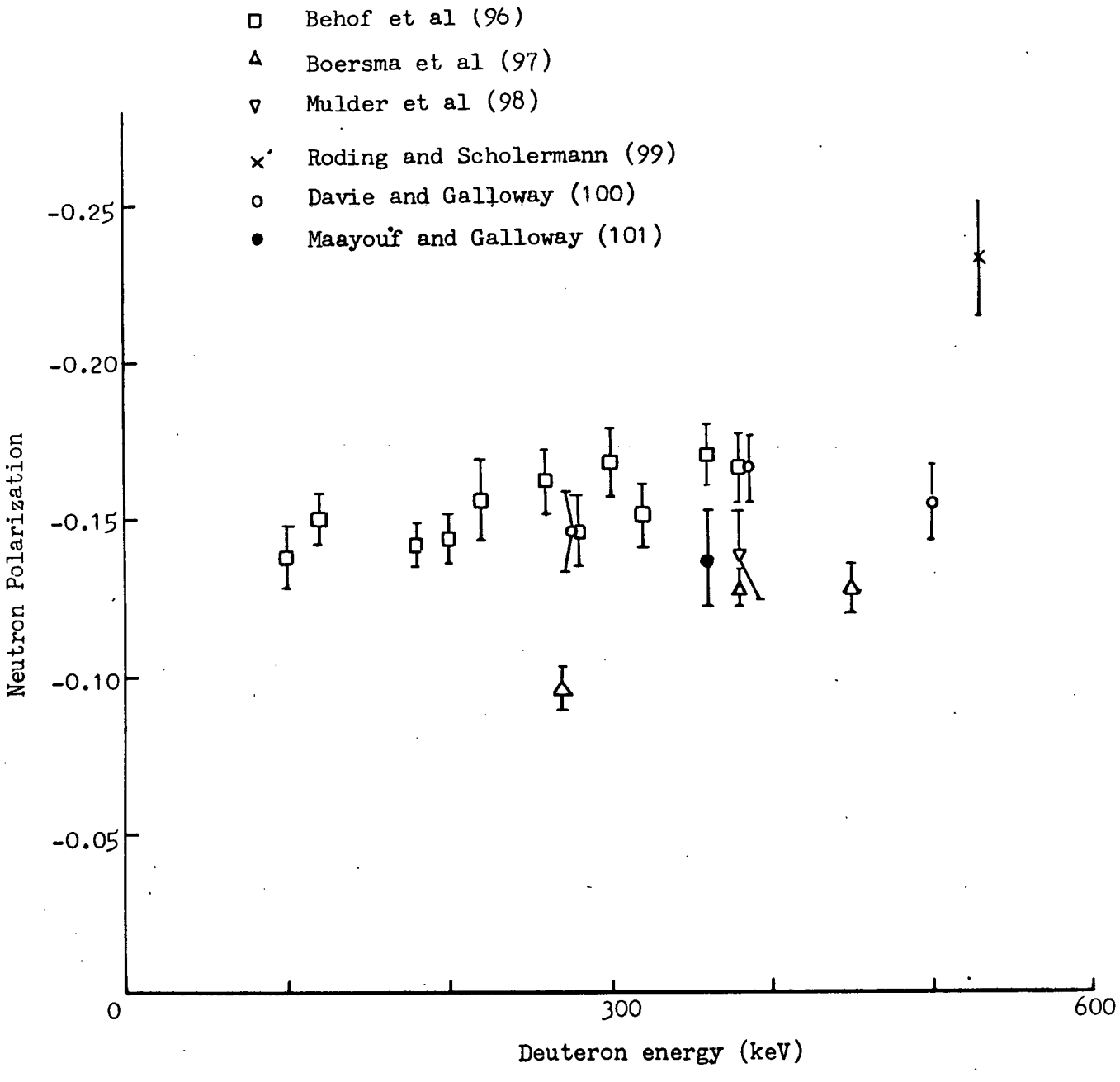

Fig. (53) Polarization of the $D(d,n)He^3$ neutrons near 49° (Lab).

value was used for the calculation of polarizations due to elastic scattering from the asymmetries measured.

4.13 Analysis of the Experimental Data and Results

The asymmetries were calculated for different scatterers using the equation (4.11.3). The equation (1.3.5) can be written as

$$P_n P_2 = \frac{N_R - N_L}{N_R + N_L} \qquad ..(4.13.1)$$

or,

$$P_n P_2 = \frac{\sigma(\theta, 0) - \sigma(\theta, \pi)}{\sigma(\theta, 0) + \sigma(\theta, \pi)} \qquad ..(4.13.2)$$

where $\sigma(\theta, 0)$ and $\sigma(\theta, \pi)$ are the differential elastic scattering cross-sections for scattering to 'right' and 'left' respectively. The above equation was used for the correction of the asymmetry measurements for multiple scattering and finite geometry effects. The values of $\sigma(\theta, 0)$ were determined for each detector using equation (4.4.6) and were averaged to give the differential cross-section for elastic scattering to the right of the scatterer. Similarly $\sigma(\theta, \pi)$, the differential elastic cross-section for scattering to the left of the scatterer was determined.

These differential cross-sections to 'left' and 'right' were corrected for finite geometry effects, multiple scattering and flux attenuation using the Monte Carlo Code[92] as described in section 4.7. From these corrected 'left' and 'right' differential elastic cross-sections the values of asymmetries were calculated from equation (4.13.2) and thus the corrected polarizations produced by different scattering nuclei obtained. The corrections for such effects were however small and within the statistical uncertainties of the

experimental values.

The polarization analysing powers from the measured asymmetries were calculated with the value $P_n = -15\%$; as discussed in Section 4.12. The experimentally determined polarizations and the values corrected for flux attenuation, finite geometry and multiple scattering are given in Tables (4.13.1) - (4.13.5). The mean neutron energy was 2.9 $\pm$ 0.1 MeV. Figs. (54-58) show the plots of the corrected polarizations produced by Fe, Cu, I, Hg and Pb respectively.

4.14 Comparison with other Results for Polarization

The results obtained were compared with those of Ellgehausen et al[37] and Zijp and Jonker[39] at 3.25 MeV and 3.2 MeV respectively. The measurements by Zijp and Jonker[39] for Fe and Cu were at only four scattering angles 30°, 45°, 60° and 75°. These published results for Fe and Cu are shown along with the present measurements in Figs. (54b) and (55b) respectively. The agreement for these nuclei is good. New points were determined at 160°; there are no previous measurements for angles larger than 140°. For I and Hg the present measurements are the only ones at this neutron energy. For Pb, the measurements by Zijp and Jonker[39] were at only four scattering angles 30°, 45°, 60° and 75°. These results are plotted along with the present measurements in Fig. (58b). The present measurements above 75° for Pb are again new measurements around 3 MeV neutron energy.

Any unpolarized inelastic contribution to the scattering would make the asymmetry small as is clear from the following expression,

$$P_2 P_n = \frac{N_R - N_L}{N_R + N_L + N_{inel.}} \qquad ..(4.14.1)$$

Tables 4.13.1 - 4.13.5

Polarizations produced in 2.9 MeV neutrons elastically scattered by Fe, Cu, I, Hg and Pb

Table 4.13.1

(Iron)

Angle	Polarization (%)	
	Experimental	Corrected
20°	-9 ± 4	-9 ± 4
34°	-4 ± 4	-5 ± 6
48°	-9 ± 6	-10 ± 7
62°	-11 ± 7	-13 ± 8
76°	+12 ± 8	+15 ± 10
90°	+18 ± 8	+21 ± 9
104°	-1 ± 10	-1 ± 11
132°	-22 ± 9	-26 ± 11
160°	+24 ± 10	+27 ± 11

Table 4.13.2

(Copper)

Angle	Polarization (%)	
	Experimental	Corrected
20°	-3 ± 5	-3 ± 5
30°	-8 ± 5	-9 ± 5
40°	-5 ± 6	-5 ± 6
50°	-10 ± 9	-12 ± 11
70°	+19 ± 11	+25 ± 14
80°	+18 ± 11	+21 ± 12
90°	+19 ± 9	+22 ± 10
104°	-3 ± 15	+3 ± 17
132°	-34 ± 17	-39 ± 19
160°	+40 ± 17	+46 ± 19

Table 4.13.3

(Iodine)

Angle	Polarization (%)	
	Experimental	Corrected
20°	-9 ± 5	-9 ± 6
34°	+10 ± 5	+11 ± 5
48°	+5 ± 7	+6 ± 8
62°	+6 ± 7	+7 ± 8
76°	+40 ± 9	+46 ± 10
90°	+35 ± 8	+41 ± 10
104°	+1 ± 14	+1 ± 16
132°	-25 ± 12	-29 ± 13
160°	+21 ± 12	+23 ± 13

Table 4.13.4

(Mercury)

Angle	Polarization (%)	
	Experimental	Corrected
20°	+16 ± 3	+17 ± 4
34°	+13 ± 4	+14 ± 5
48°	+26 ± 6	+28 ± 7
62°	+23 ± 9	+30 ± 13
76°	+35 ± 8	+42 ± 10
90°	-16 ± 8	-18 ± 9
104°	-24 ± 10	-27 ± 11
132°	-23 ± 13	-27 ± 15
160°	-27 ± 10	-30 ± 12

Table 4.13.5

(Lead)

Angle	Polarization (%)	
	Experimental	Corrected
20°	+18 ± 4	+18 ± 4
34°	+12 ± 5	+13 ± 5
48°	-11 ± 7	-12 ± 8
62°	+17 ± 8	+22 ± 10
76°	+3 ± 7	+5 ± 10
90°	+22 ± 7	+25 ± 8
104°	-39 ± 10	-45 ± 11
118°	-56 ± 14	-63 ± 16
132°	-28 ± 10	-28 ± 11
146°	+11 ± 14	+13 ± 16
160°	-24 ± 8	-27 ± 9

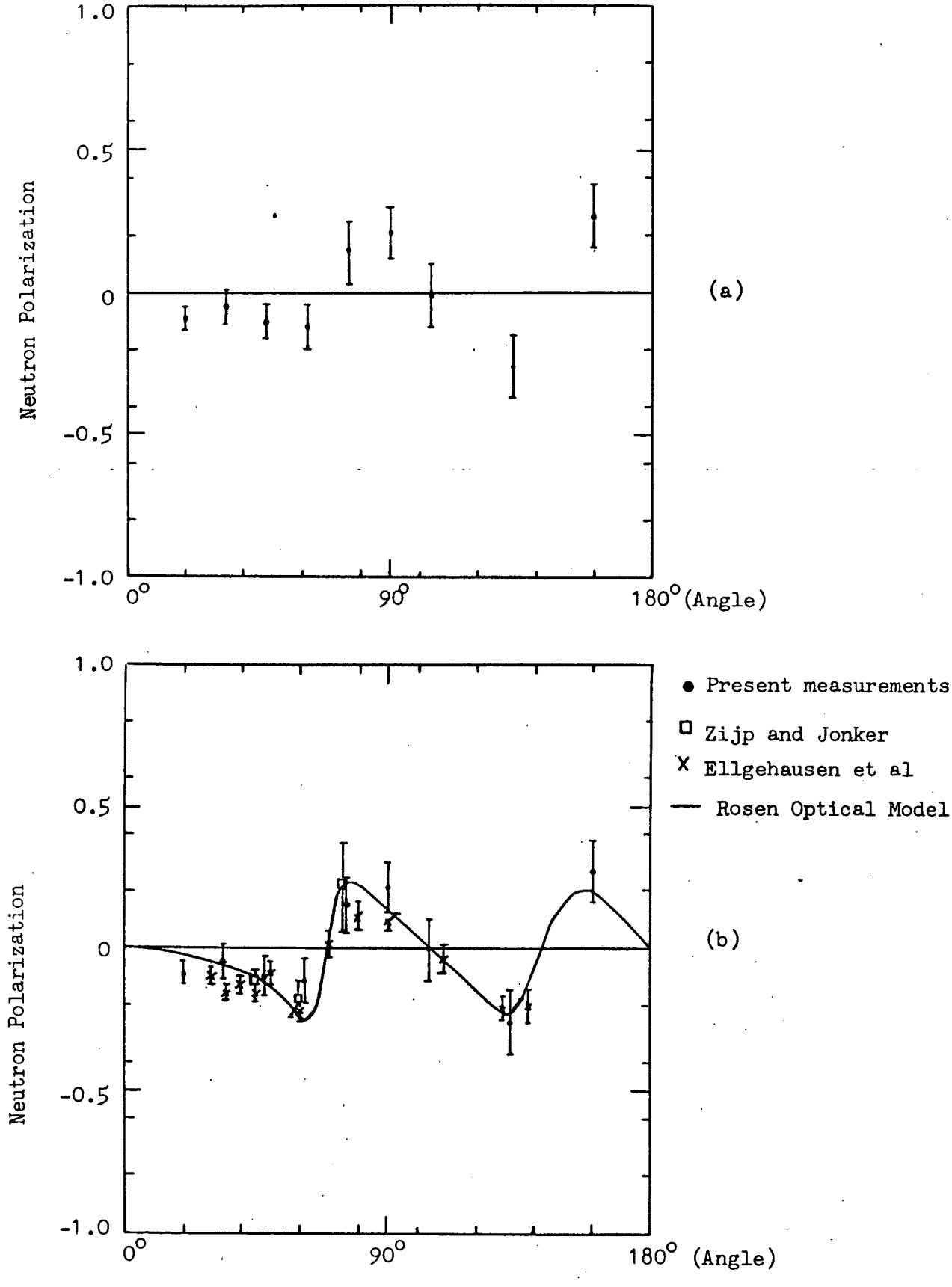

Fig. (54) The angular dependence of the polarization of neutrons elastically scattered by Fe

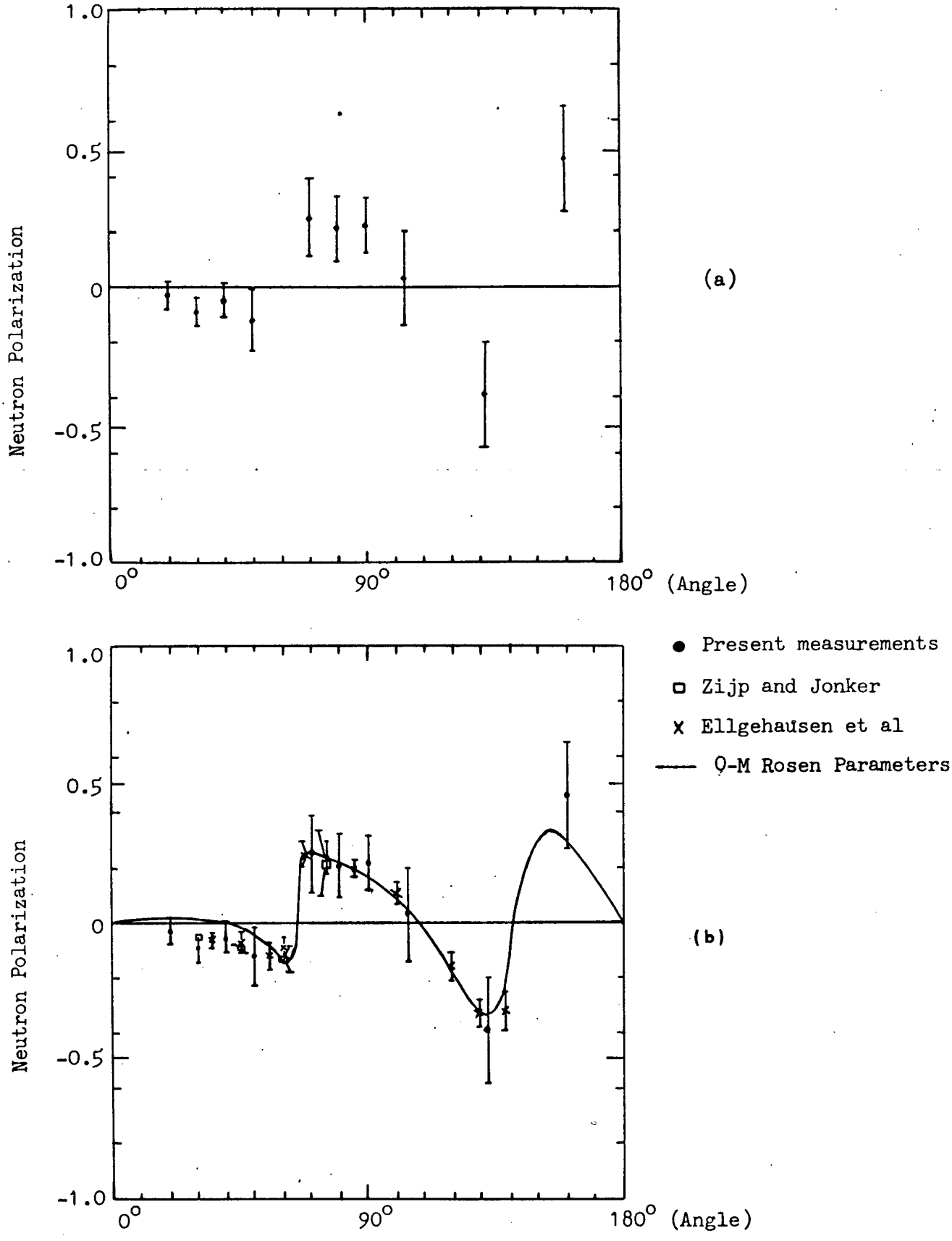

Fig. (55) The angular dependence of the polarization of neutrons elastically scattered by Copper

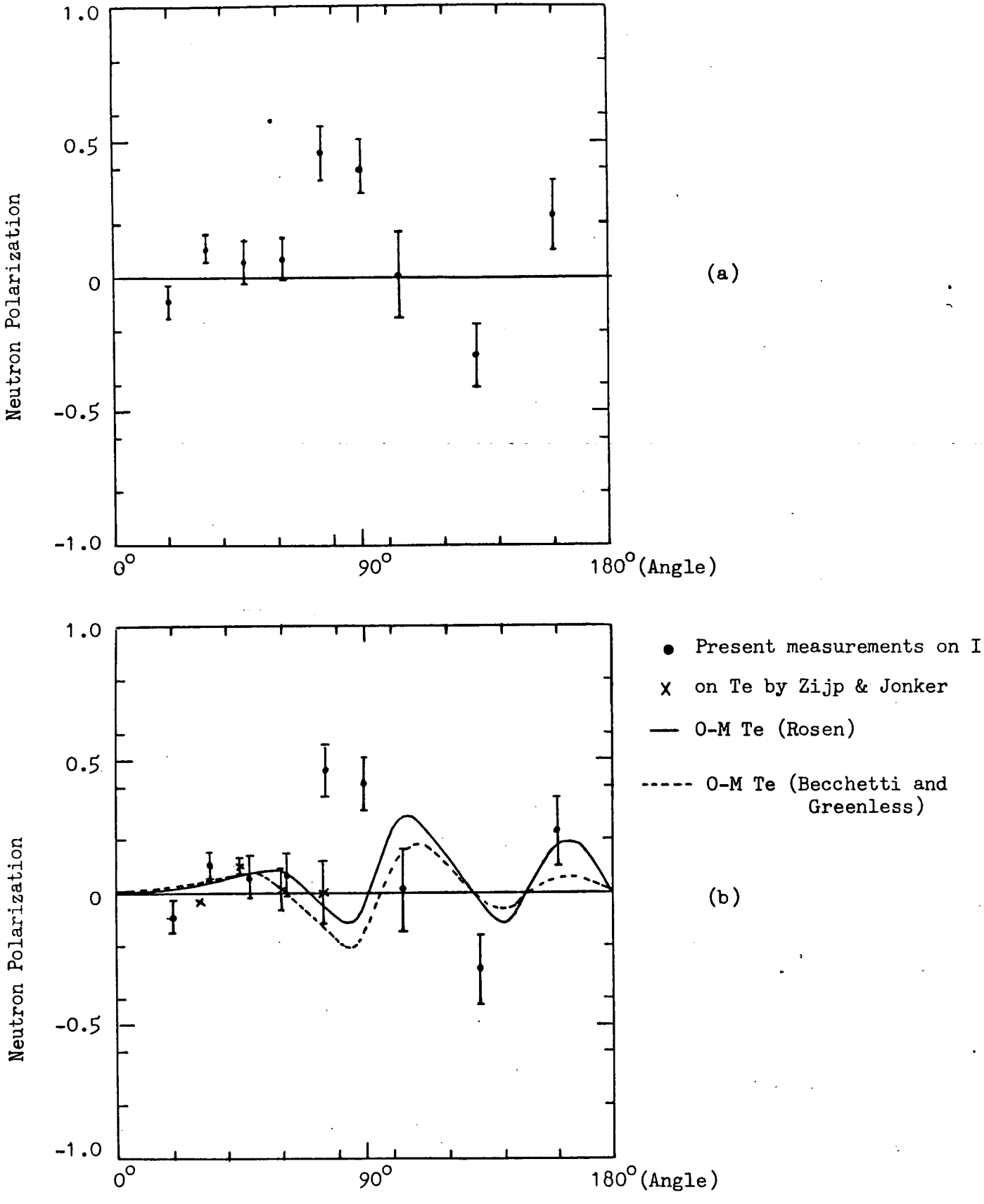

Fig. (56) The angular dependence of the polarization of neutrons elastically scattered by iodine

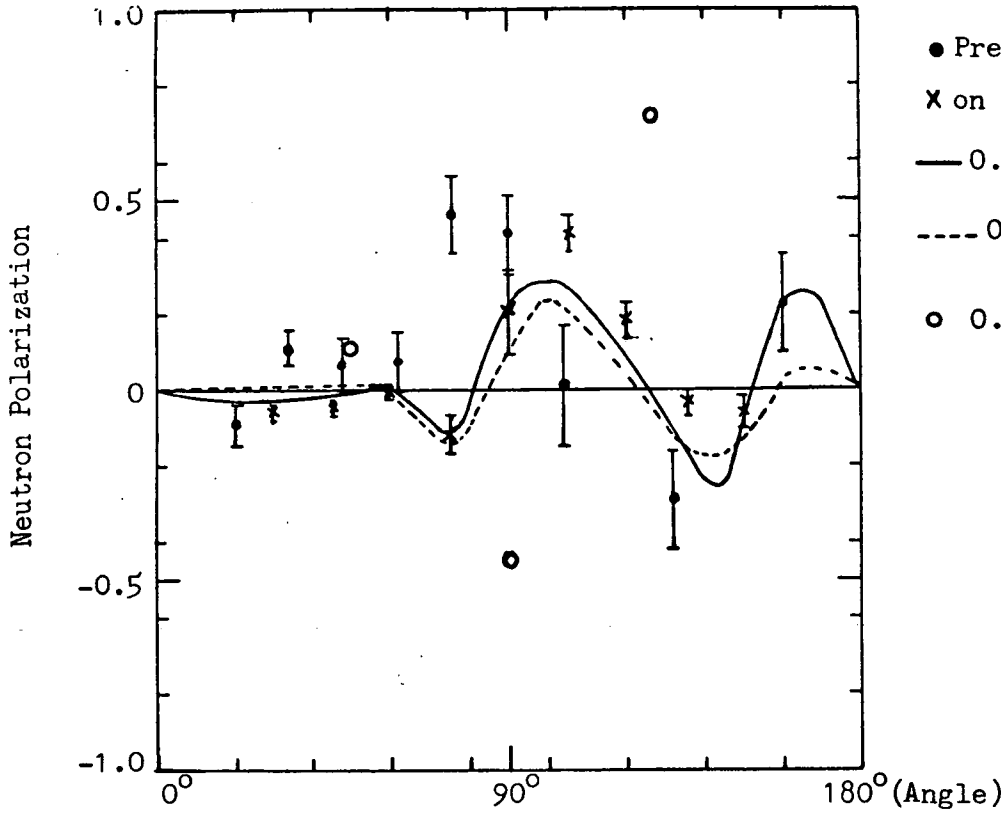

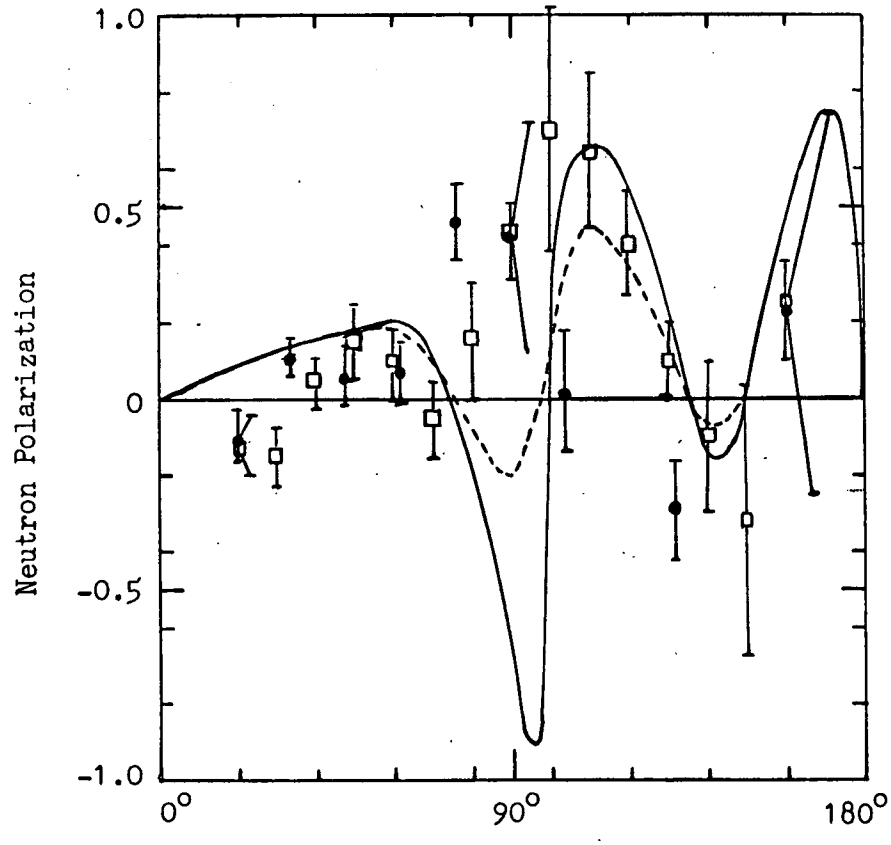

Fig. (56) Continued

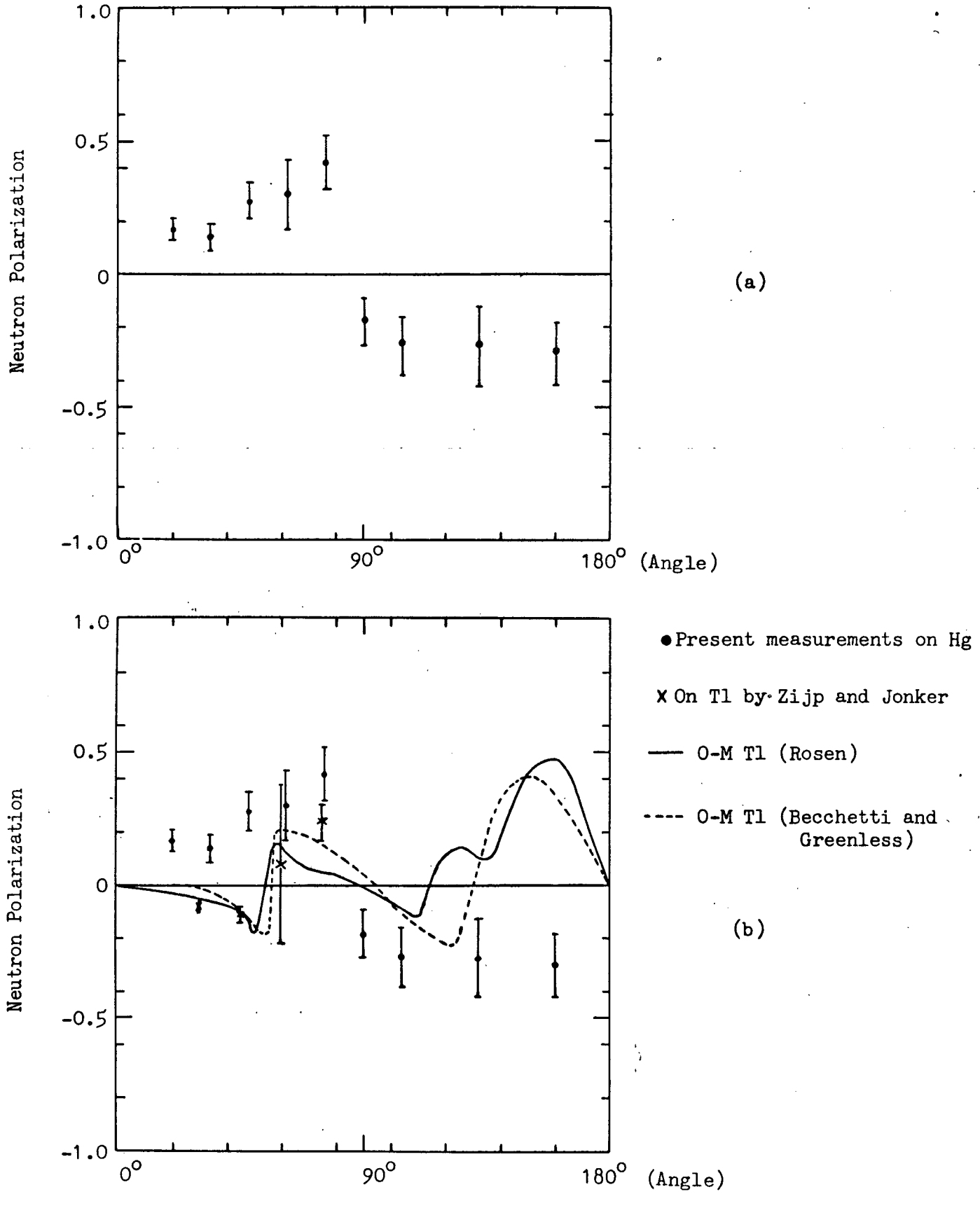

Fig. (57) The angular dependence of the polarization of neutrons elastically scattered by mercury

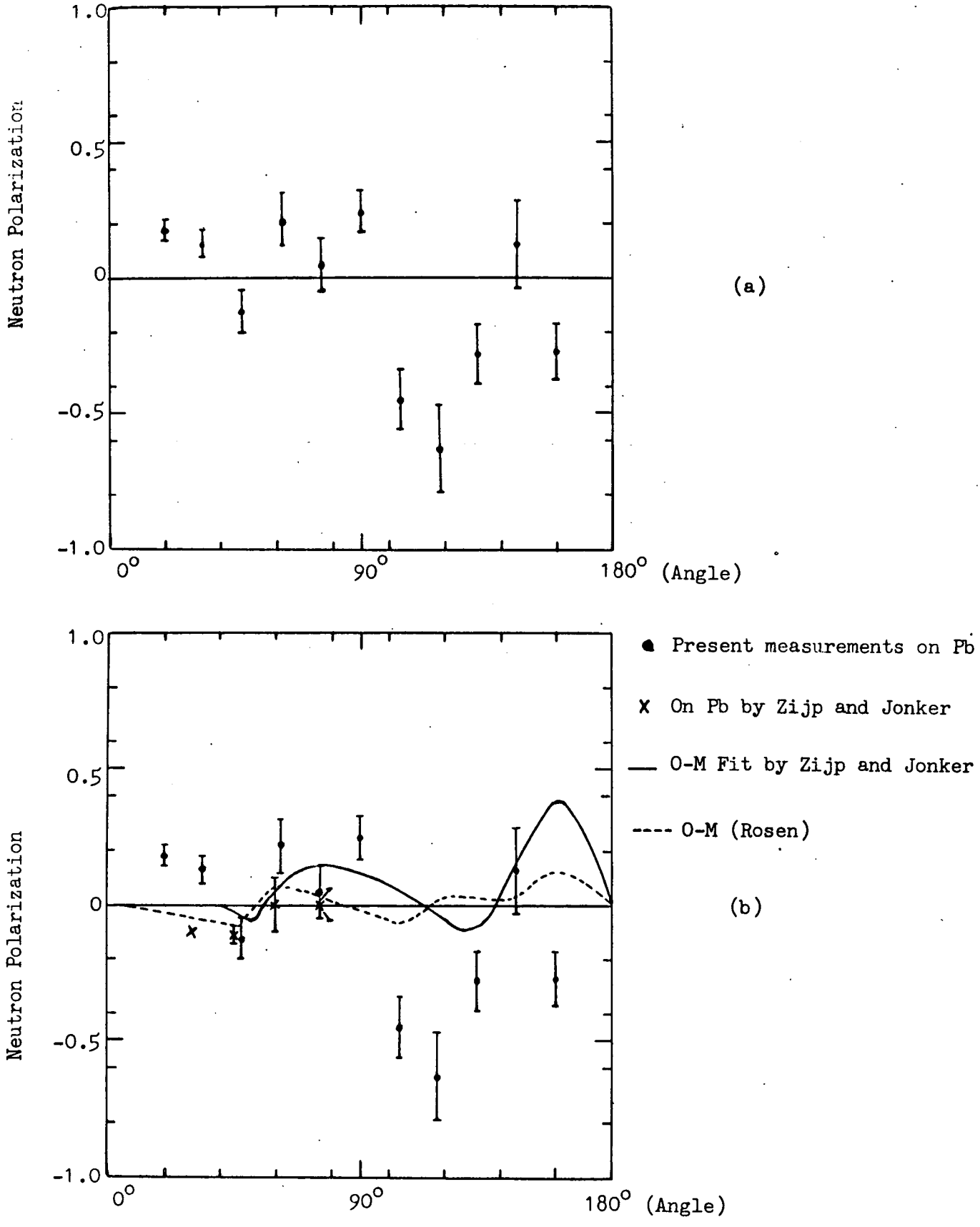

Fig. (58) The angular dependence of the polarization of neutrons elastically scattered by lead

Such an inelastic contribution could become very important at the minima of the differential elastic scattering cross-section curve. Some of the effects of any inelastic contribution to the scattering discussed in section 4.10 for Fe, Cu, I, Hg and Pb are discussed below.

For Fe although there is believed to be no inelastic contribution, still in the worst case of an estimated value of 8 mb/sr (from the data of Gilboy and Towle[105]) for inelastic contribution to the scattering at (76^{o}) the minimum cross-section value, the polarization value would become +22% instead of +15% and still would not effect the overall shape of the polarization curve. However it should be noted that the good agreement between the present measurements of differential elastic scattering cross-section and those given by Holmqvist[104] (a time-of-flight system being used in the experiment of Holmqvist) further confirms that the contribution due to inelastic scattering from Fe is zero in the present case.

For Cu the estimated value of contribution due to inelastic scattering is about 2 mb/sr. In this case the polarization value should have been, at (70^{o}) the minimum of the cross-section curve, +27% instead of +25% and similarly at 160^{o} it should have been +49% instead of +46%; a small effect and the overall shape of the angular dependence of polarization would remain essentially unchanged. It should be noted again that the good agreement between the present measurements on differential elastic scattering cross-section with those of Holmqvist[104] further confirms that the inelastic contribution to the scattering is almost zero.

For I the data is assumed to be purely elastic since little information is available about inelastic scattering.

For Hg in the worst case of 19 mb/sr contribution due to inelastic scattering at 62° (minimum of the differential elastic scattering cross-section curve) the polarization would become 55% instead of $(30 \pm 13)\%$ and at 132° the value would become -38% instead of $-(27 \pm 15)\%$. Still even with this contribution the overall shape of the angular dependence of polarization will not change substantially.

For Pb for an inelastic contribution of 5 mb/sr at 62° (minimum of the differential elastic scattering cross-section curve) the polarization value should have been +23% instead of +22% and at the second minimum (132°) the value of polarization should have been -29% instead of -28%; a small effect.

It is clear from the above discussion that at most angles for the above nuclei the effect of any inelastic scattering on the polarization values is negligible.

CHAPTER V

CHAPTER V

Scattering of 16 MeV Neutrons

5.1 Introduction

The polarization angular dependence and differential elastic scattering cross-section of Cu and Pb were measured from 20° to 90° for 16 MeV neutrons by a pulsed beam time-of-flight system. 16 MeV neutrons were produced at 75°(Lab) by the T(d, n)He^4 reaction with deuteron energy of 2.8 MeV. The polarimeter with its associated electronics were taken to the 3 MeV pulsed beam Van de Graaff accelerator IBIS at A.E.R.E., Harwell. The present measurements of both the differential elastic scattering cross-section and the polarization angular distribution are the first measurements for 16 MeV neutrons.

5.2 Scatterer and Detector Arrangement

The scatterer and the six neutron detector arrangement was essentially as described in section 4.2. The polarimeter was placed on a tower in front of the tritium gas target which was at a height of about 32 ft. above the floor. The shielding between the polarimeter and the target was a water filled tank having a tapered throated collimator. The collimator contained a cylinder of iron, as shown in Fig. (59), close to the target to provide attenuation of the neutron flux by inelastic scattering. Again around the throat brass inserts were used and in the remaining parts were tapered polythene inserts in the 5 cm diameter copper tube. The throat and taper geometry was chosen in such a way that the whole of the scattering sample was illuminated in the collimated neutron beam while the tapered inserts just failed to be directly illuminated by the target.

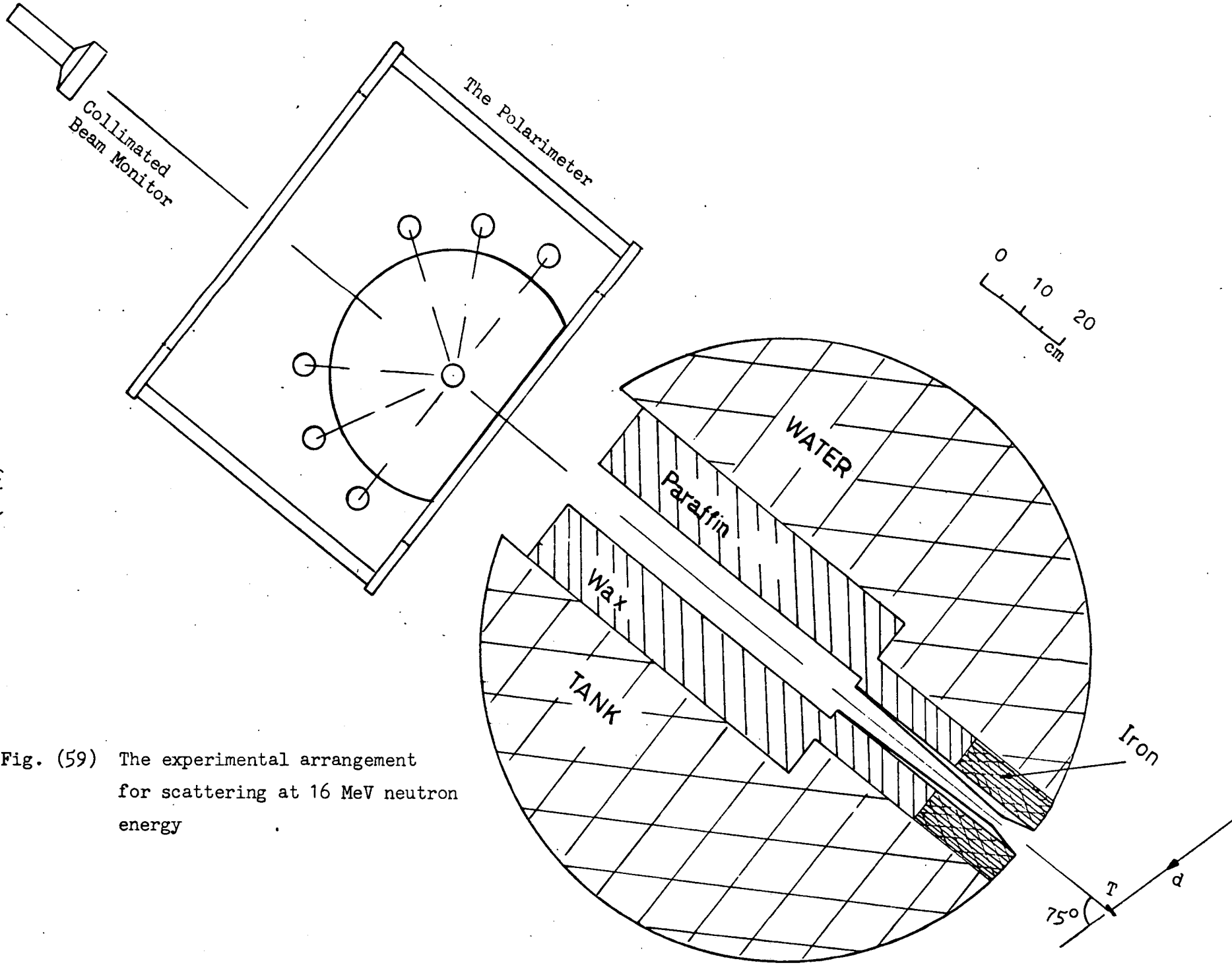

Fig. (59) The experimental arrangement for scattering at 16 MeV neutron energy

The scatterers used were of cylindrical shape, for Cu 5.08 cm diameter by 9.9 cm in height and for Pb 6 cm diameter by 9.2 cm in height, placed at a distance of 25 cm from the exit of the collimator and 166 cm from the neutron source. The scatterer was mounted in the stainless steel cup of the sample holder of the polarimeter and had its longitudinal axis parallel to the longitudinal axes of the neutron detectors and normal to the scattering plane.

The polarimeter with its collimator was first set at 75°(Lab) with respect to deuteron beam and then the axial alignment of the polarimeter to the tritium gas target was carefully adjusted. The tritium gas cell thickness was 1 cm filled to 1 atmosphere pressure and was separated from the beam tube vacuum by a 0.000244 cm thickness molybdenum foil. The energy loss of 3 MeV deuterons in the gas target window was calculated to be 175 keV. The experimental arrangement is shown in Fig. (59).

5.3 Electronics of the System

The electronics is similar to the system described in section 3.6 except that the stop pulse was provided by the pulsed beam pick-up unit and, of course, no linear He^3 pulse was involved. A 512 channel pulse height analyser with high speed tape punch was used in this work. The time resolution of the time-of-flight system was 2 nsec (FWHM).

5.4 The Experimental Measurements

After careful alignment of the polarimeter and its collimator on the target, the beam profile was measured using one of the scattered neutron detectors and is shown in Fig. (60). From Fig. (60) it is clear that the minimum scattering angle at which the pair of detectors can be set is 20°(Lab).

For cross-section calculations the ratio of efficiencies $\frac{\varepsilon_m}{\varepsilon_d}$ for each detector and the transmission factor T for both the scatterers were determined as described in section 4.4. The experimental data for polarization were collected with scatterer in and out of the neutron beam when the cradle was at an angle $\phi = 0$ (Pos. 1) and $\phi = \pi$ (Pos. 3). Measurements were also done to check on any instrumental asymmetries with the cradle at $\phi = \pi/2$ (Pos. 2) and $\phi = 3\pi/2$ (Pos. 4). The six time-of-flight spectra from each run of 2048 sec were recorded onto a paper tape by a high speed tape punch coupled to the 512 channel analyser. Measurements were done for scattering angles from 20° - 90° at 14° intervals for Cu and Pb. The measurements with scatterer out of the neutron beam were done to estimate the background number of counts under the time-of-flight peak and were normalised by the collimated beam monitor counts. The true number of scattered neutrons were determined as follows.

Let n_1 be the number of neutrons detected in one of the scattered neutron detectors for n_{m_1} neutrons in the collimated beam monitor with scatterer in and let n_{B_1} be the number of neutrons in the same detector for n_{m_B} neutrons in the collimated beam monitor with scatterer out, then the true number of scattered neutrons n_{S_1} would be,

$$n_{S_1} = n_1 - n_{B_1} \frac{n_{m_1}}{T} \frac{1}{n_{mB}} \qquad ..(5.4.1)$$

At 16.1 MeV the most severe problem was the intense background in the side detectors, 48% around 34° and 85% at 90° for Pb, despite considerable efforts to reduce it.

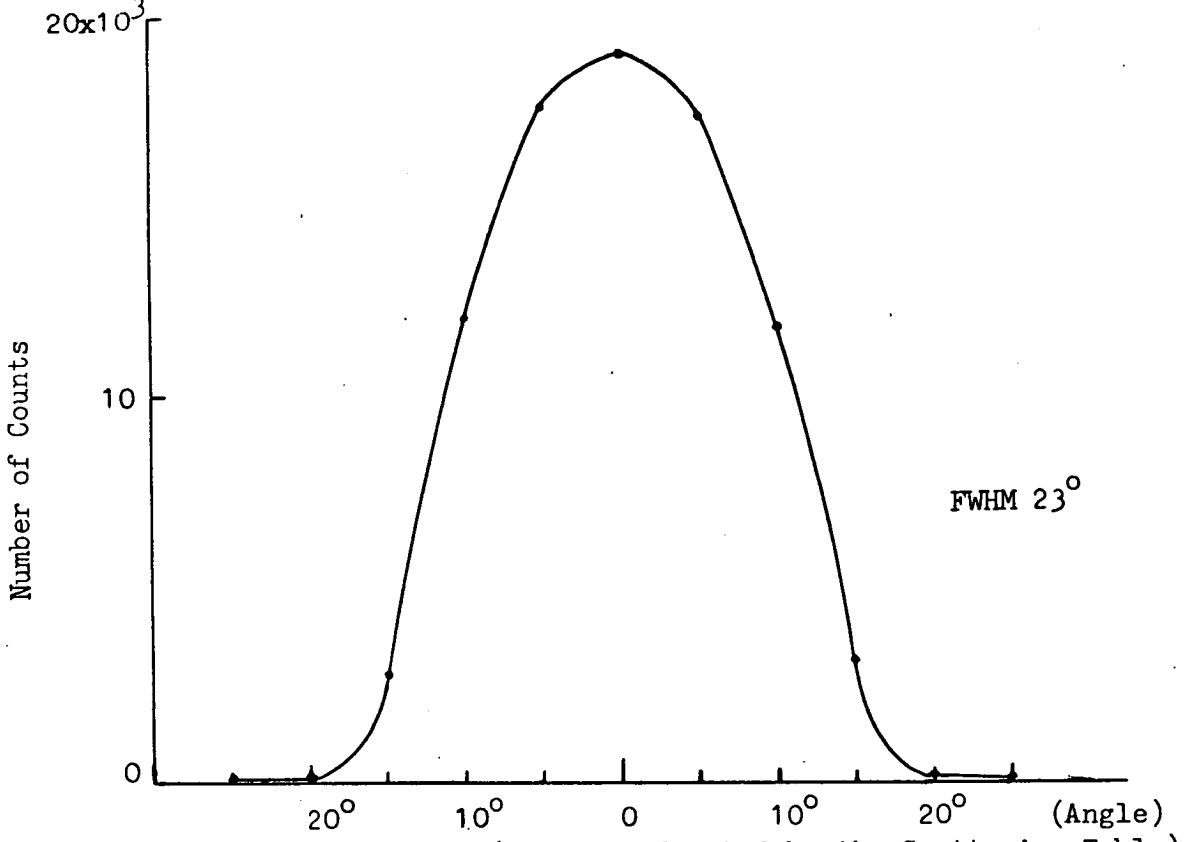

Fig. (60) The Beam Profile (angles indicated by the Scattering Table)

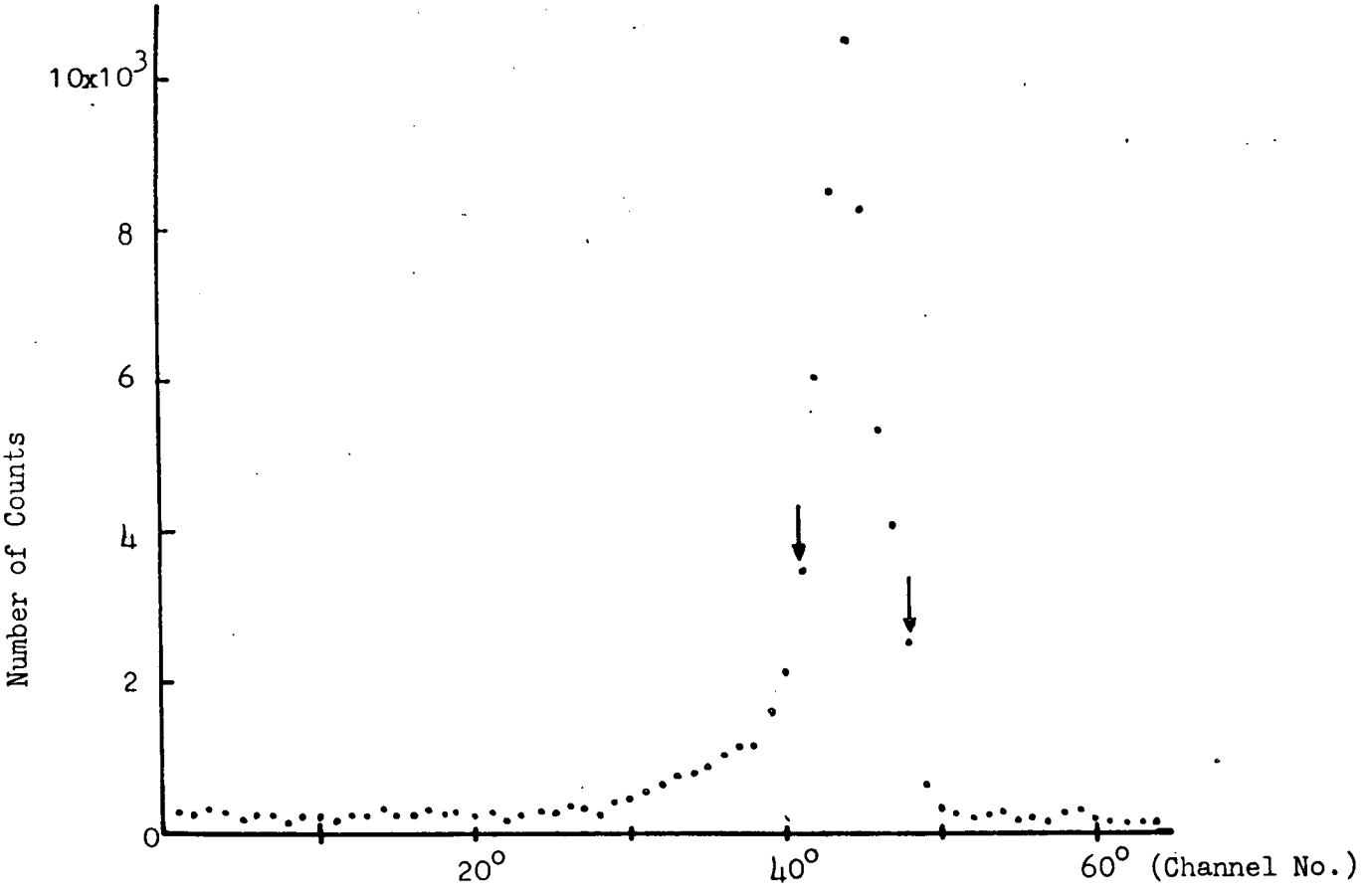

Fig. (61) Time of Flight Spectrum for neutrons elastically scattered by lead at 20°

5.5 The Experimental Data Analysis

For a particular position of the cradle the time-of-flight spectra from all the runs with scatterer in the neutron beam were summed and the corresponding background spectra with scatterer out of neutron beam were also summed. Using equation (5.4.1) the number of true scattered neutrons in each detector was calculated. The same procedure was repeated for the other positions of the cradle. Expression (4.4.6) was used to calculate the differential elastic scattering cross-sections for each detector angle for each position of the cradle. The average differential scattering cross-section was then calculated at each scattering angle from 20°-90° at 14° intervals for Cu and Pb. A typical time-of-flight spectrum for scattering at 20° from lead is shown in Fig. (61). The arrows indicate the part of the spectrum considered for the analysis of the data.

Flux attenuation, multiple scattering and finite geometry effects were corrected using the Monte Carlo Code[92] as described in Section 4.7. The multiple scattering correction is between 9% to 18% both for Cu and Pb. Total scattering cross-sections and non-elastic cross-sections for the scatterers required as the input data of the program were taken from BNL[107] and from the values given in reference (13).

5.6 The Differential Cross-Sections for Elastic Scattering

The corrected results for Cu and Pb are listed in Table (5.6.1) and shown in Figs. (62) and (63) respectively. The solid line joining the circles is the Monte Carlo calculations.

As discussed previously, in determining the differential cross-sections from equations (4.4.6) and (4.4.7) statistical uncertainties arise in the

Table 5.6.1

Differential Elastic Scattering Cross-sections of Copper and Lead

Angle (cm)	Copper $\sigma(\theta)$ mb/sr	Lead $\sigma(\theta)$ mb/sr
20°	2110 ± 24	1883 ± 20
34°	210 ± 7	695 ± 11
48°	72 ± 2	436 ± 5
62°	40 ± 3	103 ± 3
76°	50 ± 2	108 ± 4
90°	45 ± 3	30 ± 2

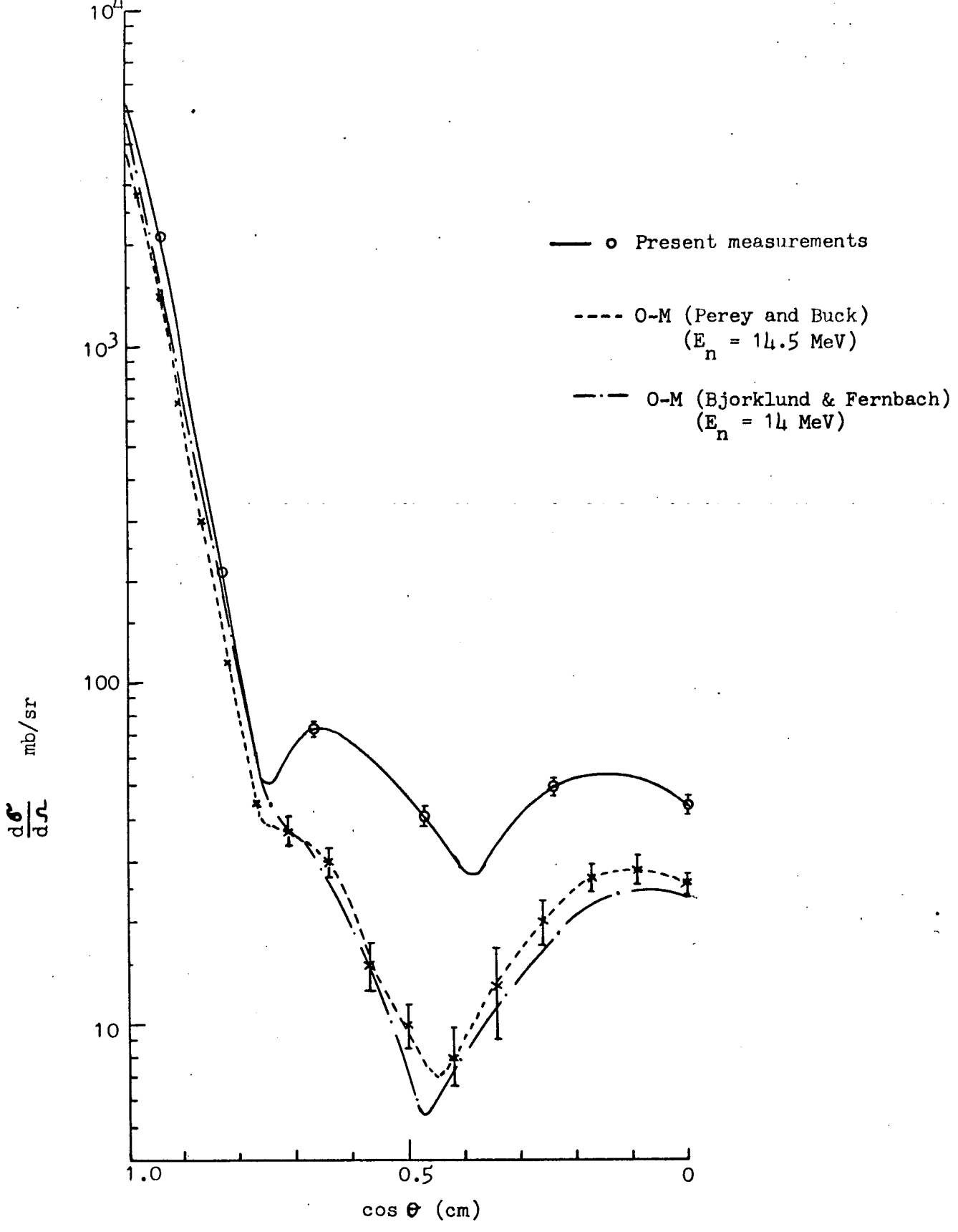

Fig. (62) Differential elastic scattering cross-section for copper

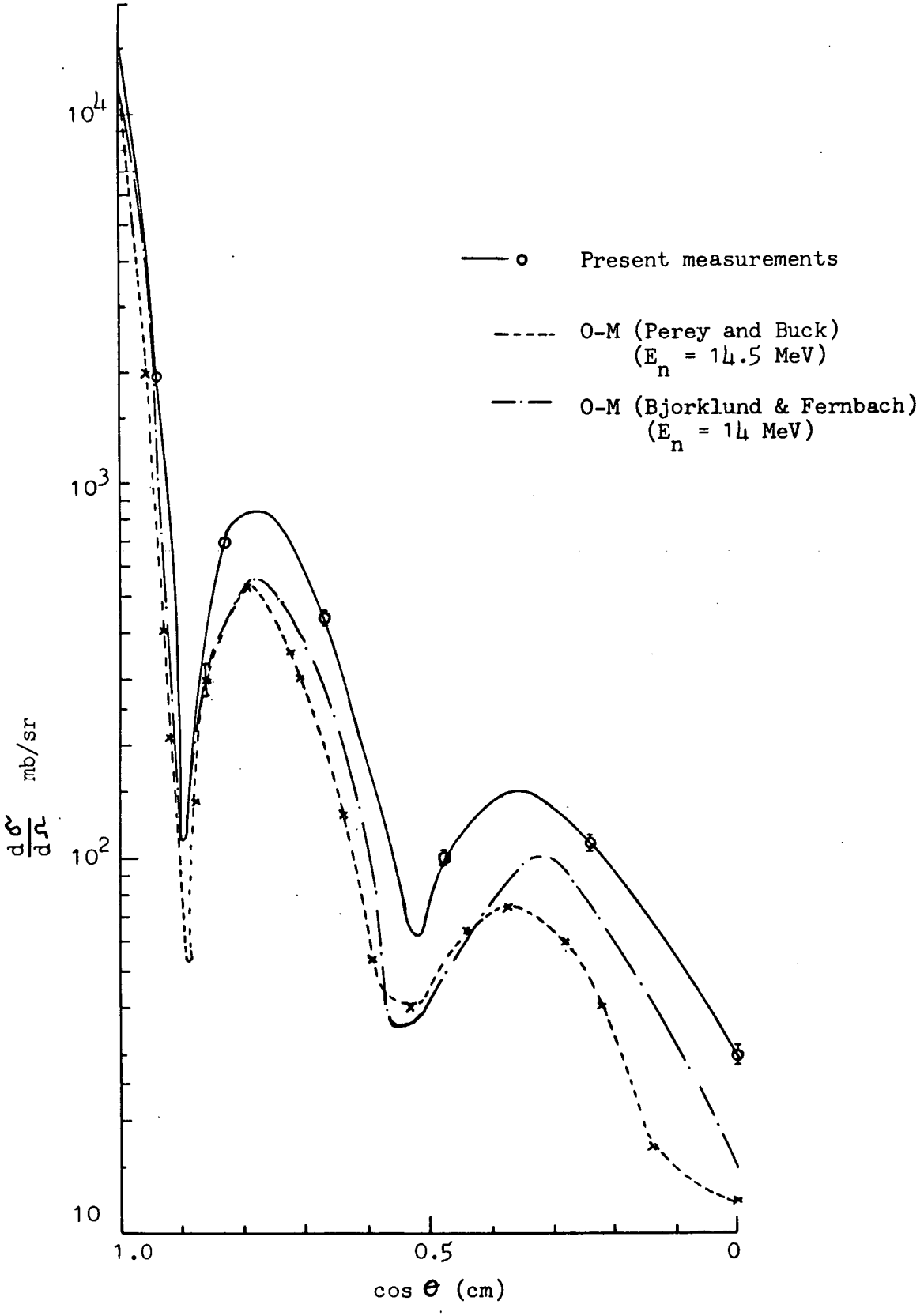

Fig. (63) Differential elastic scattering cross-section for lead

determination of n_d and n_m^1, while the results may be subject to systematic error from the determination of $\frac{\epsilon_m}{\epsilon_d}$, T, A_m, Ω_d, r_o, r_T and N. The statistical uncertainty (standard deviation) only is indicated in Table (5.6.1). The possible systematic error is estimated to be 3% based on $\frac{\epsilon_m}{\epsilon_d}$ ($\pm$ 0.7%); T ($\pm$ 0.5%); A_m ($\pm$ 2%); Ω_d ($\pm$ 1%); r_o ($\pm$ 0.4%); r_T ($\pm$ 0.4%) and N ($\pm$ 0.1%). The error bars in Figs. (62) and (63) take account of both the statistical and possible systematic uncertainties.

No 16 MeV data is available for comparison with the present results. The nearest available is for 14.5 MeV (ref. 12) and these are compared also in Figs. (62) and (63). No close agreement would be expected in view of the difference in energy although there is a general similarity.

5.7 Polarization of the T(d, n)He^4 Neutrons

The angular dependence of polarization produced by Cu and Pb is calculated from the measured asymmetries using the known value of polarization P_n of T(d, n)He^4 neutrons emitted at 75° reaction angle.

Hentschel[108] measured the polarization of the T(d, n)He^4 neutrons at 70°(Lab) for deuteron energies of 0.3 MeV - 1.83 MeV. A He gas scintillator as scatterer, plastic scintillators for scattered neutron detection and the time-of-flight technique were used for these measurements.

Christiansen et al[109] measured the angular distributions of the polarization of T(d, n)He^4 neutrons at 2.1 MeV and 2.9 MeV deuteron energy using scattering in He gas within parallel plate avalanche counters. The polarization had a maximum of -(0.169 $\pm$ 0.01) and -(0.192 $\pm$ 0.016) at 2.1 MeV and 2.9 MeV deuteron energy respectively at 75°(Lab) reaction angle.

Busse et al[110] measured the angular distributions of the polarization

of the neutrons from 3.35 MeV - 5.35 MeV deuteron energy using He gas as scatterer in parallel plate counters. Smith and Thornton[111] measured the polarization angular dependence of the T(d, n)He^4 neutrons from 1 MeV - 5 MeV deuteron energy using a liquid He analyser and the time-of-flight technique. The values observed by these authors are plotted in Fig. (64). The dotted curve through the points indicates a neutron polarization of -24% at 75° for deuteron energy of 2.8 MeV, with an uncertainty of about ± 2%. Table (5.7.1) gives the polarization values at 70°, 75° and 80° determined by the above mentioned authors.

5.8 The Experimental Results for Polarization

As discussed in Section 5.5 the true scattered neutrons for positions $\phi = 0$ and π of the cradle were determined for each detector and thus in turn numbers of 'right' and 'left' scattered neutrons were determined. The asymmetries were calculated using equation (4.11.2) in Section 4.11. The polarization analysing powers from the measured asymmetries were calculated with the value P_n = -24%. A check for any instrumental asymmetry by detecting neutrons scattered through 20° by Pb with the cradle at $\phi = \pi/2$ and $3\pi/2$ gave 0.0022 ± 0.017.

To correct the angular distributions of the polarization from Cu and Pb for finite geometry effects, flux attenuation and multiple scattering, the procedure was similar to that discussed in Section 4.13 using equation (4.13.2). The experimental values and the corrected values are given in Tables (5.8.1) and (5.8.2) for Cu and Pb respectively, and are plotted in Figs. (65) and (66).

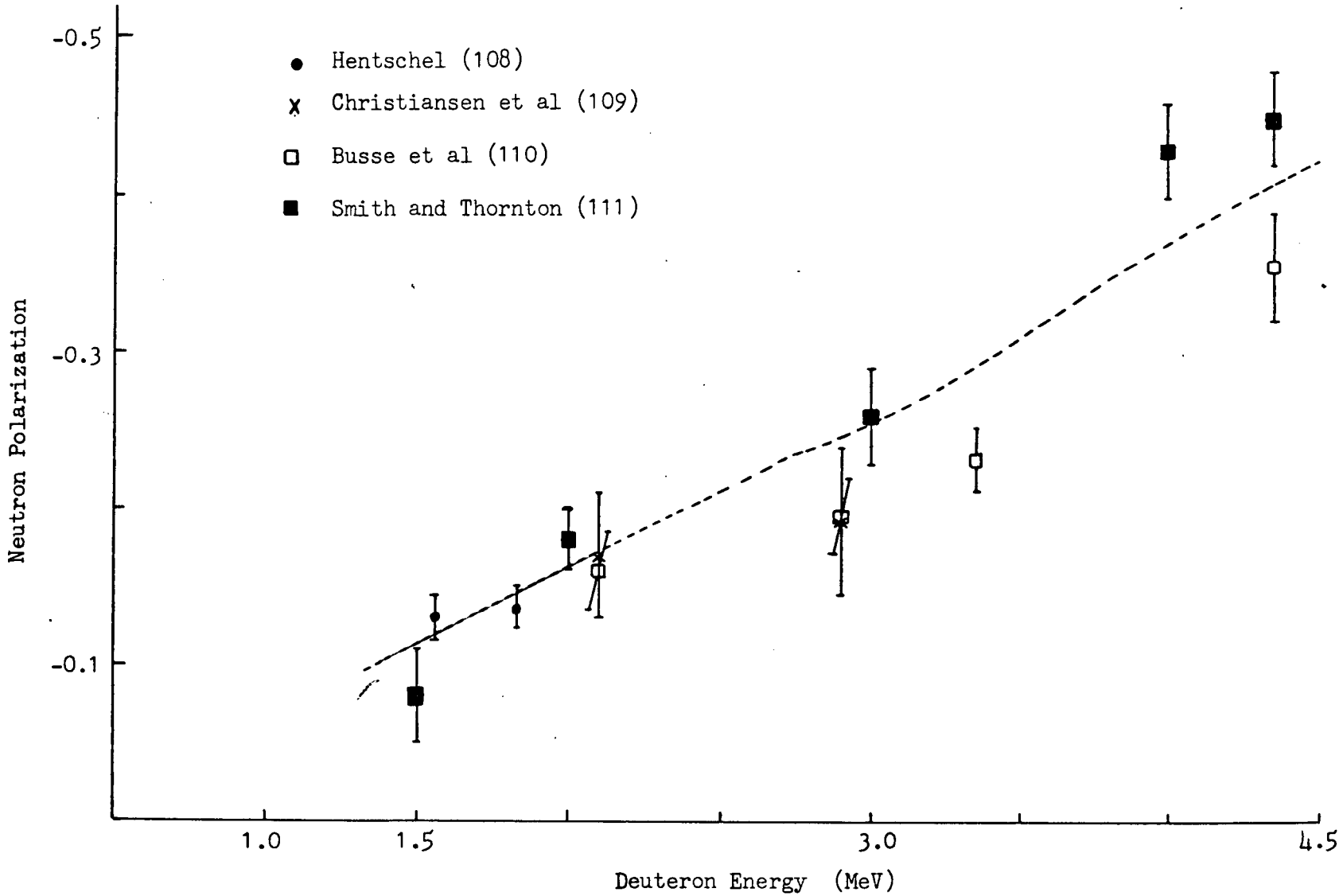

Fig. (64) Polarization of the H^3 (d,n)He^4 neutrons at $75^\circ \pm 5^\circ$

Table (5.7.1)

Polarization of $T(d, n)He^4$ Neutrons

Author	Deuteron Energy MeV	Angle (Degrees)	Polarization (P_n)
Hentschel[108]	1.56 ± 0.23	70	-0.131 ± 0.014
	1.83 ± 0.21	70	-0.135 ± 0.012
Christiansen et al (109)	2.1	75	-0.169 ± 0.04
	2.9	75	-0.192 ± 0.046
Busse et al (110)	2.1 ± 0.14	70	-0.16 ± 0.025
	2.9 ± 0.23	75	-0.197 ± 0.023
	3.35 ± 0.22	70	-0.233 ± 0.02
		80	-0.209 ± 0.014
	4.35 ± 0.19	70	-0.311 ± 0.019
		80	-0.367 ± 0.034
Smith and Thornton (111)	1.5	70	-0.08 ± 0.03
		80	-0.07 ± 0.03
	2	70	-0.18 ± 0.02
		80	-0.16 ± 0.02
	3	70	-0.26 ± 0.03
	4	80	-0.43 ± 0.03
	4.35	75	-0.45 ± 0.03
	5	80	-0.51 ± 0.03

Table 5.8.1

Polarization Produced in 16 MeV

Neutrons Elastically Scattered by Copper

Angle	Polarization (%)	
	Experimental	Corrected
20°	-39 ± 3	-39 ± 3
34°	-18 ± 8	-20 ± 9
48°	-25 ± 6	-28 ± 7
62°	-83 ± 15	-95 ± 18
76°	-21 ± 9	-24 ± 10
90°	-67 ± 19	-81 ± 23

Table 5.8.2

Polarization Produced in 16 MeV

Neutrons Elastically Scattered by Lead

Angle	Polarization (%)	
	Experimental	Corrected
20°	-71 ± 3	-72 ± 3
34°	-13 ± 4	-15 ± 5
48°	$+4 \pm 3$	$+4 \pm 4$
62°	$+41 \pm 7$	$+48 \pm 8$
76°	-24 ± 11	-28 ± 13
90°	-14 ± 13	-18 ± 17

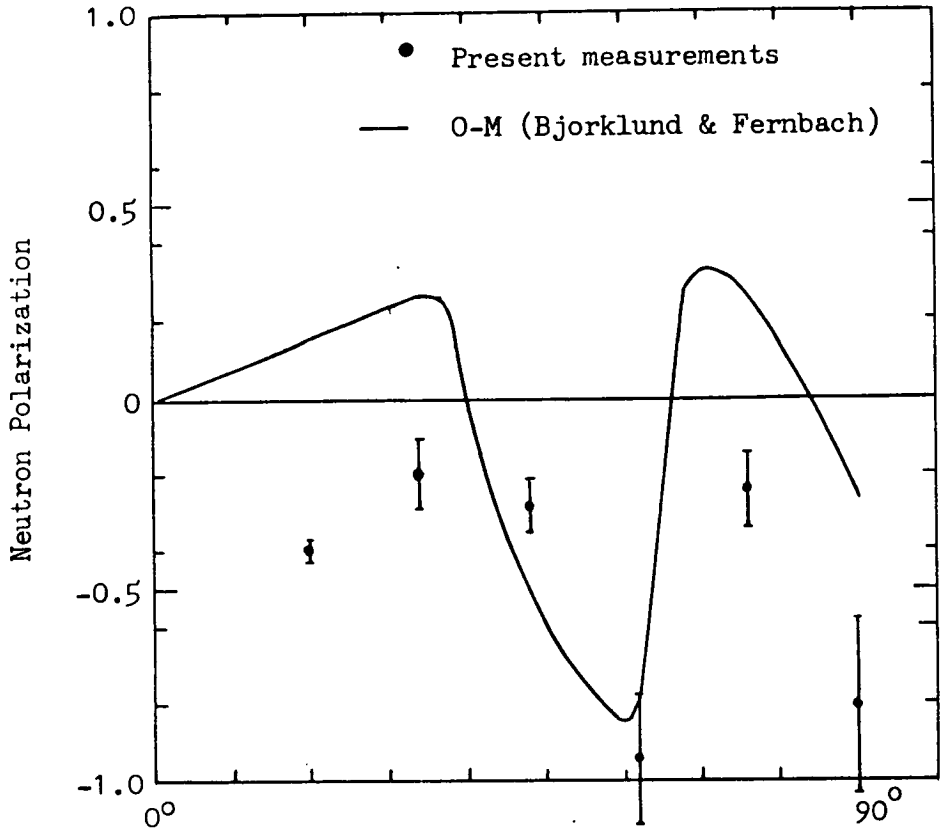

(Copper)

Fig. (65)

(a) and (b)

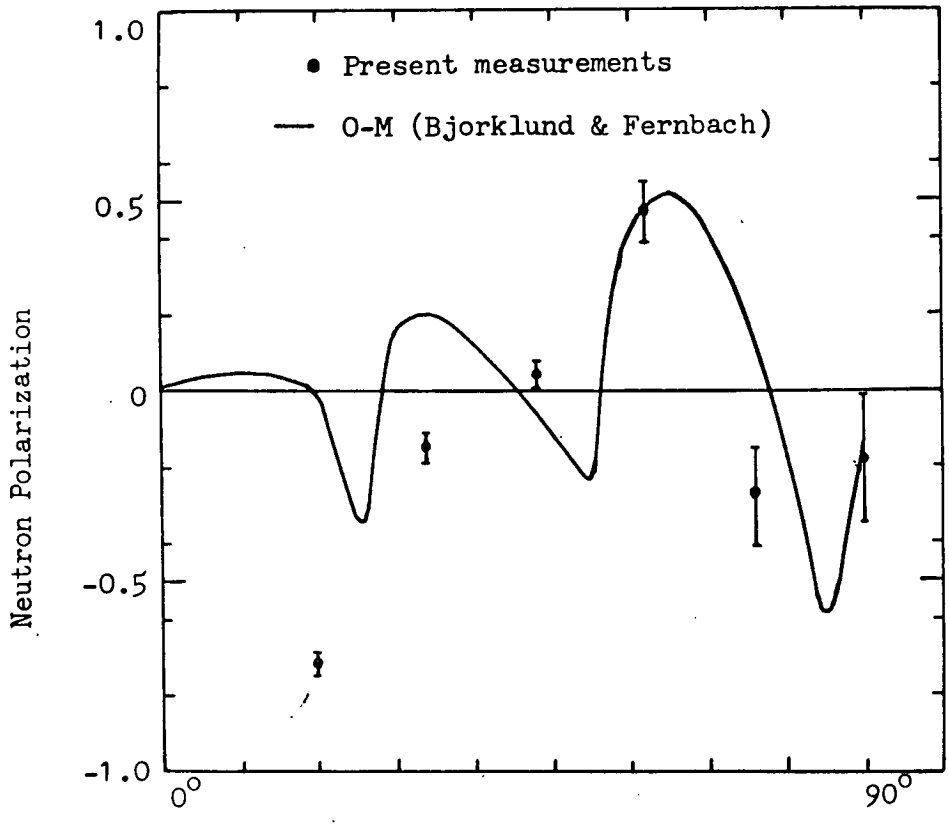

(Lead)

(Fig. (66)

(a) and (b)

The angular dependence of the polarization of neutrons elastically scattered by Cu and Pb.

5.9 Inelastic Scattering at 16 MeV

Although the time resolution of the time-of-flight system is 2 nsec, it is difficult to separate any inelastic scattering from elastic scattering due to limited flight path of 30 cm for the scattered neutrons.

At 16 MeV neutron energy a number of levels of Cu and Pb nuclei could be excited and so the inelastic contribution, depending upon the inelastic cross-section, could become important in the differential elastic cross-section minima. The contribution of inelastic scattering to the scattering can be taken into account from the published data about the angular distribution of inelastic scattering.

Coon et al[6] measured the angular distribution of inelastic scattering from Cu and Pb at 14.5 MeV for neutrons emitted due to inelastic scattering with energy greater than 9 MeV. For Cu the inelastic scattering cross-section is about 10 mb/sr at 40° and at 90° it is about 5 mb/sr. On extrapolation of the differential inelastic cross-section curve the inelastic scattering cross-section is about 12 mb/sr at 20°. For Pb on extrapolation at 20° it is about 30 mb/sr. At 40° and 90° the inelastic scattering cross-section for Pb is about 20 mb/sr and 8 mb/sr respectively.

Stelson et al[123] measured the differential cross-sections for the inelastic scattering of 14 MeV neutrons to low-lying collective states for a number of nuclei. The inelastic cross-sections associated with the 2.5 MeV and 4.1 MeV states of Pb at 20°, 40° and 90° are about 20 mb/sr, 12 mb/sr and 7 mb/sr respectively. The effects of any inelastic contribution will be discussed on taking the above mentioned inelastic cross-section values also for 16 MeV neutrons.

The values of differential inelastic cross-section for Pb at 14 MeV by Stelson et al[123] are lower than the values determined by Coon et al[6]. However the inelastic scattering cross-section for Pb is estimated to be about 7 mb/sr at 90^{o} and 9 mb/sr at 62^{o} (the minimum values of the elastic cross-sections). Due to such an inelastic contribution the polarization value would have been -23% instead of -18 $\pm$ 17% at 90^{o} and at 62^{o} the polarization value would have been 52% instead of 48 $\pm$ 8%.

Some normalisation was done to the Cu data on inelastic scattering by Coon et al[6] from comparison of the Pb data of Coon et al[6] and those of Stelson et al[123]. The inelastic cross-section at 62^{o} (minimum of the elastic scattering cross-section value) is estimated to be about 4 mb/sr. The polarization in this case at this angle would become -106% instead of -95 $\pm$ 18% and at 90^{o} the polarization value would become -89% instead of -81 $\pm$ 23%.

From the above discussion it follows that the contribution due to inelastic scattering to the elastic scattering will not change the overall shape of either the differential elastic scattering cross-section curve or the angular dependence of polarization. The inelastic contribution to the measured scattering may therefore be considered safely as negligible in the present case of Cu and Pb at 16 MeV neutron energy.

CHAPTER VI.

CHAPTER VI

Results and Discussion

6.1 Introduction

The optical model has met with considerable success in fitting experimental differential elastic scattering cross-sections[11-17]. For the fitting of experimental data on the angular dependence of polarization the optical model calculations are not so successful as has already been discussed in the first chapter. The experimental data both at 2.9 MeV and 16.1 MeV neutron energy presented in the previous chapters are compared below with the available optical model calculations.

6.2 Optical Model Potentials

As described in Section 1.2 of the first chapter, a central complex potential can be represented by,

$$V(r) = - Uf(r) - iWg(r) \qquad ..(1.2.1)$$

where U and W are the real and imaginary amplitudes of the potential respectively and f(r) and g(r) are form factors describing the radial variation of the potentials.

To describe the polarization of neutrons when elastically scattered by nuclei, a further refinement of the potential due to Bjorklund and Fernbach[11] has been the inclusion of a spin-orbit term.. Different optical model potential parameters were used by different authors in attempts to fit the experimental angular dependence of polarization and differential elastic scattering cross-section. The optical model potential is given by:

$$V = -V(r) - iW(r) - V_{so}(r)\,\bar{\sigma}.\bar{L} \qquad ..(6.2.1)$$

and can also be written as,

$$V = -V_o f(r,a,r_o) - iWg(r,b,r_o) + V_{so}\left[\frac{\hbar}{m_\pi c}\right]^2 \frac{1}{r}\frac{d}{dr} f(r,a,r_o)\,\bar{\sigma}.\bar{L} \qquad ..(6.2.2)$$

where V_o, W and V_{so} are the real, imaginary and spin-orbit potential depths respectively. $\bar{L}$ and $\bar{\sigma}$ are the orbital angular momentum and the Pauli-spin operator of the incoming neutron and $\bar{\sigma}.\bar{L}$ represents the dependence of the interaction on the relative orientation of the neutron spin and the neutron orbital momentum about the nucleus. m_π is the mass of π meson; $f(r,a,r_o)$, $g(r,b,r_o)$ and $f(r,a,r_o)$ in order of equation (6.2.2) are the form factors for real, imaginary and spin-orbit potential depths respectively.

The real part $V_o f(r,a,r_o)$ has a Saxon-Woods form factor and is given by:

$$f(r,a,r_o) = \left[1 + \exp\left(\frac{r - R}{a}\right)\right]^{-1} \qquad ..(6.2.3)$$

The radius of the real potential is defined by $R = r_o A^{\frac{1}{3}}$ where A is the mass number and a is the diffuseness parameter for the real potential depth. The real part accounts for the shape elastic scattering of the neutrons. The imaginary part $Wg(r,b,r_o)$ accounts for all processes different from the direct or shape elastic scattering[40]. Details about the optical model are given by Hodgson[14]. The above equation (6.2.2) is the general optical model potential used by different authors to calculate the differential elastic cross-sections and the angular dependence of polarization. The optical model parameters used by different authors will now be discussed.

Bjorklund and Fernbach[11] used the optical model potential given by

equation (6.2.2) with $g(r,b,r_o)$ as:

$$g(r,b,r_o) = \exp\left[-(r - R)^2/b^2\right] \qquad ..(6.2.4)$$

The authors obtained a satisfactory agreement between the calculated and observed differential elastic scattering cross-section data at 4.1, 7 and 14 MeV neutron energies. They had no polarization data available for comparison.

Perey and Buck[12] have succeeded in reproducing angular dependence of neutron elastic scattering cross-sections fairly well over an energy range from 1-24 MeV for elements from Al to Pb with a single set of parameters. The equivalent potential[17] that was utilised has the form given by equation (6.2.2). The value of $g(r,b,r_o)$ is the Saxon-Woods derivative type giving a surface absorption term;

$$g(r,b,r_o) = 4 \exp\left(\frac{r - R}{b}\right)\left[1 + \exp\left(\frac{r - R}{b}\right)\right]^{-2} \qquad ..(6.2.5)$$

The calculations were not so successful in comparison with the experimental polarization values for neutron energies of 0.38 MeV to 2.1 MeV.

The optical model potential used by Rosen[17] for the analyses of the polarization data and the differential elastic scattering cross-section is given by equation (6.2.2); the imaginary part of the central potential has the form factor,

$$g(r,b,r_o) = -4b\frac{d}{dr}\left[1 + \exp\left(\frac{r - R}{b}\right)\right]^{-1} \qquad ..(6.2.6)$$

A reasonable agreement has been obtained between the calculated and the experimental angular dependence of elastic scattering cross-section for neutron energies of 0.2 MeV to 24 MeV for elements from Al to Pb. Calculated

values were also compared with the angular dependence of polarization. At 24 MeV neutron energy (E_n) the optical model calculations give a similar distribution for Pb as the experimental one[112], but the angular dependence of polarization for the other nuclei does not fit the experimental data.

Becchetti and Greenless[16] calculated differential scattering cross-sections for elements from Fe to Bi for E_n = 1 - 24 MeV. Their optical model potential is given by;

$$V = -V_o\, f(r,a,r_o) + iW4b \frac{d}{dr} f(r,b,r_i) - iW^1\, f(r,b,r_i) + V_{so} \left(\frac{\hbar}{m_\pi c}\right)^2 \frac{1}{r}\frac{d}{dr} f(r,a,r_s)\, \bar{\sigma}.\bar{L} \qquad ..(6.2.7)$$

Good agreement was obtained for differential elastic scattering cross-sections. Good agreement was obtained also for the angular dependence of polarization data at E_n = 24 MeV for the elements Fe, Sn, Pb and Bi, but only a qualitative similarity at E_n = 4 MeV for Ni, Se and Sn.

Holmqvist[104] used the optical model potential given by equation (6.2.2) with the difference that the imaginary part of the central potential has the form factor given by;

$$g(r,b,r_w) = 4 \exp\left(\frac{r - R_w}{b}\right)\left[1 + \exp\left(\frac{r - R_w}{b}\right)\right]^{-2} \qquad ..(6.2.8)$$

and $R_w = r_{ow} A^{\frac{1}{3}}$.

The differential elastic scattering cross-sections calculated by Holmqvist[104] fitted the experimental data for elements from Al to Bi at E_n = 1.5 - 8.1 MeV. Optimum values of the real and imaginary potential depths, and real potential diffuseness parameter were calculated independently for each element and energy. Very good agreement was obtained between

the experimental and the calculated differential elastic scattering cross-sections.

The values of the optical model parameters used by the above authors are given in Table (6.2.1). In the table the parameters used by Becker et al[103] and those used by Gorlov et al[35] are also given; as their calculations are also compared with the present experimental data. The calculations of Becker et al[103], and Holmqvist[104] were only for the differential elastic scattering cross-sections.

6.3 The Optical Model Fitting at 2.9 MeV

The experimental elastic scattering cross-sections will not (depending upon the neutron energy and the nucleus) correspond to the calculated shape elastic scattering from the optical model due to the presence of compound elastic scattering. This unpolarized contribution from the compound elastic scattering would make the polarization value smaller than calculated from the optical model. Corrections for such an effect can be made from the formalism of Hauser and Feshbach[18] provided the properties of the excited states of the target nucleus are known but generally these are not known completely. However the magnitude of the total compound elastic scattering cross-section can also be estimated from the following equation;

$$\sigma_{ce} = \sigma_{a} - \sigma_{ne} \qquad ..(6.3.1)$$

where σ_{ne} is the experimental non-elastic cross-section and σ_{a} is the absorption cross-section which can be calculated from optical model data[104].

The optical model calculated angular dependence of polarization is compared with the experimental results in Figs. (54-58) for Fe, Cu, I, Hg and

Table 6.2.1

Parameters of Optical Model Potential used to compare the experimental data on neutron scattering

Authors	V(r)	W(r)	$V_{so}(r)$	Potential used
1. Bjorklund and Fernbach[11] (1958)	V_o = 44 MeV r_o=1.25(fm) a=0.65(fm)	W = 11 MeV r_o=1.25(fm) b=0.98(fm)	V_{so}=8.3MeV r_o=1.25(fm) a=0.65(fm)	Eq.(6.2.2) E_n = 14 MeV
2. Perey and Buck[12] (1962)	V_o=(48-0.29E_n)MeV r_o=1.27(fm) a = 0.66(fm)	W = 9.6MeV r_o=1.27(fm) b = 0.47(fm)	V_{so}=7.2MeV r_o=1.27(fm) a=0.66(fm)	Equivalent Potential[17] Eqs.(6.2.2) and (6.2.5)
	Equivalent Parameters were taken from Rosen[17]			
3. Rosen[17] (1966)	V_o=(49.3-0.33E_n) MeV r_o= 1.25(fm) a = 0.65(fm)	W = 5.75MeV r_o = 1.25(fm) b = 0.70(fm)	V_{so}=5.5MeV r_o=1.25(fm) a=0.65(fm)	Eqs.(6.2.2) and (6.2.6) E_n=0.2-24 MeV
4. Becchetti and Greenless[16] (1969)	V_o=(56.3-0.32E_n-24(N-Z)/A)MeV r_o = 1.17(fm) a = 0.75(fm)	W=(13-0.25E_n-12(N-Z)/A)MeV or zero whichever is greater r_i = 1.26(fm) b = 0.58(fm) W^1=(0.22E_n-1.56)MeV or zero whichever is greater	V_{so}=6.2 MeV r_s=1.01(fm) a= 0.75(fm)	Eq. (6.2.7) E_n=1-24 MeV

../cont.

Table 6.2.1

(continued)

Authors	V(r)	W(r)	$V_{so}(r)$	Potential used
5. Becker et al [103] (1966)	V_o=48.0 MeV r_o=1.25 (fm) a = 0.65 (fm)	W = 5.5 MeV r_o=1.25 (fm) b = 0.46 (fm)	V_{so}=5.2MeV r_o=1.25(fm) a=0.65(fm)	From ref.(40) E_n = 3.2 MeV
6. Gorlov et al [35] (1967)	$V_o=50(1-\frac{N-Z}{3A})$MeV r_o = 1.25 (fm) a = 0.65 (fm)	W = 8.5 MeV r_o = 1.25 (fm) b = 0.98 (fm)	V_{so}=0.17MeV r_o=1.25(fm) a=0.65(fm)	Eqs.(6.2.2) and (6.2.4) E_n = 4 MeV
7. Holmqvist (104) (1968)	(Fe) (Cu) V_o=51.1; 48.6MeV r_o=1.21; 1.24(fm) a=0.61; 0.67(fm)	(Fe) (Cu) W=10.8; 9.73MeV r_{ow}=1.15; 1.20(fm) b = 0.48 (fm)	(Fe) (Cu) V_{so}= 8MeV r_o=1.21; 1.24 (fm) a=0.61; 0.67 (fm)	Eqs. (6.2.2) and (6.2.8) E_n = 3 MeV

Pb respectively. The experimental differential elastic scattering cross-sections are also compared with the calculated angular distributions in Figs. (67-71) for Fe, Cu, I, Hg and Pb respectively.

With parameters given by Rosen[17]; Ellgehausen et al[37] calculated the angular dependence of polarization as well as the differential elastic scattering cross-section at 3.2 MeV neutron energy for Fe and Cu. The calculated values of polarization for Fe and Cu are shown in Figs. (54b) and (55b) respectively.

A good fit to the experimental data is obtained for Fe. The positive polarization indicated by the optical model calculations is in agreement with the new experimental value at 160^{o}.

The calculated values (parameters of Rosen[17]) are compared in Fig. (67) with the present experimental data on differential elastic scattering cross-section for Fe. The fitting is not good. A similar sort of behaviour is also seen in the comparison with the experimental data of Becker et al[103] done by Ellgehausen et al[37]. This suggests that the optical model fitting with the parameters of Rosen[17] is only good for the polarization data but not for the differential cross-section data. The optical model calculations by Holmqvist[104] with parameters given in Table (6.2.1) for the differential cross-section are also shown in Fig. (67). The optical model fitting to the experimental data is good. Unfortunately no polarization calculations were made by Holmqvist[104].

For Cu (Fig. 55b) at forward angle of 30^{o} the experimental polarization value is more negative than the calculated values. A similar effect is also observed in the results of Ellgehausen et al[37] and those of Zijp and Jonker[39].

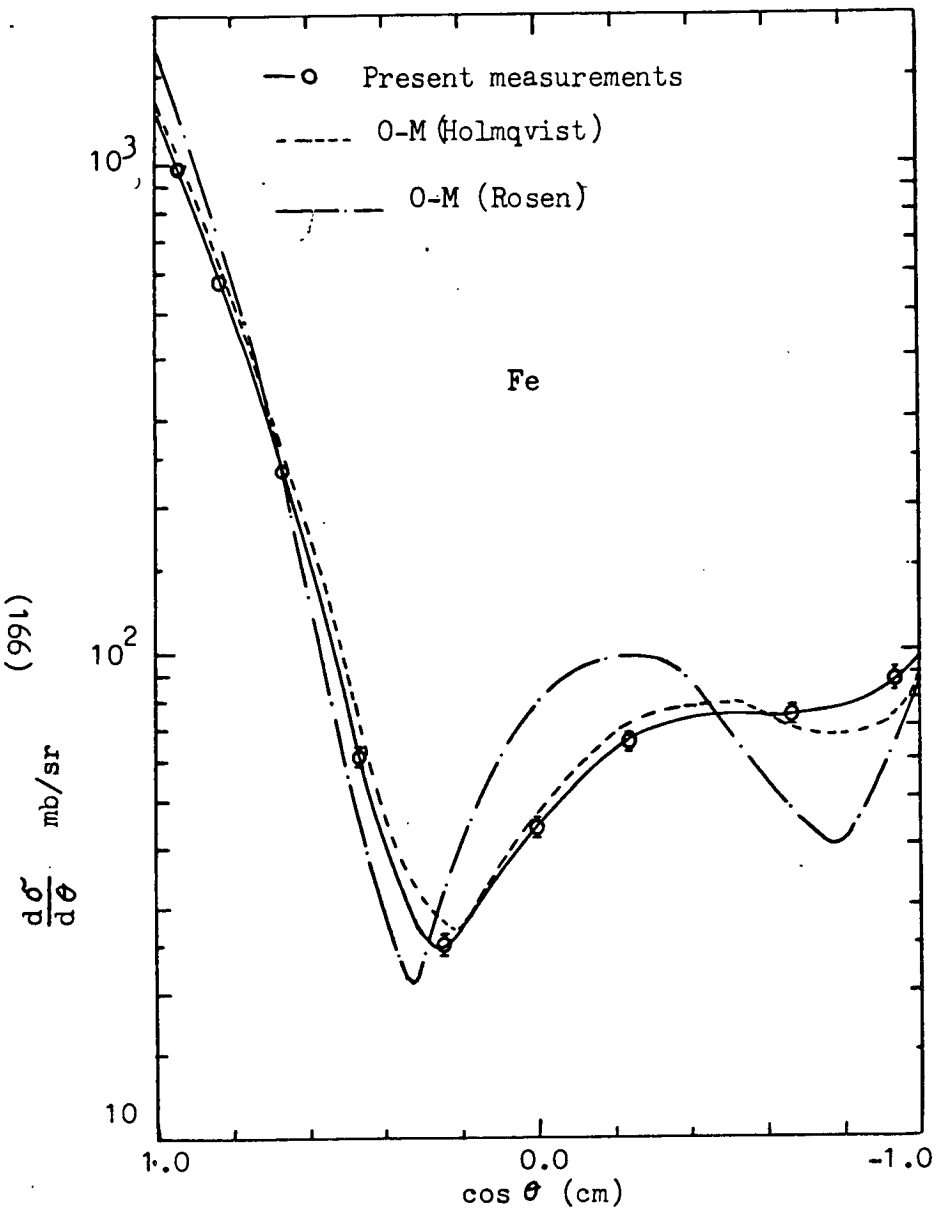

Fig. (67)

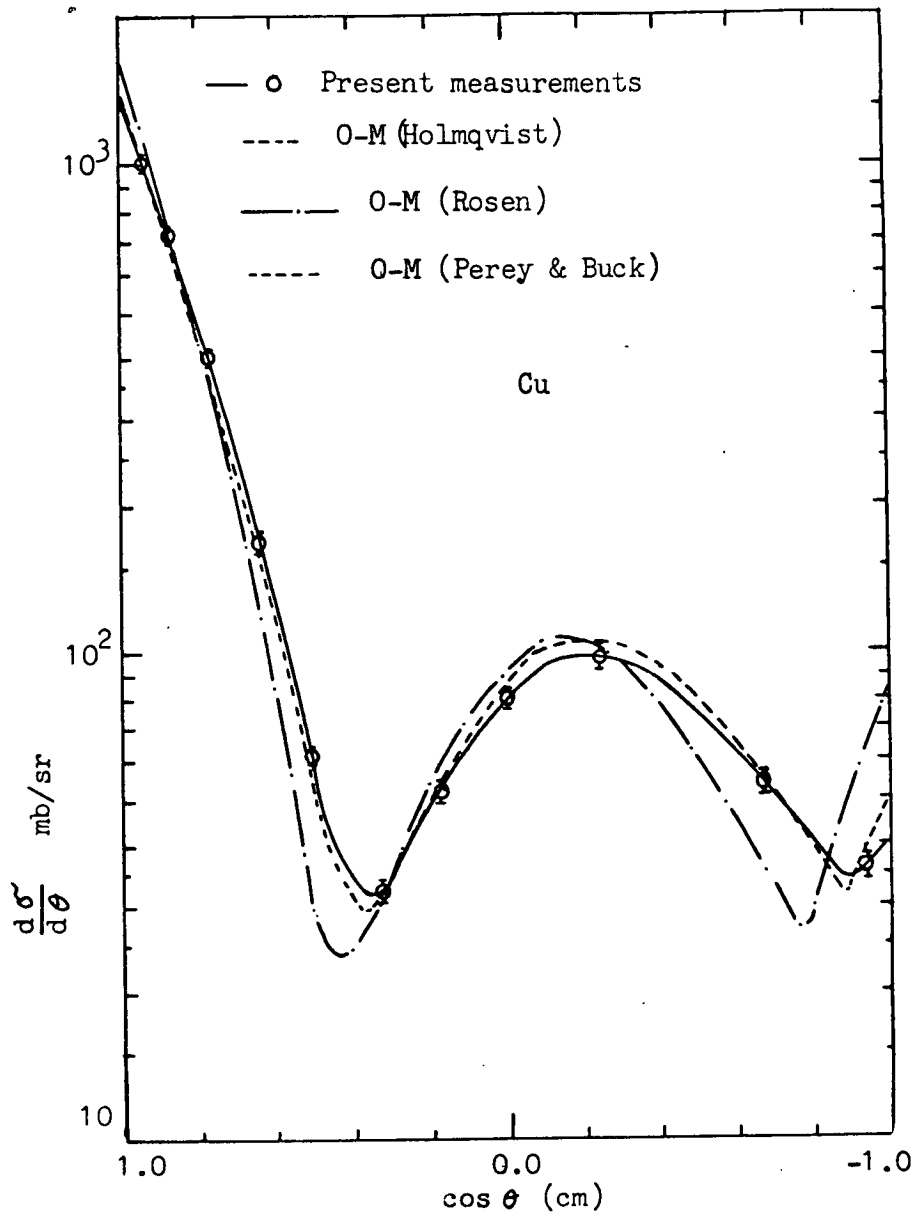

Fig. (68)

Optical Model Fit to the differential elastic scattering cross-section for Fe and Cu

At 160° the experimental polarization value confirms, within the statistical accuracy, the positive swing of the calculated curve. Thus a good fit is also obtained for Cu.

The experimental differential elastic cross-section for Cu is compared in Fig. (68) with the optical model calculated values. With the parameters of Rosen[17], the fitting is reasonable although the calculated minima appear at smaller angles than the experimental ones. In Fig. (68) the optical model calculations by Holmqvist[104] are also shown. The dotted line in the same figure also shows the optical model calculations by Perey[124]. The fitting due to both Holmqvist[104]; and Perey[124] is good although no calculated polarization values are available. The comparison suggests again that the parameters of Rosen[17] provide a good fit to the polarization data and a reasonable fit to the cross-section data for Cu.

For I^{127} there are no previous measurements on polarization around 3 MeV neutron energy. Zijp and Jonker[39] measured the polarizations for the neighbouring element $Te^{126,128,130}$ at only four scattering angles of 30°, 45°, 60° and 75° at 3.2 MeV neutron energy and compared the results with optical model calculations using the parameters of Rosen[17]. The four experimental points on Te and the calculated angular dependence of polarization are shown in Fig. (56b). In the same figure the dotted line represents the calculations by Zijp and Jonker[39] using the parameters of Becchetti and Greenless.[16]. The optical model curve based on the Rosen[17] parameters has a similar shape to the experimental data although the angles of maxima and minima differ, perhaps due to difference in mass numbers of I and Te.

The polarization angular dependence for $Ba^{137,138}$ at 3.2 MeV neutron

energy, measured by Zijp and Jonker[39] and the calculated values, are shown in Fig. (56c) along with the present measurements on I. The solid curve is due to the parameters of Rosen[17] and the dotted curve is due to the parameters of Becchetti and Greenless[16]. Again there is a general similarity to the I data. In Fig. (56c) the three circles at 50^{o}, 90^{o} and 125^{o} represent the calculations by Perey and Buck[12] for an element with A = 127 and neutron energy of 2.1 MeV. There is no similarity to the experimental values at 90^{o} and 125^{o}.

In Fig. (56d) the experimental angular dependence of polarization for I at 4 MeV neutron energy by Gorlov et al[35] is shown for comparison with the present measurements. Most of the values look to be in agreement as to sign. The solid curve represents in Fig. (56d) the calculations by Gorlov et al[35].

No optical model calculations for differential elastic cross-section for I are yet available around 3 MeV neutron energy. The calculations done by Zijp[40] with the parameters of Gorlov et al[35] for Te at 3.2 MeV neutron energy are shown in Fig. (69) along with the present measurements on I. The fit to the experimental values is good as far as the shape of the curve is concerned although the calculated values are slightly smaller in magnitude than the experimental values.

For Hg the present measurements are new ones. The calculations on angular dependence of polarization by Zijp and Jonker[39] for the neighbouring element Tl are taken for comparison as shown in Fig. (57b). The solid line curve is due to the parameters of Rosen[17] and the dotted line curve is due to the parameters of Becchetti and Greenless[16]. The difference between the

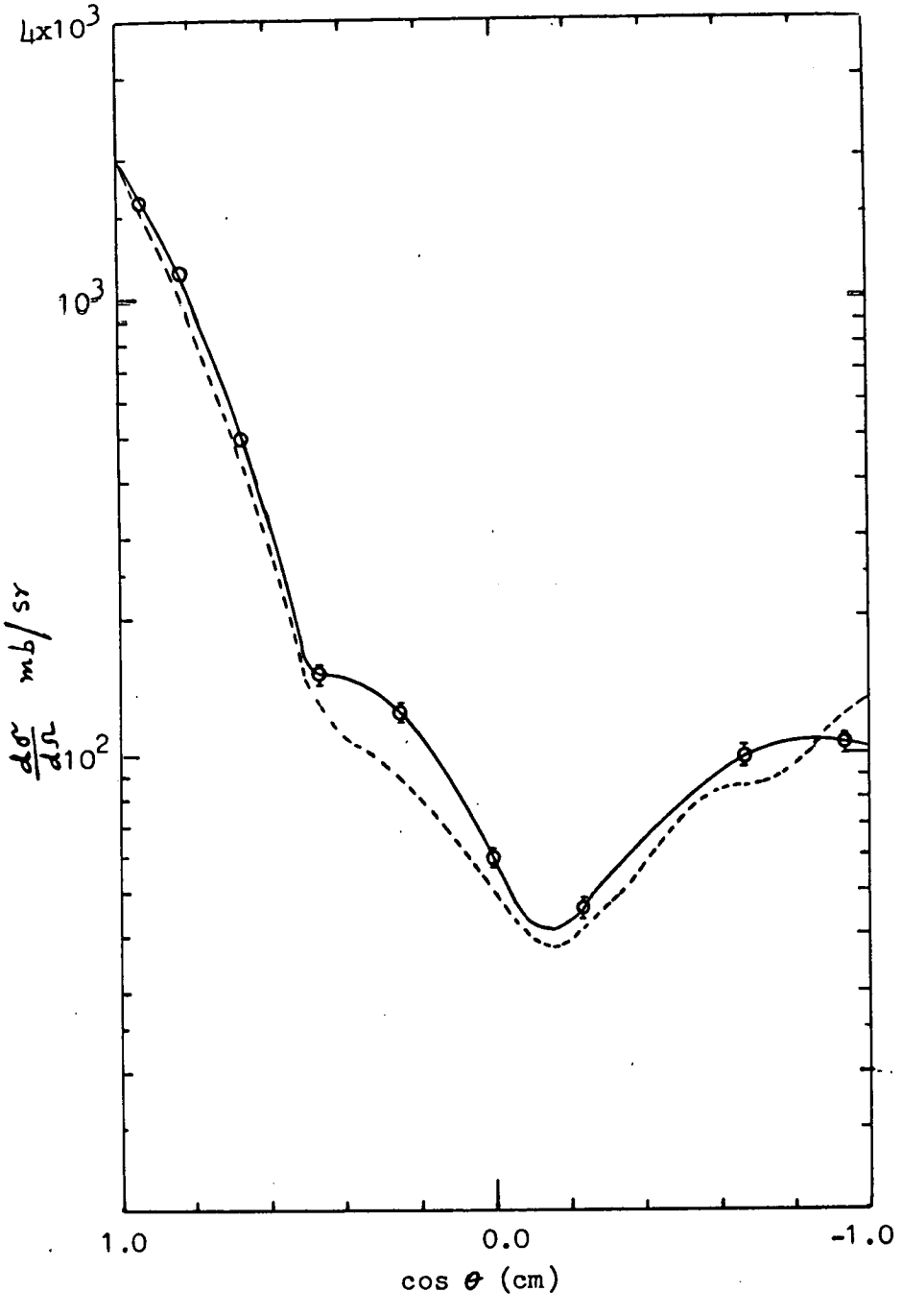

Fig. (69) Optical Model Fit to the differential elastic scattering cross-section for iodine

optical model curves and the experimental angular dependence of polarization is considerable and may be due to the difference in mass numbers of Hg and $Tl^{203,205}$. In any case the experimental values for Hg and Tl differ at forward angles.

The optical model calculations for the differential elastic cross-section by Becker et al[103] are shown in Fig. (70) for comparison with the experimental data on Hg. At angles greater than 130° the optical model calculated curve is extrapolated. The agreement is reasonable with the difference that the minima and the maximum on the calculated curve are at smaller angles compared to the experimental curve. However the present experimental data are in agreement with the experimental values determined by Becker et al[103].

For Pb the calçulated values by Zijp and Jonker[39] are shown for comparison with the present measurements on the angular dependence of polarization in Fig. (58b). The dotted lines indicate the calculations due to the parameters of Rosen[17] and the solid curve indicates calculations due to different parameters of Zijp and Jonker[39]. For Pb there is an experimental difference in sign of polarization between the present measurements and the measurements of Zijp and Jonker around 30° as shown in Fig. (58b). The difference between the optical model fit by Zijp and Jonker[39] and the present experimental data is not surprising as the calculations were based on experimental values at only four scattering angles.

The optical model calculations for Pb by Zijp[40] (parameters of Gorlov et al[35]) are compared with the experimental differential elastic cross-section in Fig. (71). The measurements are significantly higher than the calculations.

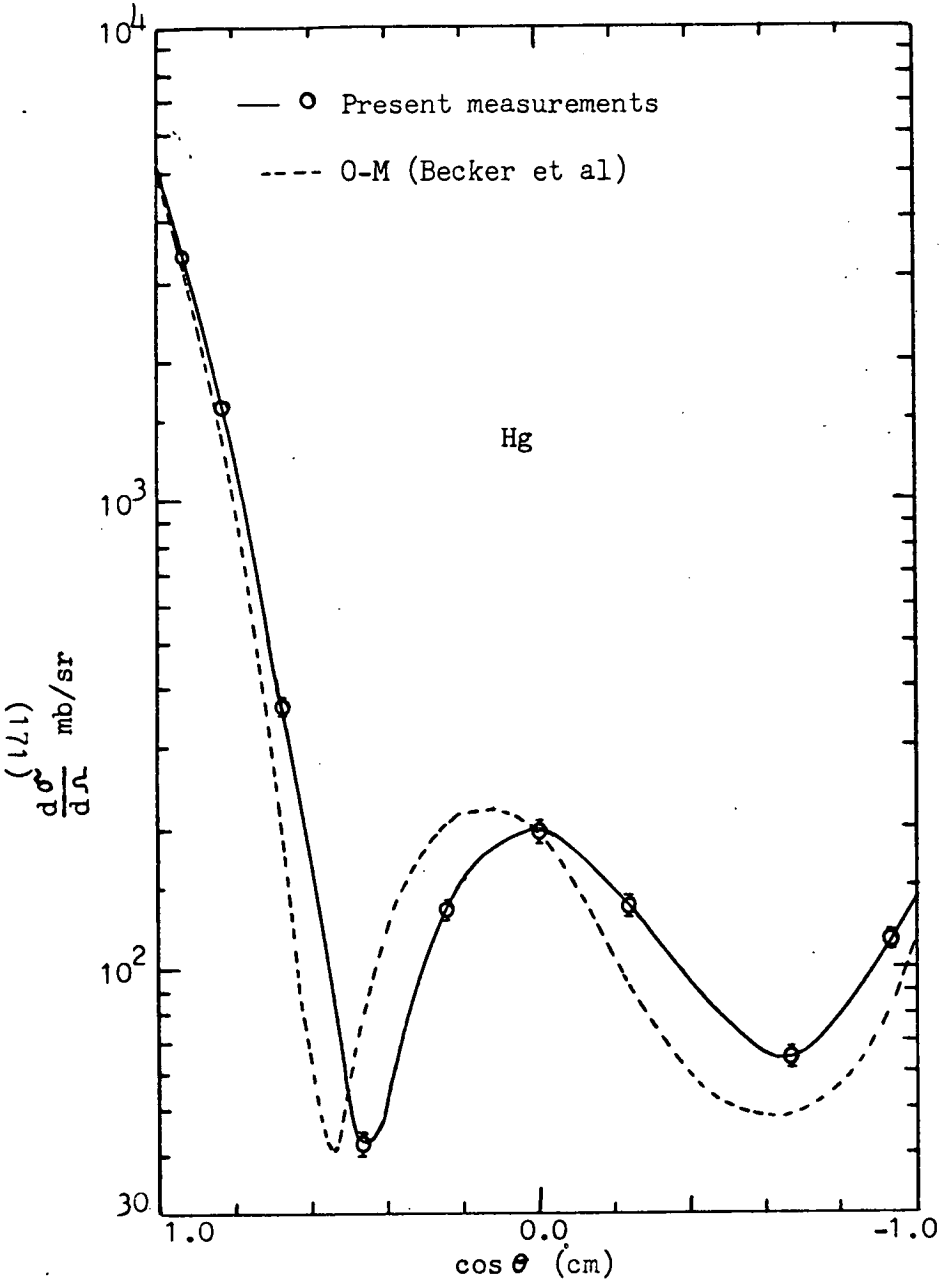

Fig. (70)

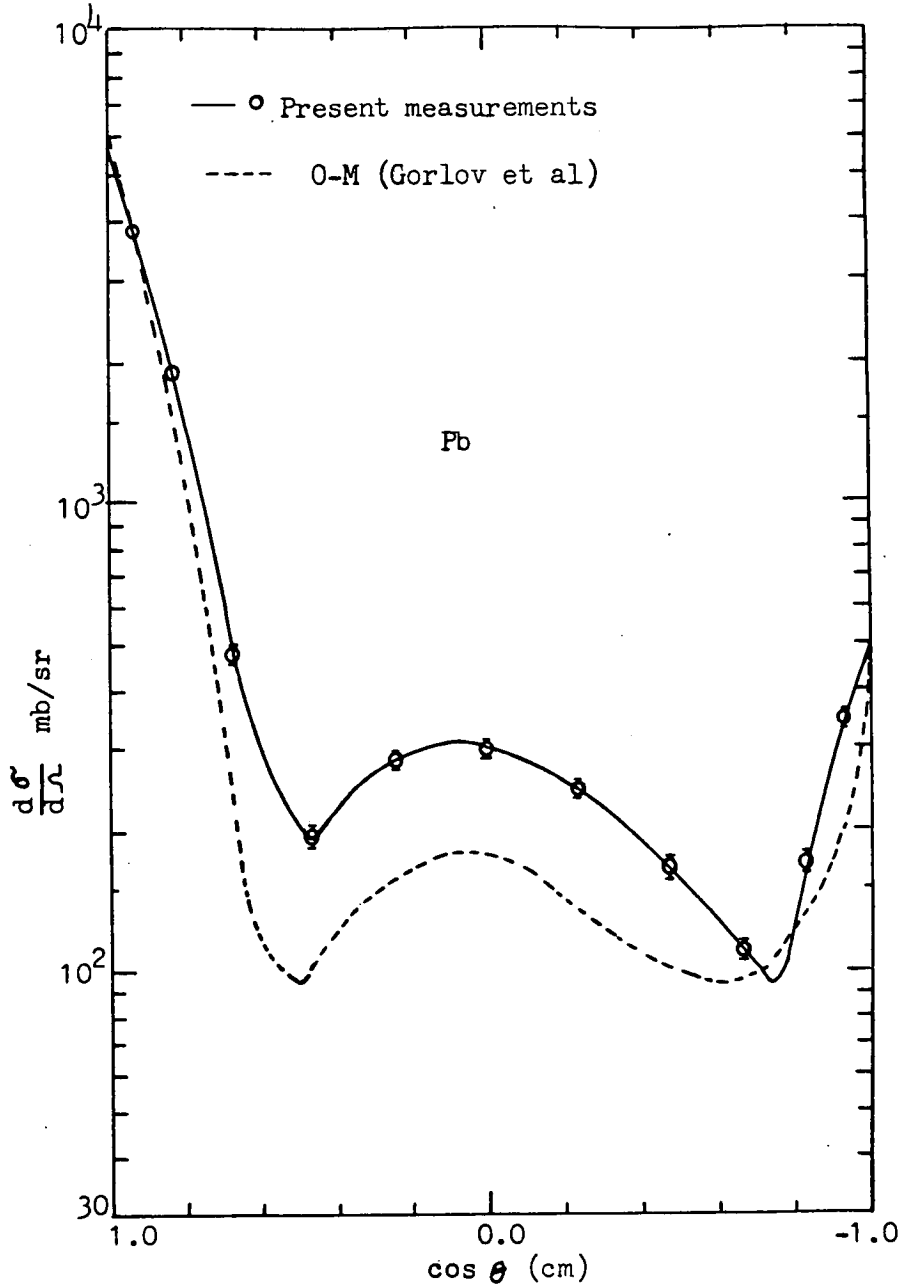

(Fig. (71)

Optical Model Fit to the differential elastic scattering cross-section for Hg and Pb

The present measurements are also compared with the previous work of Becker et al[103] in Fig. (52) and the agreement with the results of Becker et al[103] is better than with the optical model predictions. At angles greater than 130° the peaking of the optical model cross-section curve is however confirmed by the measurements.

In the present measurements with the heavier nuclei the polarization is found to be positive whereas for medium weight nuclei the polarization is negative at the forward angle of 20°.

As indicated by Zijp and Jonker[39] the success of the optical model potential with the parameters of Rosen[17] in describing the angular dependence of polarization around mass number A = 60 is good; but these parameters are not so successful in describing the differential elastic scattering cross-sections. The same is confirmed in the present work, as the polarization data for Fe and Cu are nicely described by the parameters of Rosen[17] but these parameters are not so successful in fitting the differential elastic cross-section for Fe and Cu, whereas the parameters used by Holmqvist[104] fitted the differential elastic cross-section data very nicely both for Fe and Cu. Also Perey's[124] calculations fitted nicely to the differential elastic cross-section for Cu. Similarly Zijp and Jonker[39] found that the elastic scattering cross-sections are best described by the potentials of Gorlov et al[35], and Perey and Buck[12]. The available optical model calculations have little success in fitting polarization data for the heavier nuclei.

6.4 The Optical Model Comparison at 16 MeV

The optical model calculations by Perey and Buck[12], and Bjorklund and

Fernbach[11] were used to compare with the differential elastic scattering cross-section measurements for Cu and Pb at 16 MeV neutron energy. These calculations were only for 14.5 MeV and 14 MeV neutron energy, not very far from 16 MeV. To compare the angular dependence of polarization for Cu and Pb at 16 MeV neutron energy the optical model calculations at 14 MeV neutron energy by Bjorklund and Fernbach[11] were used.

For Cu the optical model calculations due both to Perey and Buck[12] and to Bjorklund and Fernbach[11] are shown in Fig. (62) to compare with the differential elastic cross-section measurements. No close agreement would be expected in view of the difference in neutron energy, although there is a general similarity.

The angular dependence of polarization for Cu is compared with the optical model calculations in Fig. (65b). The calculations of Bjorklund and Fernbach[11] show large polarization values. Large values are also found experimentally although the distributions do not agree in detail, possibly due to the difference in energy.

For Pb the optical model calculations due both to Perey and Buck[12] and to Bjorklund and Fernbach[11] are shown in Fig. (63) to compare with the differential elastic cross-section measurements. The calculations due to Bjorklund and Fernbach[11] show values somewhat nearer to the experimental values than do the calculations by Perey and Buck[12]. There is a general similarity to the experimental data in both the calculations.

The optical model calculated angular dependence of polarization for Pb due to Bjorklund and Fernbach[11] is compared with the experimental data in Fig. (66b). The calculations again show large polarization values at

14 MeV neutron energy. There is good agreement with the calculated values at 90^{o} and 60^{o} in sign as well as magnitude.

At 16 MeV the nuclei Cu and Pb show large polarization values which is in qualitative confirmation of the optical model calculations. In all the above comparisons of 16 MeV experimental data and 14 MeV calculations no close agreement would be expected in view of the difference in neutron energy, although a general similarity is found.

6.5 Conclusion

The associated particle time-of-flight system and the polarimeter designed and developed for the differential elastic cross-section and the angular dependence of polarization measurements has worked very well. These systems could with advantage be used for further measurements on other nuclei both at 2.9 MeV and 16 MeV neutron energies for a more complate comparison with optical model calculations. The large body of new experimental data which would result could then justify new optical model parameter searches.

APPENDIX A

APPENDIX A

The electronics circuits built for the associated particle time-of-flight system are described briefly along with their circuit diagrams. The pulse shape discrimination units, variable delay units, or gate units and interface logic units were constructed following the circuits described by Davie[82].

1. Fast Pre-amplifier

A fast low noise pre-amplifier similar to that described by Sherman et al[83] was constructed for the He^3 particle fast pulse. The voltage gain of the pre-amplifier in a 50 ohms load is 9 and the rise time of the output pulse is about 1 ns. The fast signal developed across the 10 k resistor is amplified in the pre-amplifier. The circuit diagram of the fast pre-amplifier is shown in Fig. (A.1). Special care was taken when building the circuit over layout and earth connections to avoid a tendency to produce oscillations.

2. Fast Amplifier

The circuit diagram of the fast insertion amplifier is shown in Fig. (A.2) following the design of Sherman et al[83]. The voltage gain of the insertion amplifier in a 50 ohms load is 7. The He^3 particle fast signal after being amplified in the pre-amplifier was amplified in the insertion amplifier connected very close to the pre-amplifier to obtain a better signal to noise ratio. The output signal can be taken from either the collector or emitter of Q_2 depending upon the desired polarity. In the present case the output is taken from the collector of Q_2.

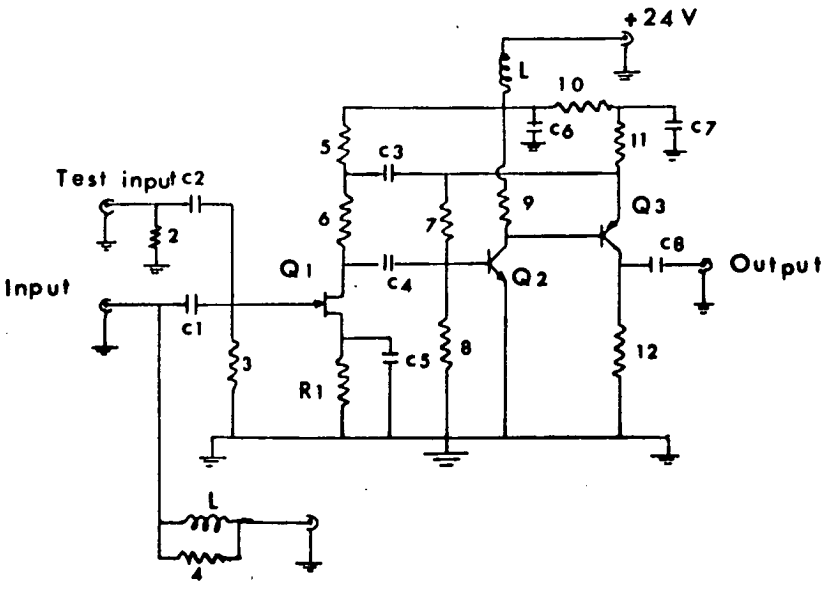

Resistors:

R_1 = 10K	7 = 90 K ohms	C_1 = 1000 PF	C_5 = 0.1 μF	Q_1 = 2N4393
2 = 50 ohms	8 = 10 K ohms	C_2 = 2 PF	C_6 = 0.05 μF	Q_2 = 2N2857
3 = 22 M ohms	9 = 4 K ohms	C_3 = 0.05 μF	C_7 = 0.05 μF	Q_3 = 2N4261
4 = 5.6K ohms	10 = 2 K ohms	C_4 = 0.05 μF	C_8 = 0.05 μF	
5 = 600 ohms	11 = 82 ohms			
6 = 1 K ohms	12 = 330 ohms			

Fig. (A.1) FAST LOW NOISE PRE-AMPLIFIER

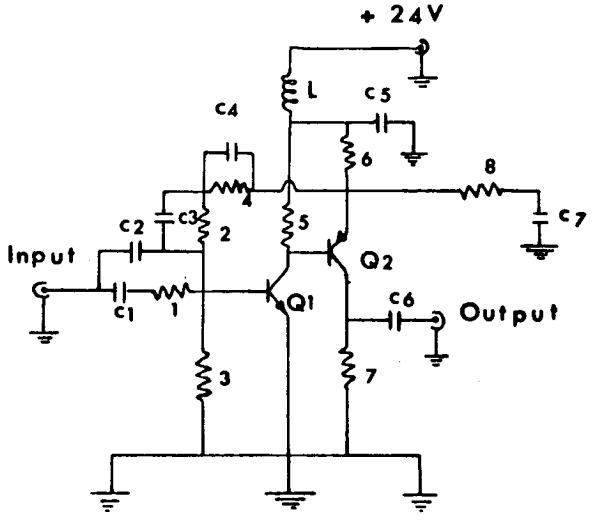

Resistors:

1 = 50 ohms	5 = 4 K ohms
2 = 365 ohms	6 = 2.2 K ohms
3 = 10 K ohms	7 = 330 ohms
4 = 90 K ohms	8 = 50 ohms

Capacitors:

C_1 = 0.1 μF	C_5 = 0.05 μF
C_2 = 5 PF	C_6 = 0.1 μF
C_3 = 2.2 PF	C_7 = 0.1 μF
C_4 = 0.1 μF	Q_1 = 2N2857
	Q_2 = 2N4261

Fig. (A.2) FAST LOW NOISE INSERTION AMPLIFIER

3. Pulse Shape Discrimination Unit (PSD)

Six pulse shape discrimination units, also called as pulse shape analysers, were constructed in standard single-width NIM modules for rejecting gamma-ray events in the neutron detectors. The circuit diagram and the photograph of its layout are shown in Fig. (A.3). For the optimum working of the unit with a particular detector the differentiation time constant R_7 C_2 was adjusted around the value 0.44 μ sec. The present circuit differs from the previous circuit of Davie[82] in that the transistors T_{5a}, T_{5b} (2C444) and T_{5c} (BFY74) are replaced by using half of a six transistors integrated circuit package CA 3049 to act as the time to amplitude converter. For better performance the pulse shape discrimination unit also requires the capacitor C_{10} to be adjusted to suit a particular neutron detector. The transistor T_6 (BFX48) was replaced by type 2N 1132, the collector of which provides an inverted and amplified output from the TAC stage. The load of the 2N 1132 transistor is a 0.6 μ sec delay with a matching resistor of 620 ohms at its input and a short circuit at its far end. Also for the best performance of the pulse shape discrimination unit some capacitors of different values were used from those used by Davie[82].

4. Variable Delay Unit

Eight variable delay units were constructed. These were used to delay the various pulses for coincidence requirements in the time-of-flight system. The circuit diagram of the delay unit and the photograph of the layout of the circuit are shown in Fig. (A.4). The Resistor-Transistor Logic (RTL) family of integrated circuits were used in the units. The NOR gate 991429 and NOT gate 992729 forms a monostable circuit. The range of the variable delay unit

Fig. (A.3) THE PULSE SHAPE DISCRIMINATION UNIT

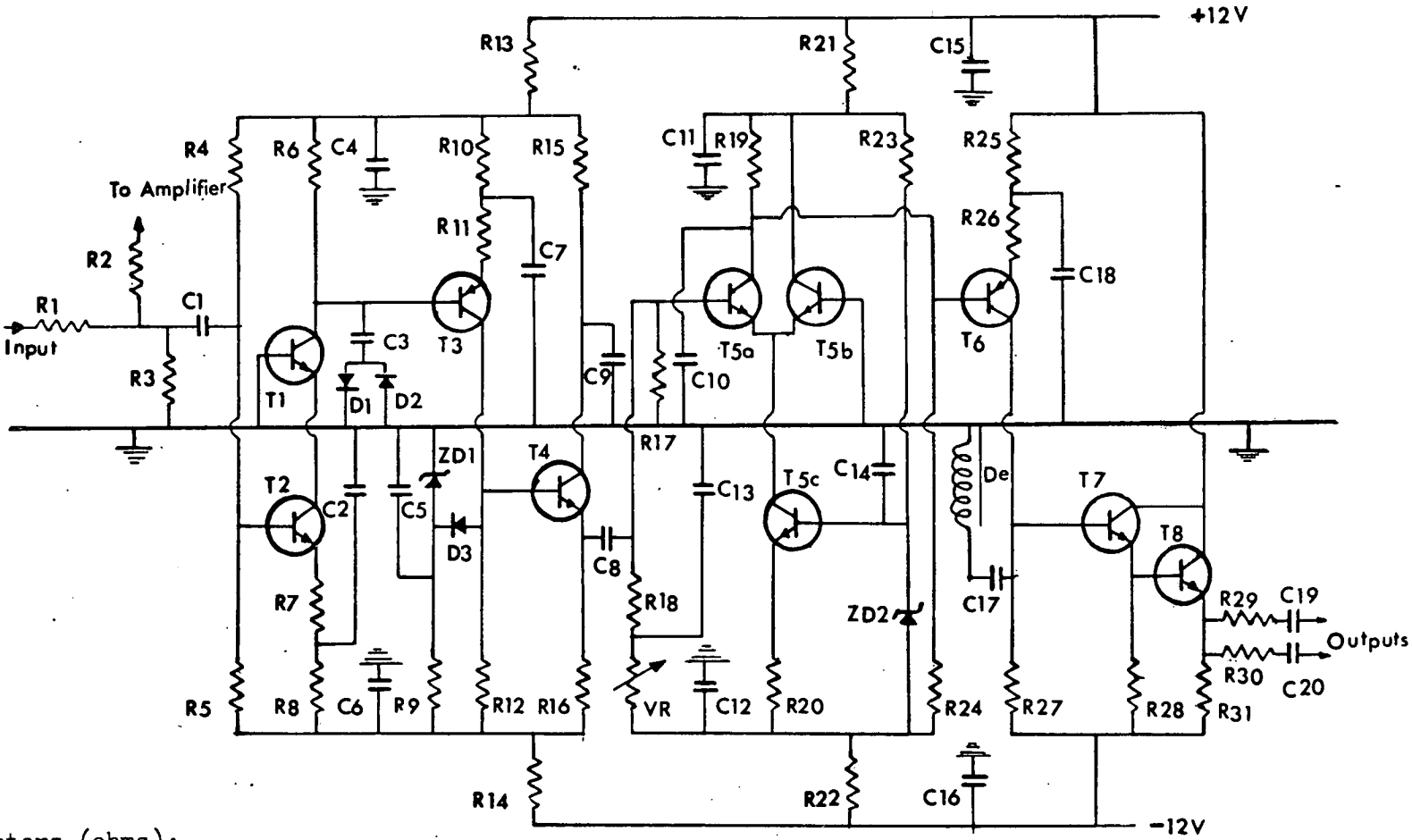

Resistors (ohms):

R_1	= 33	R_{12}	= 1.5K	R_{23}	= 4.7K	C_1	= 2.2 μF	C_{12}	= 2.2 μF	T_1	= BFY75	D_1	= 1N251		
R_2	= 33	R_{13}	= 68	R_{24}	= 18	C_2	= 6400 PF	C_{13}	= 1 μF	T_2	= BFY75	D_2	= 1N251		
R_3	= 150	R_{14}	= 68	R_{25}	= 120	C_3	= 0.47 μF	C_{14}	= 0.22 μF	T_3	= BFX48	D_3	= 1N251		
R_4	= 15K	R_{15}	= 680	R_{26}	= 39	C_4	= 2.2 μF	C_{15}	= 2.2 μF	T_4	= BFY75	ZD1	= BZY88-C4V3		
R_5	= 3.9K	R_{16}	= 680	R_{27}	= 620	C_5	= 0.22 μF	C_{16}	= 2.2 μF	T_5	= CA3049	ZD2	= BZY88-C4V3		
R_6	= 1.8K	R_{17}	= 10K	R_{28}	= 3.3K	C_6	= 2.2 μF	C_{17}	= 0.22 μF	T_6	= 2N1132				
R_7	= 68	R_{18}	= 33K	R_{29}	= 82	C_7	= 2.2 μF	C_{18}	= 1 μF	T_7	= BFY75	De	= CCCB818-7		
R_8	= 1.5K	R_{19}	= 2.2K	R_{30}	= 82	C_8	= 0.22 μF	C_{19}	= 0.22 μF	T_8	= 2N1711				
R_9	= 4.7K	R_{20}	= 1.2K	R_{31}	= 1.2K	C_9	= 0.22 μF	C_{20}	= 0.22 μF						
R_{10}	= 1.2K	R_{21}	= 100	VR	= 1M	C_{10}	= 1500PF								
R_{11}	= 100	R_{22}	= 100			C_{11}	= 2.2 μF								

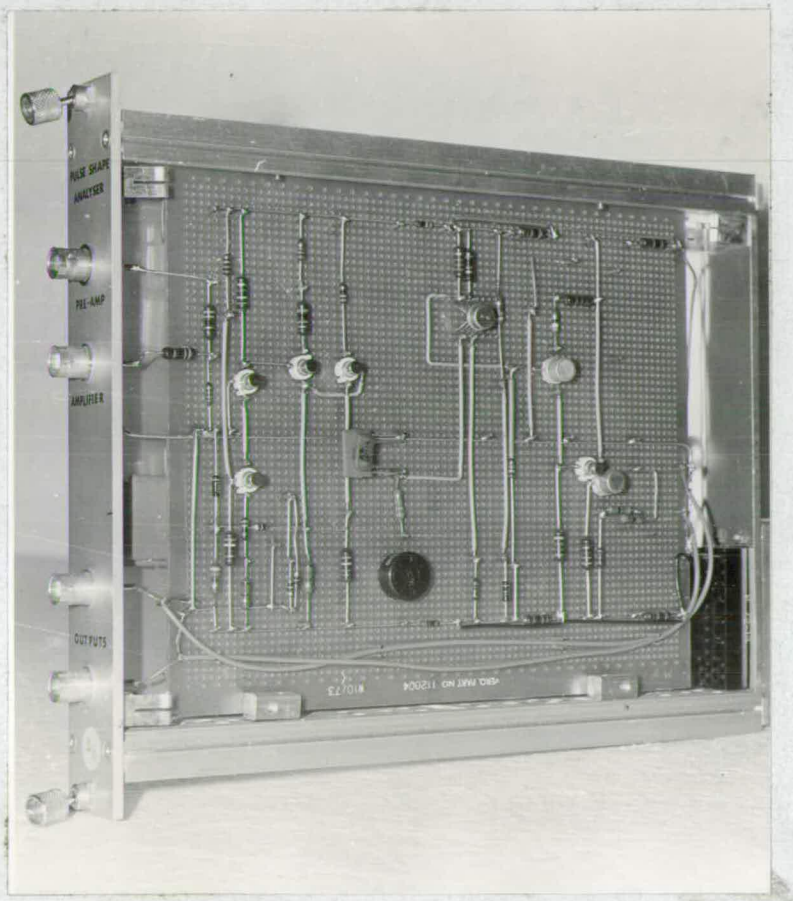

Fig. (A.3) PHOTOGRAPH OF THE PULSE SHAPE DISCRIMINATION UNIT

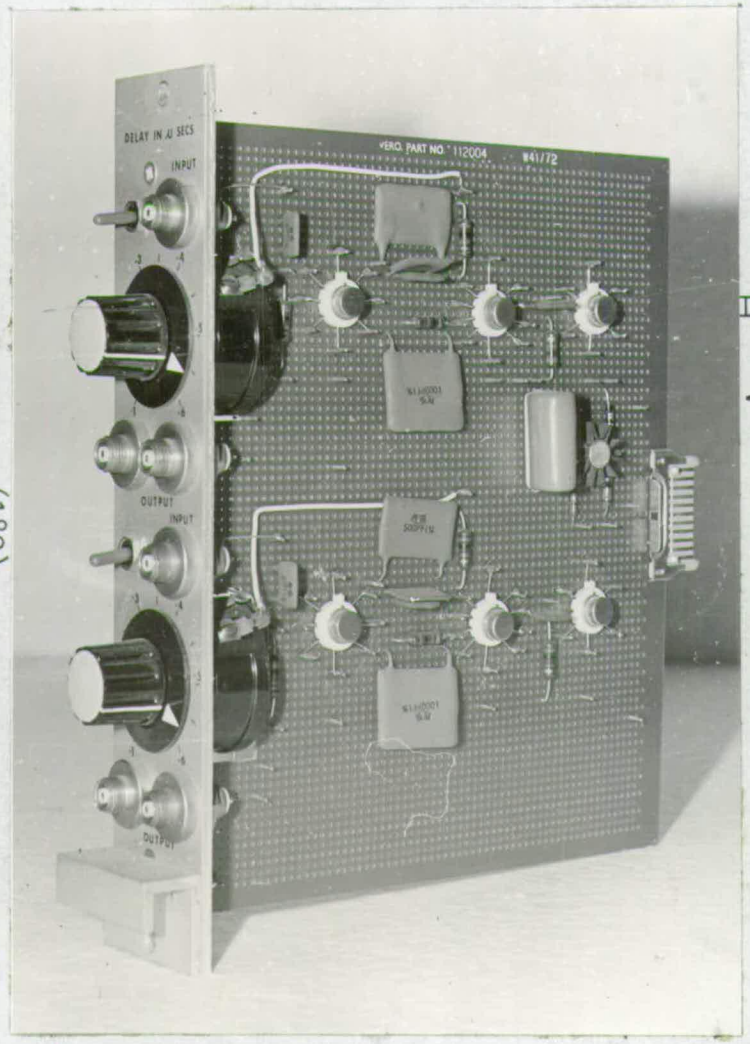

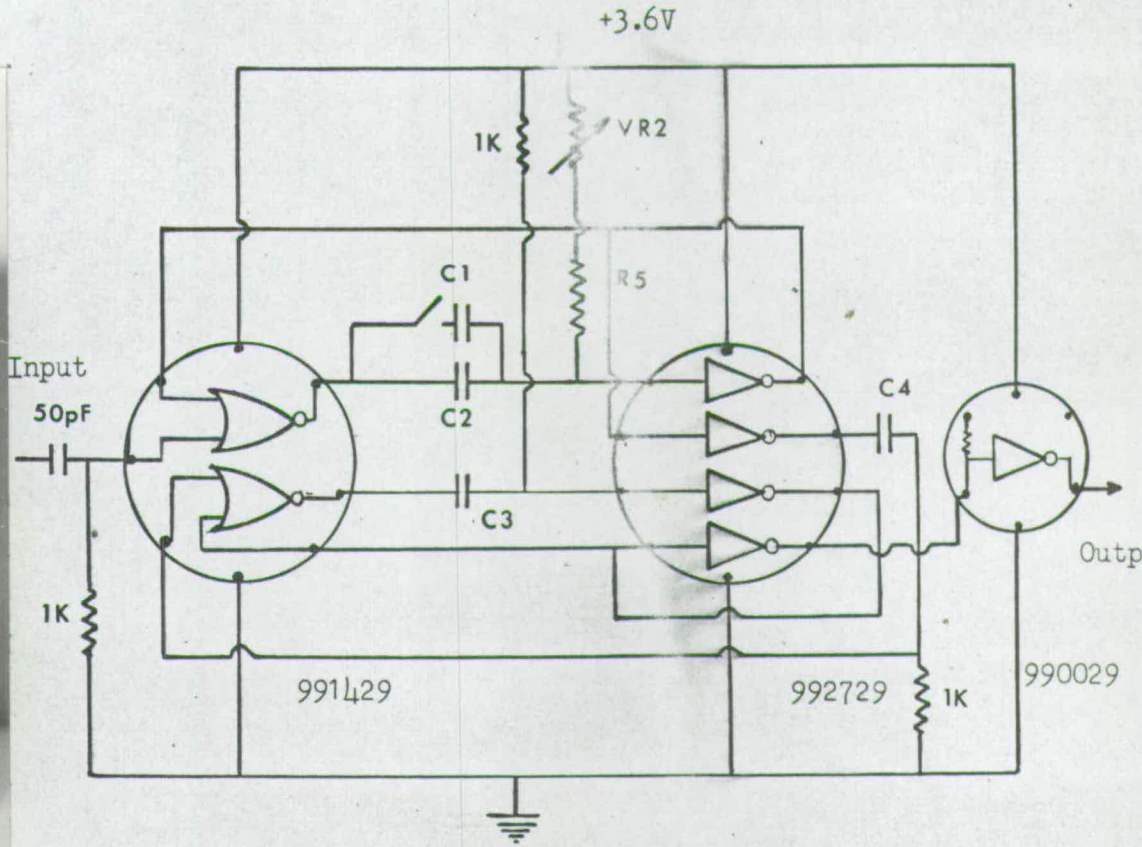

R_5	=	1K	C_3	=	1000 pF
C_1	=	500 pF	C_4	=	25 pF
C_2	=	125 pF	VR_2	=	5K

Fig. (A.4) THE VARIABLE DELAY UNIT

can be extended up to any desired value from period T_d of the monostable defined by C_1, C_2, R_5 and V_{R2}. The laboratory's standard integral discriminator pulses (positive pulses 3V in amplitude and 0.6 μ sec width) are required as the input pulses for the unit.

5. OR Gate Unit

Four OR gate units were constructed to route the time-of-flight spectra to selected sections of the memory of the multichannel pulse height analyser. The circuit diagram and the photograph of its layout are shown in Fig. (A.5). The photograph also shows the layout of an interface logic unit. The laboratory's standard integral discriminator output pulse is required as the input pulse for the OR gate unit.

6. Interface Logic Unit

Four interface logic units (K/S drive units) were constructed which accept pulses from OR units, variable delay units, coincidence units or integral discriminators and shape them properly to meet the coincidence input or routing input requirements of the Laben 400 and 512 channel analysers used in the present measurements. The circuit diagram and the photograph of its layout are shown in Fig. (A.6). The period of the output pulse about 4 μ sec is defined by R_3 and C_1. The output pulse amplitudes at A and B can be adjusted by the potentiometers shown in the diagram and were $\pm$ 5.5 volts. The positive pulses from B were used to trigger the scalers.

7. The Scaler

A six digit scaler was constructed following the design by Bradford[86]. Nixie tubes were used to display the counts. For the remote count control of

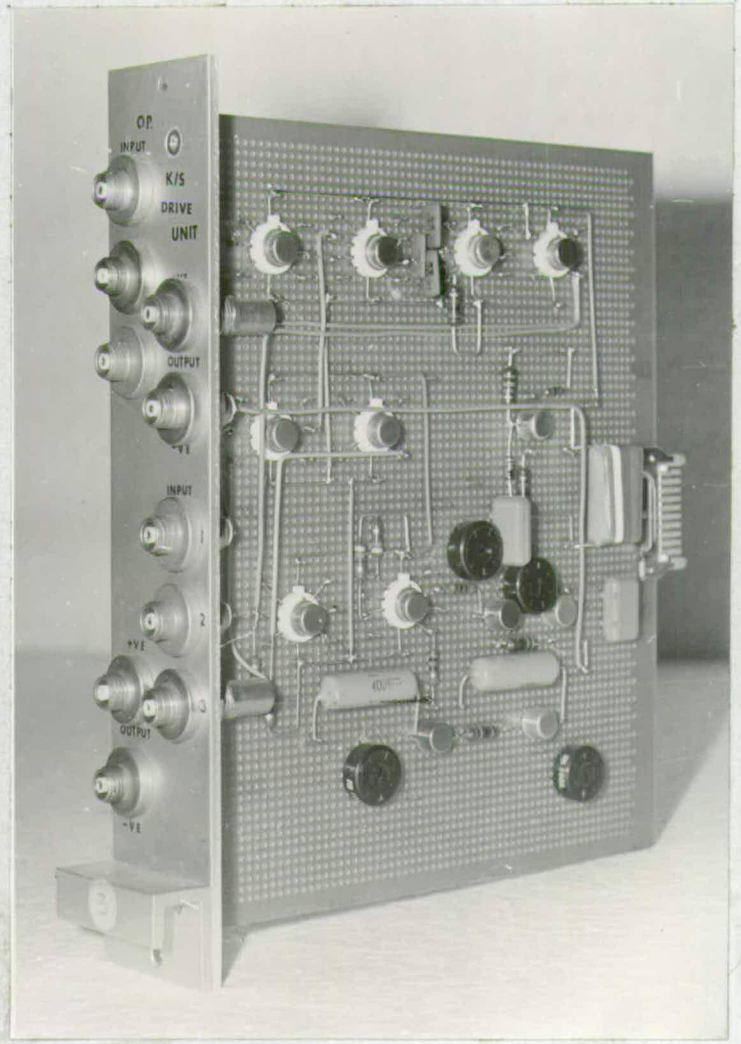

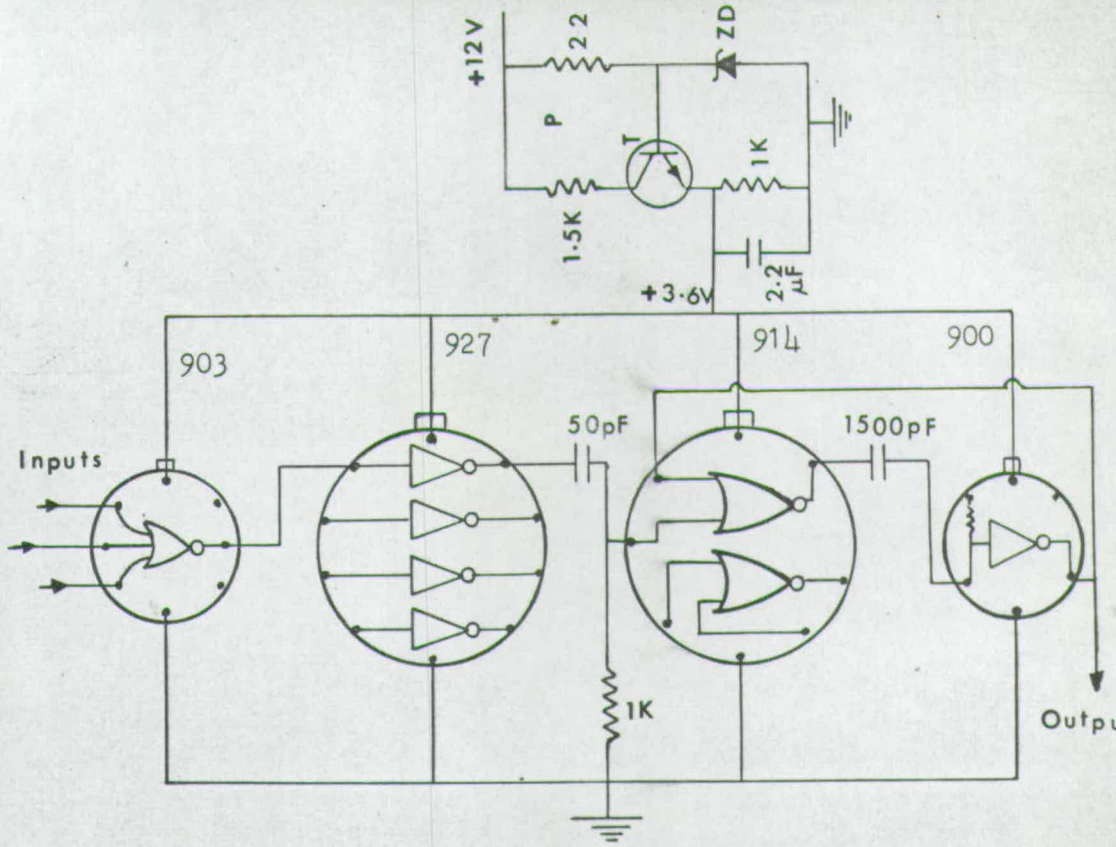

ZD = BZY88 (C4V3)

T = 2N1711

P = Circuit to produce a +3.6V supply from a +12V supply

Fig. (A.5) THE OR GATE UNIT

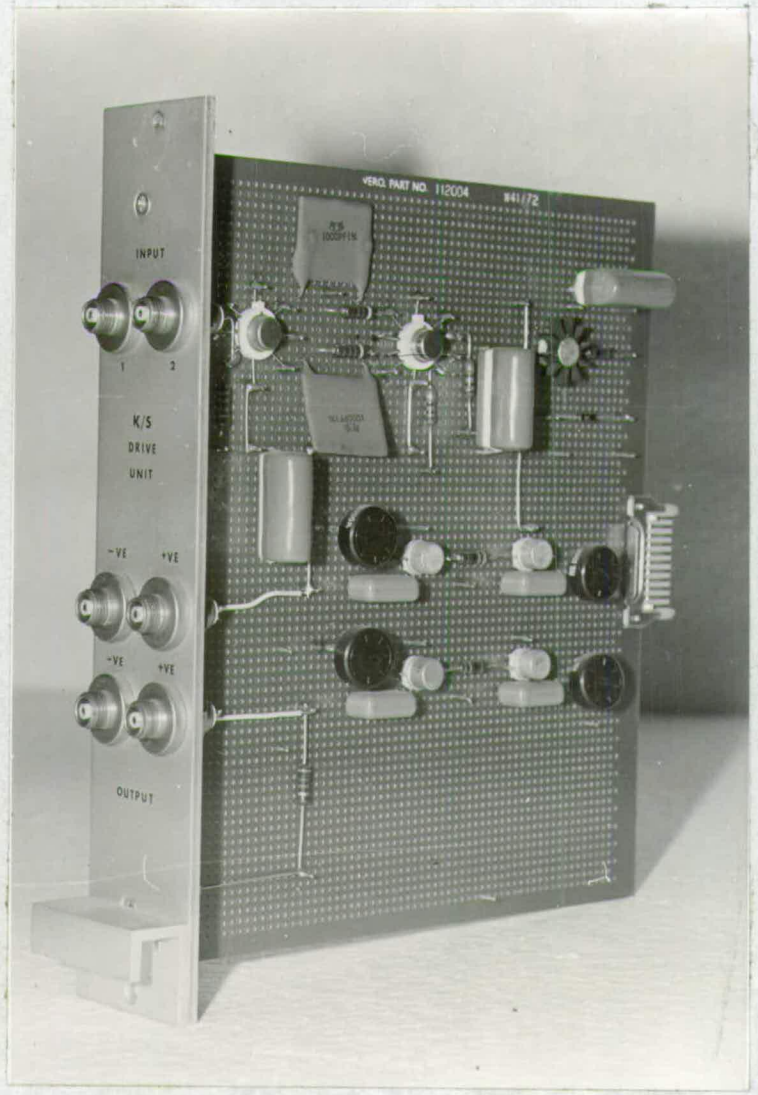

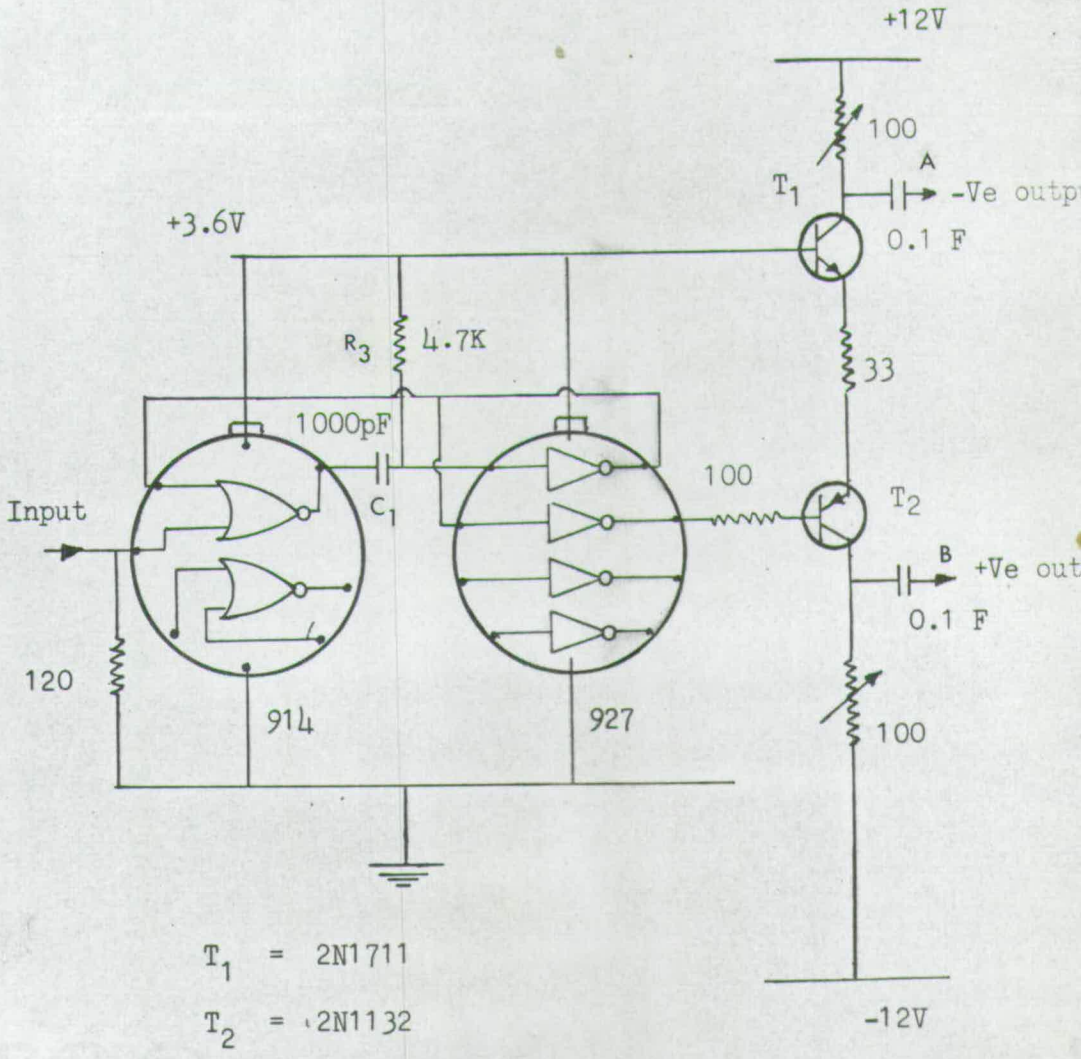

T_1 = 2N1711

T_2 = 2N1132

Fig. (A.6) THE INTERFACE LOGIC UNIT

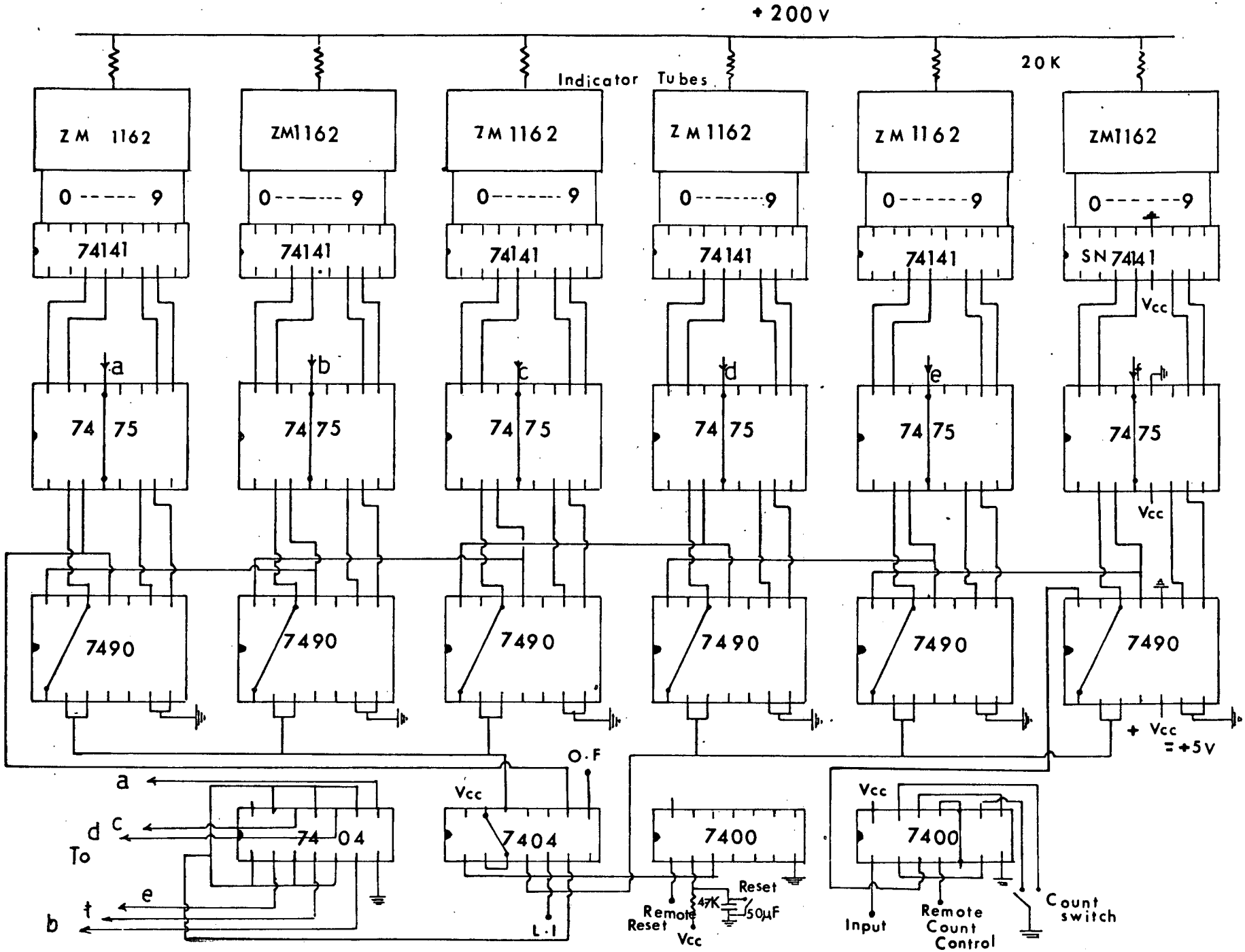

Fig. (A·7) THE SCALER

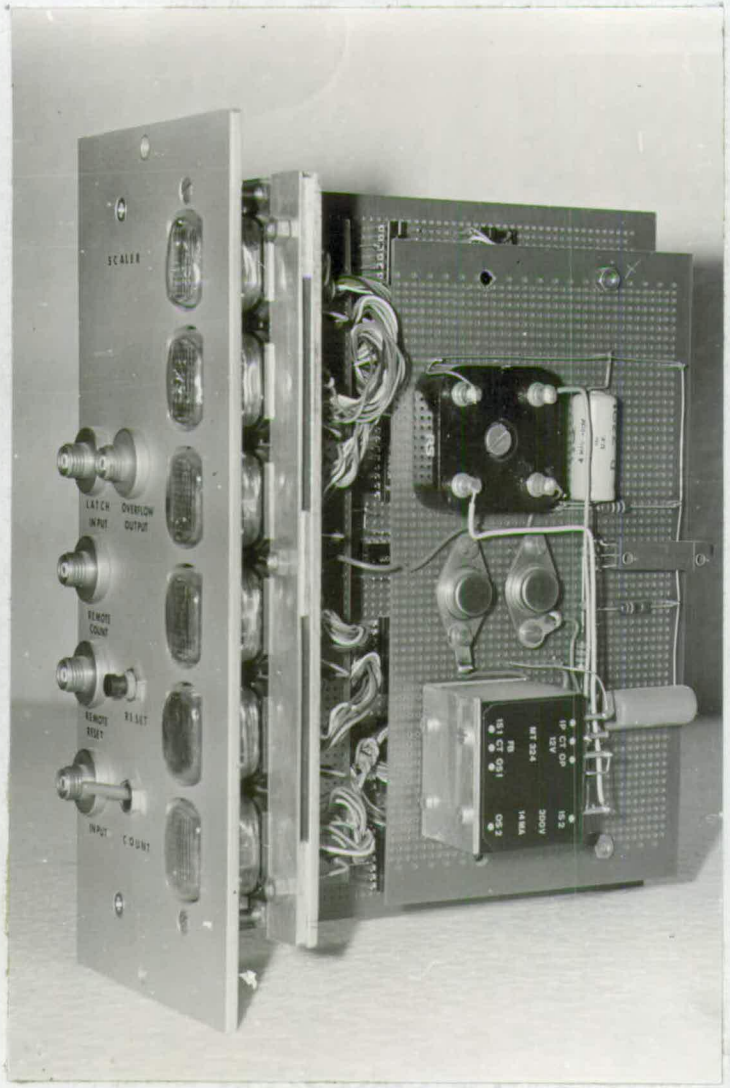

PHOTOGRAPH OF THE SCALER

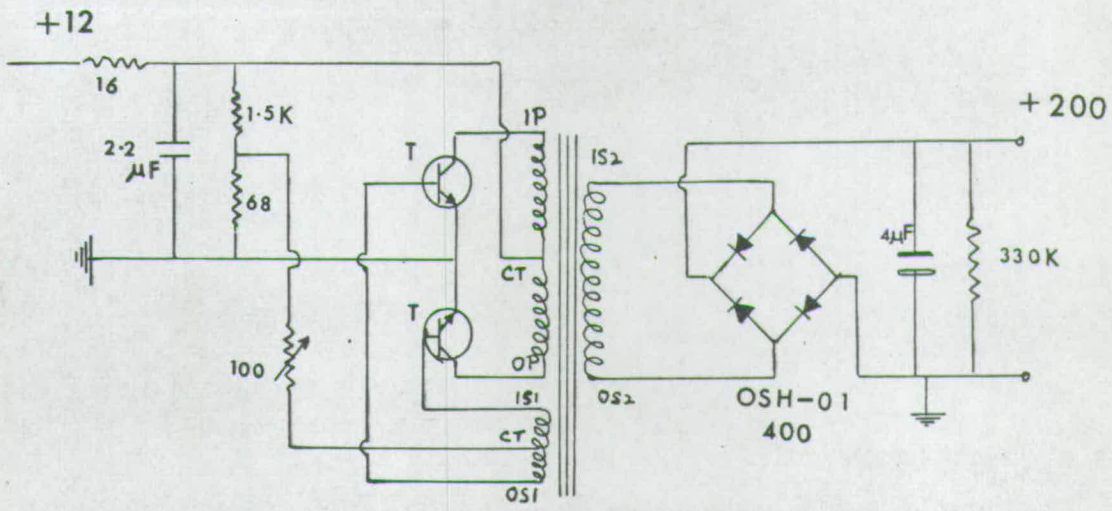

T = 2N3054

Fig. (A.7a) CONVERTER FOR 200V SUPPLY TO INDICATE TUBES

the scaler by the Laben 400 and 512 channel analysers a circuit (not shown) was built. This circuit sends a change in logic level to the remote count control section of the scaler at the end of the accumulation of the data in the analyser. The circuit diagram of the scaler and its photograph are shown in Fig. (A.7). Overflow counts can be fed to another similar scaler. A latch facility is also provided in the scaler so that the number of counts may be noted at any time during counting on terminating the latch input by a connection to earth while counting in the scaler continues. The nixie tubes required +200 volts at their anodes and a power supply was constructed to provide this, the circuit being shown in Fig. (A.7a). The scaler can also be triggered by the laboratory's standard integral discriminator pulse.

8. Timing Single Channel Analyser

For the collimated beam monitor a timing single channel analyser was constructed in a standard single-width NIM module following the circuit described by Gottlieb[85]. The difference from the original circuit is that a termination of 330 ohms was found to be necessary at the NOR gate (SN7402N) on pins 5 and 11. The circuit diagram and the photograph of its layout are shown in Fig. (A.8). In place of transistor type 2N3643 a transistor type 2N1711 was used with a 5 volt zener diode type BZY88 for the +5 volts power supply and at the input stage of the analyser a transistor type BFY75 was used. A type SN72710N integrated circuit is the high speed voltage comparator for level detection. SN7402N and SN7400N integrated circuits are the NOR and NAND gates. A type SN74121N integrated circuit is the one shot multivibrator. Two type (7402) integrated circuits constitute a flip-flop.

The lowest comparator in the figure gives a clock pulse from an input

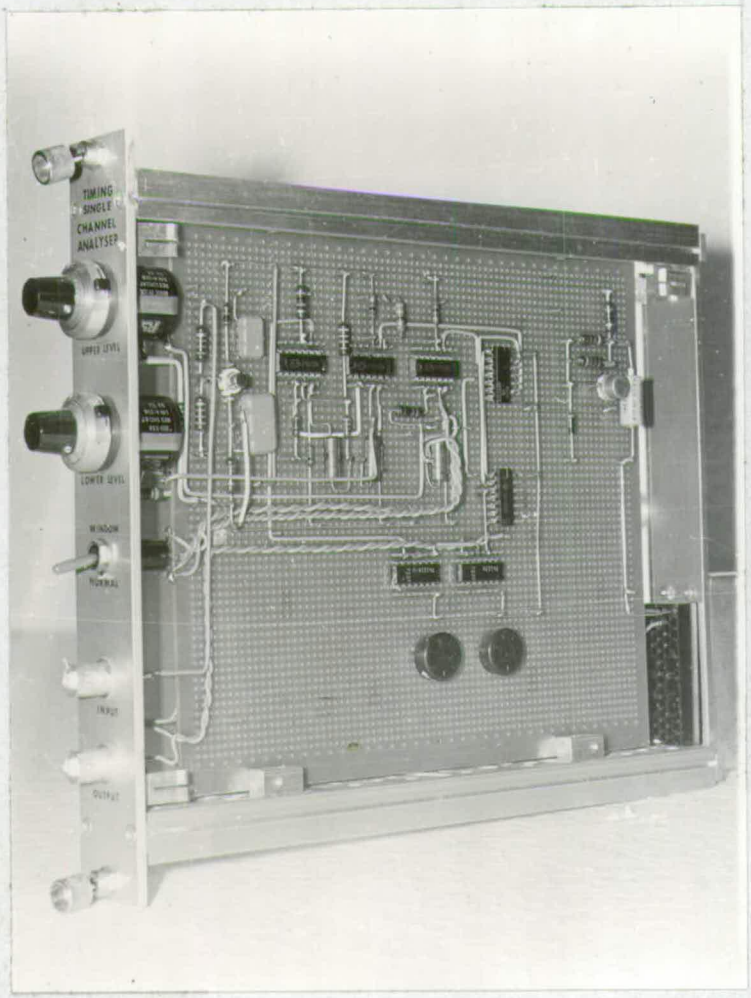

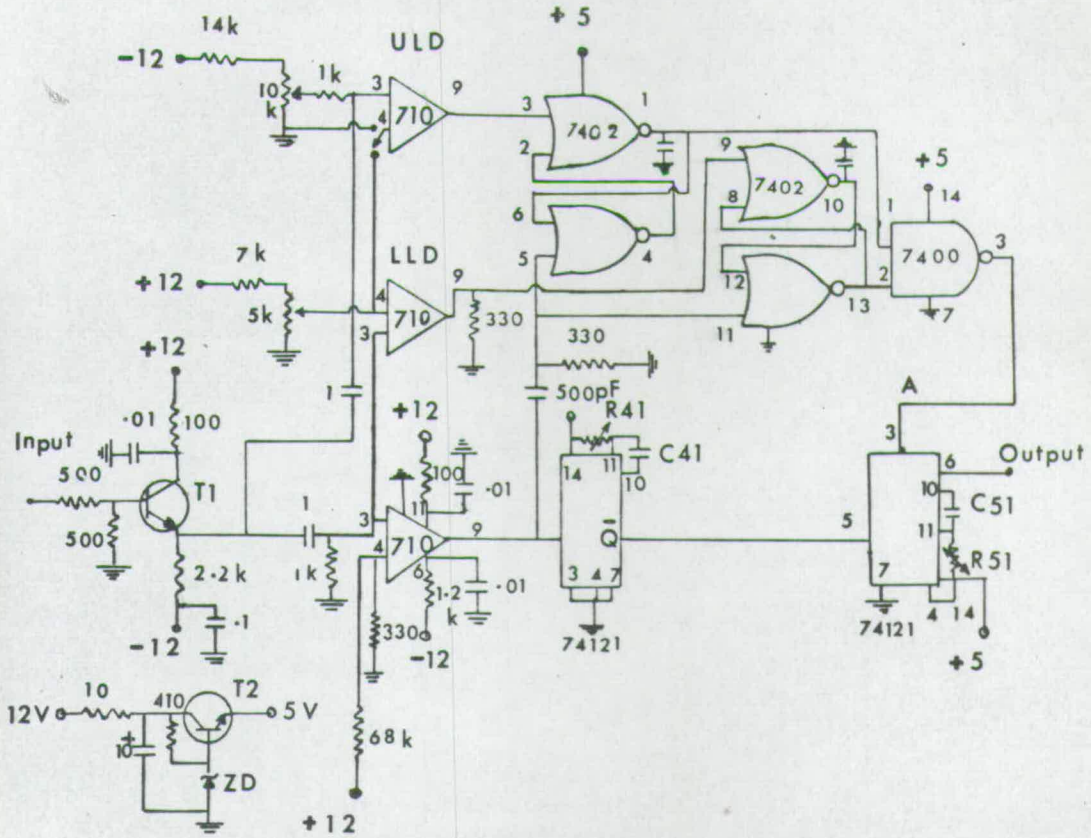

All capacitors in F, unless indicated

Capacitors on 7402 are 10 pF

R_{41} = 10K	R_{41} = 500 pF	T_1 = BFY75
R_{51} = 10K	R_{51} = 330 pF	T_2 = 2N1711

Fig. (A.8) TIMING SINGLE CHANNEL ANALYSER

which triggers the one shot multivibrator (74121) and resets both the lower level discriminator (LLD) and the upper level discriminator (ULD) flip-flops. The clock time is $T_r = R_{41} C_{41} \ln 2 \simeq 1 \mu$ sec. When an input pulse at LLD rises above the voltage on the LLD potentiometer, the LLD (710) output voltage goes high and so the voltage on pin 13 of the flip-flop (7402) becomes high. If the input pulse at ULD is not greater than the magnitude of the voltage across ULD potentiometer then ULD output voltage is low and the voltage on pin 1 of the flip-flop (7402) becomes high and so the voltage at A is low since the voltage on both pins 1 and 2 of NAND (7400) is high. If the voltage at A is low an output pulse will result at pin 6 of 74121. The amplitude of the output pulse is +3 volts and the width was adjusted by the potentiometer R_{51} and capacitor C_{51} to be 2 μ sec.

References

1. N. Bohr, Nature (London) 137, 344 (1936)

2. E. Amaldi; D. Bocciarelli; B.N. Cacciapuoti and G. C. Trabacchi, Nuovo Cimento Ser. 9, 3, 203 (1946)

3. M. Walt and H.H. Barschall, Phys. Rev. 93, 1062 (1954)

4. H. Feshbach, C.E. Porter and V.F. Weisskopf, Phys. Rev 96, 448 (1954)

5. J.R. Beyster, "Predictions of Fast Neutron Scattering Data with a Diffuse Surface Potential Well", Los Almos Scientific Lab. Report LA-2099 (1957)

6. J.H. Coon, R.W. Davis, H.E. Felthauser and D.B. Nicodemus, Phys. Rev. 111, 250 (1958)

7. W.G. Cross and R.G. Jarvis, Phys. Rev. 99, 621 (1955)

8. R.W. Hill, Phys. Rev. 109, 2105 (1958)

9. Langsdorf, Jr., R.O. Lane and J.E. Monahan, Phys. Rev. 107, 1077 (1957)

10. M. Walt and J.R. Beyster, Phys. Rev. 98, 677 (1954)

11. F. Bjorklund and S. Fernbach, Phys. Rev. 109, 1295 (1958)

12. F. Perey and B. Buck, Nucl. Phys. 32, 353 (1962)

13. D. Wilmore and P.E. Hodgson, Nucl. Phys. 55, 673 (1964)

14. P.E. Hodgson, "Nuclear Reaction and Nuclear Structure", Oxford University Press 1971

15. L. Rosen, J.G. Beary, A.S. Goldhaber and E.H. Auerbach, Ann. Phys. 34, 96 (1965)

16. F.D. Becchetti, Jr., and G.W. Greenless, Phys. Rev. 182, 1190 (1969)

17. L. Rosen, Proc. Intern. Conf. on the Study of Nuclear Structure with Neutrons, Antwerp, 1965, Page 379

18. W. Hüser and H. Feshbach, Phys. Rev. 87, 366 (1952)

19. R.G. Thomas, Phys. Rev. 97, 224 (1955)

20. D. Wilmore, A.E.R.E., R-4649 (1964)

21. J. Schwinger, Phys. Rev. 69, 681, (1946)

22. L. Wolfenstein, Phys. Rev. 75, 342 (1949)

23. E.J. Konopinski and E. Teller, Phys. Rev. 73, 822 (1948)

24. W. Haeberli, Fast Neutron Physics, Part II, Chap. V.G. (Interscience New York 1963)

25. R.K. Adair, S.E. Darden and R.E. Fields, Phys. Rev. 96, 503 (1954)

26. J.D. Clement, F. Boreli, S.E. Darden, W. Haeberli and H.R. Striebel, Nucl. Phys. 6, 177 (1958)

27. L. Cranberg, Helv. Phys. Acta Supp. 6, 311 (1961)

28. R.J. Olness, K.K. Seth and H.W. Lewis, Nucl. Phys. 52, 529 (1964)

29. A.T.G. Ferguson, R.E. White and D. Wilmore, Nucl. Phys. 76, 369 (1966)

30. A.S. Mahajan, Nucl. Phys. A95, 193 (1967)

31. B.M. McCormac, M.F. Steuer, C.D. Bond and F.L. Hereford, Phys. Rev. 108, 116 (1957)

32. D.J. Bredin, Phys. Rev. 135, B412 (1964)

33. J. Durisch, R. Gleyvod, P. Huber and E. Baumgartner, Helv. Phys. Acta 36, 269 (1963)

34. A.J. Elwyn, R.O. Lane, A. Langsdorf, Jr. and J.E. Monahan, Phys. Rev. 133, B80 (1964)

35. G.V. Gorlov, N.S. Lebedeva and V.M. Morozov, Yad. Fiz. 5, 910 (1967)
(English Trans. Soviet J. Nucl. Phys. 6, 663 (1968))

36. K. Wiedemann, E. Baumgartner, D. Ellgehausen, R. Gleyvod and P. Huber, Helv. Phys. Acta 42, 259 (1969)

37. D. Ellgehausen, E. Baumgartner, R. Gleyvod, P. Huber, A. Stricker and K. Wiedemann, Helv. Phys. Acta 42, 269 (1969)

38. M.V. Pasechnik, I.A. Korzh, I.E. Kashuba, V.M. Mishchenko, N.M. Pravdivyi and I.E. Sanzhur, Yad. Fiz. 11, 958 (1970)
(English Trans. Soviet J. Nucl. Phys. 11, 533 (1970))

39. E. Zijp and C.C. Jonker, Nucl. Phys. A 222, 93 (1974)

40. E. Zijp, Ph.D. Thesis 1972, Vrije Universiteit, Amsterdam, The Netherlands

41. I.E. Kashuba and B.D. Kozin, Ukrayin. Fiz. Zh., 13, 51 (1968)
(English Trans. Ukr. Phys. J. 13, 33 (1968))

42. R.B. Galloway, Proc. R.S.E. (A), 70, 16 (1971/72)

43. F.L. Hereford, Helv. Phys. Acta Suppl. 6, 303 (1961)

44. H. Prade and J. Csikai, Nucl. Phys. A 123, 365 (1969)

45. P. Shapiro and R.W. Higgs, Phys. Rev. 108, 760 (1957)

46. P.L. Okhuysen, E.W. Bennett, J.B. Ashe and W.E. Millet, Rev. Sci. Instr. 29, 982 (1958)

47. W.R. Dixon and J.H. Aitken, Nucl. Phys. 24, 456 (1961)

48. C.F. Cook, Nucl. Instr. and Meth. 15, 137 (1962)

49. R.A.I. Bell, N.G. Chapman and P.B. Johnson, Nucl. Instr. and Meth. 33, 13 (1965)

50. L.W. Put, C. Bot, W.J. Coenders, J.W. Koene and J. Block, Physica, 32, 1397 (1966)

51. T.H. Hsu and J.M. Robson, Nucl. Instr. and Meth. 39, 8 (1966)

52. L.F.C. Monier, G.E. Tripard and B.L. White, Nucl. Instr. and Meth. 45, 282 (1966)

53. R.W. Finlay, "Nuclear Research with low Energy Accelerators" Academic Press, New York (1967), Page 311

54. C.M. Bartle, N.G. Chapman, P.B. Johnson and J.E. Callaghan, Nucl. Instr. and Meth. 63, 39 (1968)

55. G.E. Tripard, L.F.C. Monier, B.L. White and P.W. Martin, Nucl. Instr. and Meth. 66, 261 (1968)

56. D.G. Schuster, Nucl. Instr. and Meth. 76, 35 (1969)

57. R. McFadden, P.W. Martin and B.L. White, Nucl. Instr. and Meth. 92, 563 (1971)

58. C.M. Bartle, N.G. Chapman and P.B. Johnson, Nucl. Instr. and Meth. 95, 221 (1971)

59. P.B. Johnson, J.E. Callaghan, C.M. Bartle and N.G. Chapman, Nucl. Instr. and Meth. 100, 141 (1972)

60. J.H. Neiler and W.M. Good, Fast Neutron Physics, Part I, Chap. IVA (Interscience, New York 1960)

61. V.E. Parker and R.F. King, Bull. Am. Phys. Soc. (2) 1, 70 (1956)

62. M.P. Nakada, V.J. Ashby, M. Harris and W. Klein, Bull. Am. Phys. Soc. (2) 1, 69 (1956)

63. N.N. Flerov and E.A. Tamanov, Soviet J. Atomic Energy 3, 776 (1956)

64. R.C. Mobley, Rev. of Sci. Instr. 34, 256 (1963)

65. J.B. Marion and F.C. Young, Nucl. Reaction Analysis Graphs and Tables (North Holland 1968)

66. F.S. Goulding, Nucl. Instr. and Meth. 43, 1 (1966)

67. G. Bertolini, "Semi Conductor Detectors" (North Holland 1968)

68. R.B. Galloway, Nucl. Instr. and Meth. 92, 537 (1971)

69. R.E. Warren, J.L. Powell and R.G. Herb, Rev. of Sci. Instr. 18, 559 (1947)

70. Harold V. Argo, Phys. Rev. 74, 1293 (1948)

71. S.K. Allison, S.P. Frankel, T.A. Hall, J.H. Montague, A.H. Morrish and S.D. Warshaw, Rev. of Sci. Instr. 20, 735 (1949)

72. Fowler, Lauritsen and Lauritsen, Rev Sci. Instr. 18, 818 (1947)

73. A.O. Hanson and D.L. Benedict, Phys. Rev. 65, 33 (1944)

74. F.D. Brooks, Nucl. Instr. and Meth. 4, 151 (1959)

75. W. Daehnick and R. Sherr, Rev. of Sci. Instr. 32, 666 (1961)

76. B. Sabbah and A. Suhami, Nucl. Instr. and Meth. 58, 102 (1968)

77. R.B. Owen, Nucleonics 17, 72 (1959)

78. R. Batchelor, W.B. Gilboy, A.D. Purnell and J.H. Towle, Nucl. Instr. and Meth. 8, 146 (1960)

79. F.A. Johnson, Can. J. Phys. 41, 793 (1963)

80. T.K. Alexander and F.S. Goulding, Nucl. Instr. and Meth. 13, 244 (1961)

81. F.A. Johnson, Nucl. Instr. and Meth. 58, 134 (1968)

82. H. Davie, Ph.D. Thesis, University of Edinburgh, 1972

83. I.S. Sherman, R.G. Roddick and A.J. Metz, IEEE Trans. Nucl. Sci. NS-15, No. 3, 500 (1968)

84. A.M. Alsoraya, Private Communication, Physics Dept., Edinburgh University.

85. Albert M. Gottlieb, Nucl. Instr. and Meth. 114, 193 (1974)

86. Dr. G. Bradford, Private Communication, Physics Dept., Edinburgh University

87. M. Walt, Fast Neutron Physics, Part II, Page 1033 (Interscience, New York 1963)

88. J. Block, C.C. Jonker, Physica 18, 809 (1952)

89. S.A. Cox, Nucl. Instr. and Meth. 56, 245 (1967)

90. J.B. Parker, J.H. Towle, D. Sams and P.G. Jones, Nucl. Instr. and Meth. 1, 14 (1961)

91. R.O. Lane and W.F. Miller, Nucl. Instr. and Meth. 16, 1 (1962)

92. B. Holmqvist, B. Gustavsson and T. Wiedling, Arkiv For Fysik 481, 34 (1967)

93. W.E. Kinney, Nucl. Instr. and Meth. 15, 83 (1970)

94. H. Amster, E.J. Leshan, M. Walt, Fast Neutron Physics, Part I (Interscience, New York 1960)

95. L. Drigo, C. Manduchi, G. Moschini, M.T. Russo Manduchi, G. Tornielli and G. Zannoni, Nucl. Phys. A181, 177 (1972)

96. A.F. Behof, T.H. May and W.I. McGarry, Nucl. Phys. A108, 250 (1968)

97. H.J. Boersma, C.C. Jonker, J.G. Nijenhuis and P.J. Van Hall, Nucl. Phys. 46, 660 (1963)

98. J.P.F. Mulder, Phys. Lett. 23, 589 (1966)

99. P. Roding and H. Scholermann, Nucl. Phys. A125, 585 (1969)

100. H. Davie and R.B. Galloway, Nucl. Instr. and Meth. 108, 581 (1973)

101. R.M.A. Maayouf and R.B. Galloway, Nucl. Instr. and Meth. 118, 343 (1974)

102. Dr. L. Drigo, Private Communication, Instituto di Fisica dell' Universita, Padova, Italy

103. R.L. Becker, W.G. Guindon and G.J. Smith, Nucl. Phys. 89, 154 (1966)

104. B. Holmqvist, Arkiv For Fysik Band 38 nr 25, 403 (1968)

105. W.B. Gilboy and J.H. Towle, Nucl. Phys. 64, 130 (1965)

106. R.J. Howerton, UCRL 5351, (1958)

107. D.J. Hughes and R.B. Schwarz, BNL 325 Second Edition (1958)

108. G. Hentschel, Z. Physik 219, 32 (1969)

109. J. Christiansen, F.W. Busser, F. Niebergall and G. Sohngen, Nucl. Phys. 67, 133 (1965)

110. W. Busse, J. Christiansen, D. Hilscher, U. Morfeld, J.A. Scheer, and W.U. Schroder, Nucl. Phys. A100, 490 (1967)

111. J.R. Smith and S.T. Thornton, Nucl. Phys. A187, 433 (1972)

112. C. Wong, J.D. Anderson, J.W. McClure and B.D. Walker, Phys. Rev. 128, 2339 (1962)

113. L. Cranberg and J.S. Levin, Phys. Rev. 103, 343 (1956)

114. L. Cranberg, T.A. Oliphant, J. Levin and C.D. Zafiratos, Phys. Rev. 159, 969 (1967)

115. E. Barnard, N. Coetzee, J.A.M. De Villiers, D. Reitmann and P. Van Der Merwe, Z. Fur Physik 243, 121 (1971)

116. J.A.M. De Villiers, C.A. Engelbrecht, W.G. Vonach and A.B. Smith, Z. Fur Physik, 183, 323 (1965)

117. Nuclear Data Sheets (National Academy of Sciences, National Research Council, Washington, D.C.)

118. B. Holmqvist and T. Weidling, Arkiv For Fysik 35, 71 (1968)

119. J. Felsteiner and R. Serfaty, Nucl. Phys. A148, 428 (1970)

120. J.B. Guernsey and A. Wattenberg, Phys. Rev. 101, 1516 (1956)

121. J.J. Van Loef and D.A. Lind, Phys. Rev. 101, 103 (1956)

122. H.C. Sharma and N. Nath, Nucl. Phys. A106, 241 (1968)

123. P.H. Stelson, R.L. Robinson, H.J. Kim, J. Rapaport and G.R. Satchler, Nucl. Phys. 68, 97 (1965)

124. F. Perey, Proc. Intern. Conf. on the Study of Nuclear Structure with Neutrons, Antwerp, 1965, Page 418

ACKNOWLEDGEMENTS

I wish to thank Professor N. Feather, F.R.S., for the facilities provided for this research. I extend my warm personal thanks to my supervisor, Dr. R.B. Galloway, for his guidance, encouragement and assistance. I am grateful to Dr. G. Bradford for many useful discussions. I also wish to thank my colleagues, A.S. Hall and A.M. Alsoraya for their willing assistance.

I am grateful to Mr. H.J. Napier for maintaining and operating the Van de Graaff accelerator, often at inconvenient hours, and also to Messrs. G. Turnbull and L. Harvey, the technical staff of the Neutron Physics Laboratory, for their willing assistance. Thanks are also due to Messrs. W.S. Jones and T. Montgomery of the Research Workshop for building the mechanical part of the apparatus.

I wish to thank my wife, Samina, for her encouragement and help throughout these studies.